Radiation protection dosimetry and X-ray polarimetry with hybrid pixel detectors

Strahlenschutzdosimetrie und Röntgenpolarimetrie mit hybriden Pixeldetektoren

der Naturwissenschaftlichen Fakultät

der Friedrich-Alexander-Universität Erlangen-Nürnberg

zur

Erlangung des Doktorgrades Dr. rer. nat.

vorgelegt von

Dennis Haag

aus Nürnberg

Als Dissertation genehmigt
von der Naturwissenschaftlichen Fakultät
der Friedrich-Alexander-Universität Erlangen-Nürnberg

Tag der mündlichen Prüfung: 03.06.2022

Vorsitzender des Promotionsorgans: Prof. Dr. Wolfgang Achtziger

Gutachter: PD Dr. Thilo Michel
Prof. Dr. Ivor Fleck

Mündliche Prüfer: Prof. Dr. Uli Katz
PD Dr. Thilo Michel
Prof. Dr. Hanno Sahlmann

Abstract

Hybrid pixel detectors are used for the energy-resolved measurement of ionizing radiation. They are applied in radiation protection dosimetry and X-ray polarimetry in this thesis. One of these is the Dosepix detector. It is composed of a 16×16 pixel matrix with a segmented silicon sensor. Photons deposit their energy in the sensor, and a charge signal is created, which is further processed by its ASIC. Dosepix has a unique operation mode for dosimetry applications. It sorts registered events according to their deposited energy in one of sixteen pre-defined energy bins. Only one column of the matrix is read out at a time, enabling dead-time-free measurements.

A system consisting of three Dosepix detectors is employed for dosimetry of operational quantities in radiation protection. It is important that dosemeters correctly determine the dose for a wide energy range. Therefore, the dependence of the dose measurement on the mean photon energy between 12.4 keV to 1250 keV at angles of radiation incidence up to 60° is determined and compared to official requirements. The minimum national and international requirements are well met and even surpassed for the ambient dose equivalent $H^*(10)$, the directional dose equivalents $H'(3, \Omega)$ and $H'(0.07, \Omega)$, and the personal dose equivalents $H_\mathrm{p}(10)$, $H_\mathrm{p}(3)$, and $H_\mathrm{p}(0.07)$. It is necessary to guarantee that the dosemeter for photon fields is as unresponsive as possible to β-radiation fields. The influence of β-radiation on the photon dose measurement for $H_\mathrm{p}(10)$ is investigated and shown to stay within the required limits. Additionally, a method is presented to classify electron and photon reference fields in radiation fields consisting of one particular particle type. In recent years, individual monitoring of the eye lens dose has been a topic of increased interest since its dose threshold limits were severely restricted. The prototype of the first active eye lens dosemeter comprised of a single Dosepix detector is characterized in its metrological properties in continuous and pulsed photon fields. It fulfills the investigated national and international requirements for an active personal dosemeter to monitor the eye lens dose $H_\mathrm{p}(3)$.

Timepix3 is the other hybrid pixel detector utilized in this thesis. It consists of 256×256 pixels with a pixel pitch of 55 µm and employs a silicon sensor. Timepix3 performs simultaneous measurements of position, time, and energy. The investigated application is X-ray polarimetry. Compton scattering in the sensor allows probing linear polarization of interacting X-rays. Coincident event cluster pairs are searched and correlated in their energy to determine modulation curves carrying information about the degree of linear polarization of the X-ray. Timepix3 is successfully tested in an unpolarized and a linearly polarized photon field, and it is shown that the measured modulation stems from polarized X-rays.

Kurzzusammenfassung

Hybride Pixeldetektoren werden für die energieaufgelöste Messung ionisierender Strahlung verwendet. In dieser Arbeit werden sie in der Strahlenschutzdosimetrie und Röntgenpolarimetrie eingesetzt. Einer dieser Detektoren ist der Dosepix-Detektor. Er besteht aus einer 16×16-Pixel-Matrix mit einem segmentierten Siliziumsensor. Photonen deponieren ihre Energie im Sensor, und es entsteht ein Ladungssignal, das von seinem ASIC weiterverarbeitet wird. Dosepix hat einen speziellen Betriebsmodus für Anwendungen in der Dosimetrie. Er sortiert die registrierten Ereignisse entsprechend ihrer deponierten Energie in einen von sechzehn vordefinierten Energiebins. Es wird jeweils nur eine Spalte der Matrix ausgelesen, was totzeitfreie Messungen ermöglicht.

Ein System aus drei Dosepix-Detektoren wird für die Dosimetrie von Messgrößen im Strahlenschutz eingesetzt. Wichtig ist, dass die Dosimeter die Dosis für einen großen Energiebereich korrekt bestimmen. Deshalb wird die Abhängigkeit der Dosismessung von der mittleren Photonenenergie zwischen 12,4 keV bis 1250 keV bei Strahlungseinfallswinkeln bis zu 60° ermittelt und mit den offiziellen Anforderungen verglichen. Die nationalen und internationalen Mindestanforderungen werden für die Umgebungs-Äquivalentdosis $H^*(10)$, den Richtungs-Äquivalentdosen $H'(3, \Omega)$ und $H'(0{,}07, \Omega)$ und den Personendosen $H_\mathrm{p}(10)$, $H_\mathrm{p}(3)$ und $H_\mathrm{p}(0,07)$ gut erfüllt und sogar übertroffen. Es muss gewährleistet sein, dass das Dosimeter für Photonenfelder möglichst unempfindlich gegenüber β-Strahlungsfeldern ist. Der Einfluss von β-Strahlung auf die Messung der Photonendosis $H_\mathrm{p}(10)$ wird untersucht und es wird gezeigt, dass dieser innerhalb der vorgeschriebenen Grenzen liegt. Außerdem wird eine Methode zur Klassifizierung von Elektronen- und Photonen-Referenzfeldern in Strahlungsfeldern, die aus einer bestimmten Teilchenart bestehen, vorgestellt. In den letzten Jahren ist die individuelle Überwachung der Augenlinsendosis verstärkt in den Blickpunkt des Interesses gerückt, da ihre Dosisgrenzwerte stark eingeschränkt wurden. Der Prototyp des ersten aktiven Augenlinsendosimeters, das aus einem einzigen Dosepix-Detektor besteht, wird in seinen messtechnischen Eigenschaften in kontinuierlichen und gepulsten Photonenfeldern charakterisiert. Dieser erfüllt die untersuchten nationalen und internationalen Anforderungen an ein aktives Personendosimeter zur Überwachung der Augenlinsen-Personendosis $H_\mathrm{p}(3)$.

Timepix3 ist der andere hybride Pixeldetektor, der in dieser Arbeit verwendet wird. Er besteht aus 256×256 Pixeln mit einem Pixelabstand von 55 µm und verwendet ebenfalls einen Siliziumsensor. Timepix3 führt simultane Messungen von Position, Zeit und Energie durch. Die untersuchte Anwendung ist die Röntgenpolarimetrie. Die Compton-Streuung im Sensor ermöglicht die Untersuchung der linearen Polarisation von wechselwirkenden Röntgenstrahlen. Es werden koinzidente Ereignis-Cluster-Paare gesucht und in ihrer Energie korreliert, um Modulationskurven zu bestimmen, die Informationen über den Grad der linearen Polarisation der Röntgenstrahlung enthalten. Timepix3 wurde erfolgreich in einem unpolarisierten und einem linear polarisierten Photonenfeld getestet, und es wurde gezeigt, dass die gemessene Modulation von polarisierter Röntgenstrahlung herrührt.

Contents

1. Introduction

Ionizing radiation has been present since before the dawn of humankind - may it be cosmic radiation or natural radioactivity in the environment. These contributions of natural background radiation attribute to an effective dose to a human that accumulates in the time frame of a year to an average of 2.1 mSv in Germany [1]. The major part of this dose, about 1.1 mSv/a, stems from inhalation of the radioactive noble gas radon and its decay products [1]. Due to the continuous advancement of human civilization, exposure to ionizing radiation has increased with the application of radionuclides and X-rays in industry and medicine. The main part of artificial radiation exposure stems from medical examinations, where the highest dose contributions stem from CT and interventional examinations [1].
Staff that is occupationally exposed to ionizing radiation must be monitored by law. International expert committees such as the International Commission on Radiological Protection (ICRP) recommend dose exposure limits for radiation protection quantities [2, 3], which typically are adopted by radiation protection law. Exceeding these exposure limits increases the risk of adverse health effects. Interventional procedures in medicine are one of many examples where the eye lens dose of workers might exceed the legally imposed limits [4]. In these fields, an increased risk of cataractogenesis was determined [5] which makes radiation protection dosimetry of the eye lens dose an important topic. Officially approved dosemeters are used to monitor the exposure to ionizing radiation. It is of utmost importance that these dosemeters meet strict requirements since wrongly displayed doses might result in restrictions of the practice of work of legally monitored staff if the dose is overestimated. In the worst-case scenario, the dosemeter underestimates the effective or organ dose resulting in a large undetected exposure of the bearer. So-called passive dosemeters are employed for official monitoring. They are typically read out once a month at evaluation centers. Due to the long period of dose accumulation, no immediate reaction to accident situations with large dose exposure is possible. Therefore, so-called active dosemeters are used together with their passive counterparts. An active personal dosemeter displays the dose at any time and enables warning signals when dose/dose rate thresholds are exceeded. It does not directly protect against ionizing radiation like protective clothing, but it allows its bearer to react immediately to these situations. Due to problems in pulsed photon fields, active personal dosemeters are not authorized for legal dosimetry [6]. This made the use of active personal dosemeters in pulsed radiation fields one of the main topics in radiation protection dosimetry over the last decade [7, 8, 9, 10, 11]. An active dosimetry system capable

of measuring the dose in pulsed fields for a wide range of photon energies is profitable for its user [4, 12].

The hybrid pixel detector Dosepix is utilized for radiation protection dosimetry as active area and personal dosemeter in this thesis. A system consisting of three Dosepix detectors is characterized in its metrological properties with respect to the energy and angular dependence. The area and personal dose equivalents are the operational quantities of radiation protection of interest. The same dosimetry system is tested for its influence in β-radiation fields and used to classify the particle composition of the radiation field using photon and beta reference fields. The investigations with the Dosepix detector are finalized by presenting the prototype of the first active personal eye lens dosemeter comprised of a single detector. It is applied in continuous and pulsed photon fields and compared to national and international requirements.

In the last part of this thesis, X-ray polarimetry with the hybrid pixel detector Timepix3 is presented. Polarization measurements add another dimension to the parameter space used to explore astrophysical sources [13]. They provide information about emission mechanisms and source geometries, especially the orientation and strength of magnetic fields, and help solve key questions in astronomy and astrophysics [13, 14]. The tested photon energy range of use for the Timepix3 X-ray polarimeter is 20-80 keV. Determining the interaction points of coincident event cluster pairs stemming from Compton scattering within the sensor element of Timepix3 and correlating the energies of the events allows precise probing of linearly polarized X-rays. The response of Timepix3 to unpolarized and polarized X-rays is investigated in the laboratory.

2. Theoretical Background

Contents

This chapter outlines the fundamental physical concepts and the radiation detectors utilized in this thesis. At first, an overview of the structure and working principles of hybrid pixel detectors is given. This thesis employs two different detectors, which are therefore presented, namely the Dosepix detector and the Timepix3 detector. Afterward, the interactions between photons and matter is described since investigations in this thesis are performed in photon fields. In the end, an overview of the basic quantities used in dosimetry is presented.

2.1. Hybrid Pixel Detectors

The devices utilized in this thesis are hybrid pixel detectors [15], which find their application in a variety of fields such as high-energy particle physics [16], X-ray and γ-ray imaging in medical research [17], radiation monitoring in space [18], X-ray spectroscopy [19], active personal dosimetry [20], and X-ray polarimetry [21, 22]. Depending on the specifications of the detector, hybrid pixel detectors can allow energy-, time-, and spatially-resolved measurements of different types of ionizing radiation. A hybrid pixel detector consists of a pixelated ASIC (Application Specific

Integrated Circuit) that is bump-bonded to a semiconductor sensor. Hereby, each ASIC pixel is electrically and mechanically connected to a sensor pixel via these bump bonds. Figure 2.1 shows the assembly of a hybrid pixel detector. Using a pixelated detector distributes the total flux among the pixels resulting in a reduced registered event rate per-pixel. This allows its use in high flux environments. The photons interact with the sensor element and deposit energy to an electron. It is ionizing and creates electron-hole pairs in the semiconductor. An electric field is created by applying a bias voltage to the sensor element. The potential difference yields the drift of holes and electrons in opposite directions through the sensor. The number of created charge carriers depends on the sensor material and the used doping profile. In silicon, the ionization potential is $W = 3.62\,\text{eV}$ [23] at room temperature. Typical other sensor materials are CdTe, GaAs, and CZT. The selection of the sensor material depends on the intended use case. Due to diffusion and repulsion, the transverse spread of the charge cloud is increased. The diffusion width for electrons and holes is described by [24]

$$\sigma = \sqrt{2 \cdot D \cdot t} = 23 \cdot \sqrt{\frac{d}{E}}, \tag{2.1}$$

where D is the diffusion coefficient and t is the drift time for the first expression. The right side of the equation is stated in microns and includes the detector thickness d expressed in microns and the electric field E in units of V/cm.

The repulsion models are derived in [25, 26]. The width increase due to repulsion is described for different cloud shapes, i.e., cylindrical and spherical charge clouds. The spherical one is described via

$$r_{\text{sph}} = \sqrt[3]{\frac{3 \cdot \mu_{\text{e,h}} \cdot q}{4 \cdot \pi \cdot \epsilon_r \cdot \epsilon_0} \cdot N \cdot t}, \tag{2.2}$$

where $\mu_{\text{e,h}}$ denotes the mobility of either electrons or holes, N the number of charge carriers, ϵ_r the relative permittivity, ϵ_0 the vacuum permittivity, q the charge, and t the drift time. According to [26], the charge carrier distribution created by ionizing particles in silicon is for energies above 10 keV better described by a cylindrical charge distribution. Its corresponding transverse spread is modulated via

$$r_{\text{cyl}} = \sqrt{\frac{\mu_{\text{e,h}}}{\pi \cdot \epsilon_r \cdot \epsilon_0} \cdot \rho \cdot t}, \tag{2.3}$$

with ρ the density of the sensor material. The charge carriers are collected by the pixel electrode and induce a signal in the corresponding pixel of the ASIC. The transverse spread allows the charge carrier cloud to induce a signal in several adjacent pixels. This phenomenon is called charge sharing. It is illustrated in Figure 2.2. The pixel

electronics further process the signal. The hybrid pixel detectors used in this thesis are from the Medipix detector family developed within the Medipix collaboration founded at CERN [27].

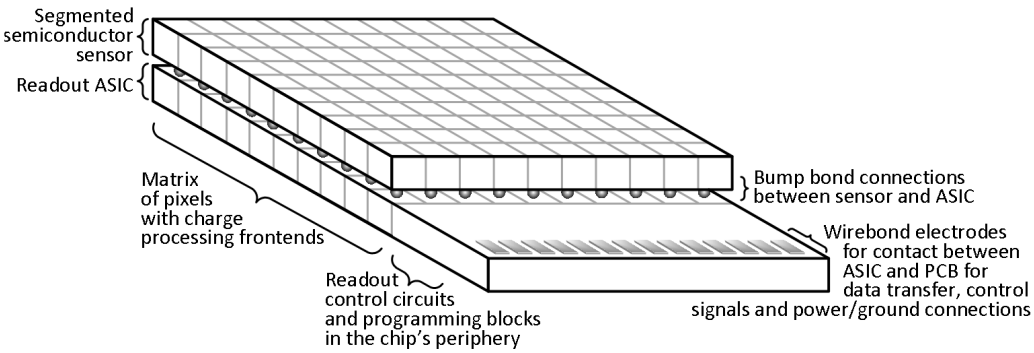

Figure 2.1.: Schematic illustration of the assembly of a hybrid pixel detector. The segmented sensor element is mechanically and electrically connected to the readout chip (ASIC) via bump-bonds. The image is taken from [28].

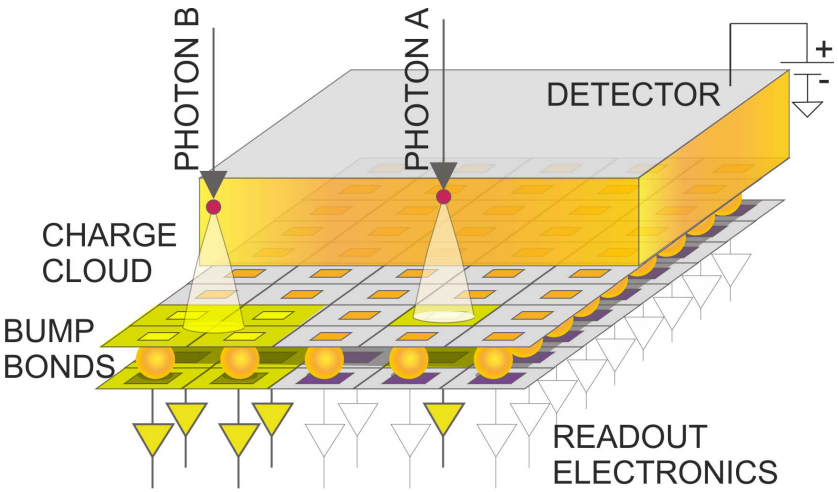

Figure 2.2.: Charge sharing in hybrid pixel detectors. Photon A triggers a response of a single pixel as its energy deposition occurs in the center of the pixel. The charge cloud of Photon B extends over four pixels since the energy deposition takes place at a corner and triggers all of them. The image is taken from [29].

2.1.1. The Dosepix Detector

Dosepix is a hybrid, pixelated, photon-counting and energy-resolving detector for ionizing radiation. The detector was designed with the use case in active personal dosimetry in continuous and pulsed photon fields. Those photon fields are measured and resolved in energy to enable a higher accuracy to the dose measurements. The pixelation allows the use in high flux environments. Dosepix' ASIC was designed by W. Wong [28] at CERN [30] in cooperation with the ECAP [31] and IBA dosimetry [32]. The information in this section is summarized from descriptions in [28, 33, 34, 35, 19]. Figure 2.3 shows a photograph of the Dosepix detector and a comparison of its size relative to a 1 cent coin.

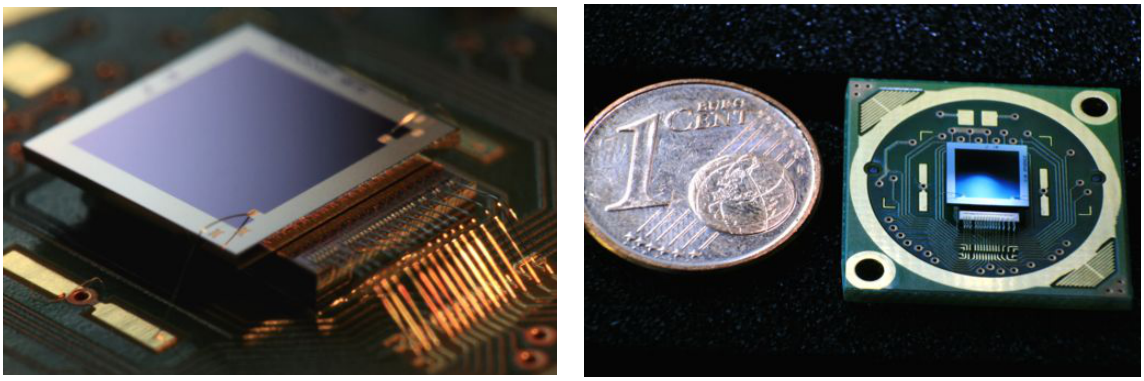

(a) Near shot (b) Comparison to a 1ct coin

Figure 2.3.: Photographs of the Dosepix detector. (a) shows the near shot of the Dosepix detector. (b) shows the Dosepix on a printed circuit board next to a 1 cent coin. The area of Dosepix is approximately as large as the earth on the 1 cent coin. Both photographs are taken from [33].

The layout of the ASIC consists of 16×16 square pixels with a pixel pitch of 220 µm and a total area of 3.55 mm×5.2 mm. Its floorplan is shown in Figure 2.4. The ASIC is bump-bonded to a 300 µm thick p-in-n doped silicon sensor. The sensor is biased with 100 V and therefore fully depleted. The top and bottom two pixel rows cover small pixels with an edge length of 55 µm and the interior 12 rows cover large pixels with an edge length of 220 µm. The sensitive area is 3.52 mm×3.52 mm. Typical problems of active personal dosemeters are their dead-time and insufficient dead-time correction factors for low pulse durations and high peak pulse dose rates [6]. The segmentation into pixels and the use of the two different pixel sizes allow counteracting the problems at high peak pulse dose rates [7, 9] due to the reduction of the event rate. The so-called *rolling shutter principle* [28] is utilized for the readout of Dosepix to counteract problems with dead-time for low pulse durations [6]. One column is read out at a time while the remaining 15 columns continue to process sensor signals. This means that 15/16 of the pixel matrix is always active at a time, i.e., the readout is dead-time-free.

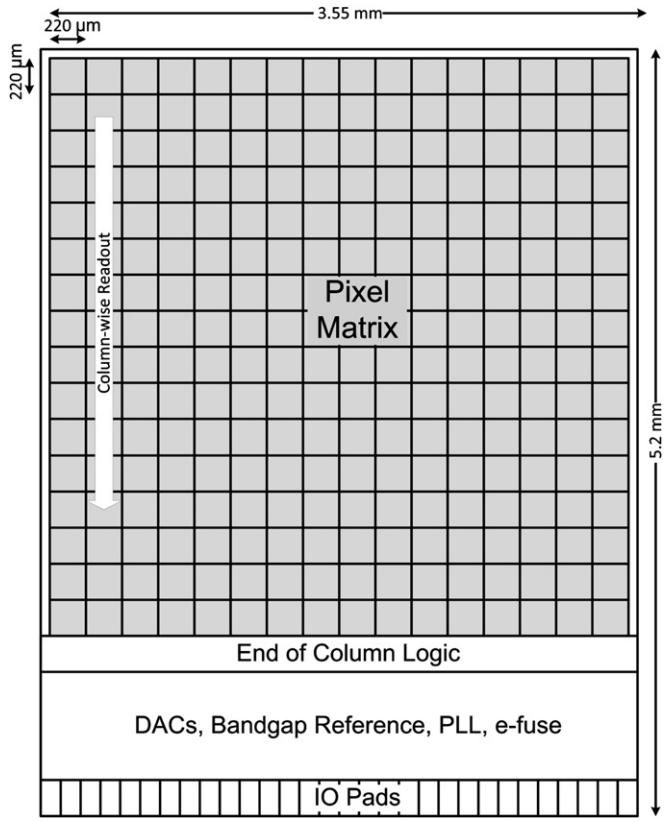

Figure 2.4.: Floorplan of the ASIC pixel matrix. Its a 16×16 pixelation with 220 µm pixel pitch. The white arrow indicates the rolling shutter which reads out one column at a time. Picture taken from [36].

In the case of Dosepix, holes are the collected charge carriers. An induction charge signal is created in the pixel electrode. It is provided to the analog frontend, where a charge sensitive amplifier shapes and amplifies it. An analog discriminator compares the amplitude of the signal to a programmable analog threshold (THL). The THL is adjusted in a way so that it lies above the noise level. While the amplitude of the signal exceeds the THL, the discriminator outputs a high. The number of digital clock periods of a 100 MHz reference clock while the amplitude of the signal exceeds the THL is counted. The number of clock cycles is the so-called time over threshold (ToT). ToT is proportional to the number of collected charge carriers and therefore proportional to the deposited energy. Figure 2.5 shows the ToT principle and Figure 2.6 the signal processing steps schematically.

Dosepix has different programmable operation modes. The detailed description of every mode is stated in [28, 38]. These modes are summarized in the following.

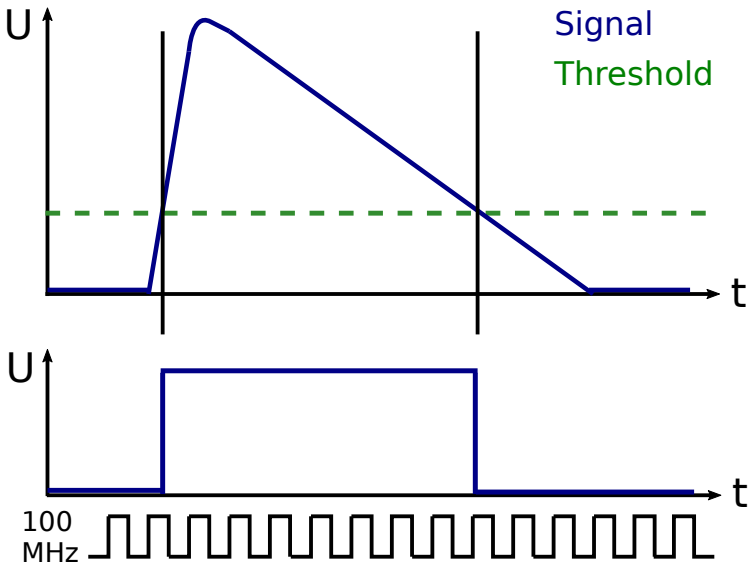

Figure 2.5.: Illustration of the ToT principle. If the signal surpasses the adjustable analog threshold the discriminator puts out a high. A 100 MHz reference clock runs in the background all the time. Its number of clock cycles while the discriminator delivers a high is the so-called ToT value. The schematics is taken from [37].

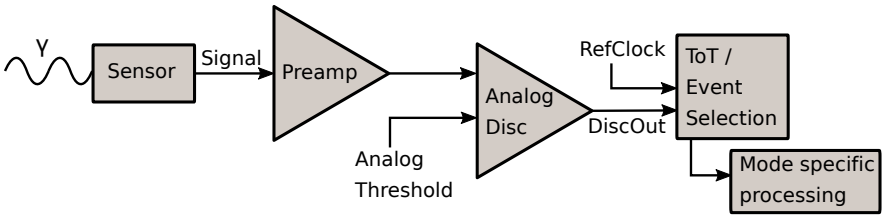

Figure 2.6.: Diagram of the signal processing. A photon induced signal in the sensor is amplified by a charge sensitive amplifier. The amplitude of the signal is compared to an analog threshold. If the signal surpasses the threshold the number of clock ticks of a reference clock while the signal stays above the threshold is counted. This value is used for further mode specific processing such as the ToT, energy-binning and integration mode. The diagram is taken from [37].

The energy-binning mode pixelwise records the deposited energy as ToT and sorts it in one of 16 histogram bins according to its energy. The so-called binning-state-machine performs the assignment of the bin register. Each pixel is equipped with its unique individually programmable energy bin edges. The bin edges are stored in digital threshold registers. The readout is performed columnwise via a rolling shutter, which introduces dead-time-free measurement. The energy-binning mode aims to provide online binning of energy spectra which is useful for real-time dose reconstruction. It is the mode used for dosimetry, and therefore typically referred to as Dosi-mode.

Another mode is the ToT-mode. The ToT of an event is determined as previously stated, and is stored in a register. If, before readout, another event is detected, the registers entry is overwritten. It is used in applications that rely on the precise measurement of energy spectra, such as the energy calibration of ToT via XRF measurements or testpulses as described in [19].

The photon-counting-mode counts the number of events above the THL until readout. It carries no information about the energy except that it is above the threshold. An electronic shutter controls the exposure time. It is typically utilized for the threshold equalization.

The final mode is the integration mode. All registered ToT values during exposure are accumulated in a sum instead of being overwritten as in the ToT-mode. It is utilized in very high flux environments where single-photon processing is impossible due to frontend pileup.

2.1.2. The Timepix3 Detector

The following description is taken from [39]. Timepix3 is a hybrid, pixelated, photon counting, energy-, and time-resolving detector for ionizing radiation. The ASIC is designed in 130 nm CMOS technology. The pixel matrix comprises 256×256 pixels with a pixel pitch of 55 µm. The sensitive area is 1.98 cm^2. For the investigations in this thesis, a 300 µm thick silicon sensor is employed. The minimum operation threshold is 500 e^-. This corresponds to an energy of around 1.8 keV in silicon.

Timepix3 uses a data-driven readout mode designed to process up to 0.4 $\mathrm{Mhits/mm^2/s}$. Data packets consisting of position information, time-of-arrival (ToA), and time-over-threshold (ToT) are sent out after the pixel's event is processed. Due to pulse processing and packet transfer, the triggered pixel has a dead-time of about 475 ns. The remaining pixels on the pixel matrix stay active. In addition to the data-driven readout, a classical frame-based readout is possible, which allows a count rate of up to 826 $\mathrm{Mhits/mm^2/s}$. Here, the readout takes place at the end of the shutter period.

ToT and ToA are sampled by a 40 MHz clock. The ToA is additionally sampled with a 640 MHz clock (fToA), resulting in a time resolution of 1.56 ns. If a pre-amplifier signal surpasses the programmed THL level (energy threshold), the discriminator output rises, and the fToA clock starts. It is stopped by the rising edge of the 40 MHz

clock. The coarse ToA time stamp is latched, and the ToT counter starts. The working principle is illustrated in Figure 2.7. The Timepix3 detector has several different operation modes: the ToT and ToA mode, the ToA only mode, the PC (photon counting) mode, and the iToT (integral ToT) mode.

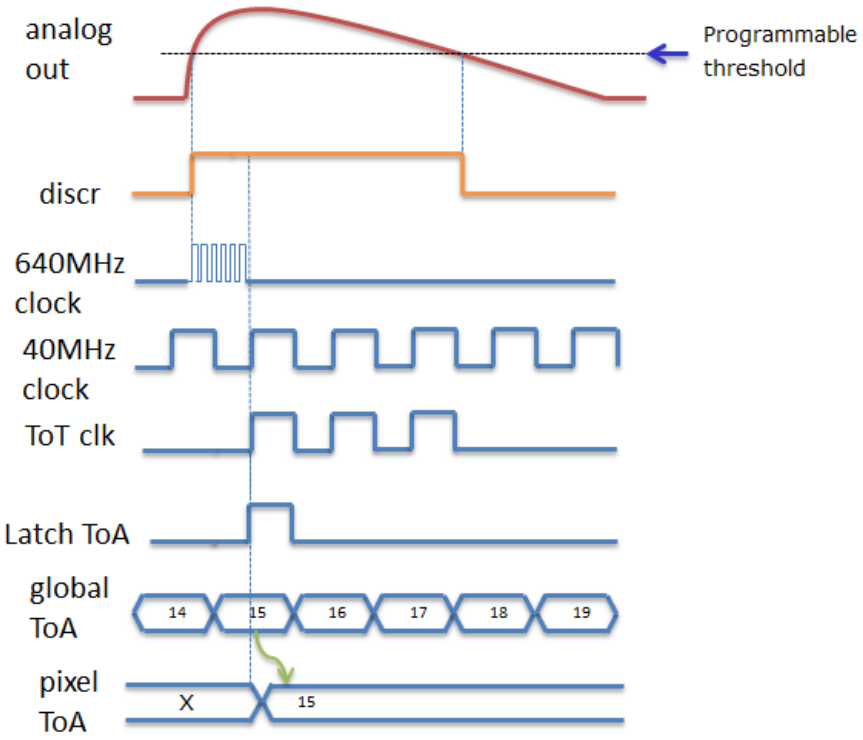

Figure 2.7.: Working principle of the Timepix3. ToA and ToT are measured at the same time and sampled with a 40 MHz reference clock. The ToA is subsampled with a 640 MHz clock to improve the time resolution. Illustration taken from [39].

2.2. Interaction of Photons with Matter

The precise knowledge of the basic interactions between photons and matter is of paramount importance for the work with X-ray detectors. This section describes the interactions between photons and matter. The used information is extracted from [40, 41, 42, 43].

A photon ensemble of the intensity I_0 impinges onto a target material with the thickness d and the density ρ. After passage through the target, the photon intensity I_0 is exponentially attenuated to the intensity I according to the Beer-Lambert law

$$I = I_0 \cdot e^{-\mu^* \cdot \rho \cdot d} \tag{2.4}$$

where μ^* denotes the mass attenuation coefficient. It is proportional to the total cross-section, which depends on the atomic number and the photon energy. The total cross-section is composed of the sum over all partial cross-sections of the possible photon-matter interactions. These are:

- Photoelectric effect
- Coherent Scattering (i.e., Rayleigh scattering)
- Incoherent Scattering (i.e., Compton scattering)
- Pair-production

Figure 2.8 depicts the mass attenuation coefficient in silicon for the different interactions and the total one in dependence of the photon energy. Dosepix and Timepix3 both employ a silicon sensor for their applications presented in this thesis. The possible photon-matter interactions are described in the following.

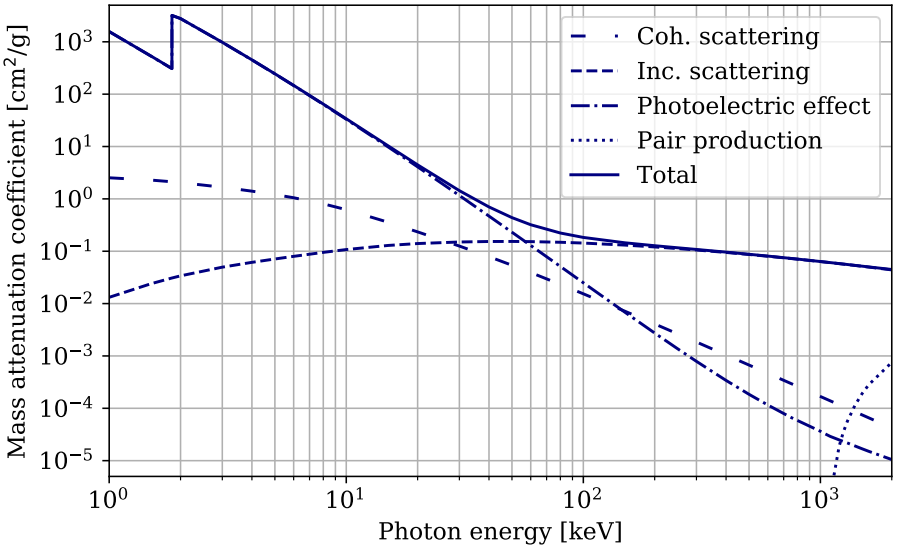

Figure 2.8.: Mass attenuation coefficient in silicon as a function of the photon energy. It is divided into coherent scattering, incoherent scattering, photoelectric effect, pair production, and the total mass attenuation coefficient. The data is extracted from the XCOM database [44].

2.2.1. Photoelectric Effect

The photoelectric effect describes the interaction of an X-ray with an atomic electron. It is the dominant interaction in silicon below 60 keV. An electron of an inner atomic orbital fully absorbs the X-ray. The total photon energy is transferred to the electron, which is subsequently left in an excited state. The electron is ejected from the atom if the energy of the photon is sufficient to ionize it. The electron is called a photoelectron and leaves the atom with the excess energy between the energy of the absorbed photon and the electron's binding energy. A small amount of energy is transferred to the recoil atom, which is usually neglected. The recoil atom is necessary to guarantee momentum conservation because a free electron cannot absorb the photon. The cross-section of the photoelectric effect exhibits a sharp increase of the interaction probability at energies slightly above the energy of the atomic shells. Every shell displays an edge at which the interaction probability is increased. If the photon's energy exceeds the energy of the K-shell, predominantly electrons from this shell are ionized. The ejected electron leaves a hole which is filled by an electron of a higher atomic orbital, leading to the emission of either Auger electrons or X-ray fluorescence photons. The differential cross-section for the interaction of an X-ray with a K-shell electron is given by [45]

$$\frac{d\sigma}{d\Omega} = r_{\mathrm{e}}^2 \cdot Z^5 \cdot \alpha^4 \cdot \left(\frac{m_{\mathrm{e}} \cdot c^2}{E_0}\right)^{7/2} \cdot \frac{4 \cdot \sqrt{2} \cdot \sin^2\theta \cdot \cos^2\phi}{(1 - \beta \cdot \cos^4\theta)} \tag{2.5}$$

where r_e denotes the classical electron radius, m_e the electron mass, Z the atomic number of the absorbing material, α the fine structure constant, E_0 the energy of the absorbed photon, β the incident particle velocity divided by the speed of light. The following description of the reference frame is taken from [21]. The polar angle ϕ is the angle of the momentum of the emitted electron to the y-axis, defined by the direction of the electric field vector of the incident photon. Its direction defines the z-axis, and the x-axis is perpendicular to both. The azimuth angle θ is the angle of the electron momentum to the z-axis. It is evident from this equation that the photoelectron is ejected in the direction of the electric field vector. This anisotropy allows the study of linearly polarized X-rays employing the photoelectric effect.

2.2.2. Coherent Scattering

Coherent scattering, i.e., Rayleigh scattering, describes the interaction of a photon with an atom. The photon changes its direction but deposits no energy to the atom. It occurs for low photon energies, and its cross-section decreases with E^{-2} above 10 keV, where E denotes the photon energy. This interaction inaccessible for the used hybrid pixel detectors, because no energy deposition by the photon in the sensor element takes place.

2.2.3. Incoherent Scattering

Incoherent Scattering, i.e., Compton scattering, describes the interaction of a photon with a loosely bound atomic electron. It is the dominant interaction above 60 keV in silicon. The photon transfers part of its energy to the recoil electron. This energy transfer depends on the scattering angle θ between the momentum directions of the incident and the scattered photon. The Klein-Nishina formula describes the differential cross-section

$$\frac{d\sigma}{d\Omega} = \frac{r_0^2}{2} \cdot \frac{E^2}{E_0^2} \cdot \left(\frac{E}{E_0} + \frac{E_0}{E} - 2\sin^2\theta \cdot \cos^2\phi\right) \tag{2.6}$$

where E_0 is the energy of the incident photon and E is the energy of the scattered photon. The azimuth angle ϕ is the angle between the vector of the electric field of the incident photon and the plane of scattering [21]. This anisotropy makes Compton scattering viable for studies of linearly polarized X-rays. The energy E of the scattered photon is calculated via:

$$E = \frac{E_0}{1 + (E_0/m_e c^2) \cdot (1 - \cos\theta)}. \tag{2.7}$$

The energy transfer to the recoil electron increases with increasing scattering angle and photon energy. At a scattering angle of $\theta = 180°$, the maximum energy is transferred to the recoil electron. Also, the differential cross-section shows that the photon scatters predominantly in the forward direction with increasing photon energy. Since only a part of the energy is deposited via Compton scattering, a second interaction within the detection volume is possible. This makes Compton scattering accessible to studies of coincident events within the sensor volume of a time-resolving detector such as the Timepix3.

2.2.4. Pair Production

Pair production can occur when the incident photon's energy exceeds double the electron rest mass (1.022 MeV). The interaction has to occur in the Coulomb field of a recoil partner such as an atomic nucleus or orbital electron to guarantee momentum conservation. The photon is converted into an electron-positron pair. The positron thermalizes in the ambient material and annihilates with an electron to at least two photons sharing twice the electron's rest mass. The two photon case displays the characteristic 511 keV annihilation line in spectroscopy.

2.3. Dosimetry

Ionizing radiation deposits its energy to matter of a certain mass. This ratio between the deposited energy and the mass is the so-called dose. Dosimetry is the field in physics that focuses on the determination and the measurement of the aforementioned dose. It is used to quantify the harm that ionizing radiation poses to biological tissue with the goal of reducing potential damages. Devices utilized in the measurement of the dose are called dosemeters. There are various types of dosemeters depending on the ionizing particle and the dose quantity of interest. A comprehensive overview can be found in [46]. Occupationally exposed workers are required by law to wear dosemeters that document the dose of exposure over a period of a time. International committees such as the ICRP (International Commission on Radiological Protection) [47] recommend dose thresholds that shall not be surpassed under any circumstance to reduce the negative impact of ionizing radiation, such as irreparable cell damage and altering the DNA (deoxyribonucleic acid). The adverse health effects caused by ionizing radiation are divided into deterministic and stochastic effects [2].
Deterministic radiation damage increases in its severity with increasing dose. The damage occurs above a certain dose threshold due to severe death of cells and subsequent malfunctioning of organs and tissue damage. The threshold dose is defined as the dose resulting in adverse reactions in tissue or organs occurring in 1% of the exposed.
Stochastic radiation damage leads to changes in the DNA with a certain probability. The probability is dependent on the dose, while the severity is not affected by the dose.

Available dose quantities follow the classification, which divides them into physical and radiation protection quantities. The latter was defined by the ICRP and the ICRU (International Commission on Radiation Units and Measurements) [48] and are suitable for the definition of exposure limits. The physical dose quantities and radiation protection quantities are explained in more detail in the following. The definitions of the physical quantities are extracted from [40, 49], and the definitions of radiation protection quantities from the PTB report Dos-23 [50].

2.3.1. Physical Dose Quantities

The fundamental physical dose quantities are based on the absorption of energy of ionizing radiation in matter. The ratio of the mean locally absorbed energy $\mathrm{d}E_{\mathrm{abs}}$ in a mass element dm_{med} of the irradiated absorber material (absorber medium: 'med') is called the absorbed dose D_{med}

$$D_{\mathrm{med}} = \frac{\mathrm{d}E_{\mathrm{abs}}}{\mathrm{d}m_{\mathrm{med}}} = \frac{1}{\rho_{\mathrm{med}}} \cdot \frac{\mathrm{d}E_{\mathrm{abs}}}{\mathrm{d}V} \tag{2.8}$$

where ρ_{med} denotes the density of the medium and $\mathrm{d}V$ its corresponding volume element. The SI unit of the absorbed dose is the Gray, $1\,\text{Gy} = 1\,\text{J/kg}$.

Another quantity is the so-called ion dose J. It is the created electrical charge $\mathrm{d}Q$ in an irradiated volume of air with the mass $\mathrm{d}m_{\text{air}}$:

$$J[C/kg] = \frac{\mathrm{d}Q}{\mathrm{d}m_{\text{air}}} = \frac{1}{\rho_{\text{air}}} \cdot \frac{\mathrm{d}Q}{\mathrm{d}V}. \tag{2.9}$$

In practical applications of low energy measurements the preferred measurand is the so-called kerma K_{med} (**k**inetic **e**nergy **r**eleased per unit **ma**ss). It is defined as the energy that is deposited by indirect ionizing radiation as kinetic energy E_{trans} onto secondary particles of first-generation divided by the mass of the medium

$$K = \frac{\mathrm{d}E_{\text{trans}}}{\mathrm{d}m_{\text{med}}}. \tag{2.10}$$

In applications of X-ray diagnostics, the air kerma K_{air}, i.e., kerma in the medium air, is used.

2.3.2. Radiation Protection Quantities

Radiation protection quantities are dose quantities that estimate the impact and help to determine the risk of ionizing radiation to the human body. They are needed to provide exposure limits and are divided into body dose and operational quantities. The body dose quantities are based on the absorbed dose. With that, the equivalent dose H can be introduced. It is defined as the absorbed dose weighted with a quality factor of the radiation type. Different radiation types are photons, electrons, neutrons, protons, and α-particles. The weighting factor w_{R} describes the radio-biological effectiveness of different types of radiation. The equivalent dose in a tissue or organ T is the weighted sum of absorbed doses over the various radiation types:

$$H_{\text{T}} = \sum\nolimits_{\text{R}} w_{\text{R}} \cdot D_{\text{T,R}}. \tag{2.11}$$

By introducing the dimensionless radiation quality factor, the unit Gray [Gy] is converted to Sievert [Sv], which is the unit measured in radiation protection dosimetry. The weighting factor w_{T} takes the different radio-sensitivities of the body organs and tissues into account. They are averaged over a population of males and females of different ages. The effective dose, E, is weighted sum of the tissue and organ equivalent doses H_{T} and their corresponding weighting factors w_{T}:

$$E = \sum\nolimits_{\text{T}} w_{\text{T}} \cdot H_{\text{T}}. \tag{2.12}$$

The body quantities are not measurable since they are defined as the mean values of organs or tissues. It, therefore, needs the definition of operational quantities for radiation protection, which dosemeters can measure. For external radiation (i.e., radiation from outside the human body, opposite of internal), two categories of operational quantities are introduced according to ICRU report 51 [51]: Area monitoring and individual monitoring. These categories fully satisfy the different tasks and goals in radiation protection. Area monitoring controls the radiation at workplaces and defines which areas are classified as controlled or restricted. It is further used for environmental monitoring in the vicinity of nuclear facilities. Individual monitoring is used for the control and limitation of individual exposures. It is determined by wearing a dosemeter. The operational quantities are dose equivalents specifically defined for strongly penetrating radiation or low penetrating radiation. One differentiates between $H_\mathrm{p}(x)$ for the personal dose equivalent in x mm depth of ICRU soft tissue and for the ambient dose equivalent $H^*(10)$, or the directional dose equivalents $H'(3,\Omega)$ and $H'(0.07,\Omega)$, where Ω represents a specified direction. The ICRU-4-element soft tissue is defined as an idealized material of density $\rho = 1\,\frac{\mathrm{g}}{\mathrm{cm}^3}$ with a mass composition of 76.2% oxygen, 11.1% carbon, 10.1% hydrogen and 2.6% nitrogen [52]. $x = 10$ approximates the effective dose, while $x = 3$ and $x = 0.07$ approximate only organ equivalent doses, i.e., the eye lens and the local skin dose, respectively. The statement is valid for both categories of operational quantities. All the quantities fulfill the requirements of being a point quantity, additive, and the same quantity for all radiation types. Table 2.1 sums up the previous discussion.

External radiation	Limiting body dose	Area dose equivalent	Personal dose equivalent
Strongly penetrating radiation	Effective dose	$H^*(10)$	$H_\mathrm{p}(10)$
Weakly penetrating radiation	Skin dose Lens of the eye	$H'(0.07,\Omega)$ $H'(3,\Omega)$	$H_\mathrm{p}(0.07)$ $H_\mathrm{p}(3)$

Table 2.1.: Definitions of the radiation protection quantities depending on the penetrability and their limiting body dose which they approximate [50].

The area dose is typically measured free-in-air, while the personal dose is measured in front of the human body. Therefore, the radiation fields interacting in the dosemeters vary due to the lack of backscattering and absorption of the human. To attribute

for this, the area monitoring quantities are defined on the so-called ICRU sphere. It consists of ICRU tissue and has a diameter of 30 cm. In order for the area monitoring quantities to suffice the requirements of additivity and point-like character, the concept of an expanded and aligned field has to be introduced.

For an expanded radiation field, the spectral fluence and the angular fluence have the same values across all points in space as in the actual field at the point of interest. There is spatial constancy (homogeneity) in such a large volume that, in the case of a further expansion of the range, the spectral and angular fluence of the particles entering an imaginary 30 cm diameter sphere will no longer change. The expansion of the radiation field ensures that the whole ICRU sphere is thought to be exposed to a homogeneous radiation field whose fluence, energy distribution, and directional distribution are the same as in the point of interest of the real radiation field.

Alignment in the expanded fields means that the momentum directions of the photon oppose the radius vector of the ICRU sphere. By doing so, the expanded and aligned field is obtained. In such a radiation field, the dose equivalent at one point of interest on the ICRU sphere displays no dependence on the angle of incidence of the real radiation field.

The ambient dose equivalent, $H^*(10)$, is a quantity defined in the expanded and aligned field. It "is the dose equivalent that would be produced by the corresponding aligned and expanded radiation field, in the ICRU sphere at a depth of 10 mm, on the radius vector opposing the direction of the aligned field" [50]. The directional dose equivalents $H'(3,\Omega)$ and $H'(0.07,\Omega)$ are only defined in an expanded field and exhibit, therefore, an angular dependence.

For definition purposes, several phantoms are introduced for the personal dose equivalents, depending on the monitored body dose. It is needed to obtain a direct relation of the quantity to the human body or suitable phantom. The phantoms all consist of ICRU-4-element tissue and are a slab phantom to approximate the human torso (30×30×15), a cylinder phantom to approximate the head (height and diameter of 20 cm), a pillar phantom to approximate a lower arm or leg (cylinder of 73 mm in diameter and 30 cm height), and a rod phantom to approximate a finger (cylinder of 19 mm in diameter and 30 cm height).

All operational radiation protection quantities are related to the air kerma K_{air}, which is determined in reference measurements by calibrated primary standard ionization chambers. The ICRU and several other publications define conversion coefficients from air kerma to dose equivalents, converting 1 Gy to 1 Sv of the particular operational quantity. These conversion coefficients can be found for the ambient dose equivalent $H^*(10)$ in [53] and [54], the directional dose equivalent $H'(3,\Omega)$ in [55], the directional dose equivalent $H'(0.07,\Omega)$ in [54] and [56], the personal dose equivalent $H_{\mathrm{p}}(10)$ on the slab phantom in [53] and [54], the personal dose equivalent $H_{\mathrm{p}}(0.07)$ on the slab phantom in [57], and the personal dose equivalent $H_{\mathrm{p}}(3)$ on the cylinder phantom in [58] and on the slab phantom in [57].

3. Area Dosimetry with Dosepix

Contents

The capability of area monitoring of external radiation with the Dosepix detector is investigated in this chapter. The operational quantities of interest are the ambient dose equivalent $H^*(10)$ and the directional dose equivalents $H'(3, \Omega)$ and $H'(0.07, \Omega)$. All irradiations are performed with the detector free-in-air, allowing the study of Dosepix's performance as a semiconductor detector for X-ray diagnostics. Its measured dose quantity is the air kerma. A system consisting of three Dosepix detectors, called the Dosepix dosimetry demonstrator, is presented. These Dosepix detectors record energy histograms that allow the determination of several sets of conversion factors for a single set of measurements. Depending on the dose quantity, a set of conversion factors is determined from the number of registered events in an energy bin of Dosepix to an ambient, directional dose equivalent or air kerma. The conversion factors

between the number of registered events in an energy bin of Dosepix and an area dose equivalent or air kerma are determined for simulation data that was created by Sebastian Schmidt during his Ph.D. thesis [19]. Additionally, measurements at the laboratory in Erlangen and measurements at reference conditions at the German Metrology Institute (PTB) are employed to modify the pre-determined conversion factors. In the end, the metrological performance with respect to the dependence on the mean photon energy and the angle of radiation incidence of the dose determination of the Dosepix dosimetry demonstrator is assessed for mean photon energies between 12.4 keV and 1250 keV for angles of radiation incidence of up to 60°.

3.1. Purpose of Area Dosimetry

An area dosemeter is defined as a meter designed to measure the ambient dose equivalent or the directional dose equivalent according to ISO 29661 [59]. These dosemeters are used for area monitoring of the operational quantities for radiation protection in terms of measurement of the ambient dose equivalent $H^*(10)$ and the directional dose equivalents $H'(3, \Omega)$ and $H'(0.07, \Omega)$. Operational quantities are used to deliver an estimate of the protection quantities, such as the effective dose or organ absorbed dose, which must be upheld by law [60]. The dose displayed by an area dosemeter states the exposure that a person would receive if they were standing in the area of the dosemeter [50]. Area dosimetry is primarily used for preventive radiation protection purposes [50]. A distinction is made between workplace and environmental monitoring. The first one relates to area monitoring of the working environment and the latter for area monitoring by measuring the dose in the environment [61]. Area dosimetry is the foundation of the hazard classification of workplace environments such controlled and restricted zones. This is needed to assess radiation safety precautions such as associated protection and safety measures. In this case, experts examine the location with handheld portable area dosemeters. Another way to utilize area dosemeters is to permanently install them in the monitored area such as the workplace, the vicinity of nuclear facilities, or designated measuring points for environmental monitoring. The latter determines the natural background radiation, which varies considerably depending on the geographical location depending on the type of soil and rocks in the area, and depending on artificial background radiation due to nuclear tests and accidents at nuclear facilities [62]. Tasks in area monitoring require an active dosemeter with direct reading on the momentary dose exposure. The key problems arise in pulsed radiation fields. So far, no active area dosemeters have been tested successfully in pulsed photon fields. The capability of workplace monitoring in X-ray diagnostics and industrial workplaces with gamma-ray sources is investigated in the following sections. More sophisticated investigations into environmental monitoring must be carried out in the future.

3.2. Dosepix Dosimetry Demonstrator

The application of the Dosepix detector in the field of dosimetry of ionizing particles - and in this case photons - is realized by a system consisting of three Dosepix detectors. They are aligned along a straight line. Each detector is glued to its printed circuit board (PCB), which is mounted via Samtec connectors to the main PCB (further mentioned as "readout board"). It supplies various voltages required to operate Dosepix and governs the communication between the detectors and control software via a microcontroller. The readout board is bolted into a black plastic box. Its side walls are 5 mm and its backside 2 mm thick. A cover consisting of 1.5 mm white acrylonitrile-butadiene-styrene (ABS) plastic is utilized. The plastic box and the ABS cover are used as preliminary dosemeter housing. The material of the box must be similar to the material of a final dosemeter housing to reproduce its scattering properties appropriately. Typically, a change of the housing will impact the performance at low-energies as the interaction probability in the housing decreases with increasing photon energy.

The Dosi-mode is utilized for measurements of the dose equivalent as described in Chapter 2. Every pixel of Dosepix has 16 individually programmable energy thresholds for the Dosi-mode. These energy thresholds are usually referred to as energy bin edges. All large and all small pixels of one particular detector are adjusted with the same values individual for the pixel type for the bin edges, which are stated in Table 3.1. As per convention, the bin indices descend with ascending energy. Filter-caps of different shapes and materials cover the detectors. The shapes of the filter-caps are half-spheres of 2 mm thick aluminum and 1 mm thick tin, and a 0.25 mm thick aluminum cylinder with a thin aluminum foil of 0.25 mm thickness on its top. This foil has a hole above the sensor, absorbing photons irradiated under an increased angle of radiation incidence only. The detectors are labeled along with the socket position, i.e., Slot 1 for the detector with the aluminum cylinder, Slot 2 for the detector with the aluminum half-sphere, and Slot 3 for the detector with the tin half-sphere. The idea behind the shapes is to reproduce the angular dependency of the personal dose equivalent $H_\mathrm{p}(10)$ in measurements. It shall happen in a way that counteracts the angular dependency to result in a dose determination independent of the angle of radiation incidence. Especially at the lower energy range (10-40 keV) a dependence on the angle of radiation incidence is observed for the $H_\mathrm{p}(10)$ for which the filter caps were initially designed. It ultimately means that a higher photon fluence is needed at angular irradiation to yield an equal dose compared to a normal incidence angle. If the detectors are not appropriately filtered with respect to $H_\mathrm{p}(10)$ measurements for angular irradiation, a higher dose than expected is measured.

Another effect induced by the filter-caps is the beam-hardening of the impinging photon field. Due to that, each detector is irradiated with a different spectrum incident to the sensor element after passage through the filter-caps. Absorption in the filter-cap reduces the number of registered events in Slot 2, Slot 3 compared to Slot 1 in a certain energy range. The lower number of registered events results in the

dominance of the dose determination for each detector at different energy regimes. In theory, the detector behind the aluminum cylinder is sensitive to soft X-rays, the detector behind the aluminum half-sphere to soft and hard X-rays, and the detector behind the tin half-sphere to hard X-rays and high energetic γ-rays of radionuclides. Above a photon energy of 250 keV, all three filter-caps have a similar degree of transmission for photons as the absorption in the filter caps decreases significantly. This means that all three detectors exhibit a similar event rate and contribute to the total dose according to the weighting introduced by their conversion factors from the number of registered events in an energy bin of Dosepix to a dose equivalent of interest.

Bin index	LP Slot 1	SP Slot 1	Bin index	LP Slot 2	SP Slot 2	Bin index	LP Slot 3	SP Slot 3
15	12.0	12.0	31	12.0	12.0	47	32.0	32.0
14	18.0	15.0	30	17.0	15.0	46	37.0	38.0
13	21.0	20.0	29	31.0	20.0	45	47.0	45.0
12	24.5	25.0	28	40.0	25.0	44	57.5	50.0
11	33.5	30.0	27	45.5	30.0	43	68.5	55.0
10	43.0	35.0	26	50.5	35.0	42	80.0	60.0
9	53.5	40.0	25	60.5	40.0	41	91.5	65.0
8	66.5	45.0	24	68.0	45.0	40	104.0	70.0
7	81.5	50.0	23	91.0	50.0	39	117.0	75.0
6	97.0	60.0	22	102.5	60.0	38	131.0	80.0
5	113.0	70.0	21	133.0	70.0	37	145.0	85.0
4	131.5	80.0	20	148.0	80.0	36	163.5	95.0
3	151.5	100.0	19	163.0	100.0	35	183.5	105.0
2	173.0	120.0	18	196.0	120.0	34	207.5	120.0
1	200.5	140.0	17	220.0	140.0	33	234.5	140.0
0	236.0	160.0	16	257.0	160.0	32	269.5	160.0

Table 3.1.: Energy bin edges and their corresponding bin index for each pixel size and detector represented by its slot in the Dosi-mode. All threshold values are stated in [keV]. The abbreviations "LP" and "SP" stand for large pixels and small pixels, respectively.

Figure 3.1 shows a photograph of the readout-board mounted with three Dosepix detectors. Their filter-caps from left to right are tin half-sphere, aluminum half-sphere and the aluminum cylinder. A true-to-scale depiction of the complete Dosepix dosimetry demonstrator is shown in Figure 3.2.

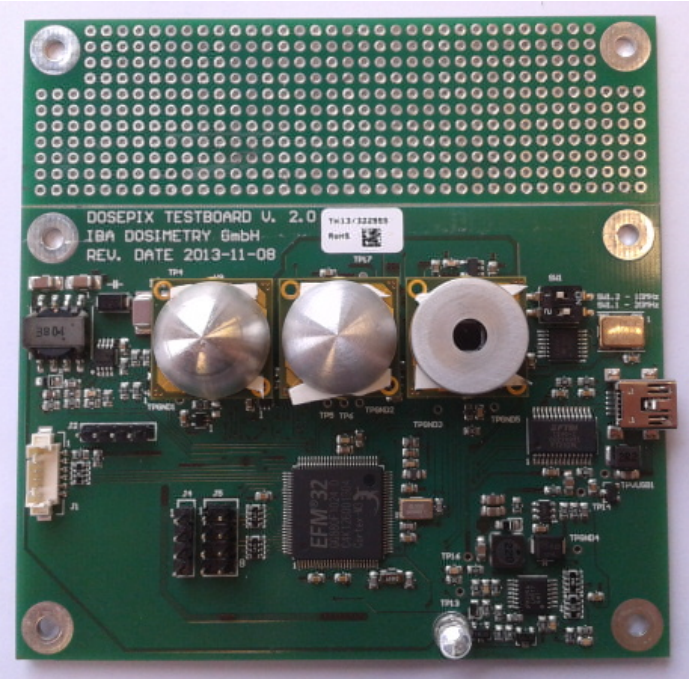

Figure 3.1.: Three Dosepix detectors mounted on the readout board, each equipped with an individual filter cap. The detector names are Slot 1 (right) for the detector with the aluminum cylinder, Slot 2 (center) for the detector with the aluminum half-sphere, and Slot 3 (left) for the detector with the tin half-sphere.

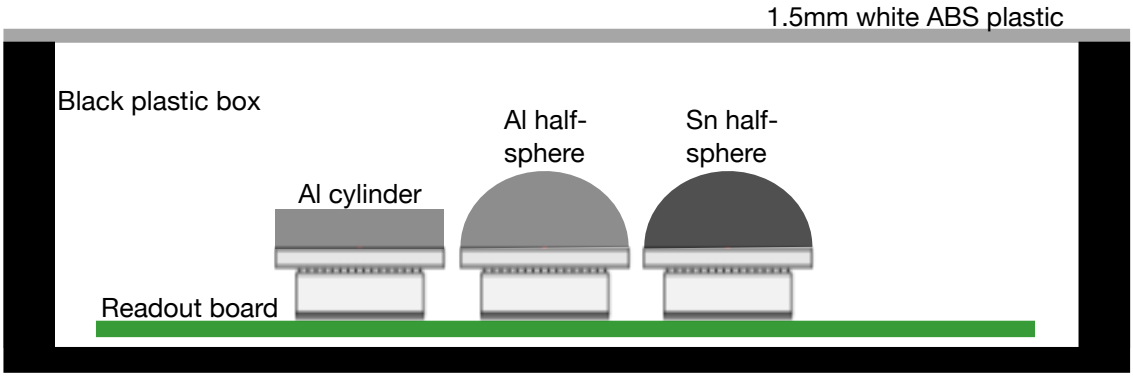

Figure 3.2.: Schematic depiction of the Dosepix dosimetry demonstrator. It illustrates the three Dosepix detectors slotted onto the readout board. Each detector has its individual filter-cap on top. They are all placed inside a thick black plastic box consisting of sidewalls of 5 mm and a backside of 2 mm thickness. Its cover consists of 1.5 mm thick ABS plastic.

3.3. Dosemeter Assessment Quantities

The first important quantity for quality assessment of a dosemeter is its response R. It is essential for characterizing a dosemeter as it states a measure of performance and is defined as the ratio of the dose calculated with Dosepix, H_{DPX}, and the reference dose H_{ref}:

$$R = \frac{H_{\mathrm{DPX}}}{H_{\mathrm{ref}}}. \tag{3.1}$$

The dose equivalent H_{DPX} measured by the Dosepix dosimetry demonstrator is determined via [63]

$$H_{\mathrm{DPX}} = \sum_{i=1}^{48} k_{\mathrm{i}} \cdot N_{\mathrm{i}} \tag{3.2}$$

where N_{i} denotes the number of registered events in energy bin i and k_{i} its corresponding conversion factor. The number 48 comes from the total number of energy bins from all three detectors combined. The conversion factors k_{i} depend on the dose equivalent at use. Uncertainty propagation assuming the uncertainty of N_{i} as $u(N_{\mathrm{i}}) = \sqrt{N_{\mathrm{i}}}$ results in the uncertainty of the measured dose $u(H_{\mathrm{DPX}})$:

$$u(H_{\mathrm{DPX}}) = \sqrt{\sum_{i=1}^{48} (k_{\mathrm{i}}^2 \cdot N_{\mathrm{i}})}. \tag{3.3}$$

Important influence quantities are of type F [64], meaning they cause a change of the response. Typical type F influence quantities are the dependencies on the mean photon energy, the angle of radiation incidence, the dose rate, the pulse duration, and the ambient temperature. They all have a minimum rated range of use that a dosemeter must adhere to as a bare minimum. The response is a systematic uncertainty of the indication of the dosemeter depending on the influence quantity at hand. This means that, e.g., at a given mean photon energy, the dosemeter will measure the dose with a certain bias of deviation to the reference dose.

The response is usually normalized to a reference response within the rated range of use of the dosemeter for this particular influence quantity. The reference value can be chosen by the applicant of the conformity assessment of the area dosemeter according to [64]. If not stated, a default value within the minimum rated range of use is applied. Using the normalized response as assessment quantity implies that either a response of 1 or a flat response across the range of use of the influence quantity is an optimum. The normalized response is defined as the response at a point x relative to the response at the reference point x_{ref}:

$$R_{\mathrm{Norm}} = \frac{R_x}{R_{x_{\mathrm{ref}}}} \tag{3.4}$$

The uncertainty of the normalized response is calculated via uncertainty propagation:

$$u(R_{\mathrm{Norm}}) = R_{\mathrm{Norm}} \sqrt{\left(\frac{u(H^x_{\mathrm{DPX}})}{H^x_{\mathrm{DPX}}}\right)^2 + \left(\frac{u(H^{x_{\mathrm{ref}}}_{\mathrm{DPX}})}{H^{x_{\mathrm{ref}}}_{\mathrm{DPX}}}\right)^2}. \tag{3.5}$$

The other important quantity to characterize the quality of the dosemeter is the coefficient of variation v. It is determined by performing a measurement series consisting of n independent measurements at constant environmental and irradiation conditions with the same dosemeter. To determine the coefficient of variation, the ratio between the standard deviation σ and the mean μ is calculated:

$$v = \frac{\sigma}{\mu}\,. \tag{3.6}$$

Its corresponding uncertainty is calculated via:

$$u(v) = v \sqrt{\left(\frac{u(\sigma)}{\sigma}\right)^2 + \left(\frac{u(\mu)}{\mu}\right)^2}. \tag{3.7}$$

A way to approximate the coefficient of variation with one measurement is by calculating the relative statistical uncertainty F_{stat}. It is defined as the ratio between the uncertainty on the measured dose ΔH_{DPX} and the measured dose H_{DPX} of Dosepix. It was shown in [20] that the relative statistical uncertainty is a good approximation of the coefficient of variation. Differences arise due to charge sharing in the detector, which results in slightly incorrect assumption of the independence of the count rate among the pixels [20, 35]. The relative statistical uncertainty is calculated via:

$$F_{\mathrm{stat}} = \frac{\sqrt{\sum_{i=1}^{48} (k_{\mathrm{i}}^2 N_{\mathrm{i}})}}{\sum_{i=1}^{48} k_{\mathrm{i}} N_{\mathrm{i}}}\,. \tag{3.8}$$

Its corresponding uncertainty after propagation of uncertainty results in:

$$u(F_{\mathrm{stat}}) = \sqrt{\sum_{i=1}^{48} \left(\frac{k_{\mathrm{i}}^2}{2u(H_{\mathrm{DPX}}) H_{\mathrm{DPX}}} - \frac{u(H_{\mathrm{DPX}}) k_{\mathrm{i}}}{H_{\mathrm{DPX}}^2}\right)^2 N_{\mathrm{i}}}\,. \tag{3.9}$$

3.4. Official Metrological Requirements

The official metrological requirements for area dosemeters are stated in PTB-A 23.3 and its complement [64, 65] on national level. Internationally the IEC 60846-1 defines the terms and requirements for area dosemeters [66]. They are summarized in Table 3.2 and relate to the irradiation of an area dosemeter by a reference photon fields, i.e., the radiation from the X-ray reference field in addition with the natural background radiation.

One important characteristic of a dosemeter is the energy dependence of its measured dose. A radiation quality is quantified by its mean photon energy and the width of the spectrum. The mean photon energy of the radiation quality is a quantity used to study the energy dependence of a dosemeter. Studies into the energy dependence are performed by utilizing photon fields of different mean energies. International standards such as the ISO 4037-1 [67] define specific photon reference fields, which are also called radiation qualities. They are created by X-ray tube spectra filtered with combinations of materials of different thicknesses and the γ-decay of radionuclides. The filters are used to beam-harden the spectrum, which results in attenuation of primarily low-energy contributions of said spectrum. The main parameters for photon reference fields created by X-ray tubes are their kVp value, the thickness of the filter materials, and the first and second HVL (half-value layer). Materials typically used for beam-hardening are aluminum, copper, tin, and lead. Applying a suitable filter material depends on the photon energies emitted by the X-ray tube. Attenuation of higher photon energies requires a material with a higher Z.

The main purpose of an active area dosemeter is to correctly display the dose that would be imparted to the body of the occupationally exposed staff member by external exposure at the position of the dosemeter at any given moment. The user must be alerted by the active dosemeter if dose/dose rate thresholds are surpassed. An ideal dosemeter displays the exact dose independently of energy and angle of radiation incidence. The investigations conducted in this chapter are into influence quantities of type F [64], which means their effect causes a change of the response. The normalized response of the influence quantities mean photon energy and angle of radiation incidence are allowed to change within

$$f_{\min} + 1 \leq R_{\text{Normalized}} \leq f_{\max} + 1\,. \tag{3.10}$$

The document PTB-A 23.3 [64] and its complement [65] define the limits of the deviation of the normalized response of the dependence on the mean photon energy and the angle of radiation incidence as $f_{\min} = -0.29$ and $f_{\max} = +0.67$. The combined influence of the dependence on the mean photon energy and the angle of radiation incidence is tested. The boundaries indicate that underestimating the dose is less tolerated than overestimating it to estimate the impact of ionizing radiation on the body conservatively. Underestimating the impact is far more dangerous due to existing

legal limits for the effective dose and absorbed dose to organ or tissue. These limits must be legally upheld and monitored. An underestimation of the dose can lead to surpassing those thresholds and, therefore, unnecessary adverse health risks to the workers of the monitored workplace.

The reference value for the normalized response must be within the range of use. A reference value deviating from the recommended one and an extension of the minimum rated range of use for the energy and angular range can be chosen by the applicant of the conformity assessment of the dosemeter. The metrological investigations are carried out in a way that the change of the response is within the permitted limits if an influence quantity is changed from its reference value to another value within the range of use [64]. ISO 29661 [59] states that the most accurate information about the energy dependence is determined by using narrow width X-ray spectra (N-series) and γ-decay-radiation. The normalized response is determined by utilizing radiation qualities of the N-series and the S-qualities, which are defined as the γ-decay-radiation of radioactive isotopes (here S-Cs and S-Co).

If the area dosemeter is to be used in the vicinity of nuclear facilities, a normalized response up to 10 MeV must be guaranteed, e.g., for the purpose of area-wide environmental monitoring. IEC 60846-1 [66] states two main workplaces: Workplaces, where gamma sources are handled, have a minimum rated range of use of 80keV-1.33MeV (S-Co), e.g., in industrial applications. Another is the X-ray applications, e.g., medical diagnostics, where a minimum rated range of use between 20-150 keV is defined.

For the calculation of the limits of the coefficient of variation a lower limit of the measurement range H_u must be stated. With a given value of H_u, the limit of the coefficient of variation v_max is calculated. Depending on the value of H_u, the coefficient of variation must stay below 5-15 % and below 1-2.6672% for K_air. H_u for $H^*(10)$ is 0.1 mSv for $H'(3, \Omega)$ is 0.3 mSv, $H'(0.07, \Omega)$ is 1 mSv. The value of H_u is not stated in [65], therefore the values of the personal dose equivalents are utilized as stated in [69]. H_u is 1000µGy for K_air [68].

3.5. Laboratory Setup at Erlangen

A MEGALIX Cat [70] X-ray tube for applications in angiography is utilized as a radiation source in laboratory setup at Erlangen. The tube voltage can be varied between 40 kV and 125 kV while the tube current is restricted to a maximum power of 2 kW. The tube exit window is 1.5 mm aluminum-equivalent. In addition to this intrinsic filtration, other filter materials are used to achieve the intended beam-hardening required for the radiation field. The Dosimax Plus from IBA dosimetry [32] with the semiconductor RQX-sensor is used to perform reference dose measurements. Its uncertainties must be below 5% in accordance with IEC 61674 [68] and its specifications state a kVp range of 50-150 kV. Measurements with this detector deliver the reference air kerma that is used to calculate the reference dose which is compared

Quantity	Minimum rated range of use	Reference value
For $H'(0.07, \Omega)$: Mean photon energy $\langle E \rangle$ and angle of radiation incidence α	30 keV to 250 keV and -45 ° $\leq \alpha \leq$ +45 °	65 keV (N-80) and 0 ° (reference orientation)
For $H'(3, \Omega)$: Mean photon energy $\langle E \rangle$ and angle of radiation incidence α	30 keV to 250 keV and -45 ° $\leq \alpha \leq$ +45 °	65 keV (N-80) and 0 ° (reference orientation)
For $H^*(10)$: Mean photon energy $\langle E \rangle$ and angle of radiation incidence α	80 keV to 1250 keV and -45 ° $\leq \alpha \leq$ +45 °	662 keV (S-Cs) and 0 ° (reference orientation)
For K_{air}	50 kV - 150 kV (RQR 3 - RQR 10)	70 kV (RQR 5)
Quantity	**Dose range**	**$v_{\max}$ [%]**
Dose H	$H < H_{\mathrm{u}}$ $H_{\mathrm{u}} \leq H < 11 \cdot H_{\mathrm{u}}$ $11 \cdot H_{\mathrm{u}} \leq H$	15 16 - H/H_{u} 5
Dose K_{air}:	$K_{\mathrm{air}} \leq H_{\mathrm{u}}$ $H_{\mathrm{u}} \leq K_{\mathrm{air}}$	0.1667 · (16-0.01 K_{air}) % 1%

Table 3.2.: Conformity assessment requirements for area dosemeters according to national and international requirements stated in PTB-A 23.3 [64, 65] and IEC 60846-1 [66]. Additionally the requirements to semiconductor detectors as used in X-ray diagnostic imaging for air kerma K_{air} according to IEC 61674 [68] are stated.

to the dose measured by Dosepix. The Dosepix dosimetry demonstrator is placed on an aluminum rail at a distance of 137 cm to the X-ray tube focus for irradiations utilized in this chapter. A large distance between source and detector is desirable to get a homogeneous field across the Dosepix detectors. The detector axis is positioned vertically to the ground floor of the measurement chamber. The RQX detector replaces the Dosepix dosimetry demonstrator after the irradiation. Its focus point is on the same position as the reference point of the Dosepix dosimetry demonstrator, where the reference point is Slot 2, i.e., the center of the readout electronics. Figure 3.3 shows a schematic depiction of the laboratory setup at Erlangen.

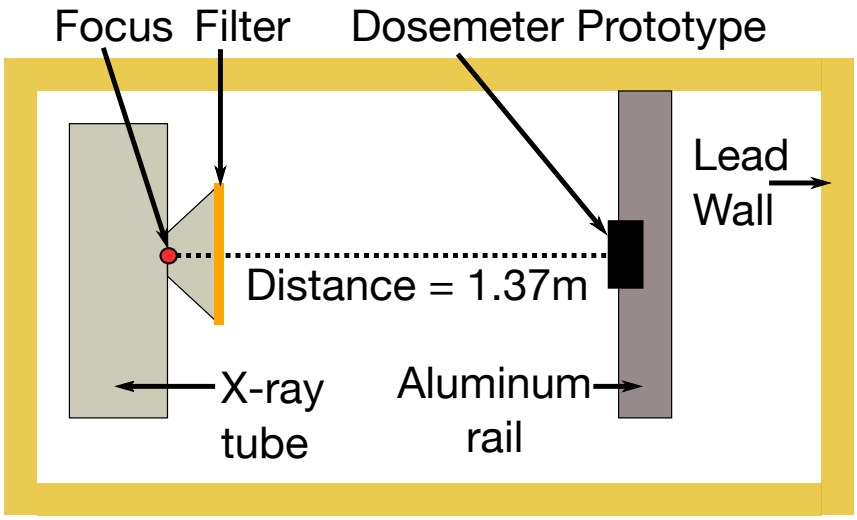

Figure 3.3.: A schematic depiction of the Erlangen setup. It is not true-to-scale. The X-ray tube emits a photon field beam-hardened by the filters in front of the exit window. The filters are chosen according to the intended radiation quality stated in Table 3.3. The dosemeter prototype is placed on an aluminum rail at a distance of 1.37 m to the X-ray tube's focus.

The irradiations at the Erlangen setup are typically used as preparatory measurements to determine a set of conversion factors before the dependence on the mean photon energy and the angle of radiation incidence is investigated at facilities of PTB. In the following section a series of spectra for the use at the Erlangen setup is defined.

3.6. Simulation of Reference Photon Fields

The International Commission on Radiation Units and Measurements (ICRU) defines several conversion coefficients between dose quantities for different organs and radiation protection quantities in its Report 57 [53]. The base for these conversion coefficients is the kerma factor $k_\Phi(E)$ (air kerma per unit fluence), which effectively relates the

fluence of a photon ensemble to air kerma. Air kerma is a basic dose quantity typically measured by ionization chambers. These are one of the most common utilities for the measurement of the photon dose. For instance, for the investigations in this chapter, the Dosimax Plus from IBA dosimetry [32] with the semiconductor RQX-sensor is used at the Erlangen setup. The monoenergetic kerma factor is calculated according to [54] via

$$k_\Phi(E) = E \cdot \left(\frac{\mu_{\mathrm{tr}}(E)}{\rho}\right)_{\mathrm{air}} \tag{3.11}$$

where E is the energy of the photon and $\left(\frac{\mu_{\mathrm{tr}}(E)}{\rho}\right)_{\mathrm{air}}$ the mass energy-transfer coefficient in air. It is sufficient to use the tabulated mass energy-absorption coefficient in air $\left(\frac{\mu_{\mathrm{en}}(E)}{\rho}\right)_{\mathrm{air}}$, found in [71] for the scope of this chapter since energies in the X-ray range are employed when this quantity is used. Main differences occur in the megaelectronvolt energy range due to radiation losses of secondary charged particles. Figure 3.4(a) shows the mass energy-absorption coefficient in air [71], and Figure 3.4(b) the corresponding monoenergetic kerma factor, which is determined via

$$k_\Phi^{\mathrm{Hubbell}}(E) = 160.218 \cdot E \cdot \left(\frac{\mu_{\mathrm{en}}(E)}{\rho}\right)_{\mathrm{air}} \tag{3.12}$$

where 160.218 is the conversion factor from MeV/g to pGy. The unit of the kerma factor is [pGy cm^2]. Air-Kerma, more precise, the collision air kerma, approximates the absorbed dose in air within the investigated mean photon energy range in this chapter (12.4 keV to 1250 keV). More importantly, it holds that [59]

$$K_{\mathrm{air,col}} = K_{\mathrm{air}} \cdot (1 - g) \tag{3.13}$$

where the factor g considers the fraction of the energy of the secondary electrons liberated by photons that is lost by radiation-emitting processes such as Bremsstrahlung, fluorescence radiation, or annihilation radiation of positrons [59]. Its value is below 0.003 for energies smaller than 1.3 MeV in air [59].

Furthermore, the ICRU defines conversion coefficients from air kerma to dose equivalents [53], the operational quantities for radiation protection. Knowing the energy distribution of the impinging photons and the air kerma of the exposure enables the calculation of reference dose values via spectrum-specific conversion coefficients from air kerma to the dose equivalent of interest. Spectroscopy of the present radiation field is necessary to determine the energy distribution, i.e., the spectrum. With that, facility-specific conversion coefficients can be determined, which allows precise calculation of the reference dose. In the case of a lack of spectroscopy, simulation tools must be employed. Such a tool for tungsten X-ray tubes to simulate the incident

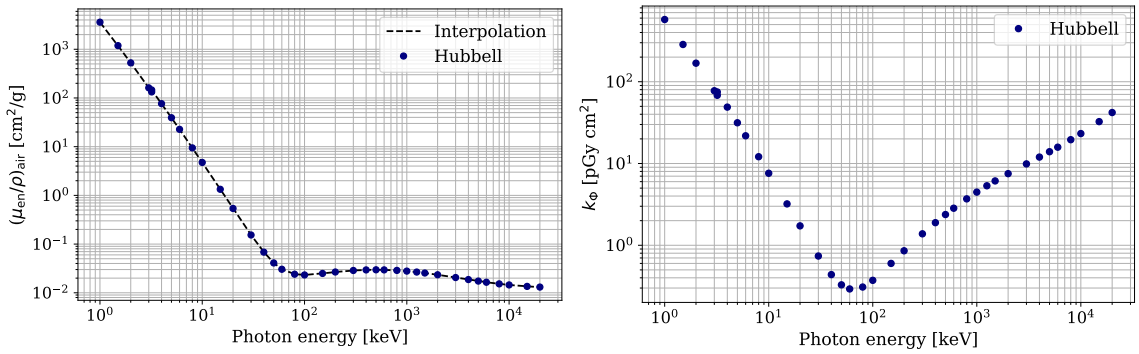

(a) Mass energy-absorption coefficient in air

(b) Kerma factor

Figure 3.4.: (a): Mass energy-absorption coefficient in air. Data taken from Hubbell [71], and interpolated using log-log two point interpolation. (b): Kerma factor calculated with data in (a).

spectra is xpecgen [72]. A python module is available on Github and published in [73]. Differences between the real spectrum and the simulated one are expected predominantly at low energies, where filter impurities induce stronger attenuation of the photon field.

Simulated incident spectra are used to determine reference area dose equivalents in the following. It requires the measured air kerma together with a spectrum-specific conversion coefficient. The weighted conversion coefficients $\langle h_k^*(x, R)\rangle$ for a spectrum R are calculated according to [54] as follows:

$$\langle h_k^*(10, R)\rangle = \frac{\int_{E_{\min}}^{E_{\max}} h_k^*(10, E)\Phi(E)k_\Phi(E)dE}{\int_{E_{\min}}^{E_{\max}} \Phi(E)k_\Phi(E)dE}, \tag{3.14}$$

where $h_k^*(10, E)$ denotes the monoenergetic conversion coefficient for the ambient dose equivalent in 10 mm depth of the ICRU sphere, $\Phi(E)$ the photon fluence, and $k_\Phi(E)$ the kerma factor. Analogous calculations are performed for directional and personal dose equivalents. The corresponding mean energy $\langle E\rangle$ of a spectrum between the lower $E_{\min}$ and upper $E_{\max}$ integration boundary is calculated according to ISO 4037-1 via [67]:

$$\langle E\rangle = \frac{\int_{E_{\min}}^{E_{\max}} \Phi(E)E\mathrm{d}E}{\int_{E_{\min}}^{E_{\max}} \Phi(E)\mathrm{d}E}. \tag{3.15}$$

A number of 45 spectra are defined for the laboratory setup at Erlangen. The parameter space for these spectra is defined by the available materials Al, Cu, Sn and the tube voltage of the used MEGALIX X-ray tube. The aim is to scan across the energy range with broad and narrow spectra that differ in their mean energies. This allows the investigation of the energy dependence of the dose determination

via Dosepix. Different detector responses are measured for all incident spectra, enabling dose calibration, i.e., determination of conversion factors, of the Dosepix dosimetry demonstrator. Figure 3.5(a) shows the corresponding energy spectra of the 45 fields. The color code is sorted by the kVp values of the spectra in ascending order. If a kVp value exists twice, the ascending mean photon energy is used as the second sorting condition. Table 3.3 lists the basic parameters, including mean photon energy, mean conversion coefficient $h_{\mathrm{k}}(x)$ from air kerma to area dose equivalent in x millimeter of the ICRU sphere, kVp, and filter thickness. The abbreviation R stands for reference and the spectra are simply consecutively numbered. The intrinsic filtration of the X-ray tube is 1.5 mm aluminum-equivalent and is included in the total value of the aluminum filtration. The mean conversion coefficients are calculated via Equation (3.11). A comparison between calculated conversion coefficients at certain mean photon energy and monoenergetic ones is shown in Figure 3.5(b). Additionally, the Dos34 conversion coefficients of the 5 N-series radiation qualities in the energy range are shown for comparison. A small systematic deviation at smaller energies is observed. Below 60 keV all calculated conversion coefficients and the literature values from Dos34 [54] are below the interpolated curve of the ICRU Report 57 [53] conversion coefficients for monoenergetic photon energies. Above 60 keV, the mean conversion coefficients can be approximated by the interpolated data of the monoenergetic conversion coefficients as the difference become small.

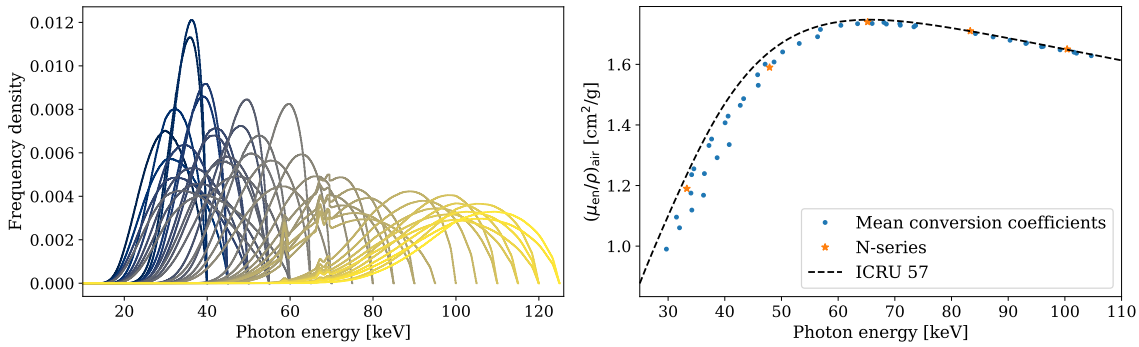

(a) Simulated reference fields

(b) $\langle h_k^*(10, R)\rangle$ and $\langle E\rangle$

Figure 3.5.: (a): Reference spectra simulated with xpecgen [72] for the determination of mean conversion coefficients $h_{\mathrm{k}}(10)$ from air kerma to ambient dose equivalent $H^*(10)$. (b): Comparison between conversion coefficients $h_{\mathrm{k}}(10)$ for monoenergetic photons from [53], five radiation qualities of the N-series (N-40 to N-120) from [54] and the ones calculated with the spectra in (a).

Code	kVp	Al	Cu	Sn	$\langle E \rangle$	$\langle h_k^*(10) \rangle$	$\langle h_k'(3) \rangle$	$\langle h_k'(0.07) \rangle$
R0	40	3.5	0.0	0.0	29.699	0.990	1.152	1.184
R1	45	3.5	0.0	0.0	32.015	1.061	1.196	1.216
R2	50	3.5	0.0	0.0	34.186	1.119	1.233	1.244
R3	55	3.5	0.0	0.0	36.246	1.168	1.265	1.268
R4	40	3.5	0.3	0.0	34.151	1.236	1.303	1.289
R5	45	3.5	0.3	0.0	37.208	1.332	1.364	1.339
R6	50	3.5	0.3	0.0	40.055	1.407	1.414	1.380
R7	55	3.5	0.3	0.0	42.731	1.465	1.455	1.412
R8	55	5.0	0.9	0.0	47.117	1.601	1.551	1.488
R9	60	5.0	0.9	0.0	50.206	1.641	1.587	1.515
R10	65	5.0	0.9	0.0	53.137	1.669	1.614	1.536
R11	70	5.0	0.9	0.0	56.369	1.691	1.637	1.555
R12	40	6.0	0.0	0.0	31.476	1.096	1.218	1.226
R13	45	6.0	0.0	0.0	34.027	1.175	1.267	1.264
R14	50	6.0	0.0	0.0	36.404	1.239	1.308	1.297
R15	55	6.0	0.0	0.0	38.649	1.292	1.343	1.324
R16	60	6.0	0.0	0.0	40.782	1.335	1.374	1.348
R17	55	6.0	0.6	0.0	45.796	1.566	1.525	1.468
R18	60	6.0	0.6	0.0	48.691	1.608	1.561	1.495
R19	40	9.0	0.2	0.0	34.544	1.255	1.315	1.298
R20	45	9.0	0.2	0.0	37.675	1.353	1.377	1.350
R21	50	9.0	0.2	0.0	40.584	1.429	1.428	1.391
R22	55	9.0	0.2	0.0	43.322	1.487	1.470	1.424
R23	60	9.0	0.2	0.0	45.903	1.531	1.504	1.451
R24	65	6.0	2.0	0.0	56.875	1.715	1.657	1.569
R25	70	6.0	2.0	0.0	60.478	1.729	1.674	1.585
R26	75	6.0	2.0	0.0	63.427	1.734	1.681	1.594
R27	80	6.0	2.0	0.0	65.998	1.735	1.684	1.600
R28	85	6.0	2.0	0.0	68.504	1.733	1.684	1.602
R29	90	6.0	2.0	0.0	70.967	1.729	1.681	1.602
R30	95	6.0	2.0	0.0	73.366	1.724	1.677	1.600
R31	80	6.0	2.9	0.0	68.066	1.738	1.689	1.606
R32	85	6.0	2.9	0.0	70.874	1.734	1.687	1.607
R33	90	6.0	2.9	0.0	73.663	1.728	1.682	1.606
R34	100	8.0	5.0	0.0	84.219	1.702	1.658	1.592
R35	105	8.0	5.0	0.0	87.337	1.691	1.648	1.583
R36	110	8.0	5.0	0.0	90.323	1.680	1.637	1.574
R37	115	8.0	5.0	0.0	93.104	1.669	1.627	1.566
R38	120	8.0	5.0	0.0	95.893	1.658	1.617	1.557
R39	110	8.0	5.0	0.5	93.227	1.671	1.629	1.568
R40	115	8.0	5.0	0.5	96.188	1.659	1.618	1.558
R41	120	8.0	5.0	0.5	99.151	1.648	1.608	1.549
R42	125	8.0	5.0	0.5	102.049	1.637	1.597	1.540
R43	120	8.0	7.0	0.5	101.615	1.640	1.600	1.542
R44	125	8.0	7.0	0.5	104.655	1.628	1.589	1.533

Table 3.3.: Parameters for the reference fields abbreviated as the R-series for measurements at laboratory in Erlangen. Material thicknesses are stated in [mm], conversion-coefficients from air kerma to area dose equivalent h_k(x) in [Sv/Gy], kVp in [kV], and the mean photon energy $\langle E \rangle$ in [keV].

3.7. Facilities at PTB

The investigations of the dependence of the normalized response and the relative statistical uncertainty on the mean photon energy and the angle of radiation incidence of the Dosepix dosimetry demonstrator regarding the performance for area dose equivalents and air kerma are conducted at three different facilities of the Physikalisch-Technische Bundesanstalt (PTB), which is the German national metrology institute. The irradiations are carried out in reference photon fields according to ISO 4037-1 [67] and with procedures according to ISO 29661 [64]. An applicant for assessment of the conformity must indicate the reference point of the dosemeter. In the case of the Dosepix dosimetry demonstrator, the reference point is the center of the sensor surface of the detector in Slot 2. Table 3.4 shows the investigated photon reference fields and the chosen angles of radiation incidence. The narrow spectra are obtained by beam hardening of an X-ray tube spectrum. The number n in N-n represents the kVp of the X-ray tube. The basic characteristic of the N-series is their small width of the spectrum. The filter thickness, acceleration voltage, mean energy, and kerma factor for all radiation qualities used in this work can be found in [67].

Facility at PTB	Radiation quality	Mean photon energy $\langle E \rangle$ [keV]	Angle of radiation incidence α [°]
120 kV	N-15	12.4	0; 30; 45; 60
	N-20	16.3	0; 30; 45; 60
	N-25	20.3	0; 30; 45; 60
	N-30	24.6	0; 30; 45; 60
	N-40	33.3	0; 30; 45; 60
400 kV	N-60	47.9	0; 30; 45; 60
	N-80	65.2	0; 30; 45; 60
	N-100	83.3	0; 30; 45; 60
	N-120	100	0; 30; 45; 60
	N-150	118	0; 30; 45; 60
	N-200	165	0; 30; 45; 60
	N-250	207	0; 30; 45; 60
	N-300	248	0; 30; 45; 60
Hartlep	S-Cs	662	0; 30; 45; 60
	S-Co	1250	0; 30; 45; 60

Table 3.4.: Specification of reference radiation fields at facilities of PTB, their mean energies $\langle E \rangle$, and the investigated angles of incidence α. Radiation qualities of the N-series and radionuclides S-Cs and S-Co according to ISO 4037-1 [67] are utilized.

There are two different X-ray facilities for small and medium (120 kV-facility) and large tube voltages (400 kV-facility), and a facility for high-activity radioactive isotopes

(Hartlep-facility). The 400 kV-facility is exemplary shown in Figure 3.6. Due to the lack of a calibration phantom, the dosemeter is positioned on a small lifting platform. The reference point is Slot 2 at 1.5 cm below the top of the box cover, which is the position of the sensor element. The reference direction is the normal to the housing cover, pointing through the back of the housing. The reference orientation is a vertical alignment of the three detector axis. The Dosepix dosimetry demonstrator is positioned on a rotary table that allows a precise adjustment of the angle of radiation incidence. For the measurements at the Hartlep facility, a PMMA build-up plate of 3 mm thickness (as recommended by ISO 4037-3 [74]) is positioned in front of the dosemeter to guarantee secondary electron equilibrium. The facilities have a systematic uncertainty of 2% on the reference dose, which is measured by a monitor chamber. It is assumed in the following that the different energies are fully correlated, which means that the systematic uncertainty cancels by investigating the normalized response. Measurements at facilities of PTB are important since conformity of a dosemeter is assessed at PTB. The reference conditions represent the reality of the dose. If a dosemeter measures the dose correctly at PTB it is inferred that it measures the dose correctly at all other instances.

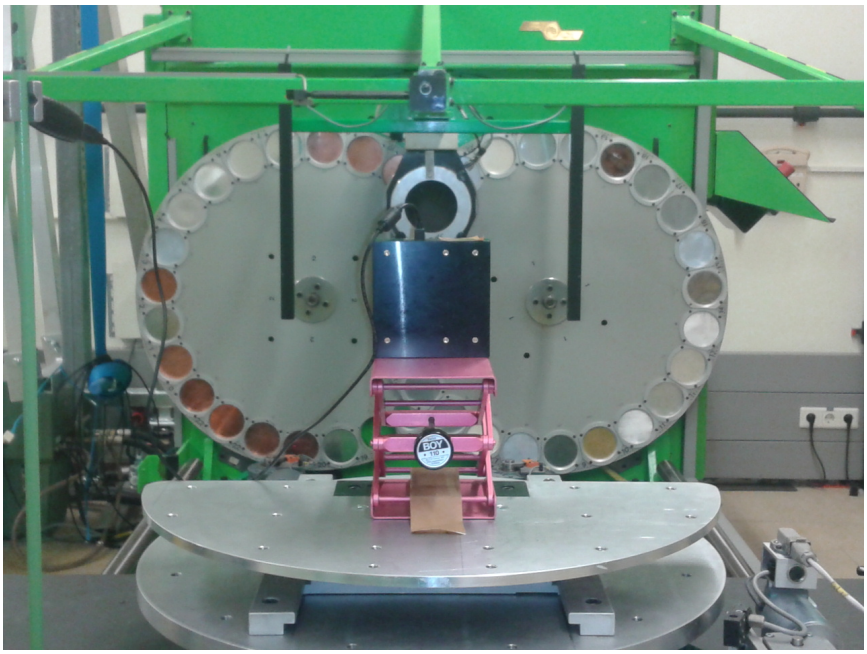

Figure 3.6.: 400 kV irradiation facility at PTB for continuous photon fields. A monitor chamber mounted in front of the exit measures the reference dose. The Dosepix dosimetry demonstrator is placed on a lifting platform standing on a rotary table. The measurements are performed free-in-air, i.e., without a calibration phantom. It also shows a wheel equipped with filter materials used to specify the radiation quality.

3.8. Determination of Conversion Factors

This section introduces the procedure to determine the conversion factors from the number of registered events per energy bin measured by Dosepix to area dose equivalents and air kerma. These are called conversion factors in short in the following. The conversion factors are the integral component of dosimetry with Dosepix. Simulations performed in the scope of a PhD-thesis [19] are used to determine conversion factors for the large pixels. The spectra introduced in Section 3.6 are utilized to adapt the conversion factors determined for the simulation to reality via measurements. Measurements of these spectra are the foundation for determining conversion factors for the small pixels. The determined conversion factors are used to validate the performance in continuous reference photon fields at facilities of PTB. The conversion factors are optimized when the ratio between calculated and true dose for a large energy range at an angle of radiation incidence of 0° is close to 1, i.e., the systematic uncertainty of the mean photon energy is small. Key indicators of optimized conversion factors are the minimum, maximum, mean response, and its corresponding standard deviation. The aim is to optimize the parameters so that the mean response is close to 1 and its standard deviation is close to zero. The conversion factors themselves must adhere to a steady trend. Such a trend does not introduce incontinuities such as spikes in the energy dependence of the response.

For the optimization of the conversion factors, a least-squares fit is performed. The python module LMFIT is used which utilizes the implemented function *minimize*() [75] and applies the fit method *least_squares*. Every optimization is accompanied by lower and upper boundaries of the parameters. The conversion factors must be positive values, guaranteed by a positive lower boundary. Negative values imply a negative dose which is nonphysical. Several parameters can be held constant to stabilize the trend of the conversion factors. Energy histograms recorded in the Dosi-mode for the measurements at the Erlangen setup or facilities of PTB are used to determine an optimized set of conversion factors. The number of registered events in a pixel bin is summed over all pixels. This results in three energy histograms per pixel type per radiation quality for the Dosepix dosimetry demonstrator. These energy histograms are concatenated to a 48×1 array $\vec{N}$ whose dot product with a 48×1 array of the conversion factors $\vec{k}$ yields the dose measured by Dosepix

$$H^{\mathrm{DPX},j} = \vec{N}^j \cdot \vec{k}^j \tag{3.16}$$

where j denotes either the large or the small pixels. For the optimization of the conversion factors a data set of the size m is used consisting of either simulations or measurements or the combination of both. The number n of the total size of varied conversion factors must remain smaller than m to determine an unique set of optimized parameters. The set of functions $f_i(x)$ that is used in the optimization of the conversion factors of one particular pixel type is

$$f_i(x) = H_i^{\mathrm{True}} - H_i^{\mathrm{DPX}} \tag{3.17}$$

where i denotes the index of the current measurement of a set of measurements of size m, H_i^{True} the reference dose and H_i^{DPX} the dose calculated with Dosepix of measurement i. The cost function whose local minimum is determined is:

$$F(x) = 0.5 \sum_{i=0}^{m-1} f_i(x)^2 \tag{3.18}$$

where m denotes the number of data points. The input components for the fit are the following. The reference dose to which the conversion factors are optimized, the Dosepix data set to be used in the optimization and the fit conditions. The important quantities for the conditions are the lower and upper boundary, the initial conversion factors, and the constant invariable bin indices. The theoretical conversion coefficients tabulated in the literature are utilized to calculate the reference dose from air kerma measurements.

3.9. Area Dosimetry with the Large Pixels

A metrological characterization of the large pixels of the Dosepix dosimetry demonstrator is performed in this section. The investigated influence quantity is the mean photon energy. The angle of radiation incidence is investigated in a separate section. The energy dependence of the response of the area dose equivalents in the mean energy range of 12.4 keV-1250 keV is determined. The dosimetric quantities of interest are $H^*(10)$, $H'(3, \Omega)$, $H'(0.07, \Omega)$, and in addition, the air kerma since all measurements were performed free in air. Several data sets are used to determine conversion factors. They are named by the location of the measurement, i.e., Erlangen and PTB. Data from a simulation created in [19] is also utilized. It is the basis of the conversion factors for the large pixels.

3.9.1. Simulation Data

A set of initial conversion factors for the large pixels between the number of registered events in an energy bin of Dosepix and an area dose equivalent or air kerma is determined before the first measurements are performed. To do so, the simulation of the Dosepix dosimetry demonstrator created and performed in [19] is utilized. In this simulation, monoenergetic X-rays in the energy range of 13 keV to 1200 keV serve as the radiation source. A Gaussian filter of a standard deviation of 1.2 keV is applied to the simulation data of the deposited energies to take the detector resolution into account. The data is binned according to the bin edges for dosimetry (see Table 3.1).

The process of applying the detector resolution and binning is exemplary shown in Figure 3.7 for each detector.

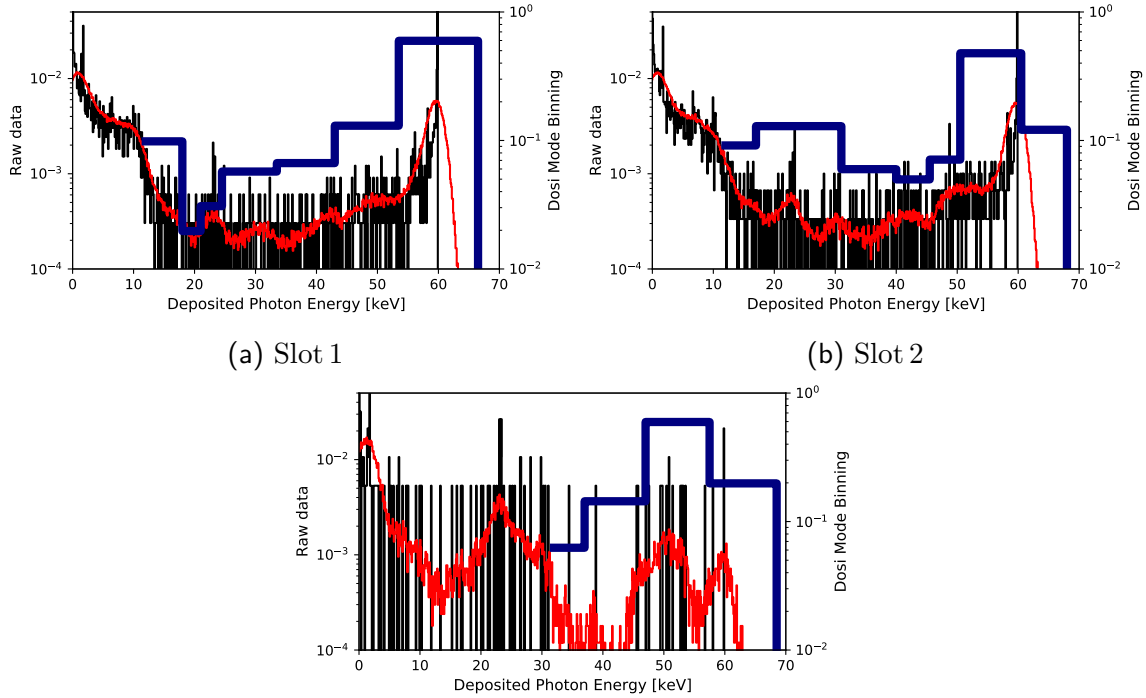

(a) Slot 1

(b) Slot 2

(c) Slot 3

Figure 3.7.: Simulation data for a monochromatic energy of 60 keV for simulations of the Dosepix dosimetry demonstrator created and performed in [19]. The three different Slots are shown in (a)-(c). The raw input data is drawn in black. A Gaussian filter with a standard deviation of 1.2 keV is applied to the raw data to take the resolution of the Dosepix detector into account, which is drawn in red. The blue histogram is the detector output resembling the processing by the Dosi-mode.

The irradiated area is 10 cm×10 cm, and the number of events is 10^8. The ratio of the number of events and the irradiated area is the fluence Φ. The reference dose is calculated via

$$H^{\text{ref}} = h_k(x) k_\Phi \Phi \tag{3.19}$$

where $h_k(x)$ denotes the conversion coefficient between air kerma and an area dose equivalent with x denoting the depth in mm in the ICRU sphere on the radius vector opposing the direction of the aligned radiation field and k_Φ the kerma factor calculated with the data of Hubbell and Seltzer [71]. In case of the reference air kerma the factor $h_k(x)$ is omitted. The reference area dose equivalents and the reference air kerma for the simulation are shown in Figure 3.8. The air kerma is stated in µGy and the dose

equivalents in µSv. With these values, the limit of F_{stat} is calculated according to Table 3.2 to 15% for every dose equivalent, and about 2.6% for air kerma.

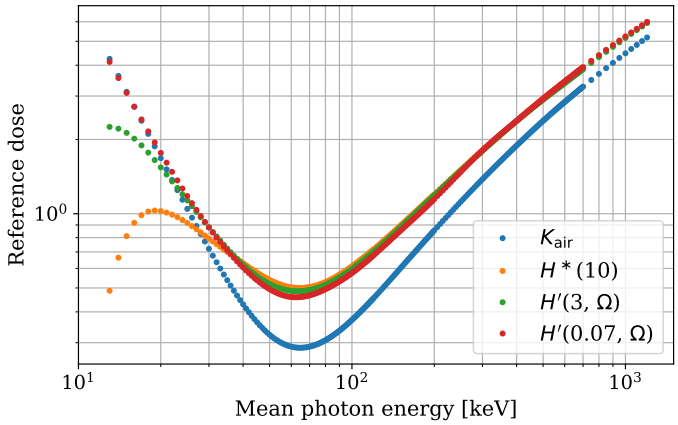

Figure 3.8.: Reference dose for 10^8 events irradiating an area of 10 cm×10 cm for monochromatic X-rays calculated according to Equation (3.19). The literature values used are the kerma factor k_Φ [71], and the conversion coefficients between air kerma and $H^*(10)$ $h_k(10)$ [54], $H'(0.07, \Omega)$ $h_k(0.07)$ [56], and $H'(3, \Omega)$ $h_k(3)$ [55]. The reference dose for K_{air} is given in [µGy] and for the area dose equivalents in [µSv].

The optimization routine described in Section 3.8 is used to determine a set of conversion factors which serves as basis for the measurements in the following sections. The boundary conditions for the fit are a start value of 3×10^{-4} µSv, no bins with constant conversion factors, and an upper boundary of infinite. The lower boundary is varied to stabilize the trend and determine bins that have a small impact on the total dose determined by Dosepix. Such bins are deemed unnecessary by the optimization routine as the value of its conversion factor is small or runs into the lower boundary. Figure 3.9 shows the conversion factors for the air kerma, $H^*(10)$, $H'(3, \Omega)$, and $H'(0.07, \Omega)$. Several bins have conversion factors equal to the lower boundary after the optimization, particularly bin 4 of Slot 1 and bins 10 to 14 of Slot 3 for the area dose equivalents $H^*(10)$, $H'(3, \Omega)$, and $H'(0.07, \Omega)$. For the air kerma, the conversion factors of bins 10 to 14 of Slot 3 are equal to the lower boundary.

The optimum value for the lower boundary for the conversion factors is determined by calculating the response R for all data points and comparing key performance indicators such as minimum, maximum, and mean response and its corresponding standard deviation. All indicators state that the best performance is achieved when they are one, except the standard deviation, which must be close to zero. Thirteen lower boundaries are sampled, and their key performance indicators are shown in Figure 3.10. They include 0 as the lowest one, which considers that there is no physical meaning in a negative dose even though there is no mathematical argument against

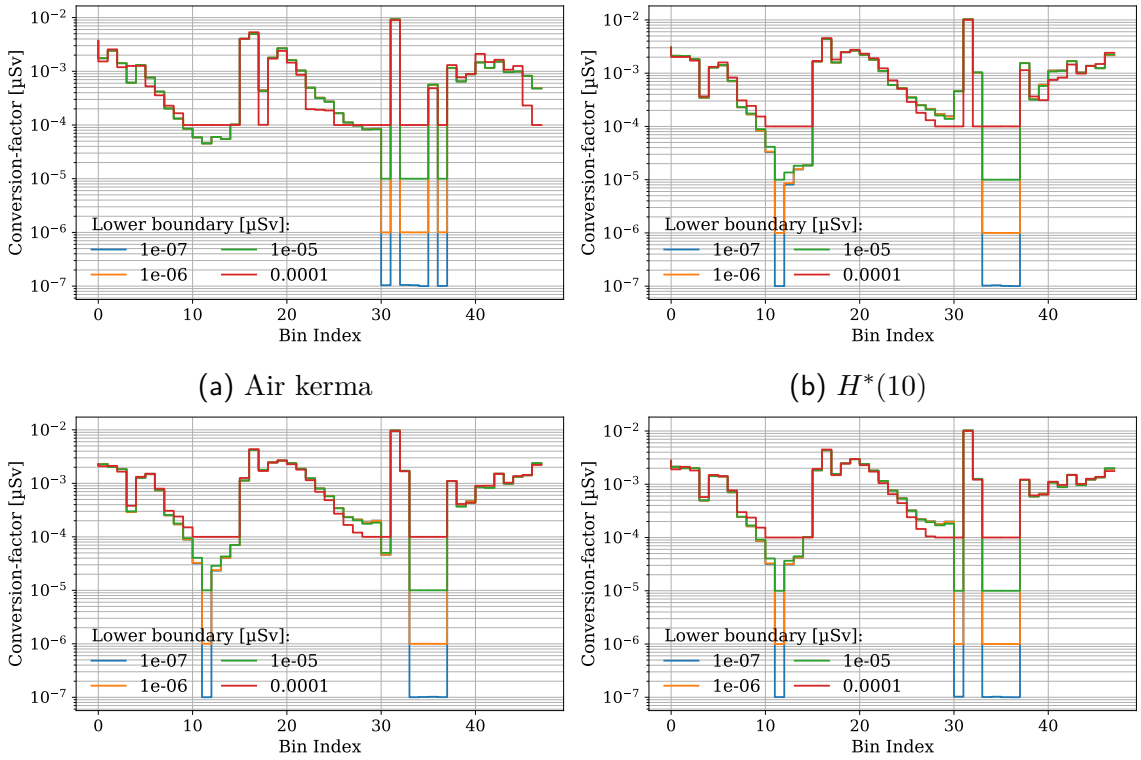

(a) Air kerma (b) $H^*(10)$

(c) $H'(3, \Omega)$ (d) $H'(0.07, \Omega)$

Figure 3.9.: Optimized conversion factors for the large pixels between the number of registered events in an energy bin of Dosepix and an area dose equivalent or air kerma. These are the air kerma (a), the ambient dose equivalent $H^*(10)$ (b), and the directional dose equivalents $H'(3, \Omega)$ (c) and $H'(0.07, \Omega)$ (d). The underlying data are from simulations of the detector response to monoenergetic X-rays [19]. Bin indices 0 to 15 resemble Slot 1, 16 to 31 Slot 2, and 32 to 47 Slot 3.

including negative conversion factors in the dose calculation. From the standpoint of radiation protection, a negative contribution is dangerous. A negative dose might potentially occur in monoenergetic radiation fields where a predominant number of entries in an energy bin with a large negative conversion factor is observed. The maximum lower boundary is 10^{-4} µSv. Between 10^{-5} µSv and 10^{-4} µSv finer sampling in steps of 10^{-5} µSv is used. The key performance indicators are constant below 9×10^{-4} µSv and become worse with an increasing lower boundary. Therefore, 10^{-5} µSv is chosen as the conservative lower boundary for the following investigations into the energy dependence with the large pixels of the Dosepix dosimetry demonstrator.

The response is calculated with these conversion factors according to Equation (3.1) and is shown in Figure 3.11. The red dashed lines indicate the limits according to [64, 68]. The response values are flat around one above a photon energy of 20 keV for all area dose equivalents and air kerma. Means of 1.007 to 1.008 and standard

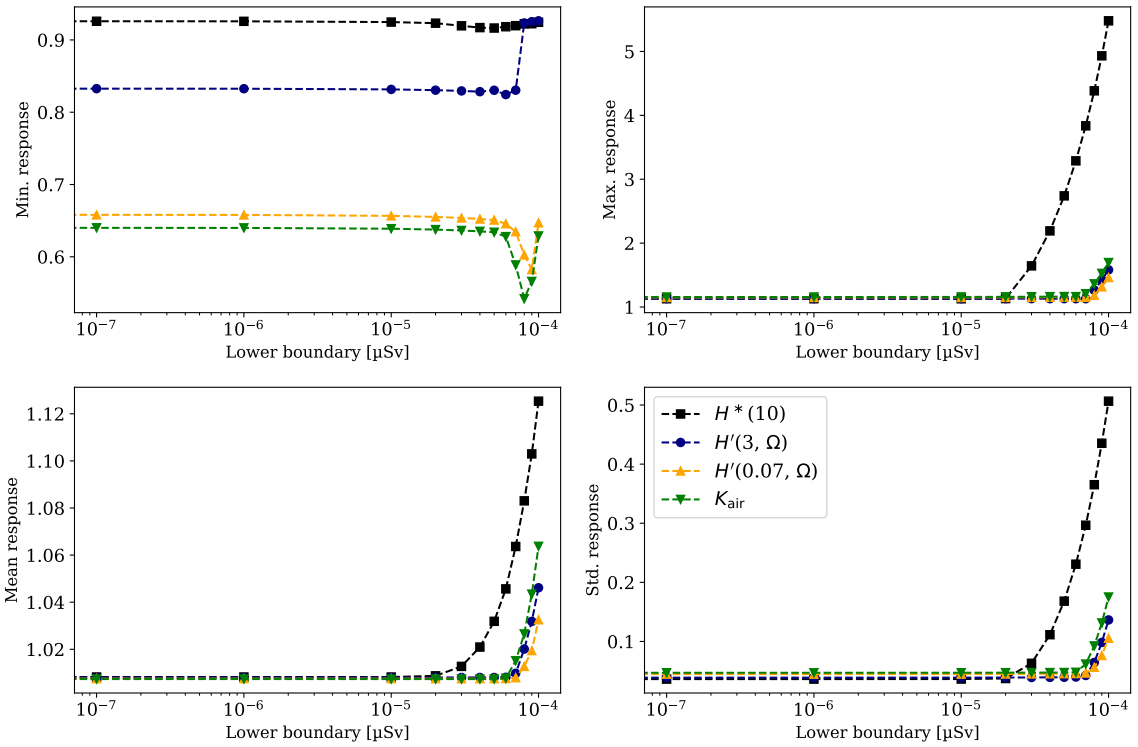

Figure 3.10.: Key performance indicators for thirteen lower boundaries. The lower boundary is sampled between 0 µSv (displayed from 10^{-7} µSv) and 10^{-4} µSv and in finer sampling in steps of 10^{-5} µSv between 10^{-5} µSv and 10^{-4} µSv.

deviations between 0.036 and 0.047 are observed, which is a good result for the area dose equivalents. The fluctuations are too large for K_{air} and exceed the limit. The impact of the definition of the dose equivalents delivers a large reference dose for low energies ($E < 20\,\text{keV}$) as seen in Figure 3.8. In particular, $H'(0.07, \Omega)$ and K_{air} are severely affected. Conversion factors can not compensate for those high values without impairing the performance for the remaining energy range. This results in response fluctuations below 20 keV trying to compensate the large reference dose. The ambient dose equivalent allows a constant response due to its smaller impact on the dose below 20 keV.

The relative statistical uncertainty is calculated according to Equation (3.8) and is shown in Figure 3.12. The red dashed line indicates the limit for the coefficient of variation, which is approximated by F_{stat}. It is below 5% for all area dose equivalents, which is in accordance with national and international standards [64, 66]. The uncertainty for the air kerma exceeds the limit of about 2.6% according to [68] at about 60 keV. The relative statistical uncertainty increases up to 100 keV and decreases henceforward. Its uncertainty ΔF_{stat} increases significantly above 300 keV. The reason for this behavior is the increase of the conversion factor, which results

in a larger uncertainty, and additionally to that, the energy dependence of the detection efficiency in silicon which reduces the number of registered events. The key performance indicators for the response R and the relative statistical uncertainty F_{stat} calculated with conversion factors of a lower boundary of 10^{-5} µSv are summarized in Table 3.5.

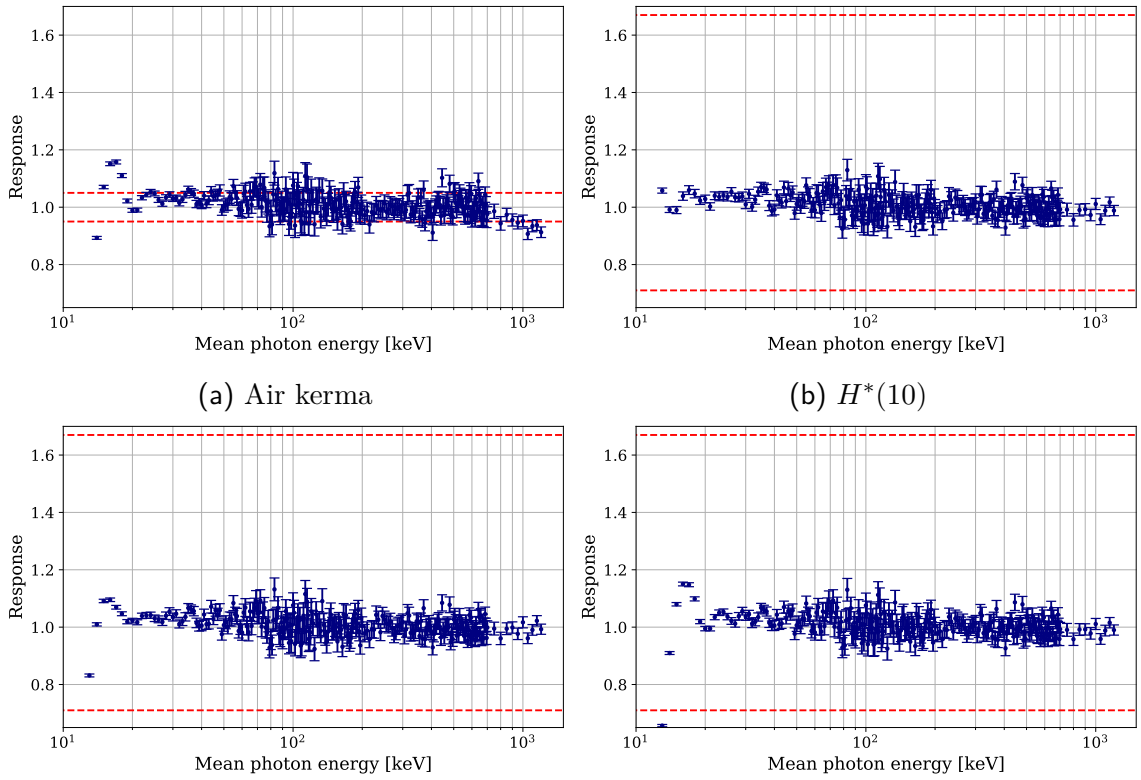

(a) Air kerma

(b) $H^*(10)$

(c) $H'(3, \Omega)$

(d) $H'(0.07, \Omega)$

Figure 3.11.: Energy dependence of the response for the simulation data for the different dose quantities K_{air} (a), $H^*(10)$ (b), $H'(3, \Omega)$ (c), and $H'(0.07, \Omega)$ (d). The energy range is 13 keV to 1200 keV. The red dashed lines indicate the limits as stated in Table 3.2.

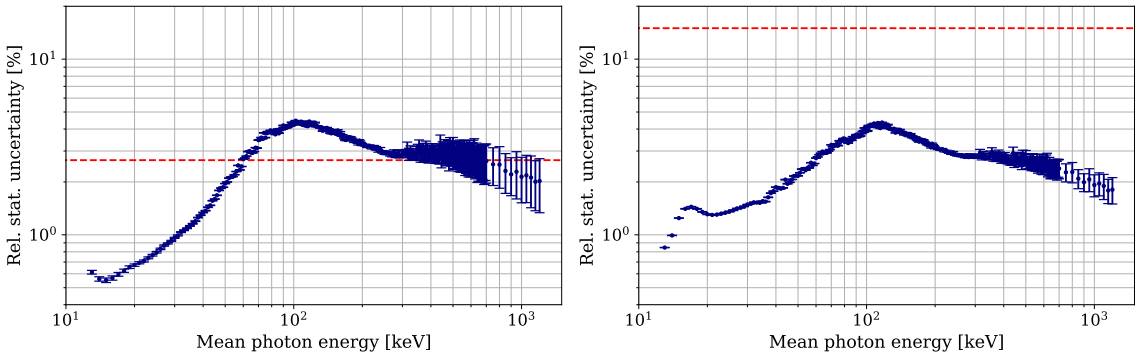

(a) Air kerma

(b) $H^*(10)$

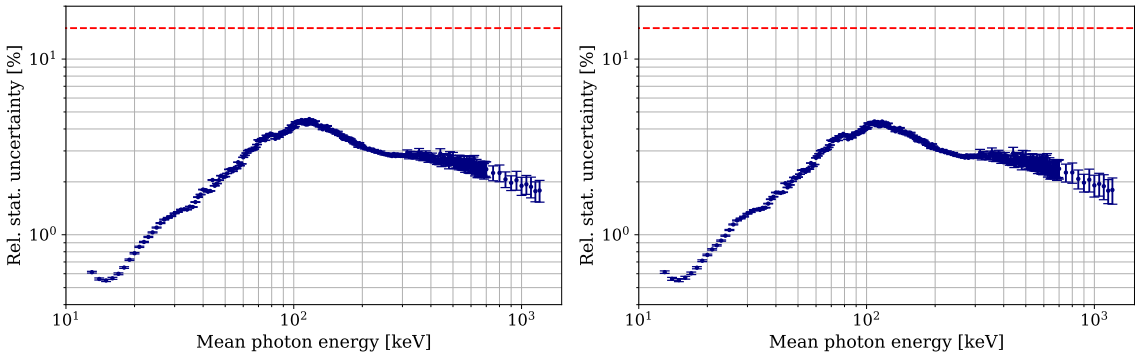

(c) $H'(3, \Omega)$

(d) $H'(0.07, \Omega)$

Figure 3.12.: Energy dependence of the F_{stat} for the simulation data for the different dose quantities K_{air} (a), $H^*(10)$ (b), $H'(3, \Omega)$ (c), and $H'(0.07, \Omega)$ (d). The energy range is 13 keV to 1200 keV. The red dashed line indicates the limits as stated in Table 3.2.

Dose	Quantity	Min.	Max.	μ	σ
$H^*(10)$	Response	0.924±0.033	1.129±0.038	1.008	0.036
	F_{stat} [%]	0.8461±0.003	4.358±0.022	2.854	0.789
$H'(3, \Omega)$	Response	0.832±0.006	1.132±0.040	1.008	0.039
	F_{stat} [%]	0.549±0.008	4.554±0.021	2.873	0.924
$H'(0.07, \Omega)$	Response	0.657±0.004	1.150±0.007	1.008	0.045
	F_{stat} [%]	0.552±0.011	4.41±0.02	2.841	0.900
K_{air}	Response	0.639±0.004	1.158±0.007	1.007	0.047
	F_{stat} [%]	0.552±0.017	4.46±0.02	2.931	0.980

Table 3.5.: Key parameters of performance calculated for the energy dependence of the response and F_{stat} for the different dose equivalents for simulation data created in [19] with the large pixels. The energy range is from 13 keV and 1200 keV. The key parameters are minimum and maximum, mean μ, and its corresponding standard deviation σ.

3.9.2. Preparation Measurements at the Erlangen Setup

Measurements are performed at the Erlangen setup with the 45 spectra stated in Table 3.3. The reference dose is determined with the RQX-sensor of Dosimax Plus. Figure 3.13 shows the reference dose in (a) and the limits for the coefficient of variation (b) for the measurements of the 45 spectra defined in Table 3.3. The reference dose is calculated by the product of the measured air kerma and the conversion coefficient of the corresponding spectrum depending on the dose quantity at hand. These reference doses are used to calculate the corresponding limit of the coefficient of variation according to Table 3.2. The energy dependence of reference dose shows groups of ascending values that correspond to variation of the kVp while keeping a set of filters. Increasing the tube voltage for a fixed set of beam hardening filters increases the photon flux and the possible maximum photon energy. This increases the measured reference dose.

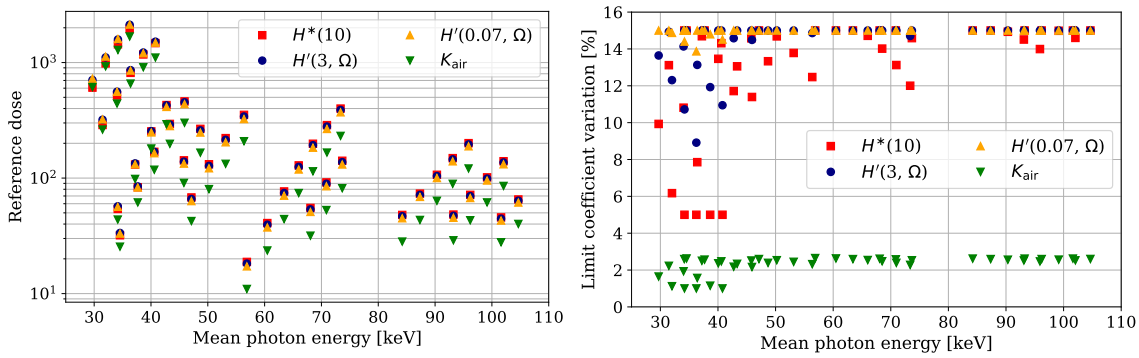

(a) Reference dose

(b) Limits

Figure 3.13.: Reference dose for the different dose quantities at the Erlangen setup. The reference dose (a) is used to calculate the limits of the coefficient of variation in (b). The reference dose for K_{air} is given in [µGy] and for the area dose equivalents in [µSv].

The recorded energy histograms from the measurements at the Erlangen setup are employed to determine the first conversion factors that include measurements. This data set consists of 45 spectra in a mean energy range of 30 keV to 105 keV. These investigations are conducted as preparation prior to the measurement campaign at PTB to guarantee an operational dosemeter prototype. The energy range is smaller than investigated at PTB, which means deviations are expected outside the tested range. Adding a real data set to the simulation is indispensable because the simulation does not take the imperfections of the Dosepix into account. These include pile-up, impurities and manufacturing errors of the filter-caps, and discrepancies of the energy thresholds due to calibration mismatches. The start parameters are the conversion factors of the simulation at a lower boundary of 10^{-5} µSv. The lower boundary for this optimization is 0.1 of the conversion factor of the particular bin, and the upper boundary is infinite. All parameters except the upper 3 of Slots 1,2 and the upper 7

of Slot 3 are variable within the stated bounds. Simulation data and measurement data are combined to determine the conversion factors.

Figure 3.14 shows the optimized and the input conversion factors for all four dose quantities. Blue indicates the conversion factors optimized for combining the Erlangen and simulation data, and the dashed orange line is the simulation only. A notable difference in the conversion factors is observed, and the smoothness of the conversion factors is notably impaired over the complete range.

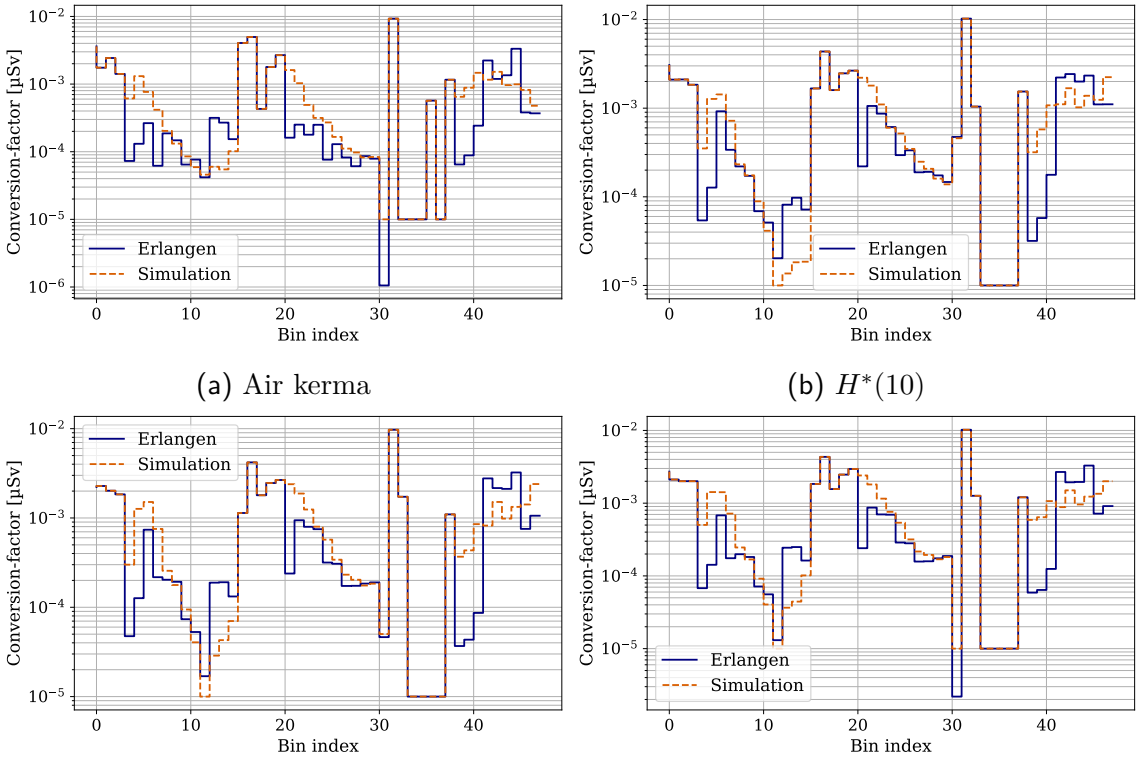

(a) Air kerma (b) $H^*(10)$

(c) $H'(3, \Omega)$ (d) $H'(0.07, \Omega)$

Figure 3.14.: Optimized conversion factors for the large pixels between the number of registered events in an energy bin of Dosepix and an area dose equivalent or air kerma. These are the air kerma (a), the ambient dose equivalent $H^*(10)$ (b), and the directional dose equivalents $H'(3, \Omega)$ (c) and $H'(0.07, \Omega)$ (d). The underlying data are from measurements at the Erlangen setup with 45 different photon fields.. Bin indices 0-15 are Slot 1, 16-31 Slot 2, and 32-47 Slot 3.

Both sets of conversion factors are used to calculate the response and the relative statistical uncertainty F_{stat}. The energy dependence of the response is displayed in Figure 3.15, Figure 3.16 shows the energy dependence of F_{stat}, and Table 3.6 shows the key performance indicators. The response is significantly optimized towards a mean much closer to 1. The conversion factors of the simulated data fluctuate around 1, with a mean value close to 1. However, their standard deviation is much larger

than the standard deviation after optimization to the Erlangen data. All response values for the Erlangen conversion factors for the area dose equivalents stay within limits. The response is insufficient for an X-ray diagnostics device measuring air kerma since two points are outside the limits. These two points deviate from the remaining ones for all four dose quantities and indicate a systematic deviation. Its origin is unknown. Nevertheless, the remaining energies are close to one and within limits. These curves show the game between the smooth trend of the conversion factors and the systematic uncertainty with respect to the influence quantity mean photon energy, i.e., the energy dependence of the response, very well. Deviating from a smooth trend allows reducing the systematic uncertainty significantly. Sticking to a smooth trend increases systematic uncertainty. However, the smooth trend reduces the statistical uncertainty of the measurement in form of F_{stat}. It is overall smaller for the simulation only conversion factors compared to the conversion factors including the measurements at the Erlangen setup. In this case the differences are not substantial. The energy dependence of F_{stat} stays below 0.6% for all energies and is within limits for all dose quantities. It increases with increasing mean photon energy. Compared to the simulation data set, the Erlangen data set has a reference dose of factor 100 higher on average, which influences the result accordingly and explains the decrease of factor 10 due to the uncertainty depending on the square root of the dose.

Dose	Quantity	Data Set	Min.	Max.	μ	σ
$H^*(10)$	Response	Simulation	0.7841±0.0005	1.0976±0.0047	0.9866	0.0764
		Erlangen	0.9701±0.0009	1.0844±0.0004	0.9996	0.0191
	F_{stat} [%]	Simulation	0.0360±0.0002	0.4527±0.0001	0.1861	0.1158
		Erlangen	0.0305±0.0002	0.4654±0.0001	0.1862	0.1241
$H'(3, \Omega)$	Response	Simulation	0.7542±0.0004	1.1174±0.0015	0.9975	0.0899
		Erlangen	0.9707±0.0008	1.0809±0.0004	0.9997	0.0186
	F_{stat} [%]	Simulation	0.0348±0.0003	0.4652±0.0001	0.1897	0.1205
		Erlangen	0.0288±0.0002	0.5041±0.0002	0.1970	0.1383
$H'(0.07, \Omega)$	Response	Simulation	0.7294±0.0004	1.1124±0.0014	0.9906	0.0956
		Erlangen	0.9708±0.0008	1.0796±0.0004	0.9997	0.0184
	F_{stat} [%]	Simulation	0.0337±0.0002	0.4591±0.0001	0.1866	0.1195
		Erlangen	0.0291±0.0002	0.5019±0.0002	0.1979	0.1387
K_{air}	Response	Simulation	0.6994±0.0003	1.0915±0.0011	0.9622	0.1010
		Erlangen	0.9710±0.0007	1.0720±0.0012	0.9997	0.0176
	F_{stat} [%]	Simulation	0.0256±0.0002	0.4735±0.0001	0.1757	0.1267
		Erlangen	0.0287±0.0003	0.6086±0.0003	0.2317	0.1766

Table 3.6.: Key parameters minimum and maximum values, mean μ, and the standard deviation σ for the energy dependence of the response and F_{stat} for the different dose equivalents for the measurements at the Erlangen setup. The energy range is from 30 keV and 105 keV.

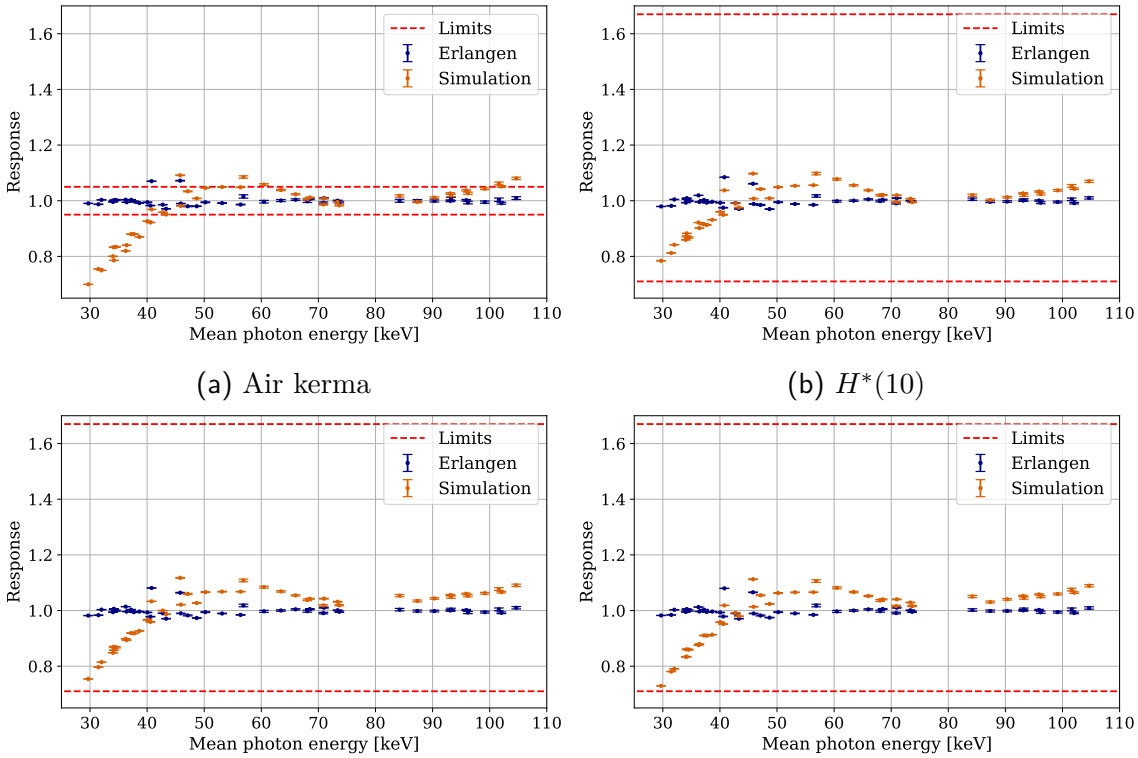

(a) Air kerma (b) $H^*(10)$

(c) $H'(3, \Omega)$ (d) $H'(0.07, \Omega)$

Figure 3.15.: Energy dependence of the response for the large pixels. The underlying data are from measurements at the Erlangen setup. The set of conversion factors is indicated in the legend. The results are presented for the different dose quantities. These are the air kerma (a), the ambient dose equivalent $H^*(10)$ (b), and the directional dose equivalents $H'(3, \Omega)$ (c) and $H'(0.07, \Omega)$ (d). The red dashed lines indicate the limits as stated in Table 3.2.

3.9.3. Measurements at Facilities of PTB

The preparatory tests at the Erlangen setup show a flat response around one in the tested energy range. With these successful tests, measurements are performed at facilities of the PTB, which delivers the truth value of the dose. Performance at these facilities represents the final metrological capabilities of the tested dosemeter. Therefore, the Dosepix dosimetry demonstrator must perform well for the conducted irradiations.

The reference dose values for 0° angle of radiation incidence and the limits for the coefficient of variation are shown in Figure 3.17. The reference dose is adjusted for $H^*(10)$ and chosen as approximately constant. PTB delivered the reference $H^*(10)$ and air kerma. The remaining area dose quantities are determined via the use of tabulated conversion coefficients [55, 56] and the reference air kerma. Especially at low mean

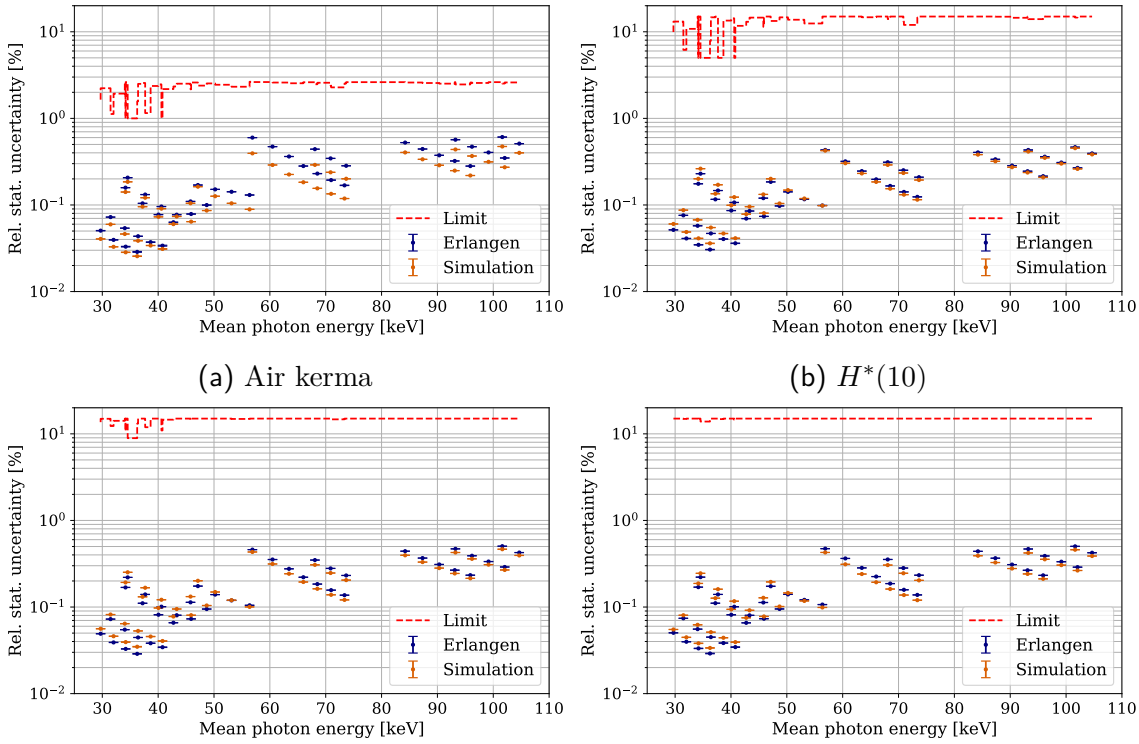

(a) Air kerma (b) $H^*(10)$

(c) $H'(3, \Omega)$ (d) $H'(0.07, \Omega)$

Figure 3.16.: Energy dependence of F_{stat} for the large pixels. The underlying data are from measurements at the Erlangen setup. The set of conversion factors is indicated in the legend. The results are presented for the different dose quantities. These are the air kerma (a), the ambient dose equivalent $H^*(10)$ (b), and the directional dose equivalents $H'(3, \Omega)$ (c) and $H'(0.07, \Omega)$ (d). The red dashed lines indicate the limits as stated in Table 3.2.

photon energies, a large difference in the reference dose is observed, corresponding to the conversion coefficients. All exposure times are 60 s, except for the radiation qualities N-15, S-Cs, and S-Co, which are 100 s. The limits for the coefficient of variation are calculated via information in Section 3.4 and are located at the upper end of the possible limit range, e.g., it is about 14.5% for the ambient dose equivalent $H^*(10)$.

The recorded energy histograms are employed to investigate if the Dosepix dosimetry demonstrator is capable of correctly determining the dose in a wide energy range at reference conditions in photon reference fields according to [67] at PTB. A new set of conversion factors is determined employing the simulation and the PTB data. The input conversion factors are the conversion factors optimized to the simulated data. The lower boundary is 0.1 of the value of the corresponding conversion factor, whereas the upper boundary is infinite. The conversion factors of all energy bins are varied. The

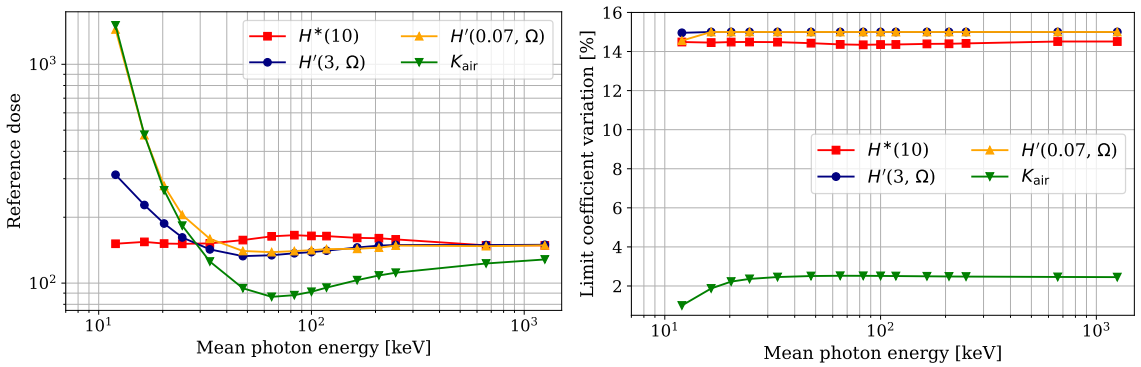

(a) Reference dose

(b) Limits

Figure 3.17.: Reference dose for the different dose quantities at PTB (a) is used to calculate the limits of the coefficient of variation in (b). The reference dose for K_{air} is given in [µGy] and for the area dose equivalents in [µSv].

optimized conversion factors are compared to the previously determined simulation factors and the combination of simulation and measurements at the Erlangen setup. Figure 3.18 shows the optimized conversion factors for all four dose quantities for all three sets of determined conversion factors. They are displayed together with the conversion factors determined in the previous two subsections. All three sets of conversion factors are used to calculate the response and the relative statistical uncertainty for the measurements at PTB for 0° angle of radiation incidence.

Figure 3.19 and Figure 3.20 show the calculated response and the relative statistical uncertainty for different radiation qualities, i.e., different mean photon energies. Table 3.7 shows the corresponding key indicators such as minimum value, maximum value, mean value, and its corresponding standard deviation for the three sets of conversion factors, which are labeled by their place of measurement or as simulation, applied to the PTB data. The results for the conversion factors of simulation only and simulation combined with measurements at PTB show the best results. Their mean response is close to one for all dose quantities. The conversion factors for the simulation combined with measurements at PTB show the smallest standard deviation of the response. Nevertheless, applying only the simulation results in a very good representation of the energy dependence of the response. It demonstrates how well the simulation of the Dosepix dosimetry demonstrator created in [19] reflects the reality. The conversion factors for simulation combined with measurements at the Erlangen setup show the worst performance for all dose quantities with several data points outside the limits. The maximum response is at about 4.0 for the ambient dose equivalent $H^*(10)$. The energies between 30-40 keV in the Erlangen measurements showed a large deviation to 1 in the form of an underresponse for the conversion factors optimized to the simulated data. Assuming that these factors allow correct dose determination as shown when applied to the PTB measurements, an overestimation of the reference dose must have occurred. This potentially stems from the RQX sensor,

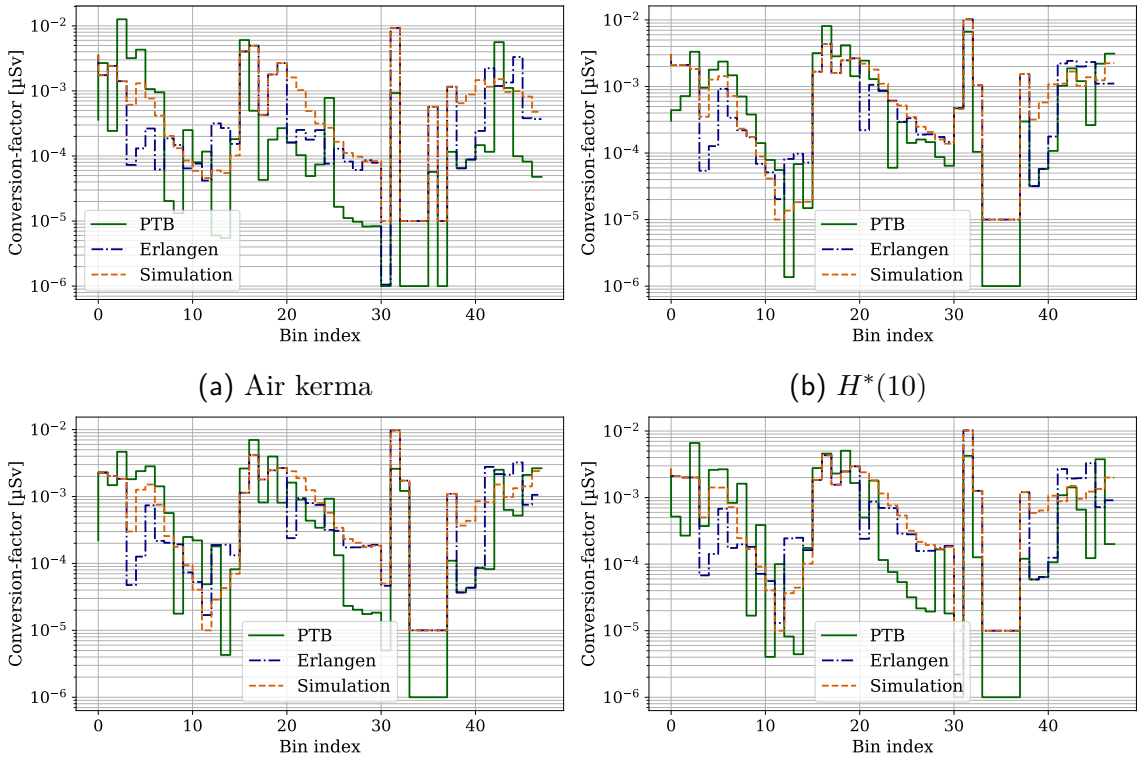

(a) Air kerma (b) $H^*(10)$

(c) $H'(3, \Omega)$ (d) $H'(0.07, \Omega)$

Figure 3.18.: Optimized conversion factors for the large pixels between the number of registered events in an energy bin of Dosepix and an area dose equivalent or air kerma. These are the air kerma (a), the ambient dose equivalent $H^*(10)$ (b), and the directional dose equivalents $H'(3, \Omega)$ (c) and $H'(0.07, \Omega)$ (d). The underlying data are from measurements at the facilities of PTB. Bin indices 0-15 are Slot 1, 16-31 Slot 2, and 32-47 Slot 3.

which has a kVp range of 50-150 kV. Since its reference dose values were used to optimize conversion factors at the Erlangen setup, it is assumed that the optimization overcorrected this deviation and determined conversion factors that are too high. This results in overestimating the response for energies below 40 keV at the reference photon fields of PTB, which agrees well with the observed behavior. A more thorough investigation into the reference dosemeter at the Erlangen setup must be carried out to confirm the findings. In the following, conversion factors are determined for the small pixels utilizing the Erlangen measurements. Their results must always bear in mind the overestimation of the reference dose below 40 keV.

Overall a flat energy response is observed with the conversion factors for the PTB data set. The response is within limits from 20.3 keV to 1250 keV for the air kerma. This demonstrated the capability of the Dosepix dosimetry demonstrator as a semiconductor detector as used in X-ray diagnostic imaging for air kerma with respect to its energy

dependence. Further investigations into the typically tested reference fields RQX and RQA must be carried out in the future to validate the results.

The relative statistical uncertainty is within limits for all data points. It increases with increasing mean photon energy for all sets of conversion factors applied to the PTB data. It is largest for all dose quantities when using the PTB conversion factors. This increase is not substantial to exceed the limits. Therefore, these factors are used in the following to investigate angular dependence.

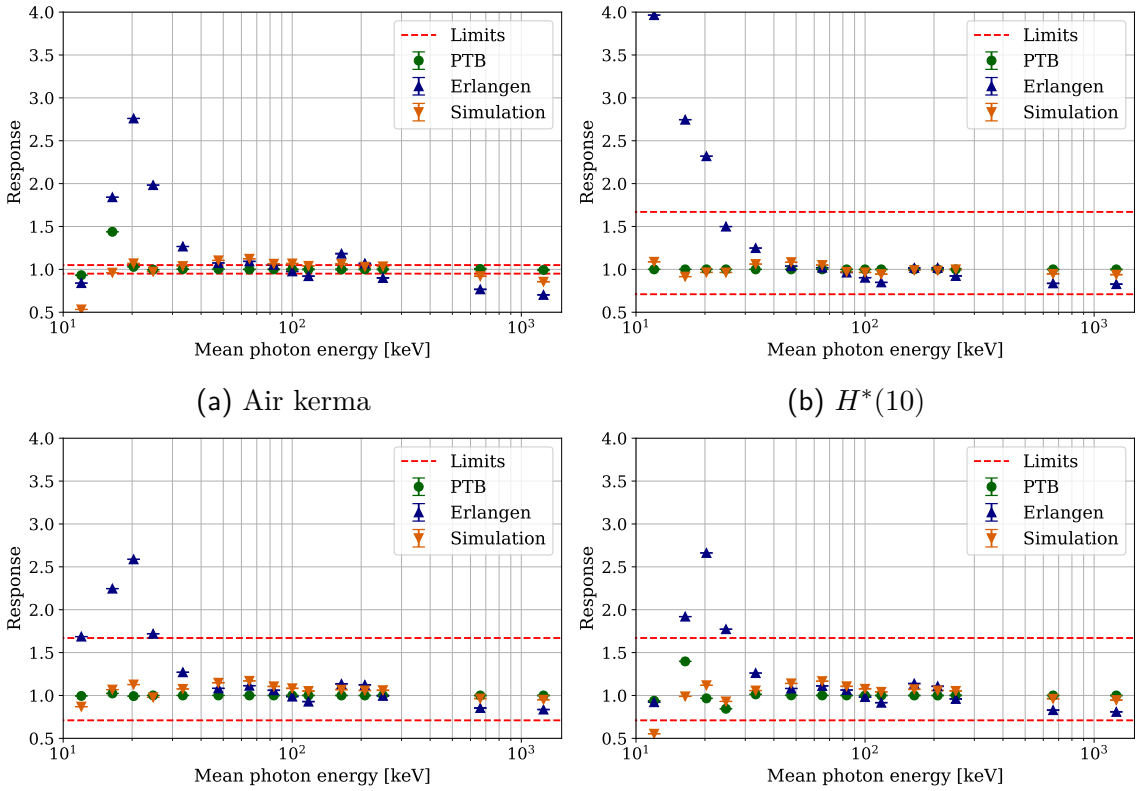

(a) Air kerma (b) $H^*(10)$

(c) $H'(3, \Omega)$ (d) $H'(0.07, \Omega)$

Figure 3.19.: Energy dependence of the response for the large pixels. The underlying data are from measurements at facilities of PTB. The set of conversion factors is indicated in the legend. The results are presented for the different dose quantities. These are the air kerma (a), the ambient dose equivalent $H^*(10)$ (b), and the directional dose equivalents $H'(3, \Omega)$ (c) and $H'(0.07, \Omega)$ (d). The red dashed lines indicate the limits as stated in Table 3.2.

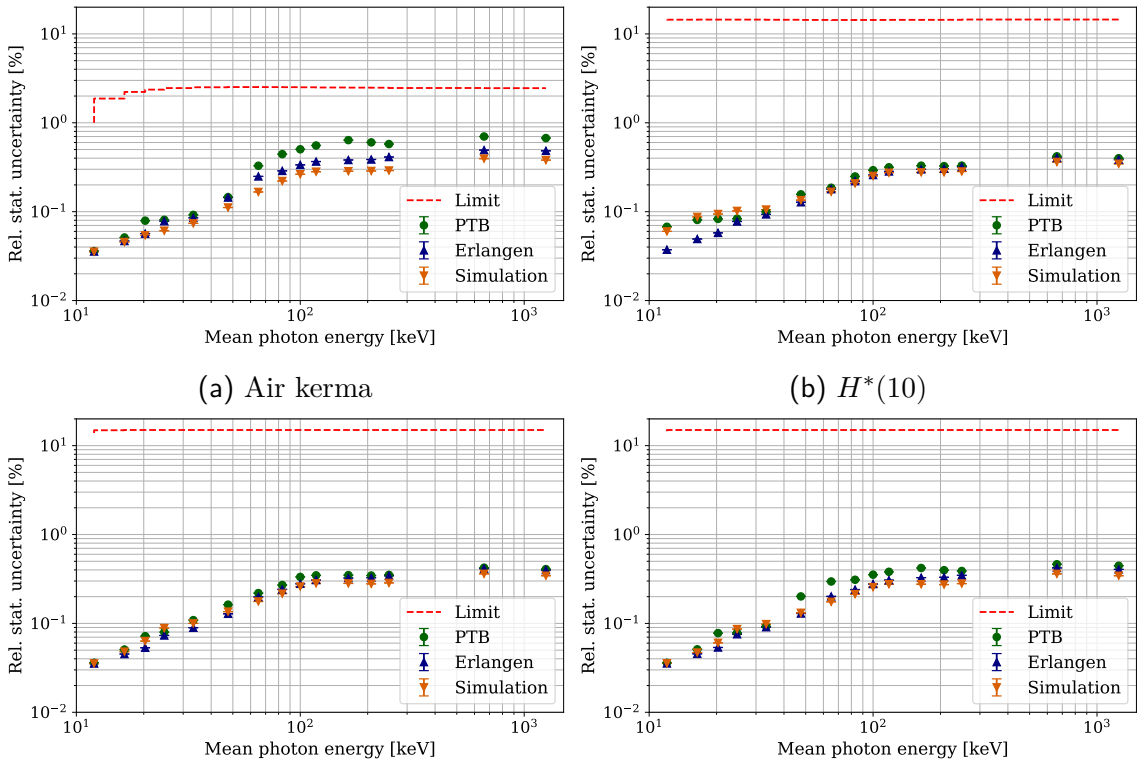

(a) Air kerma

(b) $H^*(10)$

(c) $H'(3, \Omega)$

(d) $H'(0.07, \Omega)$

Figure 3.20.: Energy dependence of F_{stat} for the large pixels. The underlying data are from measurements at facilities of PTB. The set of conversion factors is indicated in the legend. The results are presented for the different dose quantities. These are the air kerma (a), the ambient dose equivalent $H^*(10)$ (b), and the directional dose equivalents $H'(3, \Omega)$ (c) and $H'(0.07, \Omega)$ (d). The red dashed line indicates the limits as stated in Table 3.2.

Dose	Quantity	Data set	Min.	Max.	μ	σ
$H^*(10)$	Response	Simulation	0.9156±0.0008	1.0879±0.0007	0.9912	0.0527
		Erlangen	0.8280±0.0032	3.9650±0.0015	1.4115	0.8736
		PTB	0.9997±0.0008	1.0001±0.0008	1.0000	0.0001
	F_{stat} [%]	Simulation	0.0600±0.0000	0.3624±0.0001	0.2020	0.0973
		Erlangen	0.0373±0.0000	0.4025±0.0001	0.2064	0.1217
		PTB	0.0676±0.0000	0.4194±0.0002	0.2279	0.1214
$H'(3, \Omega)$	Response	Simulation	0.8695±0.0003	1.1701±0.0021	1.0519	0.0778
		Erlangen	0.8357±0.0033	2.5876±0.0014	1.3084	0.5046
		PTB	0.9924±0.0007	1.0235±0.0005	1.0007	0.0065
	F_{stat} [%]	Simulation	0.0354±0.0000	0.3611±0.0001	0.1971	0.1075
		Erlangen	0.0354±0.0000	0.4137±0.0001	0.2172	0.1312
		PTB	0.0360±0.0000	0.4234±0.0001	0.2372	0.1350
$H'(0.07, \Omega)$	Response	Simulation	0.5533±0.0002	1.1664±0.0020	1.0181	0.1412
		Erlangen	0.8087±0.0033	2.6621±0.0014	1.2355	0.4883
		PTB.	0.8449±0.0007	1.3972±0.0007	1.0108	0.1111
	F_{stat} [%]	Simulation	0.0355±0.0000	0.3608±0.0001	0.1943	0.1069
		Erlangen	0.0355±0.0000	0.4214±0.0001	0.2192	0.1328
		PTB	0.0360±0.0000	0.4629±0.0001	0.2661	0.1538
K_{air}	Response	Simulation	0.5326±0.0002	1.1234±0.0019	0.9923	0.1405
		Erlangen	0.7026±0.0034	2.7598±0.0016	1.2288	0.5352
		PTB	0.9321±0.0003	1.4383±0.0007	1.0267	0.1116
	F_{stat} [%]	Simulation	0.0354±0.0000	0.3949±0.0001	0.1968	0.1213
		Erlangen	0.0357±0.0001	0.4926±0.0001	0.2562	0.1612
		PTB	0.0360±0.0001	0.7009±0.0005	0.3671	0.2500

Table 3.7.: Key parameters of performance calculated for the energy dependence of the response and F_{stat} for the different dose equivalents for measurements at PTB with the large pixels. The energy range is from 12.4 keV and 1250 keV. The key parameters are minimum and maximum, mean μ, and its corresponding standard deviation σ.

3.10. Area Dosimetry with the Small Pixels

The starting set of conversion factors from the number of registered events in an energy bin of Dosepix to an area dose equivalent or air kerma for the small pixels are already existing conversion factors for the personal dose equivalent $H_p(10)$ taken from [37]. These factors are slightly modified by utilizing the monochromatic $H_p(10)$, $H^*(10)$, $H'(3, \Omega)$, and $H'(0.07, \Omega)$ conversion coefficients from air kerma to the area dose equivalent of interest. The conversion coefficients can be found in [53, 54] for the $H^*(10)$ and $H_p(10)$, in [55] for the $H'(3, \Omega)$, and in [56] for the $H'(0.07, \Omega)$. They are interpolated via a cubic log-log interpolation. The mean energy between two adjacent bins is used as a grid point for the interpolated function. The correction factor is the ratio of the conversion coefficient of the area dose equivalent of interest and the personal dose equivalent $H_p(10)$ at the energy mean energy between two adjacent bins. In the case of air kerma, conversion factors are only corrected by the conversion coefficients of $H_p(10)$. The conversion coefficients and the adapted conversion factors are shown in Figure 3.21. The modified conversion factors are called initial conversion factors in the following.

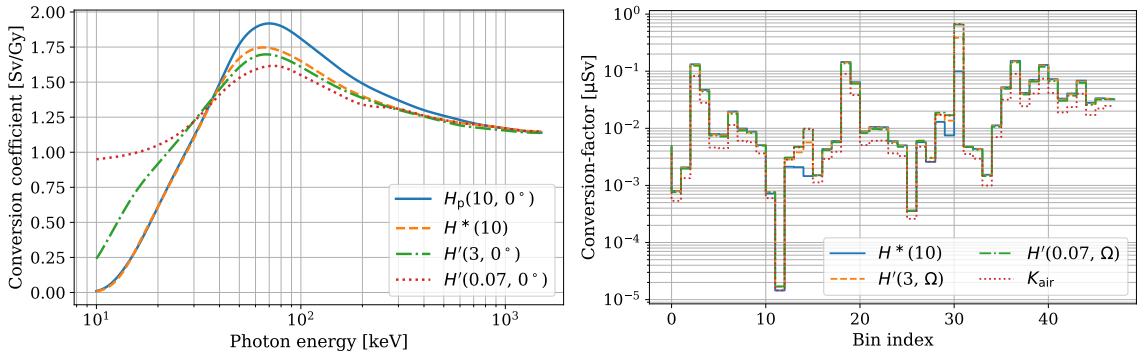

(a) Conversion coefficients (b) Adapted conversion factors

Figure 3.21.: (a): Monoenergetic conversion coefficients for $H_p(10, 0°)$, $H^*(10)$, $H'(3, 0°)$, $H'(0.07, 0°)$ [53, 54, 55, 56]. The mean energies of adjacent bin edges are used to determine the interpolated conversion-coefficients for the correction of the initial conversion factors in (b).

3.10.1. Preparation Measurements at the Erlangen Setup

The energy histograms recorded in the Dosi-mode are utilized to investigate the energy dependence of the response and the relative statistical uncertainty for the small pixels. The energy range is 30-105 keV. A total of 45 measurements are performed. These energy histograms are utilized to determine conversion factors between the number of registered events in an energy bin and a dose quantity. The dose quantities of interest are the air kerma and the area dose equivalents $H^*(10)$, $H'(3, \Omega)$, and $H'(0.07, \Omega)$.

The conversion factors are optimized as described in Section 3.8. Start values for every bin are the initial conversion factors. Their values for the energy bins of Slot 3 are held constant to introduce overall stability since no additional simulation data is used for the small pixels. This was the case for previous investigations with the large pixels, where all 48 conversion factors were variable. Further constant bins are the 0,1,2 of Slot 1 and 16,17,18 of Slot 2 since no events are expected in these energy bins. The lower boundary is 0.1 times the value of the initial conversion factor of this bin to reduce fluctuations. The upper boundary is infinite. The number of variable parameters is therefore 26. Utilizing the 45 spectra of the data set is sufficient to determine a unique set of optimized conversion factors. Figure 3.22 shows the initial and optimized conversion factors. Small fluctuations, deviating from a smooth trend, are introduced. Overall, a stable trend is still recognizable.

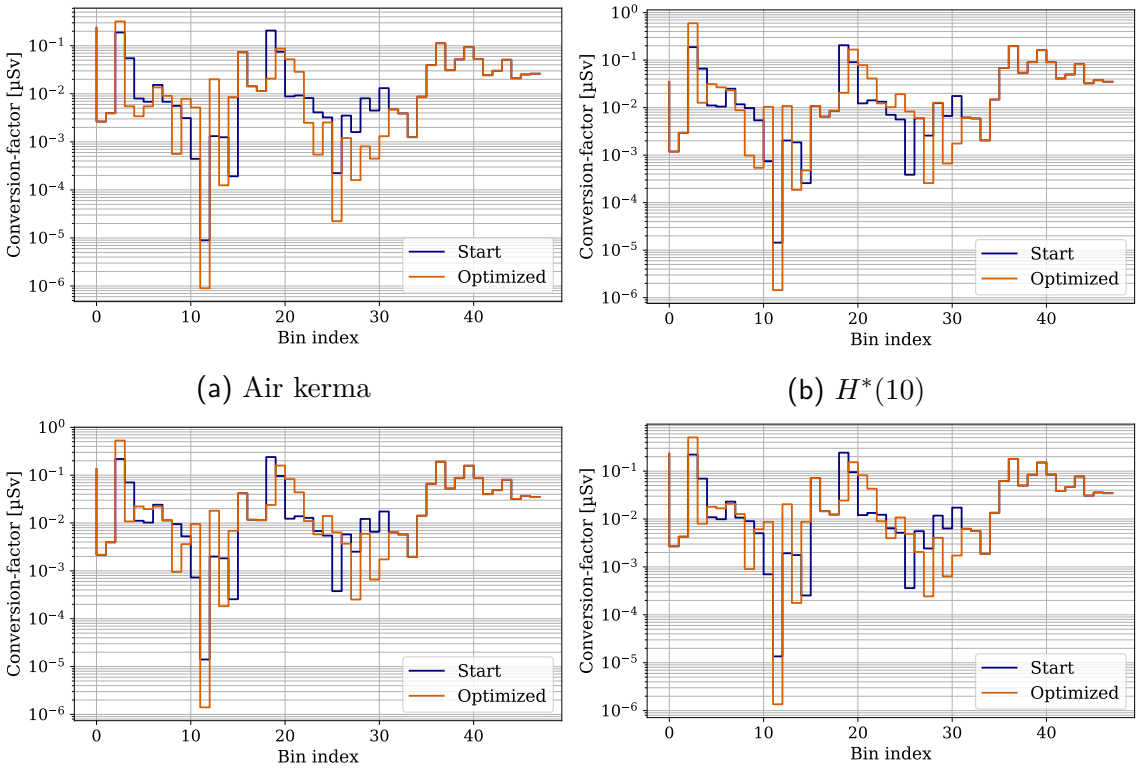

(a) Air kerma

(b) $H^*(10)$

(c) $H'(3, \Omega)$

(d) $H'(0.07, \Omega)$

Figure 3.22.: Optimized conversion factors for the small pixels between the number of registered events in an energy bin of Dosepix and an area dose equivalent or air kerma. These are the air kerma (a), the ambient dose equivalent $H^*(10)$ (b), and the directional dose equivalents $H'(3, \Omega)$ (c) and $H'(0.07, \Omega)$ (d). The underlying data are from measurements at the Erlangen setup with 45 different photon fields. Bin indices 0-15 are Slot 1, 16-31 Slot 2, and 32-47 Slot 3.

The response and the relative statistical uncertainty are calculated, and their energy dependence is shown in Figure 3.23 and Figure 3.24 respectively. The key performance indicators are summarized in Table 3.8. After the optimization, the responses for all dose quantities are close to 1 for the complete energy range. The mean response is 1.000 for all dose quantities, and their corresponding standard deviation is close to 0 with a maximum value of 0.21. The energy dependence of K_{air} exceeds the limits of $\pm 5\%$ for the same two data points as the large pixels. The dose equivalents are all within limits. The dip of the energy dependence of the response calculated with the initial conversion factors demonstrates that the applied correction to the conversion factors of $H_{\mathrm{p}}(10)$ was not sufficient. In this energy range, the largest contribution for backscattering is expected. This misses in the measurement of the area dose equivalent since no slab phantom is placed behind the detector. The steep decline from 50 keV downward is attributed to a reference dose that is effectively too large.

F_{stat} is between 0.24% and 5.2% for all data points and it increases with increasing mean photon energy. The values are slightly increased. F_{stat} stays within limits for the dose equivalents and exceeds the limit for K_{air} above about 80 keV. These measurements show that the Dosepix dosimetry demonstrator can measure the dose for its small pixels with a small systematic uncertainty for the energy dependence in the range of 30-105 keV. The statistical uncertainty is much larger than for the large pixels, which only poses a problem for the strict limits for the air kerma. These measurements are used as preparatory tests of the Dosepix dosimetry demonstrator prior to measurements at facilities of PTB, which are presented next.

Dose	Quantity	Min.	Max.	μ	σ
$H^*(10)$	Response	0.969±0.008	1.082±0.003	1.000	0.021
	F_{stat} [%]	0.238±0.011	5.137±0.054	1.663	1.303
$H'(3, \Omega)$	Response	0.970±0.032	1.082±0.003	1.000	0.020
	F_{stat} [%]	0.240±0.012	4.935±0.043	1.642	1.262
$H'(0.07, \Omega)$	Response	0.970±0.032	1.083±0.003	1.000	0.020
	F_{stat} [%]	0.252±0.012	4.926±0.041	1.666	1.256
K_{air}	Response	0.968±0.031	1.079±0.004	1.000	0.019
	F_{stat} [%]	0.292±0.015	4.779±0.034	1.746	1.203

Table 3.8.: Key parameters of performance calculated for the energy dependence of the response and F_{stat} for the different dose equivalents for the measurements at the Erlangen setup. The energy range is from 30 keV and 105 keV. Key parameters are minimum and maximum values, mean μ, and its corresponding standard deviation σ.

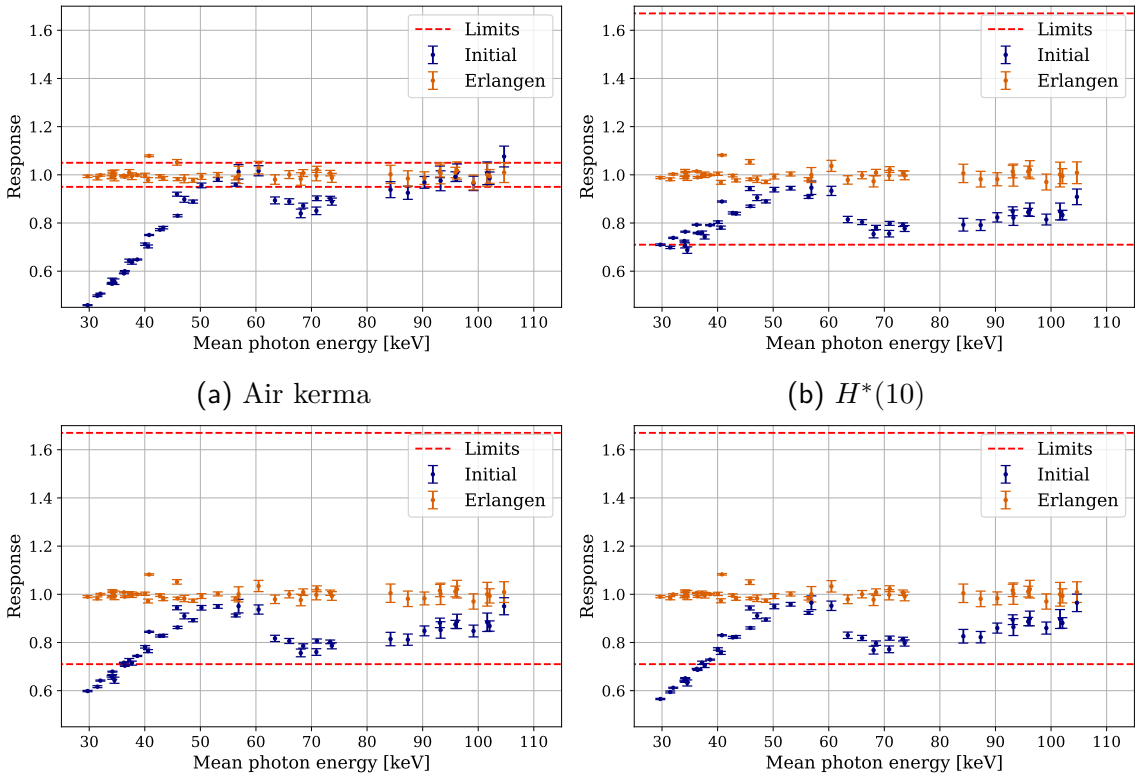

(a) Air kerma (b) $H^*(10)$

(c) $H'(3, \Omega)$ (d) $H'(0.07, \Omega)$

Figure 3.23.: Energy dependence of the response for the small pixels. The underlying data are from measurements at the Erlangen setup. The set of conversion factors is indicated in the legend. The results are presented for the different dose quantities. These are the air kerma (a), the ambient dose equivalent $H^*(10)$ (b), and the directional dose equivalents $H'(3, \Omega)$ (c) and $H'(0.07, \Omega)$ (d). The red dashed lines indicate the limits as stated in Table 3.2.

3.10.2. Measurements at Facilities of PTB

The recorded energy histograms of the measurements at the Erlangen setup and facilities of PTB are employed to adapt the conversion factors to a larger energy range. This new energy range extends from 12.4 keV (mean photon energy of N-15) to 1250 keV (S-Co). The optimization routine is described in Section 3.8. Start values of the conversion factors are those optimized onto the energy histograms recorded at the Erlangen setup. The constant bin indices are 0-3 of Slot 1, 16-19 for Slot 2, and 32-39 for Slot 3. Overall, there are 32 variable parameters and 60 radiation fields, which is enough to determine a unique set of optimal parameters. The lower boundary is 0.01 times the value of the initial conversion factor in this bin. The upper boundary is infinite. Figure 3.22 shows the Erlangen and PTB conversion factors. Slot 3 shows effectively smaller values of the conversion factors compared to

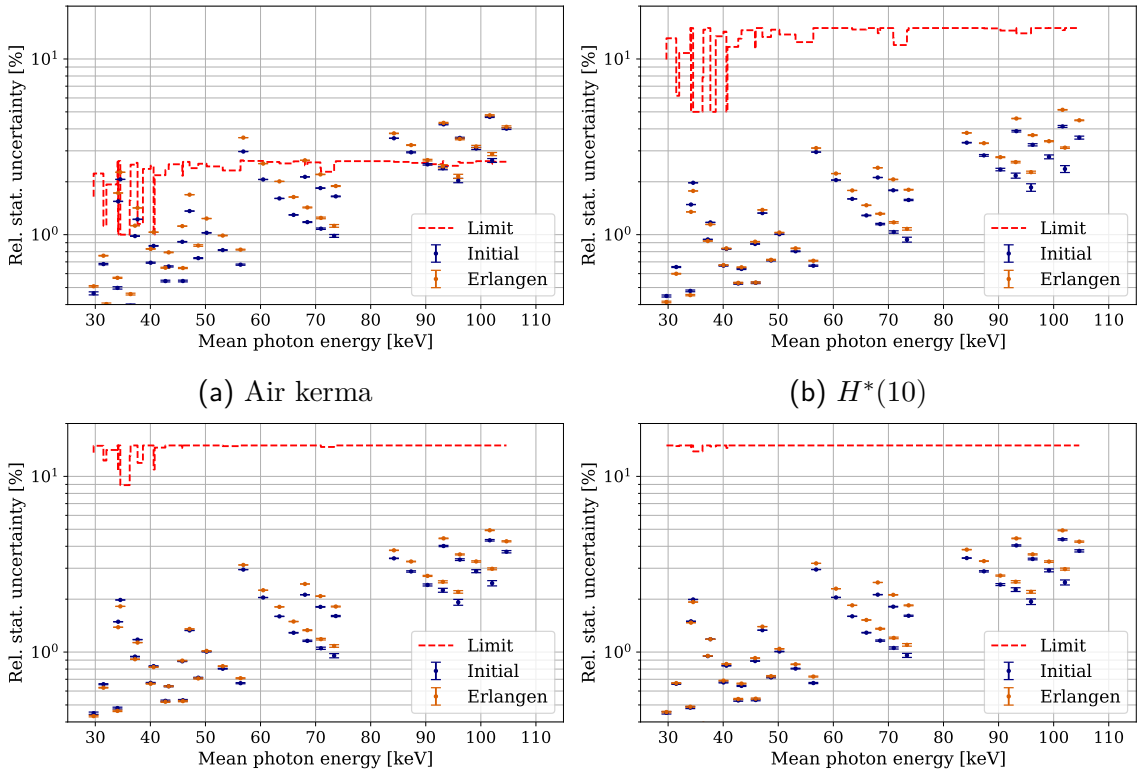

(a) Air kerma

(b) $H^*(10)$

(c) $H'(3, \Omega)$

(d) $H'(0.07, \Omega)$

Figure 3.24.: Energy dependence of F_{stat} for the small pixels. The underlying data are from measurements at the Erlangen setup. The set of conversion factors is indicated in the legend. The results are presented for the different dose quantities. These are the air kerma (a), the ambient dose equivalent $H^*(10)$ (b), and the directional dose equivalents $H'(3, \Omega)$ (c) and $H'(0.07, \Omega)$ (d). The red dashed lines indicate the limits as stated in Table 3.2.

the conversion factors determined with the Erlangen measurements. Overall, larger fluctuations are introduced due to the inclusion of Slot 3.

The response and the relative statistical uncertainty are calculated. Their energy dependence is shown in Figure 3.26 and Figure 3.27. The key indicators are summarized in Table 3.9. Both sets of conversion factors deliver a mean response close to 1. The response with the preparatory Erlangen conversion factors shows higher response fluctuations than the PTB ones and, therefore, a larger corresponding standard deviation. This is especially the case for the photon energy range below 40 keV, where a too large reference dose is assumed at the Erlangen setup. This results in an overestimation of the conversion factors, resulting in an overestimation in reference photon fields at PTB. The responses of N-25 and N-30 are either close to the upper limit or exceed it for the area dose equivalents. For the conversion factors optimized

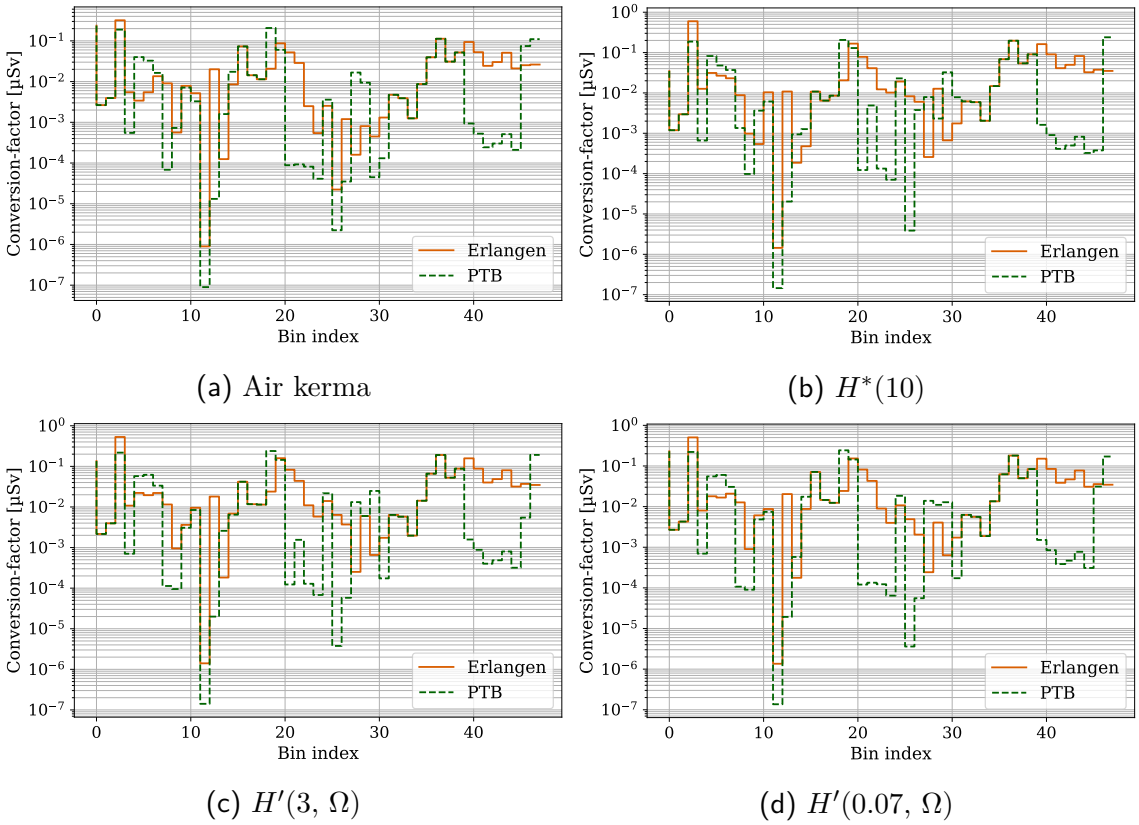

(a) Air kerma (b) $H^*(10)$

(c) $H'(3, \Omega)$ (d) $H'(0.07, \Omega)$

Figure 3.25.: Optimized conversion factors for the small pixels between the number of registered events in an energy bin of Dosepix and an area dose equivalent or air kerma. These are the air kerma (a), the ambient dose equivalent $H^*(10)$ (b), and the directional dose equivalents $H'(3, \Omega)$ (c) and $H'(0.07, \Omega)$ (d). The underlying data are from measurements at the facilities of PTB. Bin indices 0-15 are Slot 1, 16-31 Slot 2, and 32-47 Slot 3.

to the measurements at Erlangen and at facilities of PTB, the results of the dose equivalents are reasonably within limits, while they exceed the limits for air kerma. A bump in the energy dependence is observed at N-40, corresponding to the previous discussion with respect to the overestimation of the reference dose. F_{stat} is between 0.3% and 3.3% for all data points calculated with the PTB conversion factors. It increases with the mean photon energy. Each dose equivalent exhibits a F_{stat} within limits. K_{air} exceeds its limits above 100 keV. The statistical uncertainties become slightly larger for the conversion factors optimized for the measurements at PTB due to increased fluctuation of the conversion factors. Nevertheless, the results for the area dose equivalents are well within limits. Overall, it can be summarized that fluctuations from a steady trend in the conversion factors reduce the systematic uncertainty of the energy dependence of the response but increase its statistical uncertainty at the same time. The determined conversion factors are used in the following to study the energy and angular dependence of the Dosepix dosimetry demonstrator.

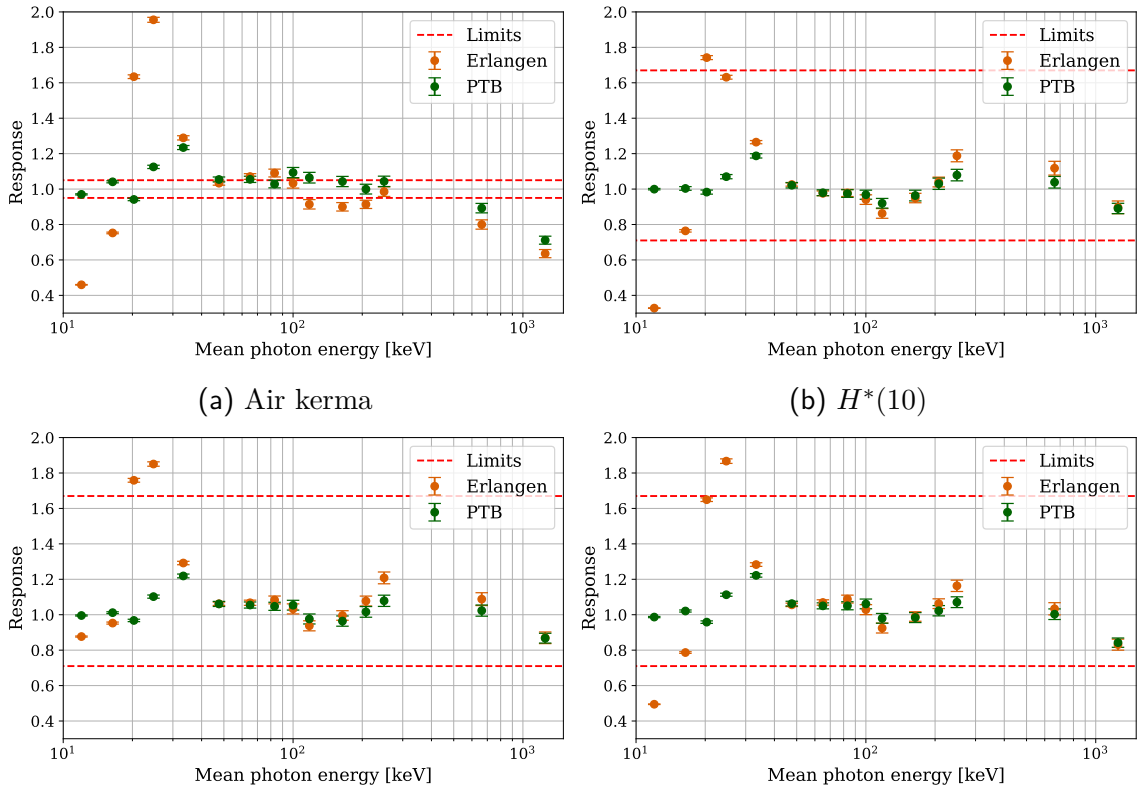

(a) Air kerma

(b) $H^*(10)$

(c) $H'(3, \Omega)$

(d) $H'(0.07, \Omega)$

Figure 3.26.: Energy dependence of the response for the small pixels. The underlying data are from measurements at facilities of PTB. The set of conversion factors is indicated in the legend. The results are presented for the different dose quantities. These are the air kerma (a), the ambient dose equivalent $H^*(10)$ (b), and the directional dose equivalents $H'(3, \Omega)$ (c) and $H'(0.07, \Omega)$ (d). The red dashed lines indicate the limits as stated in Table 3.2.

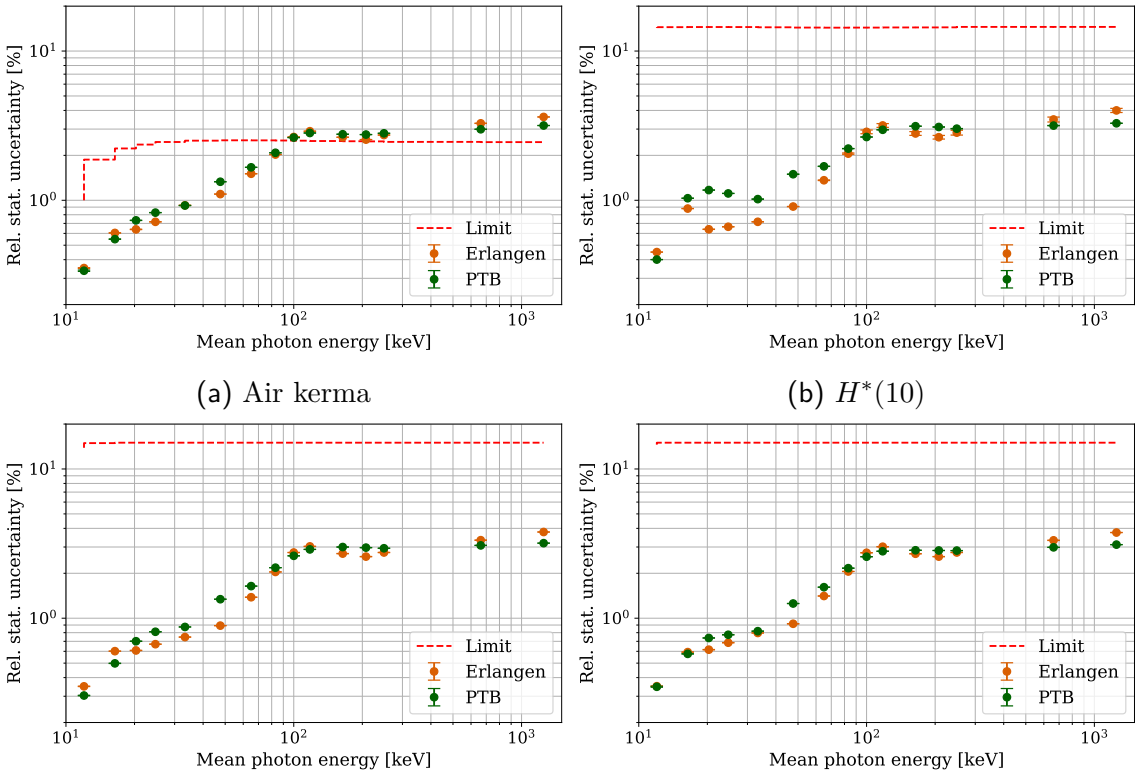

(a) Air kerma

(b) $H^*(10)$

(c) $H'(3, \Omega)$

(d) $H'(0.07, \Omega)$

Figure 3.27.: Energy dependence of F_{stat} for the small pixels. The underlying data are from measurements at facilities of PTB. The set of conversion factors is indicated in the legend. The results are presented for the different dose quantities. These are the air kerma (a), the ambient dose equivalent $H^*(10)$ (b), and the directional dose equivalents $H'(3, \Omega)$ (c) and $H'(0.07, \Omega)$ (d). The red dashed line indicates the limits as stated in Table 3.2.

Dose	Quantity	Data set	Min.	Max.	μ	σ
$H^*(10)$	Response	Erlangen	0.3280±0.0015	1.7421±0.0111	1.0470	0.3247
		PTB	0.8905±0.0292	1.1875±0.0121	1.0072	0.0685
	F_{stat} [%]	Erlangen	0.4497±0.0001	4.0015±0.1271	1.9661	1.1725
		PTB	0.4007±0.0003	3.2810±0.0057	2.0973	0.9694
$H'(3, \Omega)$	Response	Erlangen	0.8698±0.0329	1.8506±0.0124	1.1435	0.2813
		PTB	0.8676±0.0276	1.2189±0.0106	1.0292	0.0753
	F_{stat} [%]	Erlangen	0.3495±0.0011	3.7810±0.0077	1.8829	1.1361
		PTB	0.3034±0.0011	3.1836±0.0023	1.9354	1.0520
$H'(0.07, \Omega)$	Response	Erlangen	0.4946±0.0017	1.8670±0.0128	1.0884	0.3183
		PTB	0.8423±0.0262	1.2221±0.0100	1.0285	0.0800
	F_{stat} [%]	Erlangen	0.3503±0.0014	3.7504±0.0071	1.8870	1.1238
		PTB	0.3473±0.0026	3.1124±0.0020	1.8873	1.0044
K_{air}	Response	Erlangen	0.4597±0.0016	1.9555±0.0140	1.0311	0.3606
		PTB	0.7115±0.0226	1.2344±0.0114	1.0198	0.1122
	F_{stat} [%]	Erlangen	0.3514±0.0020	3.6177±0.0056	1.8835	1.0623
		PTB	0.3372±0.0034	3.1696±0.0023	1.8933	0.9887

Table 3.9.: Key parameters of performance calculated for the energy dependence of the response and F_{stat} for the different dose equivalents for measurements at PTB with the small pixels. The energy range is from 12.4 keV and 1250 keV. The key parameters are minimum and maximum, mean μ, and its corresponding standard deviation σ.

3.11. Energy and Angular Dependence

According to national and international requirements summarized in Section 3.4, the angular dependency must be tested in a minimum range of ±45° for the area dose equivalents $H^*(10)$, $H'(3, \Omega)$, and $H'(0.07, \Omega)$. The investigations are performed up to ±60° angle of radiation incidence to extend the rated range of use potentially. The angular dependence of the dose measurement of air kerma is not investigated in this section since it is not required. The combined influence of the dependence of the normalized response on the mean photon energy and the angle of radiation incidence is determined for the measurements at facilities of PTB. The conversion factors determined for the measurements at PTB for 0° angle of radiation incidence for the large and the small pixels are employed for this purpose.

The energy and angular dependence of the response normalized to S-Cs at 0° is shown in Figure 3.28. The dose equivalents $H^*(10)$ and $H'(3, \Omega)$ are flat around one over the complete energy range for the large pixels, while $H'(0.07, \Omega)$ shows an oscillation below energies of N-40. Such oscillations stem from overcompensating the large reference dose of $H'(0.07, \Omega)$ at low energies. The bump at N-40 for all area dose equivalents for the small pixels results from the incorrect reference dose delivered by the RQX detector at energies outside of its range of use. The small pixels underestimated the dose at S-Co, while it is not the case for the large pixels. For the three area dose equivalents and both pixel types, a decrease of the response with increasing angle of radiation incidence is observed in the lower energy range of up to N-40. The underresponse at low energies is stronger for $H^*(10)$ and $H'(0.07, \Omega)$ compared to $H'(3, \Omega)$. This results from the definition of the conversion coefficients from air kerma to area dose equivalent of interest. $H^*(10)$ has no angular dependency, while the conversion coefficients for $H'(0.07, \Omega)$ extracted from [56] show only a small influence on the angle of radiation incidence. The conversion coefficients for the $H'(3, \Omega)$ show a noticeable angular dependence since they decrease with increasing angle of radiation incidence. This lower reference dose compensates for the strong underestimation of the dose under angular irradiation. Such compensation is not observed for the other two area dose equivalent due to the missing or weak angular dependence.

The angular dependence at low photon energies is explained with Figure 3.29. It shows the number of registered events in a particular slot over all pixel of a type for the different angles of radiation incidence. Slot 1 shows a significant reduction of the number of registered events under angular irradiation. This is due to the filter-cap of Slot 1. It is intended for dosimetry of the personal dose equivalent $H_\mathrm{p}(10)$ and compensates its angular dependence at low energies. For $H_\mathrm{p}(10)$, when increasing the angle of radiation incidence a larger reference air kerma must be applied by PTB to keep the reference dose equivalent constant since the conversion coefficients between air kerma and $H_\mathrm{p}(10)$ decrease at the lower energy range with increasing angle of radiation incidence. The larger reference air kerma means a larger flux of photons impinging onto the detector and therefore a larger registered number of

events in Dosepix. Photons absorbed in the filter-cap of Slot 1 are missing for the determination of $H^*(10)$ since it is not dependent on the angle of radiation incidence, i.e., a constant air kerma is applied by PTB for all angles or radiation incidence. This explains the measured angular dependence of the Dosepix dosimetry demonstrator for angular irradiation. Slots 2, and 3 show a small reduction of the number of events for both pixel types at their particular lower energy range. Measurements without the filter-cap of Slot 1 must be performed for future application of area dosimetry with Dosepix. This will increase the rated range of use of a potential active area dosemeter. Table 3.10 summarizes the key parameters of the normalized response for the different angles of radiation incidence and pixel types.

Figure 3.30 shows the energy dependence of the relative statistical uncertainty for the ambient dose equivalent $H^*(10)$, and the directional dose equivalents $H'(3, \Omega)$ and $H'(0.07, \Omega)$ for both pixel types. The curves are nearly identical for all angles of radiation incidence except in the low-energy range. At these energies, an increasing angle of radiation incidence decreases the the number of registered events, which increases the statistical uncertainty. The energy dependence of the relative statistical uncertainty increases with increasing mean photon energy and becomes nearly flat at around 100 keV. Overall, all values for the three area dose equivalents are below 0.5% and 3.3% for the large and the small pixels, respectively. To yield a conservative estimate for the coefficient of variation, a conservative multiplicity factor of 1.45 must be applied to the measured relative statistical uncertainty [20]. It takes into account that one photon can trigger several pixels, which inflates the event rate and incorrectly decreases the relative uncertainty. All values stay within the limit after multiplication with 1.45 (1.75 for the small pixels as will be shown in Chapter 4). Therefore, a fulfillment of the requirements with respect to the coefficient of variation is achieved.

The determined rated range of use has an upper boundary of at least 1250 keV for all area dose equivalents and pixel types. The lower boundary of the range of use can be summarized as follows for the large pixels: 16.3 keV, 45° or 24.6 keV, 60° for the ambient dose equivalent $H^*(10)$, 16.3 keV, 45° or 20.3 keV, 60° for the directional dose equivalent $H'(3, \Omega)$, and 24.6 keV, 45° or 33.3 keV, 60° for the directional dose equivalent $H'(0.07, \Omega)$. Furthermore, the lower range of for the small pixels is: 16.3 keV, 45° or 24.6 keV, 60° for the ambient dose equivalent $H^*(10)$, 16.3 keV, 45° or 20.3 keV, 60° for the directional dose equivalent $H'(3, \Omega)$, and 20.3 keV, 45° or 24.6 keV, 60° for the directional dose equivalent $H'(0.07, \Omega)$. In summary, the minimum rated range of use is fulfilled and even surpassed by at least one influence quantity. Therefore, it is shown that the Dosepix dosimetry demonstrator can be successfully applied in the area monitoring of operational quantities as it fulfills the requirements for area dosemeter stated in [64, 65, 66]. The results show applicability of the Dosepix dosimetry demonstrator workplace monitoring at industrial workplaces (80-1.25 MeV) for all area dose equivalents and pixel types of up to 60° and medical (20-150 keV) workplaces for $H^*(10)$ and $H'(3, \Omega)$ for both pixel types and $H'(0.07, \Omega)$ for the small pixels for angles of radiation incidence of $\pm 45°$.

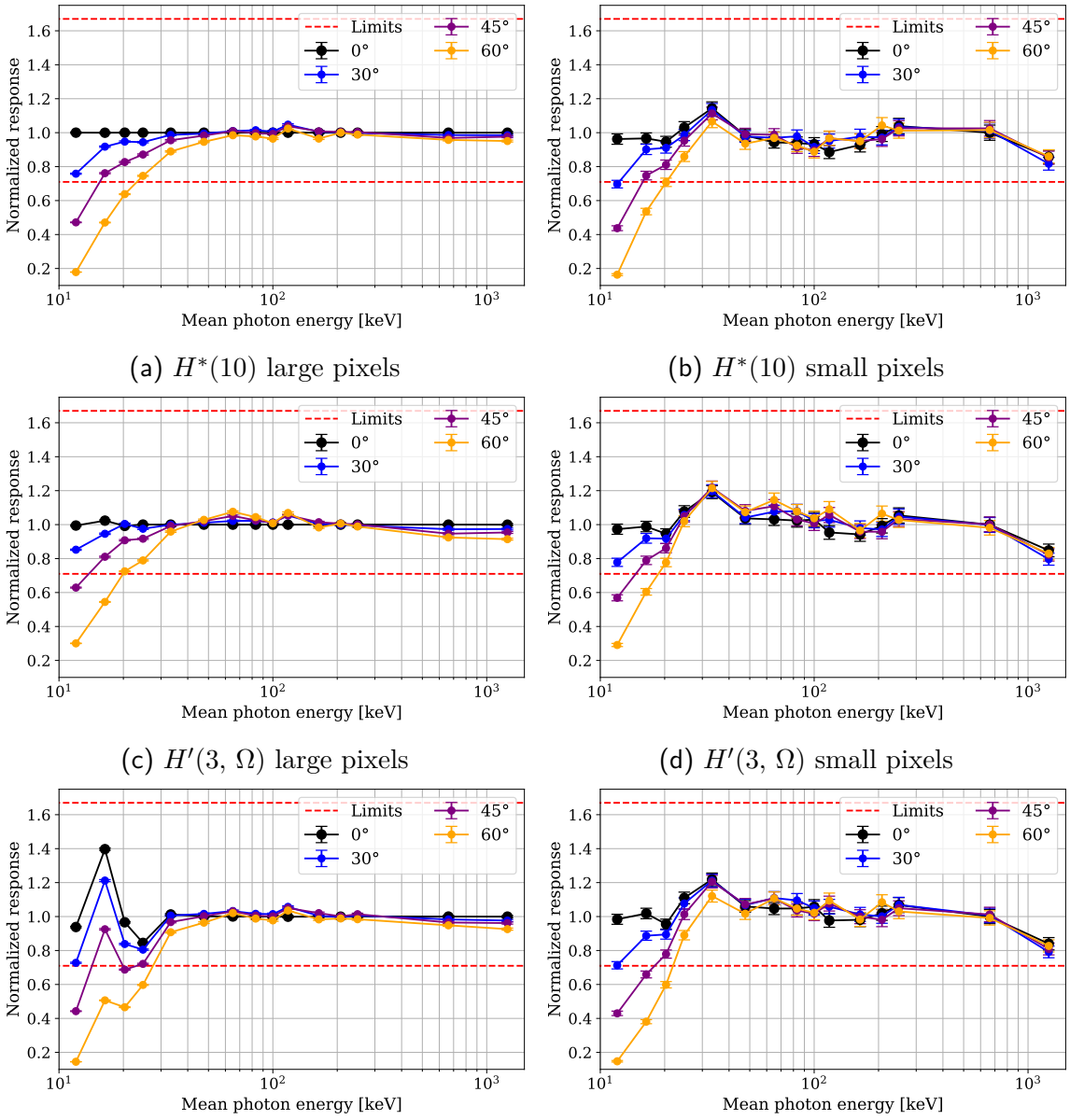

(a) $H^*(10)$ large pixels

(b) $H^*(10)$ small pixels

(c) $H'(3, \Omega)$ large pixels

(d) $H'(3, \Omega)$ small pixels

(e) $H'(0.07, \Omega)$ large pixels

(f) $H'(0.07, \Omega)$ small pixels

Figure 3.28.: Energy and angular dependence of the normalized response for different area dose equivalents for the large and the small pixels. The energy range is from 12.4 keV to 1250 keV for reference photon fields. The red dashed lines indicate the limits as stated in Table 3.2.

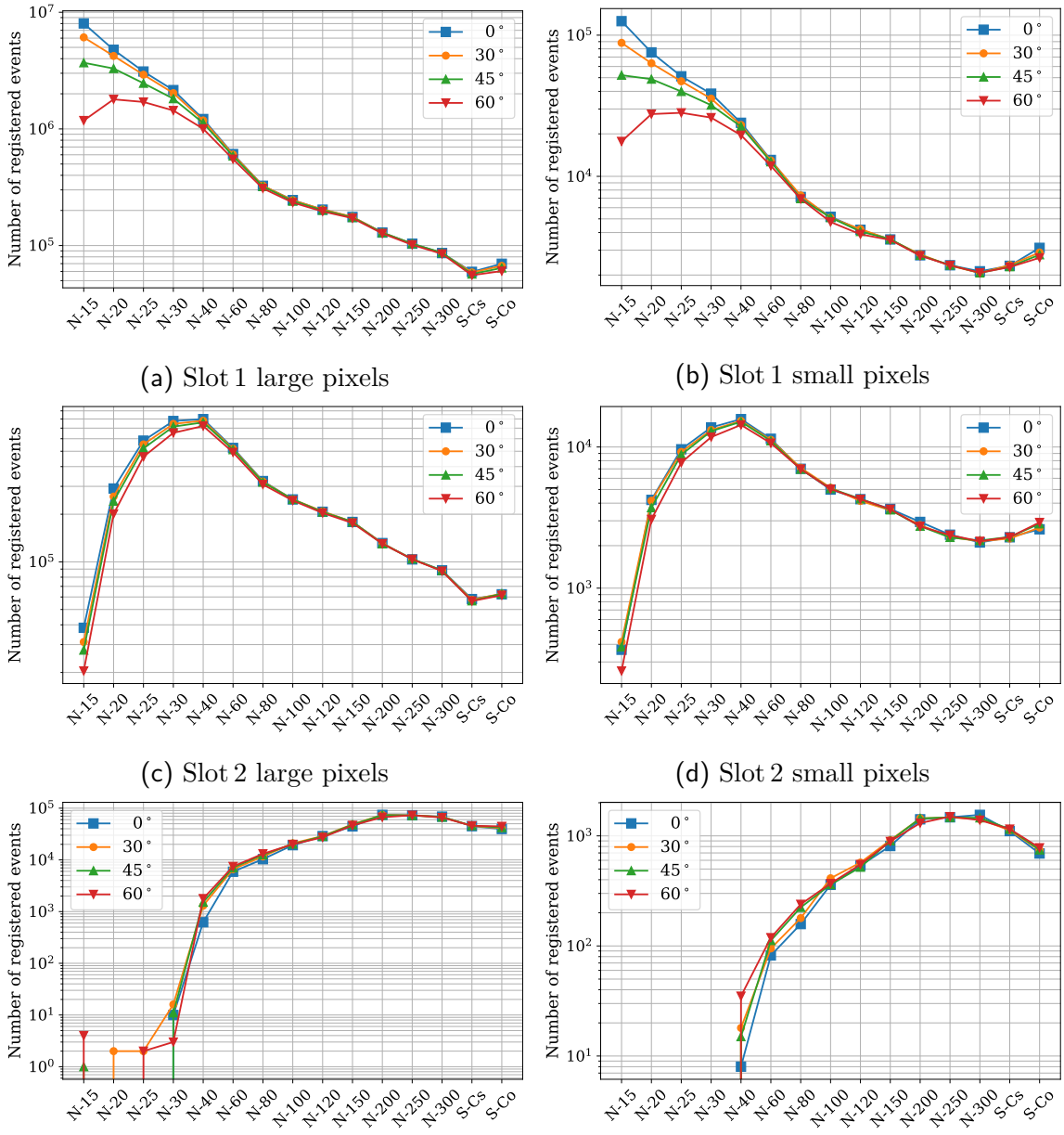

(a) Slot 1 large pixels

(b) Slot 1 small pixels

(c) Slot 2 large pixels

(d) Slot 2 small pixels

(e) Slot 3 large pixels

(f) Slot 3 small pixels

Figure 3.29.: Energy dependence of the total number of registered events for the different detectors, pixel types and angles of radiation incidence. The used angles of radiation incidence are 0°, 30°, 45°, and 60°.

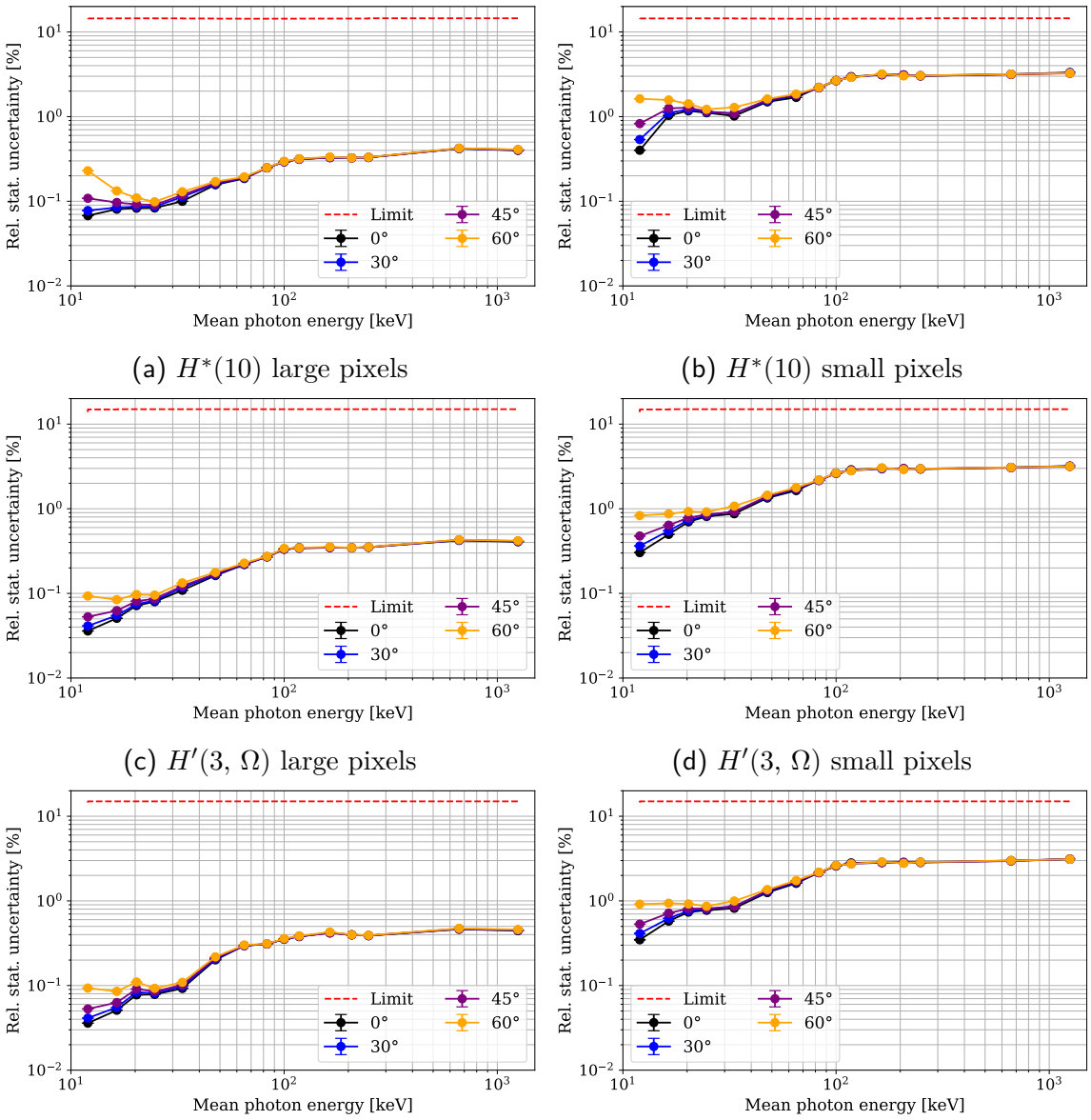

(a) $H^*(10)$ large pixels

(b) $H^*(10)$ small pixels

(c) $H'(3, \Omega)$ large pixels

(d) $H'(3, \Omega)$ small pixels

(e) $H'(0.07, \Omega)$ large pixels

(f) $H'(0.07, \Omega)$ small pixels

Figure 3.30.: Energy and angular dependence of the relative statistical uncertainty for different area dose equivalents for the large and the small pixels. The energy range is from 12.4 keV to 1250 keV for reference photon fields. The red dashed line indicates the limits as stated in Table 3.2.

Dose	α [°]	Pixel size [µm]	Min.	Max.	µ	σ
$H^*(10)$	0	55	0.857±0.040	1.143±0.038	0.970	0.066
		220	0.9997±0.0043	1.0002±0.0043	1.0000	0.0001
	30	55	0.697±0.022	1.134±0.038	0.949	0.095
		220	0.758±0.003	1.047±0.006	0.973	0.065
	45	55	0.437±0.014	1.113±0.037	0.909	0.154
		220	0.472±0.002	1.038±0.006	0.925	0.142
	60	55	0.164±0.006	1.066±0.037	0.860	0.228
		220	0.179±0.001	1.024±0.006	0.846	0.234
$H'(3, \Omega)$	0	55	0.847±0.038	1.191±0.038	1.006	0.074
		220	0.992±0.004	1.023±0.004	1.001	0.007
	30	55	0.778±0.024	1.197±0.038	0.994	0.105
		220	0.852±0.004	1.054±0.006	0.990	0.044
	45	55	0.569±0.018	1.218±0.039	0.970	0.152
		220	0.629±0.003	1.055±0.006	0.956	0.107
	60	55	0.291±0.009	1.215±0.040	0.947	0.229
		220	0.301±0.001	1.076±0.005	0.891	0.211
$H'(0.07, \Omega)$	0	55	0.839±0.036	1.219±0.038	1.026	0.080
		220	0.844±0.004	1.397±0.007	1.011	0.111
	30	55	0.713±0.022	1.212±0.038	1.003	0.126
		220	0.728±0.003	1.212±0.006	0.979	0.110
	45	55	0.430±0.013	1.206±0.037	0.950	0.193
		220	0.443±0.002	1.050±0.007	0.920	0.164
	60	55	0.148±0.005	1.121±0.036	0.889	0.280
		220	0.145±0.001	1.036±0.006	0.829	0.260

Table 3.10.: Response normalized to S-Cs at 0°, R_{Norm}, for the different area dose equivalents and angles of incidence α. The key parameters are minimum and maximum R_{Norm} values, mean R_{Norm} µ, and its standard deviation σ.

3.12. Conclusion

A dosimetry demonstrator consisting of three Dosepix detectors was used for application in dosimetry of the ambient dose equivalent $H^*(10)$, the directional dose equivalents $H'(3, \Omega)$ and $H'(0.07, \Omega)$, and additionally as semiconductor detector as used in X-ray diagnostic imaging measuring the air kerma. Dosepix's sensor matrix comprises two different pixel types, which were investigated separately.

45 spectra for the setup at Erlangen were defined and used for dosimetry. Their mean energies and mean conversion coefficients for the area dose equivalents were stated in this chapter. These reference fields allow determining conversion factors from the number of registered events in an energy bin of Dosepix to an area dose equivalent of the dosimetry demonstrator in the energy range from 30 keV to 105 keV.

The combined influence of the energy and angular dependence of the normalized response for the area dose equivalents was investigated and compared to national and international requirements according to [64, 65, 66]. The tested energy range of use is from 12.4 keV to 1.25 MeV and the range of the angle of radiation incidence between 0° and 60°. The corresponding reference photon fields are from the N-series (N-15 to N-300) and the γ reference radionuclides S-Cs and S-Co according to ISO 4037-1 [67]. For all three area dose equivalents, the tendency to an underresponse with decreasing mean photon energy and increasing angle of radiation incidence is observed. Overall, the minimum requirements are fulfilled by the Dosepix dosimetry demonstrator for all three area dose equivalents. The rated range of use for the combined influence of the influence quantities mean photon energy and angle of radiation incidence can be summarized as follows with the upper range of use of 1250 keV: 16.3 keV, 45° or 24.6 keV, 60° for the ambient dose equivalent $H^*(10)$, 16.3 keV, 45° or 20.3 keV, 60° for the directional dose equivalent $H'(3, \Omega)$, and 24.6 keV, 45° or 33.3 keV, 60° for the directional dose equivalent $H'(0.07, \Omega)$ for the large pixels. For the small pixels the rated range of use is determined as 16.3 keV, 45° or 24.6 keV, 60° for the ambient dose equivalent $H^*(10)$, 16.3 keV, 45° or 20.3 keV, 60° for the directional dose equivalent $H'(3, \Omega)$, and 20.3 keV, 45° or 24.6 keV, 60° for the directional dose equivalent $H'(0.07, \Omega)$. With this, applicability in area monitoring is shown at industrial workplaces (80-1.25 MeV) for all area dose equivalents and pixel types of up to 60° and medical workplaces (20-150 keV) for $H^*(10)$ and $H'(3, \Omega)$ for both pixel types and $H'(0.07, \Omega)$ for the small pixels for angles of radiation incidence of $\pm 45°$.

Additionally, conversion factors from the number of registered events in an energy bin of Dosepix to air kerma were determined to assess the potential of Dosepix as a semiconductor detector as used in X-ray diagnostic imaging according to [68]. The relative statistical uncertainty is outside the limits for the small pixels, which makes their application unfeasible. The large pixels are within limits from 20.3 keV to 1250 keV. For smaller energies, a fluctuation in the energy dependence is observed since the applied reference dose becomes too large. The tested reference photon fields were the N-series according to ISO 4037-1 [67], whereas X-ray diagnostic detectors are

typically tested via photon reference fields of the RQR and RQA qualities according to IEC 61267 [76] as required by IEC 61674 [68]. Further tests in these reference photon fields are required to confirm the use of Dosepix as a diagnostic dosemeter.

All in all, it was shown that Dosepix had been successfully applied in the field of area dosimetry with respect to its energy and angular dependence of the normalized response. Further investigations regarding the extension of the energy range for usage in nuclear facilities and natural background monitoring are required. Tests must be performed for mean photon energies of up to 10 MeV.
Optimization of the dosimetry demonstrator is needed to increase the rated range of use. Removing the filter cap of Slot 1 will reduce the influence of the angle of radiation incidence since no incident photons are absorbed, and only the decrease of the effective area and the increase of the effective sensor thickness affect the event rate. A rated range of use down to 12 keV for $H^*(10)$, $H'(3, \Omega)$ and $H'(0.07, \Omega)$ is expected with this fix. Investigations of the remaining requirements of PTB-A 23.3 must be carried out, such as the temperature dependence and the dependencies on the dose rate and the pulse duration.

4. Personal Dosimetry with Dosepix

Contents

It has been shown that a dosimetry demonstrator comprised of three Dosepix detectors correctly measures the personal dose in continuous photon fields with its large pixels [20]. The investigated operational quantities of radiation protection were the personal dose equivalent $H_{\mathrm{p}}(10)$ and the personal dose equivalent $H_{\mathrm{p}}(0.07)$. These measurements are recapitulated in this chapter and extended by the eye lens dose $H_{\mathrm{p}}(3)$. Furthermore, investigations into the metrological properties of the small pixels are conducted. The measurements are performed on the ISO water slab

phantom. Conversion coefficients between air kerma and one of the three personal dose equivalents defined on the ICRU slab phantom are used to determine the reference dose to utilize a single measurement campaign. An important capability of a personal dosemeter is the correct response to the particle type of the impinging radiation field. When interacting with the sensor element of the dosemeter, direct ionizing radiation will always induce a signal. Dosemeters intended for dosimetry of photon fields must be as unresponsive as possible for direct ionizing radiation such as electrons. Therefore, the influence of β-radiation on the photon dose indication is investigated. At the end of this chapter, the prototype of the first active personal dosemeter for the monitoring of the eye lens dose $H_\mathrm{p}(3)$ is presented. $H_\mathrm{p}(3)$ is subject to increased interest over the last decade since legal exposure limits were severely restricted as recommended in [77]. The related project is called EXTRA (Electronic X-Ray Tracker) within the Medical Valley Award 2018. For this purpose, the number of used Dosepix detectors is reduced to a single one, and a prototype for applications in energy regimes between 12.4 keV and 248 keV is developed. First metrological characterizations of a single Dosepix detector and subsequent validation of an eye lens dosemeter prototype with measurements at the German metrology institute (PTB) are presented.

4.1. Active Personal Dosemeter

A personal dosemeter is defined as a meter to measure the personal dose equivalent $H_\mathrm{p}(x)$, with x denoting the depth in mm of ICRU 4-element tissue [59]. It is typically worn on the trunk (operational quantity $H_\mathrm{p}(10)$ for a whole-body personal dosemeter), at the extremities (operational quantity $H_\mathrm{p}(0.07)$ for an extremity personal dosemeter), and close to the lens of the eye (operational quantity $H_\mathrm{p}(3)$ for an eye lens personal dosemeter) [59]. Personal dosemeters are categorized as either passive or active ones. An active personal dosemeter (APD) directly displays the imparted dose at any given time and alerts its wearer when dose/dose rate thresholds are surpassed. Possible alerts are, for example, an alarm sound, a pulsing light source, or vibration of the APD. This helps increase the wearers' awareness of unintentional high exposures. It also allows them to appropriately react to the situation by taking active precautions like stepping away from the radiation source, adjusting existing mounted shields, and adding protection equipment such as protection glasses, thyroid shields, or lead aprons if not already equipped. Compared to their active counterparts, passive dosemeters are read out monthly after being sent to national distributions centers where the accumulated dose is determined. Typical passive variants are luminescence dosemeters, e.g., OSL/TLD (optically stimulated luminescence/thermoluminescent dosemeters). A dosimetry system utilizing OSL dosimetry of beryllium oxide is presented in [78]. The latter passive dosemeter is paired with a readout system to analyze the exposure directly after the procedure. However, there is no direct alert that would minimize the exposure significantly, which is especially critical in accident situations. Consequently,

applications such as training of the staff in movements reducing the exposure are not feasible due to lack of direct feedback of the passive personal dosemeter.

Several studies into APDs suggest that dosemeters utilizing silicon diodes are the most commonly used active personal dosemeters in hospitals [11] and that they yield the best results in regards to the energy and angular dependence of the dose indication [7, 79, 12]. Even though APDs exhibit favorable features, they are not state-of-the-art devices in monitoring occupationally exposed workers since they are not permitted for legal dosimetry. It is due to the problems of APDs in radiation fields of pulsed nature (pulse duration smaller than 10 s [80]), mainly due to high peak pulse dose rates and short radiation pulse durations [6, 81]. Due to dead-times current APDs, may miss the exposure if the pulse durations are short. Furthermore, an accident situation might occur with dose rates of several hundreds of Sieverts per hour due to exposure to the direct beam of a pulsed radiation field [81]. Hybrid pixel detectors such as the Dosepix detector are promising candidates to show excellent energy and angular dependence of the dose indication [20] and extraordinary response to high peak pulse dose rates and short radiation pulse durations [82].

4.2. Requirements for a Personal Dosemeter

A personal dosemeter does not protect against ionizing radiation. It, nevertheless, gives the occupationally exposed staff member a sense of security. Exposure to ionizing radiation must be limited due to its hazardous nature. Regulators and international expert committees define exposure limits, monitored by personal dosemeters. It is therefore of utmost importance that personal dosemeters must meet strict requirements. The conformity assessment of a personal dosemeter in Germany is performed by the PTB, which states its requirements in PTB-A 23.2 and its complement [83, 69]. An excerpt is displayed in Table 4.1. The metrological characterization of APDs is typically performed by looking into their dependencies of the mean photon energy, the angle of radiation incidence, dose linearity, pulse duration, dose rate, and the coefficient of variation. This chapter deals with the metrological requirements such as energy and angular dependence and their statistical reproducibility for the Dosepix dosimetry demonstrator and additionally the pulse duration and the dose rate dependence for the eye lens dosemeter prototype. The corresponding assessment quantities are the normalized response R_{Norm} and the relative statistical uncertainty F_{stat} as an approximation of the coefficient of variation v. It is referred to Section 3.3 for their exact definitions and corresponding uncertainties.

The metrological tests investigate whether the change of an influence quantity, such as the energy and angular dependence, affects the dose indication (dose value provided by the dosemeter) and therefore leads to a change of the normalized response (response normalized to a response at reference conditions) within the officially permitted limits. A flat response for energy dependence is the targeted behavior. In the best case, the

response R should be equal to 1. If this is not the case, but the response is flat, a correction factor can be introduced that corresponds to the reciprocal response. The limits defined for the energy and angular dependence should not exceed the boundary values $f_{\min}$ =-0.29 and $f_{\max}$ =+0.67 where the value of R_{Norm} holds the following condition true:

$$f_{\min} + 1 \leq R_{\text{Norm}} \leq f_{\max} + 1\,. \tag{4.1}$$

The influence of the dose rate is limited to $f_{\min}$ =-0.13 and $f_{\max}$ =+0.18 [83, 84], and for the pulse duration to $f_{\min}$ =-0.2 and $f_{\max}$ =+0.2 [83]. The limits of the coefficient of variation are calculated depending on the lower limit of the measurement range H_u. It is 1 mSv for $H_{\text{p}}(0.07)$, 0.3 mSv for $H_{\text{p}}(3)$, and 0.1 mSv for $H_{\text{p}}(10)$. The requirements stated in Table 4.1 relate to photon irradiations. The irradiations are performed in reference photon fields according to ISO-4037-1 [67] and with procedures stated in ISO-29661 [59]. Additionally, the influence of β-radiation on the indication of the personal dose for photons is investigated. The dosemeter is irradiated by radionuclides such as ^{147}Pm, ^{85}Kr, ^{90}Sr/^{90}Y, and ^{106}Ru/^{106}Rh recommended as β reference fields in ISO 6980-1 [85]. The indication of $H_{\text{p}}(10)$ for photons is restricted to a maximum value of 10% of the reference $H_{\text{p}}(0.07)$ for electrons when the dosemeter is irradiated in β reference fields.

4.3. Three Dosepix Detectors

4.3.1. Methods and Materials

The energy and angular dependence of the normalized response and the statistical reproducibility of Dosepix for the personal dose equivalents $H_{\text{p}}(10)$, $H_{\text{p}}(3)$, and $H_{\text{p}}(0.07)$ are investigated in the following. For this purpose, the Dosepix dosimetry demonstrator presented in Section 3.2 is utilized. The measurements of the energy and angular dependence of the normalized response are performed with a detector housing made of 1.5 mm thick PMMA. The notable difference compared to the Dosepix detector dosimetry demonstrator for dosimetry of the area dose equivalent is the dosemeter housing, i.e., the sidewalls and the back wall. The side walls have a negligible influence on the dose as the lateral dimensions of the housing are large and do not attenuate the radiation beam even at different angles of radiation incidence. The expected contribution is scattering in the side walls. The material of the housing influences the amount of backscattering from the phantom. This influences the response as the thicker backside of the housing absorbs more backscattered photons from the phantom. A lower value of the response is expected, i.e., a lower value of the dose is measured with the Dosepix dosimetry demonstrator. In both cases, the front side is covered with 1.5 mm white ABS plastic. As for the nomenclature used in the following: The detector with the filter cap consisting of an aluminum cylinder and an

Quantity	Minimum rated range of use	Reference value
For $H_p(0.07)$: Mean photon energy $\langle E \rangle$ and angle of radiation incidence α	30 keV to 250 keV and -60 ° $\leq \alpha \leq$ +60 °	65 keV (N-80) and 0 ° (reference orientation)
For $H_p(3)$: Mean photon energy $\langle E \rangle$ and angle of radiation incidence α	30 keV to 250 keV and -60 ° $\leq \alpha \leq$ +60 °	65 keV (N-80) and 0 ° (reference orientation)
For $H_p(10)$: Mean photon energy $\langle E \rangle$ and angle of radiation incidence α	80 keV to 1250 keV and -60 ° $\leq \alpha \leq$ +60 °	662 keV (S-Cs) and 0 ° (reference orientation)
Dose rate	0.1 µSv/h to 1 Sv/h	1 mSv/h
Radiation pulse duration	1 ms to 10 s	Continuous radiation
Quantity	**Dose range**	**v_{max} [%]**
Dose H	$H < H_u$ $1 \cdot H_u \leq H < 11 \cdot H_u$ $11 \cdot H_u \leq H$	15 16 - H/H_u 5

Table 4.1.: Excerpt of the conformity assessment requirements to personal dosemeters according to PTB-A 23.2 and its complement [83, 69] and international requirements IEC 61526 [84]. Radiation qualities of the N-series and S-Cs are defined in ISO 4037-1 [67]. The investigated influence quantities are the mean photon energy $\langle E \rangle$, the angle of radiation incidence α, the dose rate, the pulse duration, and the coefficient of variation. H_u denotes the lower limit of the measurement range. The requirements for the pulse duration are taken from [83].

aluminum foil with a hole above the sensor is called Slot 1. The detectors with the half-spheres of aluminum and tin are called Slot 2 and Slot 3 respectively.

The irradiations with reference photon fields are performed at PTBs 120 kV, 400 kV, and the Hartlep facility for γ-decay radiation of high activity radionuclides. Table 4.2 summarizes the used reference photon fields. The best reference photon fields for the investigation of the energy dependence are of the N-series (narrow series) and monoenergetic γ-emission lines due to their narrow nature. Reference photon fields produced by radioactive sources carry the letter S in combination with the chemical symbol of the radionuclide, i.e., S-Cs and S-Co [67].

Radiation quality	$\langle E \rangle$[keV]	α [°]
N-15	12.4	0; 30; ±60
N-20	16.3	0; 30; ±60
N-25	20.3	0; 30; ±60
N-30	24.6	0; 30; ±60
N-40	33.3	0; 30; ±60
N-60	47.9	0; 30; ±60
N-80	65.2	0; 30; ±60
N-100	83.3	0; 30; ±60
N-120	100	0; 30; ±60
N-150	118	0; 30; ±60
N-200	165	0; 30; ±60
N-250	207	0; 30; ±60
N-300	248	0; 30; ±60
S-Cs	662	0; 30; ±60
S-Co	1250	0; 30; ±60

Table 4.2.: X-ray and γ reference fields according to ISO 4037-1 [67] used for measurements with the Dosepix dosimetry demonstrator at PTB. These radiation qualities are associated by their mean photon energy $\langle E \rangle$. Additionally, the angles of radiation incidence α at which the irradiations are performed are stated.

The Dosepix dosimetry demonstrator is attached to the center front of the ISO water slab phantom as the irradiation conditions are chosen for the personal dose equivalent $H_\mathrm{p}(10)$. The ISO water slab phantom has an irradiation cross-section of 30 cm×30 cm with a depth of 15 cm. It consists of a combination of PMMA and water. The PMMA walls have a thickness of 10 mm, except for the front wall with a thickness of 2.5 mm. The axis passing through the three detectors is horizontal to the rotation axis of the reference point, i.e., both vectors are orthogonal and lie in the plane of the phantom surface. Slot 2 at 1.5 cm behind the housing cover is the reference point. The

symmetry of the setup is investigated at angles of radiation incidence of ±60 °. The main question is if the absorption of the impinging photon field due to the tin filter cap of Slot 3 results in shading effects in the remaining two detectors. Furthermore, the reference direction is parallel to the incident photon field at an angle of radiation incidence of 0 ° and goes through the reference point. A schematic depiction of the setup defining the key parameters reference point, reference direction, axis of rotation, and angle of radiation incidence is shown in Figure 4.1.

The reference value of the $H_{\mathrm{p}}(10)$ is constant 150 µSv with an exposure time of 60 s for all radiation qualities except N-15, whose irradiation of the dosemeter has a reference dose of 50 µSv in 180 s. The reference value of the dose is equal for all angles of radiation incidence. References [74] and [57] tabulate conversion coefficients for reference photon fields from air kerma to $H_{\mathrm{p}}(0.07)$ and $H_{\mathrm{p}}(3)$ on the ICRU slab phantom. These conversion coefficients are utilized to calculate the reference dose equivalents $H_{\mathrm{p}}(0.07)$ and $H_{\mathrm{p}}(3)$ from the reference air kerma measured by monitor chambers by PTB. The calibration of the monitor chambers is traceable to national primary measurement standards. The reference dose equivalents are shown in Figure 4.2(a). For a clear view, only 0 ° and ±60 ° are shown. The reference dose increases significantly for an increased angle of radiation incidence for $H_{\mathrm{p}}(0.07)$ and $H_{\mathrm{p}}(3)$. With these values, the limit for the coefficient of variation is calculated according to Table 4.1, which is shown in Figure 4.2(b). The limits are predominantly at the maximum value of 15 % because the reference dose is smaller than the lower limit of the measurement range H_u. The increased dose at low energies for 60 ° leads to a lower limit for the coefficient of variation.

4.3.2. Measurement Data

The energy deposition spectra of different radiation qualities are measured in the Dosi-mode, designed for dosimetry applications. Each detector registers its individual energy histogram for the small and large pixels. Excerpt of data of six reference fields for the irradiations at 0 ° angle of radiation incidence for the large and the small pixels are shown in Figure 4.3. It displays the total number of events per bin per Slot for both pixel types on the sensor matrix.

Slot 1 of the large pixels shows entries in energy bins at energies higher than the kVp value of the radiation field due to pile-up. The affected radiation qualities are of smaller kVp values. In this energy regime Slot 1 exhibits attenuation of the radiation field by only the 1.5 mm ABS. The number of events is sufficiently small compared to the number of entries in the energy bins in which the events are expected, which attributes to a natural amount of pile-up occurrences. The small pixels show the expected behavior due to their smaller volume. The number of events in the energy histograms decreases towards the cutoff energy coinciding with the kVp. Even for large energies of the impinging radiation field, no significant number of events is measured in the high-energy bins. Due to the small volume of the small pixels in

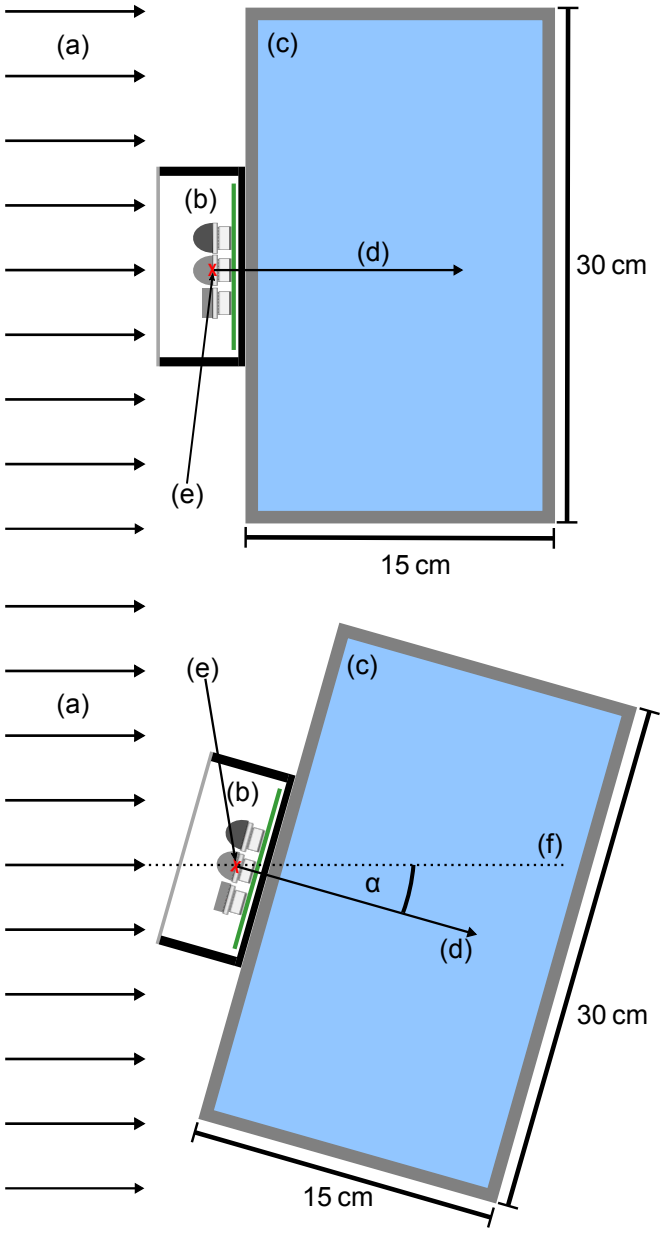

Figure 4.1.: Dosemeter (b) on the ISO water slab phantom (c) according to ISO 29661 [59]. The reference radiation field is indicated by (a), which is parallel to the reference direction of the dosemeter (d). The red cross (e) indicates the reference point of the dosemeter. It is the point of rotation. The angle of radiation incidence is 0 °, if the reference direction and the direction of the radiation field are parallel. Rotation around the reference point changes the angle of radiation incidence α which is the angle between the vector of the extension line of photon field (f) going through the reference point and the reference direction of the dosemeter.

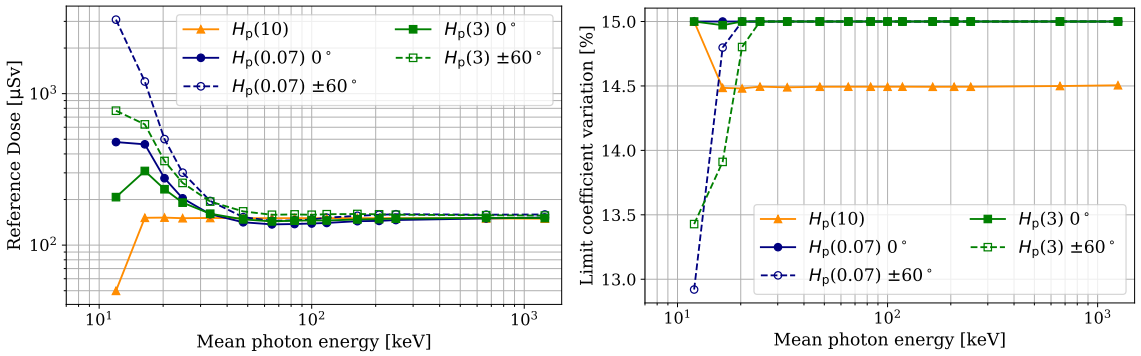

(a) Reference dose (b) Limits

Figure 4.2.: Reference dose for the investigated personal dose equivalents. $H_p(10)$ shows no angular dependence of the reference dose due to setting of this dose. The remaining ones are illustrated for 0° and ±60°. The reference dose in (a) is used to calculate the limits of the coefficient of variation in (b).

which, on average, a maximum deposited energy of 160 keV is expected. The energy bin edges of the small pixels are chosen to end at 160 keV [37], because no significant number of events is expected above this energy even for high energies of the expected radiation field.

Slot 2 beam hardens the impinging radiation field further, decreasing the number of events seen in the energy histograms. For N-15, for instance, no events in energy bins higher than the maximum physical possible energies are measured in the large pixels. Energies of the N-40 radiation fields are sufficiently large to transmit the filter cap without interaction, which increases the number of events. This leads to the occurrence of pile-up events, which are small compared to the remaining events. The small pixels exhibit the expected behavior.

The large pixels of Slot 3 show in total eight events for N-15, i.e., almost no events at all due to its energy threshold at 32 keV and for this energy absorption by the tin of the filter cap. N-40 has its mean energy around the threshold. The corresponding energy histogram looks like a cut into the N-40 energy distribution. The energy histograms of the remaining radiation qualities show cutoffs at the kVp values. The small pixels exhibit the expected behavior.

The overall per-pixel event rate, i.e., the sum of all entries in the energy histogram divided by the exposure time and the number of pixels, is shown in Figure 4.4 for both pixel types. Significant differences in the event rate arise at small energies. They are attributable to the beam hardening of the filter caps. Slot 1 is important at energies below 30 keV. Above that, the event rate of Slot 1 and Slot 2 are similar, which means that the absorption of the 2 mm thick aluminum half-sphere becomes negligible compared to transmission. Above about 200 keV, the event rate of Slot 3

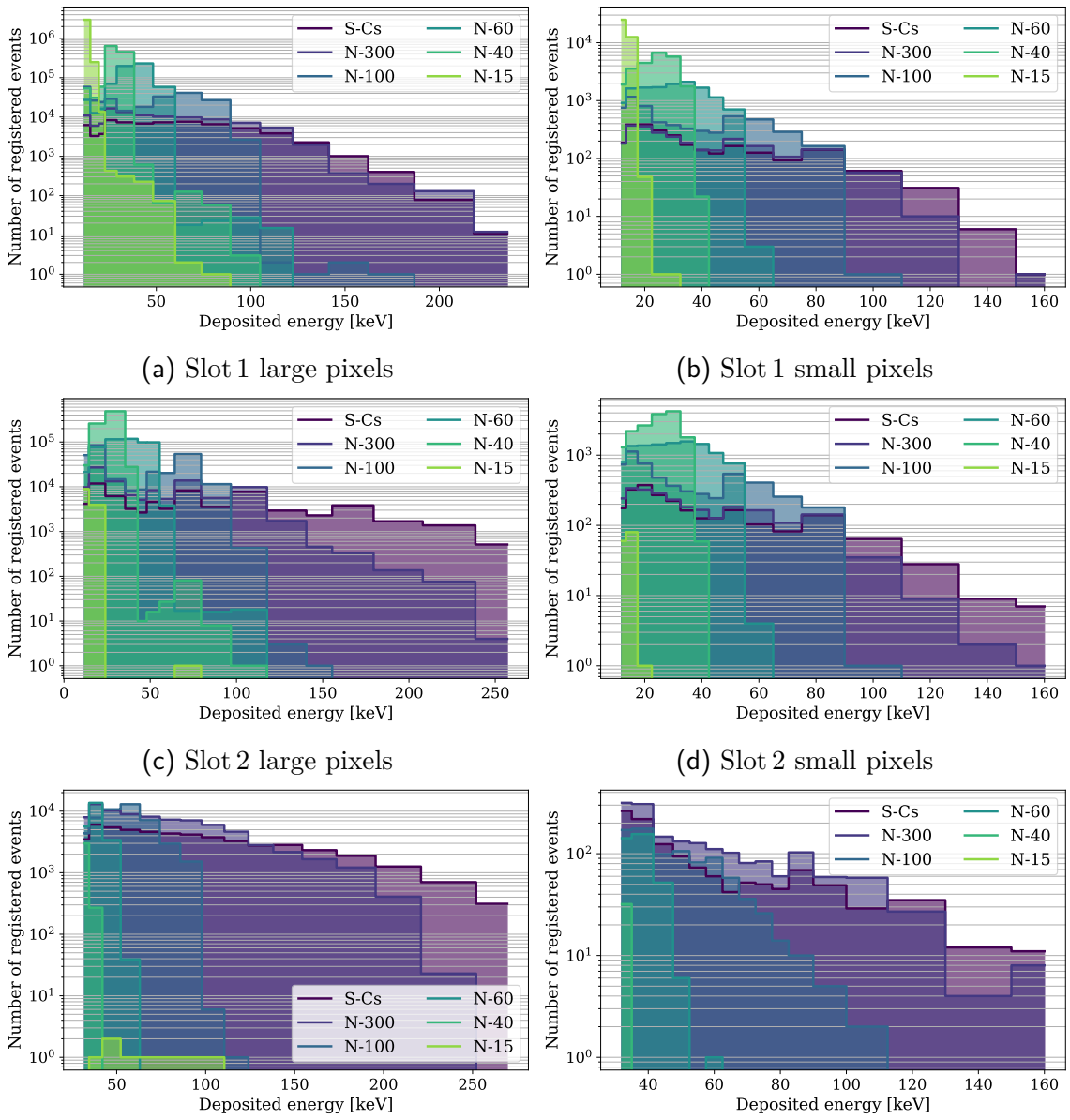

(a) Slot 1 large pixels

(b) Slot 1 small pixels

(c) Slot 2 large pixels

(d) Slot 2 small pixels

(e) Slot 3 large pixels

(f) Slot 3 small pixels

Figure 4.3.: Excerpt of measurements of 6 different radiation qualities in the Dosimode. Energy histograms are shown for each slot and pixel type. The histograms include all pixels of a certain pixel type on the matrix and are yielded from the summation of all pixel individual energy histograms.

is similar to the event rate of the other two Slots as the influence of the 1 mm tin cap becomes negligible. The curves for the large and small pixels are similar and differ primarily in their event rate, except for the small pixels of Slot 3. There, the event rate difference to the remaining two Slots is larger compared to the large pixels. Figure 4.4(c) shows the ratio between the event rate of the large and the small pixels per slot. A ratio of 16 is expected which corresponds to the ratios between the volumes of a large and a small pixel. Slot 1 and 2 show both a ratio above 16 for radiation qualities with mean energies below N-40 (33 keV). Similar behavior is observed for Slot 3 below N-80. At the threshold of each detector, the ratio between the event rate of the large and the small pixels increases as the diffusion of charge carriers at the edge of the pixel effectively decreases the volume of the pixels. This effect is stronger for the small pixels due to their larger circumference-area ratio, which increases the event rate ratio close to the energy threshold.

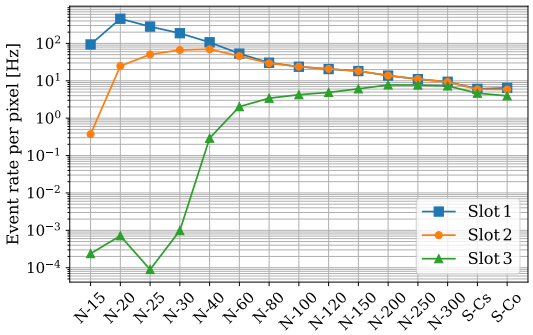

(a) Large Pixels

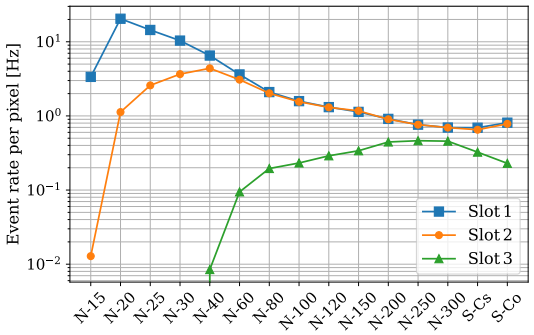

(b) Small Pixels

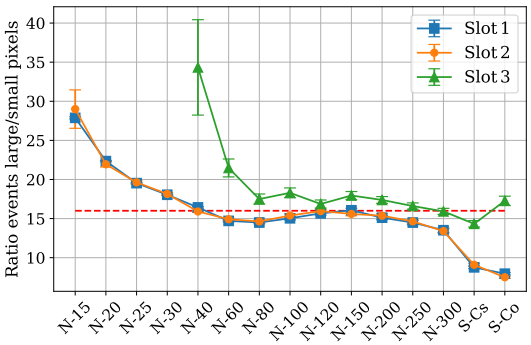

(c) Ratio large pixels small pixels

Figure 4.4.: Per-pixel event rate for different radiation qualities representing mean photon energies. Large pixels (a) and small pixels (b) show similar trends of the event rate. Additionally the ratio between the event rates is calculated in (c). The red dashed line represents the volume ratio of 16.

4.3.3. Conversion Factors

The determination of conversion factors between the total number of events measured in one of the 48 energy bins of the Dosepix dosimetry demonstrator and the personal dose equivalent of interest follows the methods described in Section 3.8. The input conversion coefficients for the large pixels were already determined via simulation data from [19] for the three detector setup on the ISO water slab phantom, which were already used in [37]. A randomized fit approach is chosen to adapt them to the measurements. The number of data points equals 15, and the number of parameters is 48. Therefore, a maximum of 14 conversion factors are optimized, while the remaining ones are held constant. A random number of conversion factors between 4 and 14 is drawn. This value is used to draw random numbers between 0 and 47, denoting the bin indices of three Dosepix detectors. The conversion factors of these bins are optimized. The constraints on the fit are a lower boundary of 1e-5 µSv and an upper boundary of 1e-1 µSv. Optimizing only several conversion factors introduces small trend fluctuations contrary to a smooth one. Fluctuations of the conversion factors introduce a low systematical uncertainty, i.e., a flat normalized response at a given set of influence quantities. In this case, the influence quantity is the mean photon energy of the reference field. A small systematic uncertainty for the energy dependence potentially results in a potential instability regarding changes in ambient conditions, i.e., temperature. No difficulties with such conversion factors are expected since the gradients between conversion factors are typically not extensive, and the dose is always calculated as the combination of three detectors. This increases the overall stability of dose reconstruction. Further investigations into this must be performed in the future. The best-determined set of conversion factors is the minimum deviation of the response to one.

The input conversion factors for the small pixels are identical to the ones used in [37]. Those conversion factors were determined by inter-calibration to the response of the large pixels. The optimization routine of the conversion factors is the same as for the large pixels. The difference to the measurements in [37] is the orientation of the detector axis, which is vertical and is horizontal for these measurements. $H_\mathrm{p}(3)$ is not investigated in [37], which is why the conversion factors of $H_\mathrm{p}(0.07)$ are used as input. This assumption is viable as the conversion coefficients are similar for both dose quantities and publications into the monitoring of the eye lens suggested that in pure photon fields, dosemeters measuring the $H_\mathrm{p}(0.07)$ are viable [86]. Here, the constraints on the fit are a lower boundary of 0.1 times the initial conversion factor in the particular energy bin and an upper boundary of 1 µSv.

Figure 4.5 shows the optimized conversion factors for the large and the small pixels for the different personal dose equivalents, which are used to determine the dose measured by the Dosepix dosimetry demonstrator in the following.

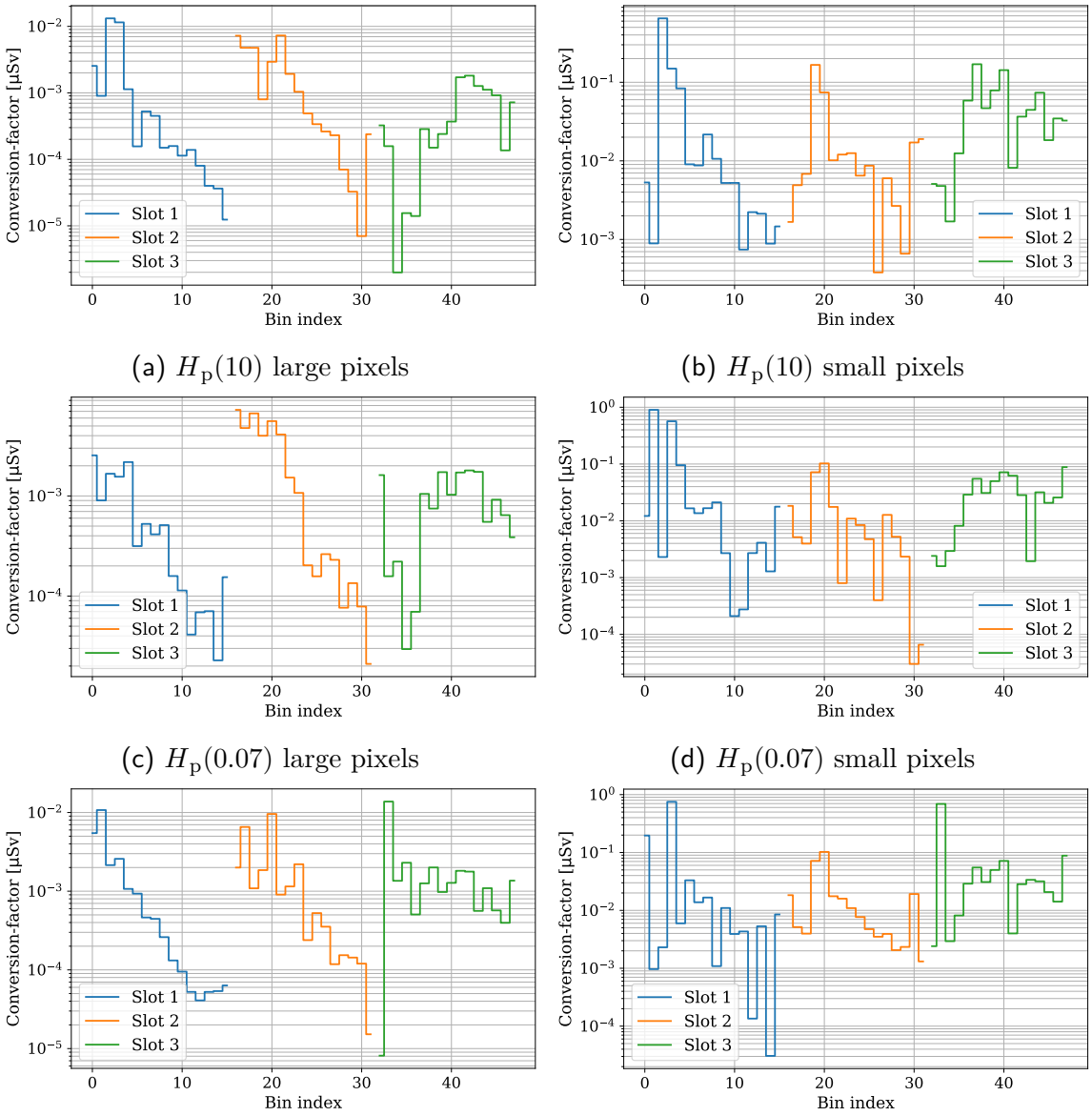

(a) $H_p(10)$ large pixels

(b) $H_p(10)$ small pixels

(c) $H_p(0.07)$ large pixels

(d) $H_p(0.07)$ small pixels

(e) $H_p(3)$ large pixels

(f) $H_p(3)$ small pixels

Figure 4.5.: Conversion factors between total number of registered events per energy bin measured by Dosepix and the personal dose equivalents $H_p(x)$ in units of [µSv]. The variable x denotes the depth in mm in the ICRU 4-element tissue. The conversion factors are displayed for the large and the small pixels.

4.3.4. Results and Discussion

The combined influence of dependence of the normalized response on the mean photon energy and the angle of radiation incidence is determined for the personal dose

equivalents $H_p(10)$, $H_p(3)$, and $H_p(0.07)$. The reference radiation quality is S-Cs with a photon energy of 662 keV, and the reference angle of radiation incidence is 0 °. The energy and angular dependence of the normalized response for the different personal dose equivalents is shown in Figure 4.6 for the large and the small pixels. A flat normalized response is observed for 0 ° angle of radiation incidence across the complete energy range from mean energies of 12.4 keV to 1250 keV. Fluctuations arise for $H_p(3)$ and $H_p(0.07)$ below 24.6 keV due to the definition of the dose as shown in Figure 4.2. At those energies, the applied dose is much higher than for $H_p(10)$ because a higher dose is deposited in depths of 3 mm and 0.07 mm compared to 10 mm. The entries at these energies are in the low-energy bins. This is compensated by other bins, resulting in the response fluctuation. The increase in the reference dose is not compensated by adjusting the Dosepix conversion factors without impairing the response for higher energies as the event rate stays constant even though the reference dose increases for the different dose equivalents. At S-Co, all dose quantities decrease in their normalized response due to the larger energies that have a reduced detection efficiency in the 300 µm thick silicon sensor. Additionally to this, the secondary electron track lengths exceed the pixel volume due to the large energy, i.e., not the complete energy is deposited in the pixel. The influence of the dose definition is especially shown for an increasing angle of radiation incidence. The impact is in accordance with the increase of the reference dose (see Figure 4.2(a)). In regards to the angle of radiation incidence, the personal dose is overestimated for the $H_p(10)$. It is explained by the decreasing value of the conversion coefficients from air kerma to $H_p(10)$ with larger angles of radiation incidence. Lower values of conversion coefficients require an increase of the tube current to yield a constant reference $H_p(10)$. Increasing the tube current means a linear proportional increase of the photon fluence. Dosepix's conversion factors between the number of registered events and a personal dose equivalent of interest are determined for 0 ° angle of radiation incidence. The increase of the event rate in the energy histograms under angular irradiation is not compensated by the conversion factors as it is the case for the definition of the air kerma to $H_p(10)$ conversion coefficients. The normalized response is therefore overestimated for $H_p(10)$ for $R_{Norm}(\alpha)$, with $|\alpha| > 0$ °. Between the values of the normalized response for ±60 ° only small deviations are observed, demonstrating the setup's symmetry. The angular dependence of the $H_p(3)$ and $H_p(0.07)$ is mainly driven by the dose definition. If the reference dose increases due to the conversion coefficients between dose equivalent and air kerma, a decrease of the normalized response is observed as the number of events in Dosepix's energy histogram does not increase according to the dose definition. The small increase in the number of events is insufficient to counteract the dose definition, and such behavior is not compensated for as no angle-dependent conversion factors exist.

Figure 4.7 depicts the number of registered events in each slot of each pixel type for different angles of radiation incidence. Slot 1 measures no significant difference in its number of counts per radiation quality for different angles of radiation incidence. The idea behind Slot 1 is the reproduction of the angular dependence of $H_p(10)$. Therefore, the hole above the sensor will not absorb any radiation at a photon field

direction parallel to the reference axis of the Dosepix dosimetry demonstrator. Under angular irradiation, parts of the radiation field are attenuated by the foil on top of the aluminum cylinder around the detector. The attenuation is sufficient to hold the number of registered events at a constant level compared to 0° angle of radiation incidence. The situation is different for Slot 2 where an increase of the number of registered events at low energies for angular irradiation is observed. The filter cap is not sufficiently thick on the sides to replicate the $H_p(10)$ angular dependence. Due to this, an overestimation of the response for $H_p(10)$ is observed. Slot 3 shows a nearly constant event rate across the different angles of radiation incidence. Its filter-cap is sufficiently designed to compensate the angular dependence of $H_p(10)$.
The key parameters such as the minimum and maximum values of R_{Norm}, the mean normalized response, and its standard deviation are summarized in Table 4.3. All dose quantities are sufficiently well covered by the large pixels with low maximum deviations from a response of 1. The dose determination with the small pixels corresponds to the large pixels with the difference of higher fluctuations and uncertainties. In summary, the rated range of use for the different dose quantities is equal for the large and small pixels for angles of radiation incidence between ±60 °. They are determined as 12.4 keV to 1250 keV for the $H_p(10)$, 20.3 keV to 1250 keV for the $H_p(3)$, and 24.6 keV to 1250 keV for the $H_p(0.07)$.
Figure 4.8 shows the relative statistical uncertainty F_{stat} in dependence of the energy for the large and small pixels. Additionally, the coefficient of variation $v = \mu/\sigma$ of the measured dose is looked into for the radiation qualities N-300 and S-Co. The number of measurements is 10. F_{stat} is below 1 % for all data points of the large pixels and shows no differences for the variation of the angle of radiation incidence, and below 4% all data points for the small pixels for the $H_p(10)$ and below 5% for the remaining two dose equivalents. The results for $H_p(3)$ and $H_p(0.07)$ show a larger F_{stat} and a lower coefficient of variation at N-300 than for $H_p(10)$. The reason for this must be in the chosen set of conversion factors since the measurement data is identical. This behavior is seen for both $H_p(3)$ and $H_p(0.07)$ since their input conversion factors are the same. Further measurements are needed to optimize better sets of conversion factors for $H_p(3)$ and $H_p(0.07)$ which will resolve the precise reason for this discrepancy. At S-Co a much larger coefficient of variation is determined for $H_p(0.07)$ and $H_p(3)$ which is attributed to the large values of several conversion factors in high energy bins. Statistical fluctuation of the number of registered events is amplified by these high conversion factors which increases the coefficient of variation. Without the data points at N-300 for $H_p(3)$ and $H_p(0.07)$, the coefficient of variation v is slightly larger than F_{stat}. The explanation for this is taken from [20]. A larger v means that the real statistical uncertainty is larger than the calculated uncertainty assuming a Poisson uncertainty and independence of the event rate among the pixels. This assumption is slightly incorrect due to charge sharing among the pixels in Dosepix. As stated in Chapter 2, charge sharing describes the process of the distribution of charge carriers created by one ionizing particle among several pixels due to hole diffusion and repulsion and sufficiently large primary electron track lengths. It means that one incident photon triggers several pixel hits incorrectly, inflating the event

rate. This results in an amplification of the statistical uncertainty in the number of registered events and, consequently, an increased statistical uncertainty of the calculated dose. The multiplicity is significantly involved in the increase of uncertainty. The multiplicity is defined as the number of pixels triggered by one primary particle [87]. It is energy-dependent and increases with the photon energy. In summary, the relative statistical uncertainty F_{stat} does overall underestimate the coefficient of variation v. The ratio between the two is not too large. Therefore, it is possible to use F_{stat} as an approximation of v by using a conservative global multiplicity of 1.45 for the large and 1.75 for the small pixels for mean energies larger than 250 keV. Both values depend heavily on the set of conversion factors which explains the large spread of the ratio between the personal dose equivalents of a pixel type. Overall, the coefficient of variation and F_{stat} as its approximation are within according to [69].

Personal dose equivalent	α [°]	Pixel size [µm]	Min.	Max.	µ	σ
$H_{\mathrm{p}}(10)$	0	55	0.780±0.036	1.082±0.044	0.993	0.063
		220	0.960±0.008	1.011±0.007	0.998	0.011
	30	55	0.809±0.038	1.070±0.039	0.990	0.063
		220	0.934±0.007	1.082±0.006	1.014	0.035
	+60	55	0.762±0.035	1.335±0.045	1.118	0.147
		220	0.916±0.007	1.169±0.007	1.082	0.071
	-60	55	0.746±0.035	1.455±0.049	1.147	0.167
		220	0.923±0.007	1.179±0.007	1.096	0.070
$H_{\mathrm{p}}(3)$	0	55	0.773±0.049	1.084±0.063	0.977	0.071
		220	0.915±0.007	1.048±0.005	0.990	0.031
	30	55	0.787±0.035	1.105±0.059	0.942	0.082
		220	0.853±0.004	1.018±0.006	0.971	0.044
	+60	55	0.275±0.013	1.081±0.059	0.877	0.212
		220	0.249±0.002	1.034±0.006	0.883	0.216
	-60	55	0.269±0.013	1.143±0.066	0.895	0.226
		220	0.247±0.002	1.048±0.006	0.893	0.221
$H_{\mathrm{p}}(0.07)$	0	55	0.809±0.047	1.118±0.054	1.002	0.067
		220	0.910±0.006	1.068±0.005	0.993	0.036
	30	55	0.680±0.026	1.160±0.054	0.953	0.116
		220	0.765±0.004	1.024±0.005	0.970	0.066
	+60	55	0.148±0.006	1.186±0.057	0.859	0.282
		220	0.141±0.001	1.077±0.005	0.855	0.269
	-60	55	0.143±0.006	1.181±0.059	0.867	0.297
		220	0.141±0.001	1.096±0.005	0.862	0.277

Table 4.3.: Response normalized to S-Cs at 0°, R_{Norm}, for the different personal dose equivalents and angles of radiation incidence α. The key parameters are minimum and maximum R_{Norm} values, mean R_{Norm} µ, and its standard deviation σ.

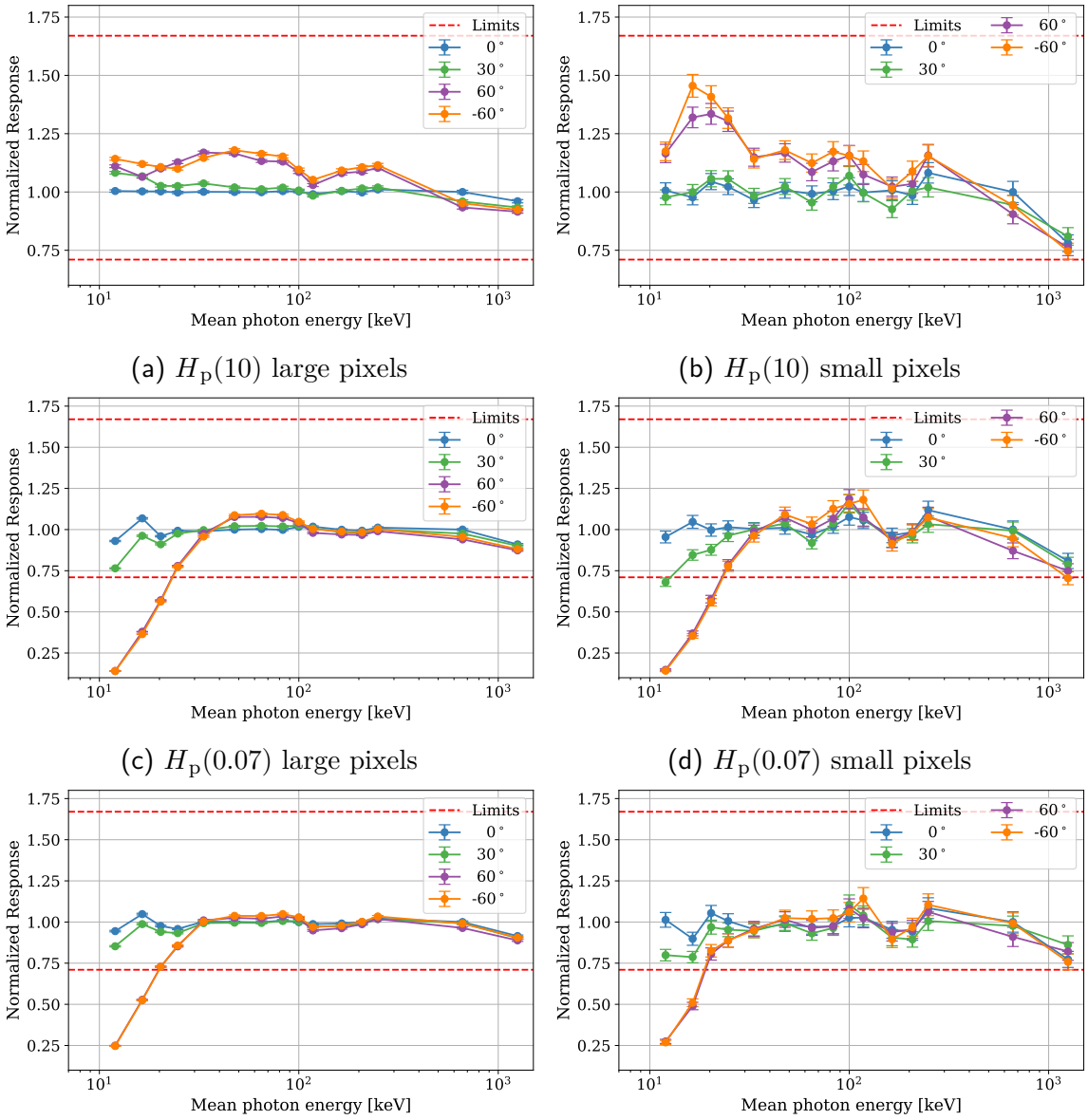

(a) $H_p(10)$ large pixels

(b) $H_p(10)$ small pixels

(c) $H_p(0.07)$ large pixels

(d) $H_p(0.07)$ small pixels

(e) $H_p(3)$ large pixels

(f) $H_p(3)$ small pixels

Figure 4.6.: Energy and angular dependence of the normalized response R_{Norm} for different dose equivalents for the large and the small pixels. (a) and (c) are already published in [82]. The red dashed lines indicate the national and international legal limits stated in PTB-A 23.2 and its complement [83, 69], and IEC 61526 [84]. The used angles of radiation incidence are 0°, 30°, ±60°.

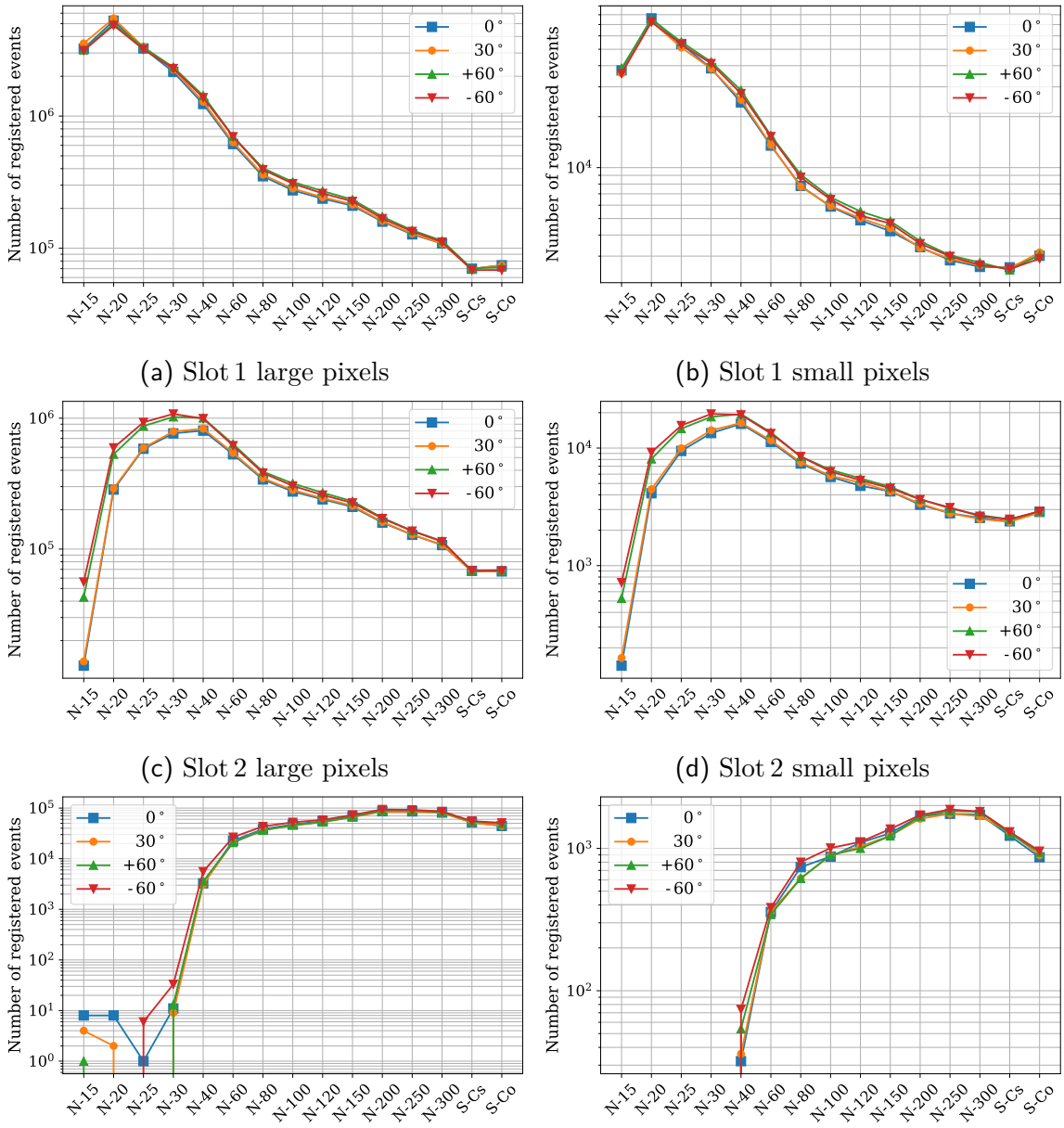

(a) Slot 1 large pixels

(b) Slot 1 small pixels

(c) Slot 2 large pixels

(d) Slot 2 small pixels

(e) Slot 3 large pixels

(f) Slot 3 small pixels

Figure 4.7.: Energy dependence of the total number of registered events for the different detectors, pixel types and angles of radiation incidence. The used angles of radiation incidence are 0°, 30°, ±60°.

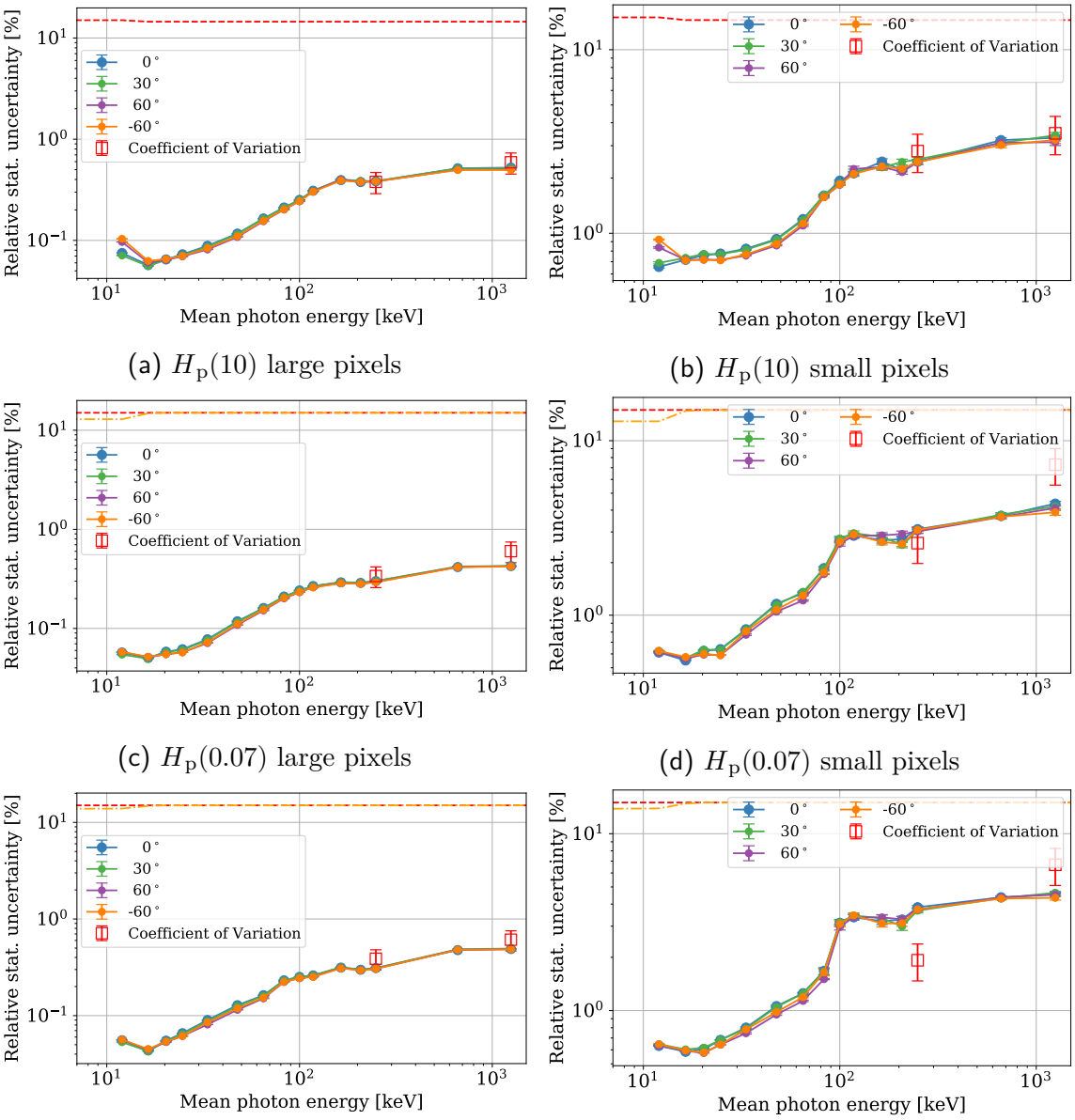

(a) $H_p(10)$ large pixels

(b) $H_p(10)$ small pixels

(c) $H_p(0.07)$ large pixels

(d) $H_p(0.07)$ small pixels

(e) $H_p(3)$ large pixels

(f) $H_p(3)$ small pixels

Figure 4.8.: Energy and angular dependence of the relative statistical uncertainty F_{stat} for different personal dose equivalents for the large and small pixels. (a) and (c) are already published in [82]. The red dashed line indicates the legal limits stated in PTB-A 23.2 and its complement [83, 69]. For the radiation qualities N-300 and S-Co the coefficient of variation is calculated for 10 measurements, which is indicated by the red square markers.

Personal dose equivalent	Pixel size [µm]	Radiation quality	F_{stat} [%]	v [%]	Ratio
$H_{\text{p}}(10)$	55	N-300	2.456 ± 0.076	2.802 ± 0.661	1.141 ± 0.271
		S-Co	3.313 ± 0.128	3.503 ± 0.827	1.057 ± 0.253
	220	N-300	0.384 ± 0.002	0.379 ± 0.090	0.988 ± 0.233
		S-Co	0.524 ± 0.002	0.592 ± 0.140	1.130 ± 0.267
$H_{\text{p}}(3)$	55	N-300	3.837 ± 0.087	1.926 ± 0.454	0.502 ± 0.119
		S-Co	4.541 ± 0.120	6.678 ± 1.580	1.471 ± 0.350
	220	N-300	0.311 ± 0.002	0.388 ± 0.092	1.250 ± 0.295
		S-Co	0.489 ± 0.002	0.611 ± 0.144	1.249 ± 0.294
$H_{\text{p}}(0.07)$	55	N-300	3.109 ± 0.075	2.589 ± 0.611	0.833 ± 0.197
		S-Co	4.356 ± 0.127	7.291 ± 1.727	1.674 ± 0.400
	220	N-300	0.301 ± 0.001	0.338 ± 0.080	1.123 ± 0.265
		S-Co	0.426 ± 0.001	0.603 ± 0.142	1.416 ± 0.334

Table 4.4.: Relative statistical uncertainty F_{stat}, coefficient of variation v, and their ratio. The measured reference photon fields are N-300 and S-Co. All uncertainties are calculated by using Equation (3.7) and Equation (3.9).

4.4. Influence of Beta-Radiation Fields

Indirect ionizing particles, such as photons, need to interact with a converter material, e.g., the silicon sensor of Dosepix, to deposit their energy. As described in Chapter 2, the possible interactions in the X-ray regime are the photoelectric effect and Compton-scattering. Both interactions transfer energy to a directly ionizing particle, i.e., an electron that provides a signal to the readout electronics as a measure of the deposited energy. If a radiation field consists of electrons with sufficiently high energy to penetrate the air between the source and dosemeter and additionally the dosimeter housing and the filter-caps, these electrons will result in a signal in the detector. Usually, photon fields are accompanied by electrons that induce an interfering contribution in a photon dosemeter when passing through at least one of the detectors unless adequately shielded. Therefore, personal dosemeters for photon radiation fields must be as unresponsive as possible to electrons. Consequently, measurements of the influence of electrons on the photon dose indication are required to determine this interfering influence.

4.4.1. Methods and Materials

Reference radiation fields consisting of electrons are created by radionuclides undergoing β^--decay for the following investigations. The β-radiation sources ^{147}Pm, ^{85}Kr, ^{90}Sr/^{90}Y, and ^{106}Ru/^{106}Rh, in the following also mentioned as β reference fields according to ISO 6980-1 [85], are used at PTB's facility for β-radiation BSS2 (**B**eta

Secondary **S**tandard **2**). Information about key characteristics regarding BSS2 is taken from [88, 89] and summarized in the following.
Figure 4.9 illustrates the complete setup at BSS2. The β-radiation source (a) is placed with a closed shutter in its holder. The sources are enclosed in a stainless-steel case, and their built-in shutter is opened during the irradiations. Energy loss in air requires calibration at fixed distances of 11 cm, 20 cm, 30 cm, and 50 cm. These calibrations are performed with and without a beam flattening filter (b). Such a beam flattening filter establishes a flat depth dose distribution and is placed between the source and the Dosepix dosimetry demonstrator. It is barely visible on the photograph due to its transparent material. It is made of polyethylenterephtalate and fixed to eyelets by nylon wires. The Dosepix dosimetry demonstrator (d) is placed on an electron replacement phantom (c) with dimensions of 200 mm × 200 mm × 20 mm (according to ISO 6980-3 [90]) instead of the ISO water slab phantom.

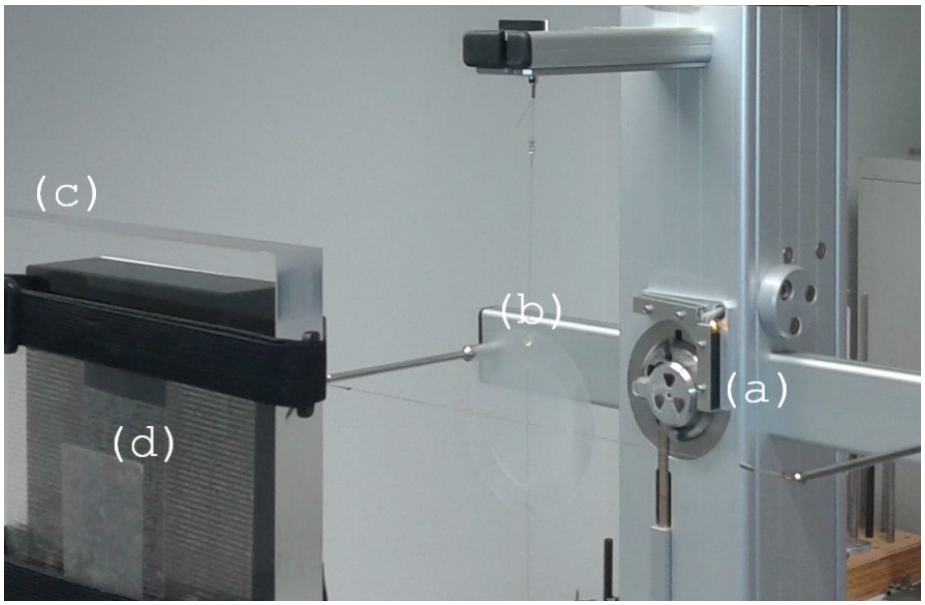

Figure 4.9.: Photograph of the BSS2 setup. The β-radiation source (a) sits in a holder. A control mechanism opens its shutter when irradiations are performed. The beam flattening filter (b) is fixed by nylon wires to eyelets. It is barely visible as it is transparent. The dosemeter housing (d) is placed on a phantom (c) with dimensions of 200 mm × 200 mm × 20 mm according to ISO 6980-3 [90].

Table 4.5 states the source distances and reference dose values for the $H_{\mathrm{p}}^{\mathrm{ref}}(0.07)$ for electrons. The source distance denotes the distance between the reference point of the dosimetry demonstrator and the source. As before, the reference position of the Dosepix dosimetry demonstrator is the sensor's surface of the detector of Slot 2. Figure 4.10 shows the β and photon contributions of the absolute fluence spectra at reference distance impinging onto the dosimetry demonstrator [88, 91].
The 1.5 mm thick white ABS plastic cover is modified by a hole above Slot 1 to

investigate β dosimetry. This hole is covered with 25 µm thick polyamide foil. The modified ABS cover is called the β window in the following. One measurement with and one without the β window are performed. The concept of a β window is well known in dosimetry: For example, the EPD Mk2 utilizes differently filtered PIN diodes for photon dosimetry and another one covered with a foil acting as β window for dosimetry of the skin dose $H_\mathrm{p}(0.07)$ for β radiation [92]. Covering the electron entry window with a polyamide foil is necessary as dosemeters must be dust- and water-tight. Electrons of up to on average 600 keV are fully stopped by the 1.5 mm ABS cover of the housing of the Dosepix dosimetry demonstrator [93]. Its cover equipped with a β window allows lower-energy electrons to reach the detector's uncovered silicon sensor as their energy loss in the foil is not substantial. It enables the study of the energy deposition spectra of β-radiation sources in Dosepix, which in turn allows investigations regarding dosimetry of the personal dose equivalent $H_\mathrm{p}(0.07)$ for electrons of β reference fields.

Radionuclide	Source distance [cm]	Mean β energy [MeV]	$H_\mathrm{p}^\mathrm{ref}(0.07)$ [mSv]
^{147}Pm	20	0.071	0.1
^{85}Kr	30	0.254	1
^{90}Sr/^{90}Y	30	0.806	1
^{106}Ru/^{106}Rh	20	1.159	0.1

Table 4.5.: Radionuclides utilized for measurements at BSS2, their source distance, and reference electron dose $H_\mathrm{p}^\mathrm{ref}(0.07)$. The source distance denotes the distance between the reference point of the Dosepix dosimetry demonstrator and the β radiation source. Additionally, the mean β energy is stated.

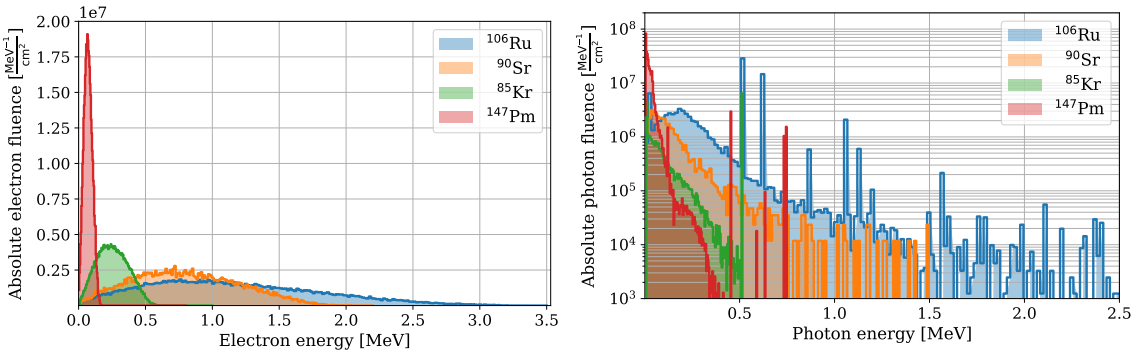

(a) β spectrum

(b) Photon spectrum

Figure 4.10.: Incident reference fields at PTBs BSS2 for a reference dose of 1 mSv, separated into the spectra of the incident β-particles (a), and the photon contribution from Bremsstrahlung and γ-decay lines (b). The data is provided by courtesy of PTB's Rolf Behrens and is published in [88, 91].

4.4.2. Measurement Data

All recorded energy histograms are displayed in Figure 4.11 and Figure 4.12 for the large and small pixels, respectively. When using the β window, no significant differences are observed for Slots 2 and 3 compared to using the cover without β window as it is located above Slot 1. Slot 1 typically registers a number of events over a magnitude larger than Slot 2. The number of registered events for Slot 3 is small and several numbers of magnitude smaller than for Slot 1. For the small pixels - compared to the large ones - a much lower number of events is registered, especially in Slot 3. The shapes of the energy deposition spectra for the small pixels are skewed towards lower deposited energies due to the small pixel volumes. The following discussions are tailored to the large pixels. The small pixels are only mentioned when a dose is calculated to test the interfering influence.

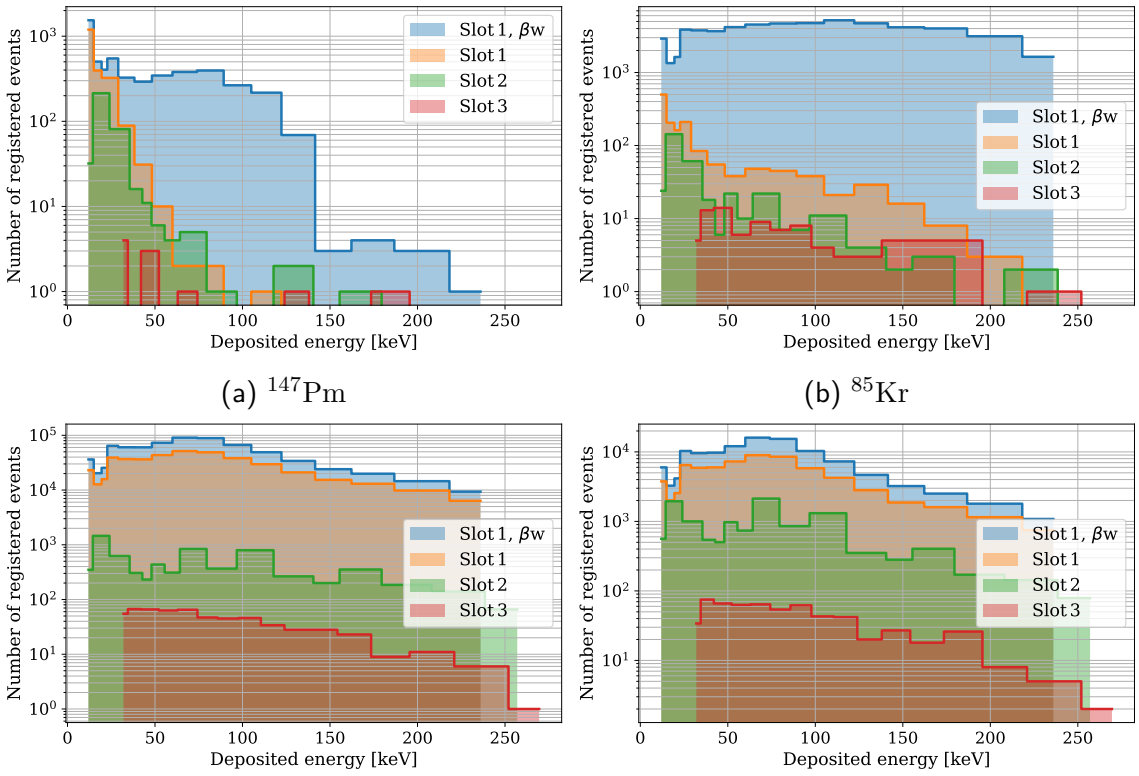

(a) ^{147}Pm (b) ^{85}Kr

(c) ^{90}Sr/^{90}Y (d) ^{106}Ru/^{106}Rh

Figure 4.11.: Energy histograms of the β reference fields at the BSS2 recorded in the Dosi-mode with the large pixels. Histograms for Slot 1 are shown with and without β window (βw). Histograms for Slot 2 and 3 are shown for the irradiation without β window.

Using the β window for ^{147}Pm allows the measurement of its deposition spectrum as the incident electrons have energies of up to 175 keV. These energies have a high

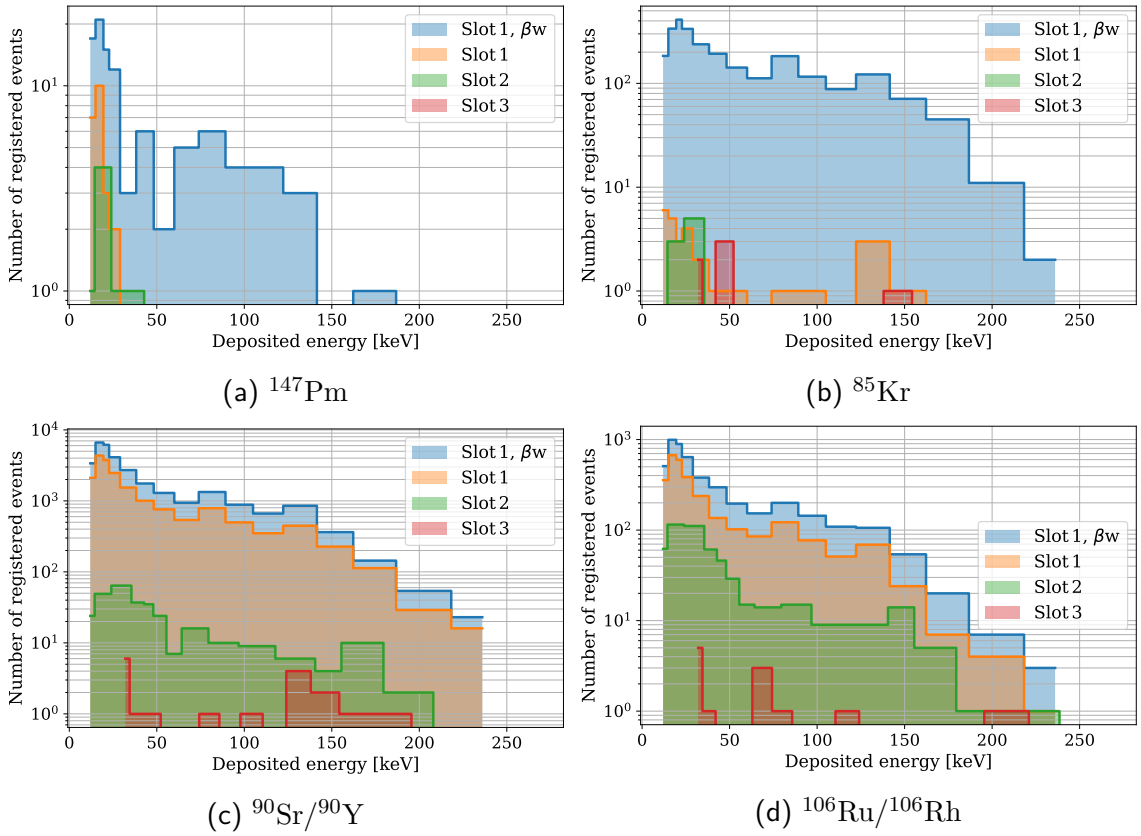

(a) ^{147}Pm (b) ^{85}Kr

(c) ^{90}Sr/^{90}Y (d) ^{106}Ru/^{106}Rh

Figure 4.12.: Energy histograms of the β reference fields at the BSS2 recorded in the Dosi-mode with the small pixels. Histograms for Slot 1 are shown with and without β window (βw). Histograms for Slot 2 and 3 are shown for the irradiation without β window.

chance of depositing their complete energy in the sensor volume. Its mean energy of the deposition spectrum coincides well with the one of the incident spectrum. The β radiation is fully stopped without the β window. ^{85}Kr shows small electron contributions above 50 keV without β window. The ABS cover does not fully stop all particles at the high energy tail and additionally Bremsstrahlung contributions emerging in the ABS cover are expected. Using the β window leads to a broad energy deposition spectrum. Energies of the corresponding reference field are within the range of energies fully stopped in the sensor volume (about 230 keV for a straight path through 300 µm silicon [93]). It, therefore, does not show a Landau distribution, which is characteristic for energy deposition of charged particles in thin materials, in the detector. ^{90}Sr/^{90}Y (mean energy of 0.806 keV) and ^{106}Ru/^{106}Rh (mean energy of 1.159 keV) show both a Landau distribution with a large tail in the energy deposition spectrum. When the β window is used, a larger number of events are registered for both reference fields compared to the unmodified ABS cover. Part of the electron field is deflected in the ABS cover and is no longer incident to the sensor element of Slot 1. The deflection is much less for the β window because of its smaller thickness.

Slots 2, and 3 detect events as the electron energies of both reference fields are now sufficient to penetrate the ABS plastic cover and the filter caps. Even though 1 mm tin and 2 mm aluminum should both stop electrons of up to about 1 MeV [93], a smaller number of registered events is observed in Slot 3. Again, the argument is deflection in the tin cap as its density is larger than the density of aluminum. Photon contributions are visible for ^{147}Pm and ^{85}Kr as the energy histograms Slots 1 and 2 coincide well for the irradiation without β window. The dominant photon contribution is for low photon energies. A lower number of events is registered as the photons are attenuated by the aluminum half-sphere of Slot 2. The photon contributions to the total measured dose are negligible for ^{147}Pm and ^{85}Kr since the number of registered events is small.

4.4.3. Results and Discussion

The personal dose equivalent $H_\mathrm{p}(10)$ is measured with the Dosepix dosimetry demonstrator for the β reference fields of BSS2. The measured dose is used to calculate the response to the reference electron dose $H_\mathrm{p}(0.07)$. The mean energies of the β spectra are used as a measure for the energy dependence of the response. The influence of the β reference fields on the photon dose indication of $H_\mathrm{p}(10)$ needs to stay below 10 % as a minimum requirement for irradiation with ^{90}Sr/^{90}Y according to [83], and subsequently, all sources with mean β energies below the mean energy of ^{90}Sr/^{90}Y. Figure 4.13 shows the ratio between the measured $H_\mathrm{p}(10)$ for photons and the reference electron dose $H_\mathrm{p}(0.07)$ in dependence on the mean β energy with and without β window for the large and small pixels. The interfering electron influence on large and small pixels show the same trend with the key difference that the influence on the dose indication is more severe for the large pixels.

The response to ^{147}Pm demonstrates a neglectable influence on the $H_\mathrm{p}(10)$ indication due to its small electron energies. Its electrons are fully stopped by the ABS plastic, and only a small number of events due to photon contributions are registered. Using the β window allows the measurement of the β radiation of ^{147}Pm with energies up to 175 keV. For both dosemeter covers, the contribution of the measured $H_\mathrm{p}(10)$ in relation to the reference $H_\mathrm{p}(0.07)$ of electrons is negligible.

The influence of ^{85}Kr stays below 10 % with the ABS cover while it exceeds the limit with a β window for the large pixels. As previously mentioned, the electrons with the energies of ^{85}Kr are predominantly stopped in 1.5 mm ABS. Without the β window, a significant amount of events is registered, resulting in a measurable influence.

The influences of ^{90}Sr/^{90}Y and ^{106}Ru/^{106}Rh on the $H_\mathrm{p}(10)$ photon indication are both above the limit of 10 %. The energies for both β reference fields are sufficient to penetrate the ABS plastic cover and deposit energy in the sensor element of Dosepix, especially in the uncovered Slot 1. Figure 4.14 shows the contribution to the total dose of each slot together with the angular dependence. The range of angles of radiation incidence is 0 ° to 75 ° for ^{90}Sr/^{90}Y and 0 ° to 60 ° for ^{106}Ru/^{106}Rh. Both sources

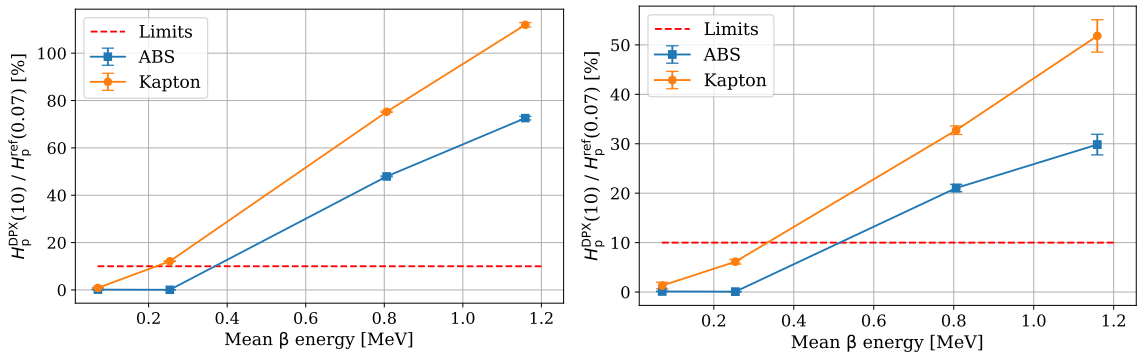

(a) Large Pixels

(b) Small Pixels

Figure 4.13.: Energy dependence of the electron influence on the photon dose indication of $H_p(10)$ for the large (a) and small pixels (b). The x-axes correspond to the mean energies of the β spectra of the β reference fields ^{147}Pm, ^{85}Kr, ^{90}Sr/^{90}Y, and ^{106}Ru/^{106}Rh at BSS2. The uncertainties denote the uncertainty on the measured dose divided by the reference dose. The red dashed line indicates the limit according to PTB-A 23.2 [83].

have a decreasing influence on the dose indication with increasing angle of radiation incidence. The reason is more material the electron has to traverse, which increases the amount of energy transferred to the dosemeter case and the aluminum cylinder surrounding the detector in Slot 1. The dominant contribution to the total dose stems from Slot 1 with the uncovered detector for both β-radiation sources.

The dose per bin is shown in Figure 4.15 for 0° angle of radiation incidence to investigate this further. Both pixel types are displayed. Since Slot 1 has the dominant contribution to the number of registered events. It also shows a dominant contribution to the measured dose. A contribution to the total dose is mainly observed in the energy bins below bin index 12, i.e., above the fourth energy bin. Two energy bins show a disproportional large dose contribution for the large pixels and three bins for the small pixels. It is attributed to the high value of their corresponding conversion factor, which are determined for photon fields. These decrease in their interaction probability with increasing photon energy, resulting in larger values of conversion factors for the high energy bins. The upper energy bins pose a problem as the influence exceeds the allowed limit of 10% for both pixel types. Improvements for the problems with the large influence due to β radiation are proposed and tested in the following. Every fix must be performed in a way that the changes do not impair dosimetry in photon fields.

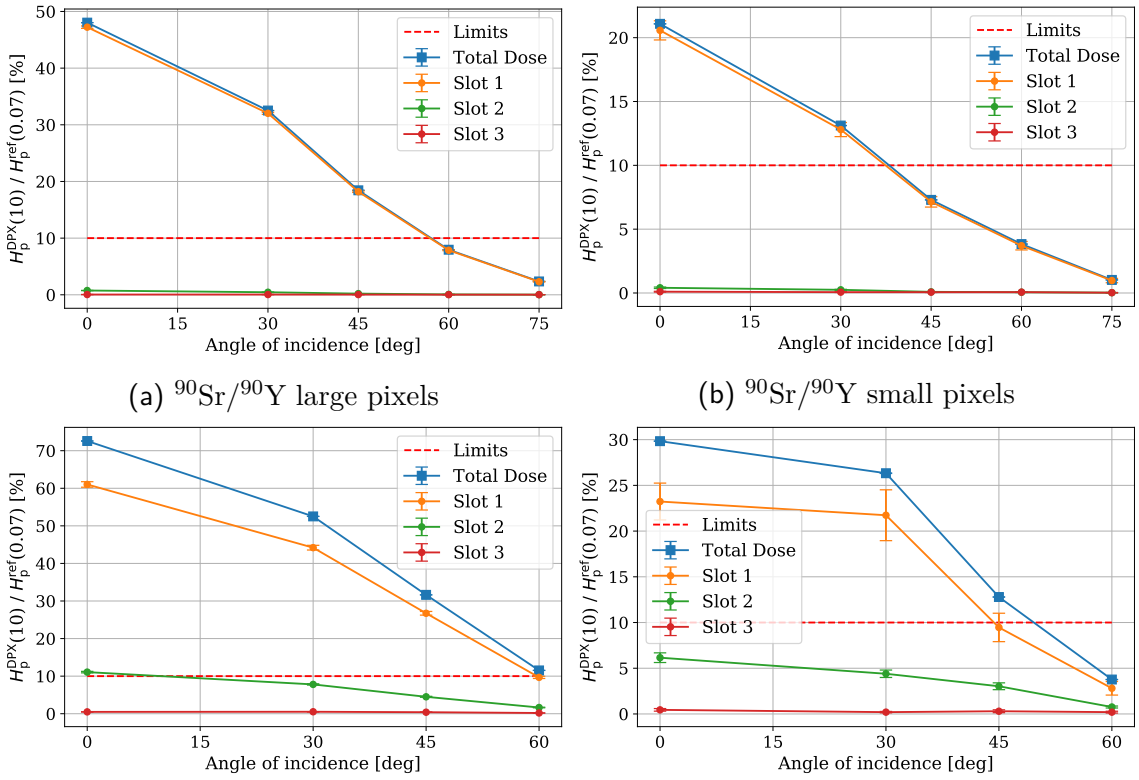

(a) ^{90}Sr/^{90}Y large pixels

(b) ^{90}Sr/^{90}Y small pixels

(c) ^{106}Ru/^{106}Rh large pixels

(d) ^{106}Ru/^{106}Rh small pixels

Figure 4.14.: Angular dependence of the electron influence on the photon indication of $H_p(10)$ for the large and small pixels for two β reference fields according to [85]. The reference dose $H_p^{ref}(0.07)$ for electrons is used to calculate the response. The response is divided into the individual response contributions of each slot. The red dashed line indicates the limit of 10% [83]. The share of the total dose measured by Slot 1 dominates the share of the total dose. Contributions of Slot 2 become non-negligible for ^{106}Ru/^{106}Rh due to its increased electron energies.

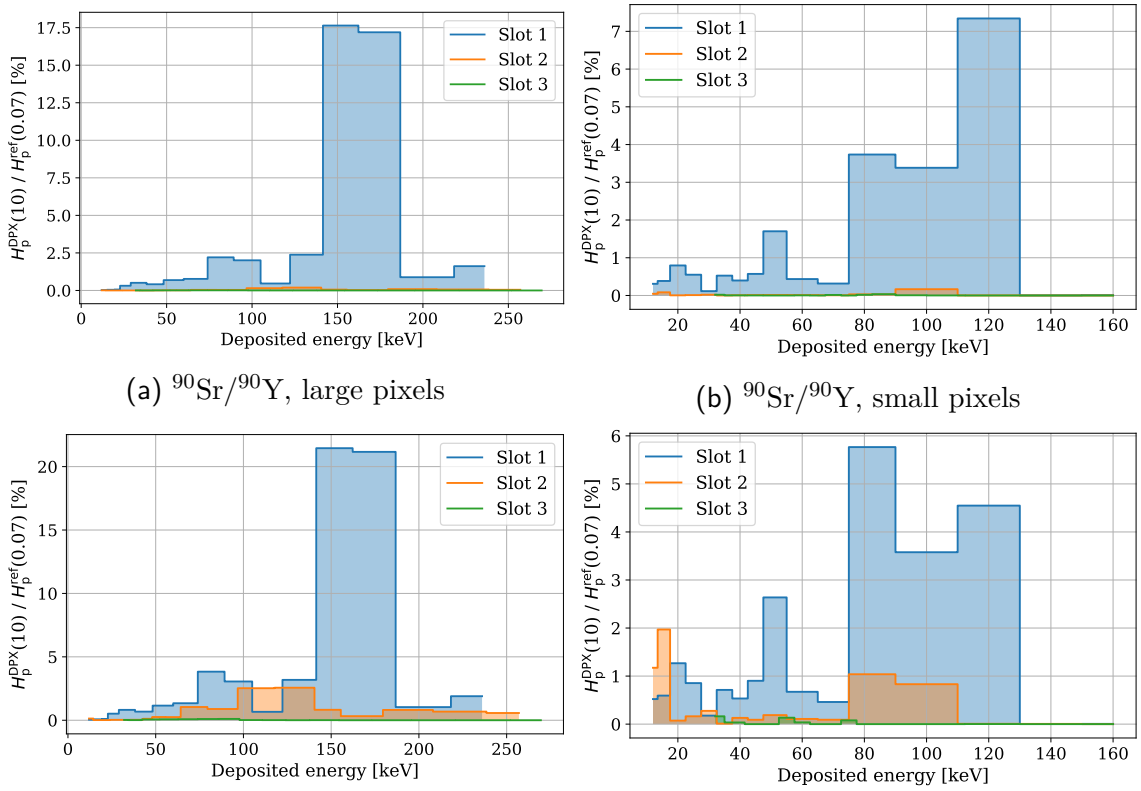

(a) ^{90}Sr/^{90}Y, large pixels

(b) ^{90}Sr/^{90}Y, small pixels

(c) ^{106}Ru/^{106}Rh, large pixels

(d) ^{106}Ru/^{106}Rh, small pixels

Figure 4.15.: Dose per bin for each slot for the large (a) and (c) and small pixels (b) and (d) and two β reference fields according to [85]. The reference dose for ^{90}Sr/^{90}Y is 1 mSv and 0.1 mSv for ^{106}Ru/^{106}Rh. Slot 1 registers a significantly larger number of events compared to the other slots, which corresponds to a dominant dose contribution for both pixel types. It is above 10% for both reference fields. In particular, two conversion factors for the large pixels and three for the small pixels yield a disproportionate large proportion to the total dose compared to the remaining energy bins.

Improving the electron influence

It is tested if the combination of Slots 2 and 3 is sufficient for photon dosimetry. In this case, Slot 1 might be completely omitted or re-purposed. The measurements with the β window showed a relatively high contribution to the photon dose by ^{85}Kr and an energy deposition spectrum recorded for the irradiation with ^{147}Pm that corresponds well to the incident spectrum. A possible idea for a dosemeter is to equip Slot 1 with a β window and to use it to measure the $H_\mathrm{p}(0.07)$ of electrons. Not using Slot 1 at all results in an influence of below 10% for ^{90}Sr/^{90}Y on the indication of the photon dose of $H_\mathrm{p}(10)$ below 10%. However, Slot 1 is beneficial for photon dosimetry as it shows dominant event rate contribution for X-ray energies below 30 keV.

Another idea is to set all conversion factors in Slot 1 above the fourth energy bin to zero, since the major part of the dose of ^{90}Sr/^{90}Y and ^{106}Ru/^{106}Rh stems from the energy bins above the fourth bin for the large pixels. The energy value of the bin edge of the fourth bin of Slot 1 is 24.5 keV for the large and 25 keV for the small pixels. Therefore, all conversion factors for the small pixels above the fourth bin are also set to zero. This allows consistency with the investigations of the large pixels. Using only the lower four bins of Slot 1 results in a change of the energy dependence of the response. Therefore, a new set of conversion factors is determined. It utilizes the measurements at facilities of PTB, that are shown in Section 4.3.2. The optimization follows the procedures described in Section 3.8 and utilizes a randomized approach as performed in Section 4.3.3. Figure 4.16 shows the adjusted conversion factors, the energy and angular dependence of the normalized response, and the relative statistical uncertainty F_stat together with the coefficient of variation v for radiation qualities N-300 and S-Co. Additionally, the key indicators of performance are shown in Table 4.6 for the response and Table 4.7 for F_stat and the coefficient of variation.

Personal dose equivalent	α [°]	Pixel size [µm]	Min.	Max.	µ	σ
$H_\mathrm{p}(10)$	0	55	0.812±0.072	1.057±0.066	0.998	0.060
		220	0.961±0.008	1.039±0.007	1.008	0.018
	30	55	0.777±0.067	1.093±0.068	1.000	0.076
		220	0.955±0.008	1.092±0.007	1.023	0.035
	+60	55	0.852±0.077	1.357±0.086	1.134	0.133
		220	0.985±0.009	1.220±0.008	1.090	0.067
	-60	55	0.911±0.087	1.459±0.093	1.181	0.140
		220	0.990±0.009	1.217±0.007	1.103	0.061

Table 4.6.: Response normalized to S-Cs at 0°, R_Norm, for $H_\mathrm{p}(10)$ for different angles of radiation incidence α with the modified conversion factors which reduce the electron influence. The key parameters are minimum and maximum R_Norm values, mean R_Norm µ, and its standard deviation σ.

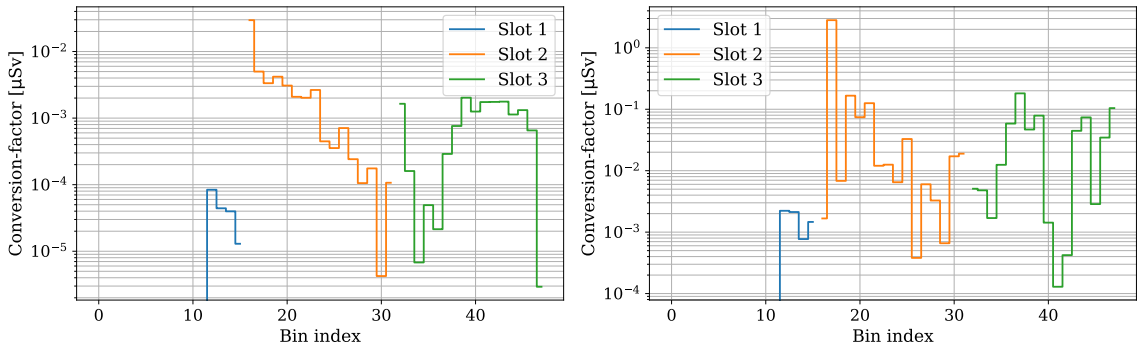

(a) Conversion factors large pixels

(b) Conversion factors small pixels

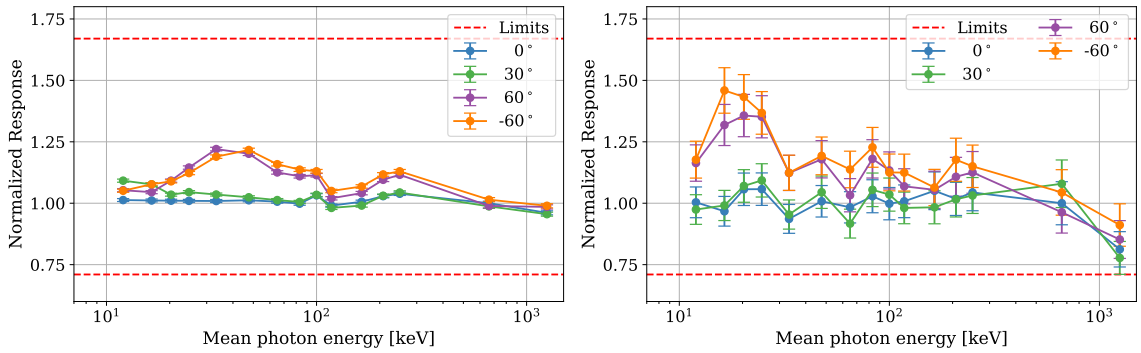

(c) R_{Norm} large pixels

(d) R_{Norm} small pixels

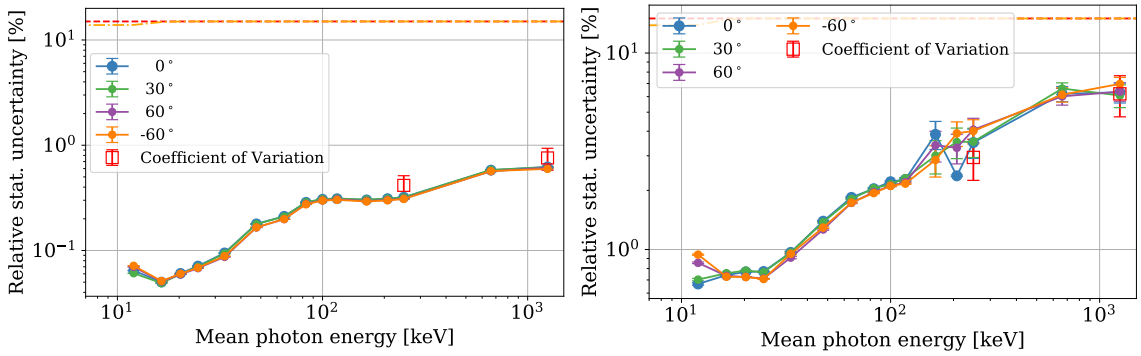

(e) F_{stat} and v large pixels

(f) F_{stat} and v small pixels

Figure 4.16.: Conversion factors for $H_{\mathrm{p}}(10)$ with a reduced number of energy bins in Slot 1 for the large (a) and small pixels (b), the corresponding energy and angular dependence of the normalized response (c) and (d), and the energy dependence of the relative statistical uncertainty F_{stat} together with two radiation qualities, N-300 and S-Co, for the coefficient of variation v for both pixel types in (e) and (f).

The normalized response is flat around one for both pixels types for 0 ° angle of radiation incidence. A systematic offset towards responses slightly higher than one is observed for the large pixels. As this occurs after normalization to S-Cs, it means that S-Cs shows an underresponse. This means that the lack of Slot 1 is not compensated to 100% at large mean photon energies. However, the small pixels remain in their response similar to the analysis with 48 conversion factors. Overall, the response is not significantly impacted by reducing the number of energy bins in the dose determination as the mean normalized response remains close to one and the corresponding standard deviation is not increasing significantly for the utilized measurements. Overall, a higher relative statistical uncertainty is observed due to the reduced event rate. It increases significantly for the small pixels. The coefficient of variation is above F_{stat} for the large pixels, where the ratio between both increases compared to using 48 conversion factors. Both quantities coincide within their uncertainties for the small pixels. In summary, the performance remains excellent but becomes slightly impaired compared to utilizing all 48 energy bins of the Dosepix dosimetry demonstrator, especially for the statistical uncertainties.

Personal dose equivalent	Pixel size [µm]	Radiation quality	F_{stat} [%]	v [%]	Ratio
$H_{\mathrm{p}}(10)$	55	N-300	3.503 ± 0.595	2.943 ± 0.700	0.840 ± 0.244
		S-Co	6.313 ± 0.744	6.201 ± 1.467	0.982 ± 0.260
	220	N-300	0.321 ± 0.001	0.416 ± 0.098	1.295 ± 0.305
		S-Co	0.622 ± 0.006	0.757 ± 0.178	1.217 ± 0.287

Table 4.7.: Relative statistical uncertainty F_{stat}, coefficient of variation v, and their ratio for $H_{\mathrm{p}}(10)$ with the modified conversion factors which reduce the electron influence. The measured reference photon fields are N-300 and S-Co. All uncertainties are calculated by using Equation (3.7) and Equation (3.9).

Now, the response for the electron reference fields is calculated utilizing the modified conversion factors. The energy dependence of the electron influence on the $H_{\mathrm{p}}(10)$ photon indication with modified conversion factors is shown in Figure 4.17. The influence of $^{90}\mathrm{Sr}/^{90}\mathrm{Y}$ is below 2% for the large pixels and below 3% for the small pixels. It is below the limit of 10%, which is in accordance with the requirements. The influence of $^{106}\mathrm{Ru}/^{106}\mathrm{Rh}$ still exceeds the limit. The angular dependence and the dose per slot are shown in Figure 4.18. Applying the new conversion factors results in a suppressed contribution of Slot 1. The dominant part of the dose stems from Slot 2 for the aforementioned reasons. β-radiation with energies above 1 MeV requires thicker aluminum to be fully stopped. The impact of Slot 2 is increased due to the modified conversion factors as they must compensate the omitted ones for Slot 1. Moreover, the contribution to the total dose of Slot 3 is negligible. Overall, omitting the upper twelve energy bins of Slot 1 fixes the influence of β radiation on the indication of $H_{\mathrm{p}}(10)$ via Dosepix. With this fix, the performance of the Dosepix

dosimetry demonstrator is in accordance with all tested PTB requirements with these improvements.

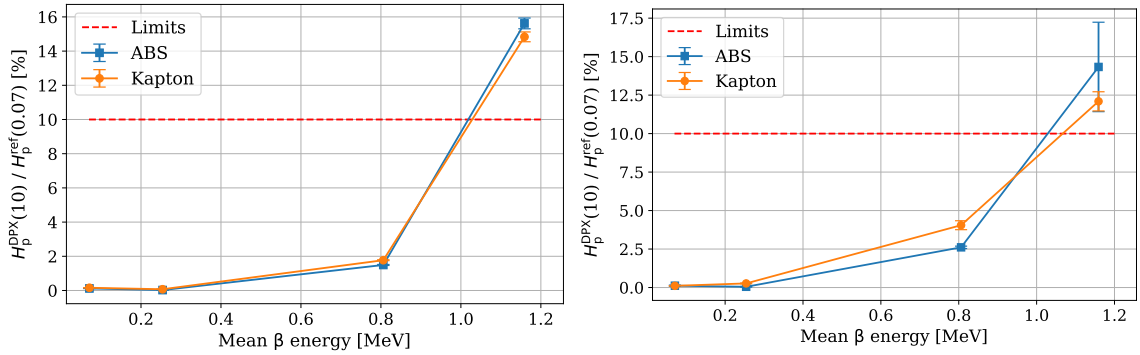

(a) Large pixels

(b) Small pixels

Figure 4.17.: Energy dependence of the electron influence on the photon dose indication of $H_p(10)$ for the large (a) and small pixels (b) with the modified conversion factors. The x-axes correspond to the mean energies of the β spectra of the β reference fields ^{147}Pm, ^{85}Kr, ^{90}Sr/^{90}Y, and ^{106}Ru/^{106}Rh at BSS2. The uncertainties denote the uncertainty on the measured dose divided by the reference dose. The red dashed line indicates the limit according to PTB-A 23.2 [83].

4.4.4. Branching Algorithm

If a whole body dosemeter comprised of three Dosepix detectors is intended to measure the personal dose equivalents $H_p(10)$, $H_p(0.07)$, and $H_p(3)$ for photons, and additionally the $H_p(0.07)$ for electrons, several changes must be made. Only Slot 2 and Slot 3 and the lower four energy bins of Slot 1 are used for photon dosimetry, as suggested and demonstrated earlier. Utilized conversion factors will depend on the application and the personal dose equivalent to be monitored. The highest 12 energy bins of Slot 1 are equipped with photon conversion factors with a value set to zero and are utilized for electron dosimetry. In order to achieve that, the housing cover has a hole above Slot 1 covered with a β window in form of a Kapton foil. The set of conversion factors for the electron dose is zero for all energy bins except the upper twelve energy bins of Slot 1. Only large pixels are investigated regarding the branching algorithm in the following.

A branching algorithm must be implemented to correctly use the conversion factors as the upper 12 energy bins will register events indifferent to the used conversion factors. Such an operation faces the challenge of preserving the dead-time-free measurement method, which requires no delays in the discrimination between a photon and an electron field. There will be no issues adding several operations to the event readout

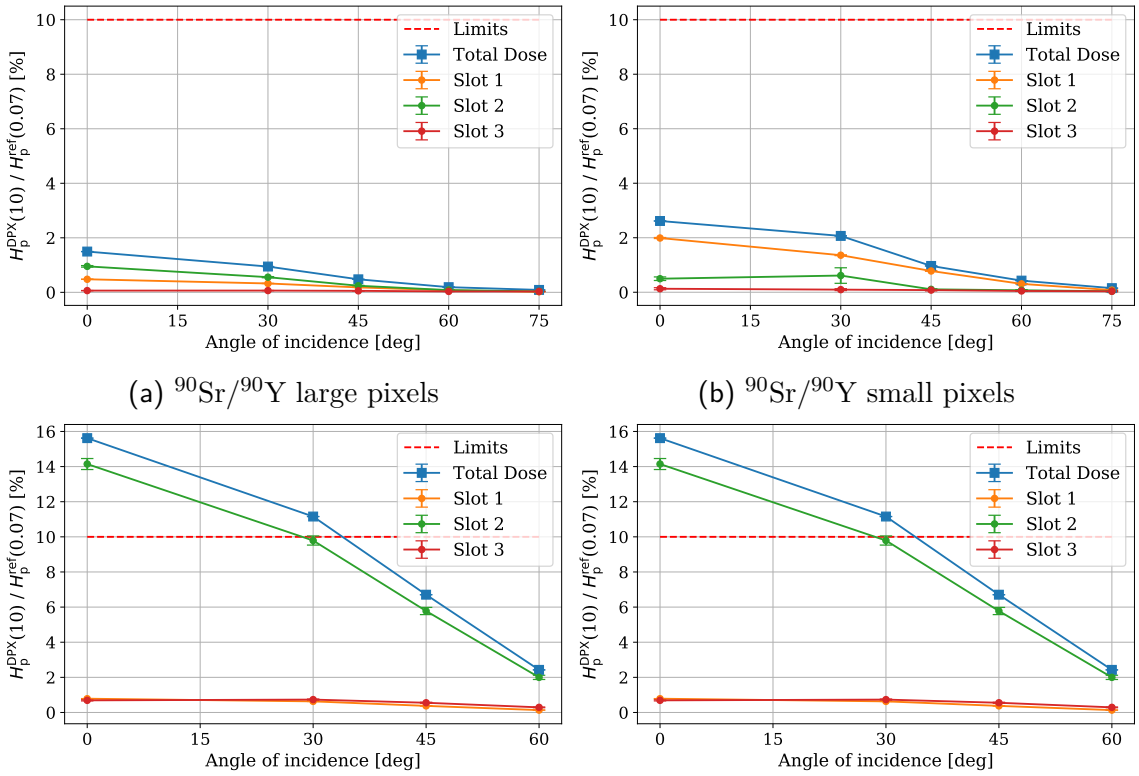

(a) ^{90}Sr/^{90}Y large pixels

(b) ^{90}Sr/^{90}Y small pixels

(c) ^{106}Ru/^{106}Rh large pixels

(d) ^{106}Ru/^{106}Rh small pixels

Figure 4.18.: Angular dependence of the electron influence on the photon indication of $H_p(10)$ for the large and small pixels for two β reference fields according to [85] with the modified conversion factors for Slot 1. The reference dose $H_p^{ref}(0.07)$ for electrons is used to calculate the response. The response is divided into the individual response contributions of each slot. The red dashed line indicates the limit of 10% [83].

before calculating the dose value. If the number of performed operations is low, the actualization of the current value of the personal dose equivalent is in the magnitude of seconds. It aims to determine a differentiation between radiation fields through a low number of mathematical operations. Determining the energy range of use for electron radiation fields is a rather sophisticated task. Since the detection volume of a Dosepix detector is finite, the maximum energy deposited to a Dosepix detector is limited. Electrons with energies above several MeV are not stopped by the 1.5 mm ABS plastic cover and the 2 mm thick aluminum or the 1 mm tin half-sphere filter caps. They will then deposit their energy in the sensor of the Dosepix detector and, if the energy is sufficient, leave the detection volume. The energy deposition spectra for such electrons look similar for all three Dosepix detectors utilized in the dosimetry demonstrator. It is found in the case of a photon field that the event rate for the three detectors converges to a similar value for mean photon energies above 200 keV, as previously shown in Figure 4.4. This observation is explained by the low interaction

probability of the photons with the filter caps, which are almost transparent (only around 6% of photons interact in the filter caps for photon energies of about 250 keV) for the aforementioned photon energies.

Understanding the key differences of the energy deposition spectra for photon and electron fields is necessary to determine conditions for a branching algorithm. At first, energy deposition spectra of the radionuclides ^{60}Co, ^{137}Cs, and ^{90}Sr/^{90}Y are compared to each other. They are recorded with Slot 1 via ToT-mode and are shown in Figure 4.19. All three spectra show energy depositions greater than 236 keV, which corresponds to the last energy bin edge of Slot 1 for the large pixels. The spectra between ^{90}Sr/^{90}Y and ^{60}Co are similar above 120 keV, where the one of ^{90}Sr/^{90}Y has a more concise Landau distribution than the one of ^{60}Co. The Landau distribution is characteristic for energy depositions by ionizing particles with high energies in thin sensor materials. It is centered at around 80 keV with a long tail to about 300 keV. Interaction of a ^{60}Co photon with an electron of the sensor material deposits its energy predominantly via Compton scattering to the interaction partner. The transferred are of several hundreds of kiloelectron volts. The Landau distribution is not as clear for ^{60}Co when compared to ^{90}Sr/^{90}Y. Since the track of the β particle emitted from the radiation source traverses the complete pixel volume, a distinct energy loss distribution is obtained. In the case of ^{60}Co, different interaction depths occur, which limits the track length and introduces a broader Landau distribution. ^{137}Cs has its Compton edge at 477.34 keV, which does not yield as high an energy contribution as the other two radionuclides. The transferred energy is not sufficient to result in a distinct Landau distribution in the recorded energy deposition spectrum.

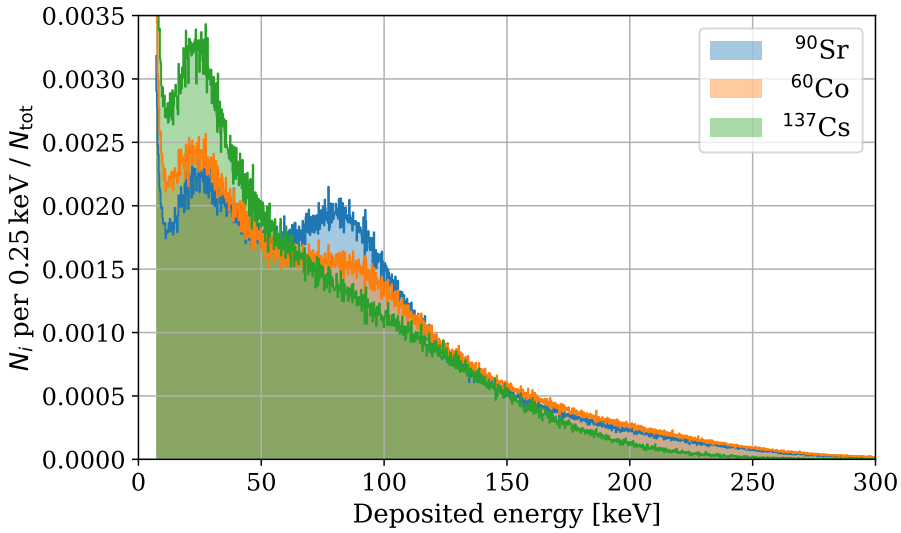

Figure 4.19.: Energy deposition spectra recorded in ToT-mode with Slot 1 for the radionuclides ^{90}Sr/^{90}Y, ^{60}Co, and ^{137}Cs for the larger pixels. Each number of events N_i in bin i of a width of 0.25 keV is normalized to the total number of events N_{Tot}.

Furthermore, the same radionuclides are used to record energy deposition spectra in the Dosi-mode for all three slots. Figure 4.20 shows the registered energy histograms. A critical difference of photon radiation is that the event rates of Slots 2 and 3 are in the same order of magnitude as in Slot 1. Slot 3 has typically a lower event rate since its threshold is higher. For ^{90}Sr/^{90}Y only Slot 1 shows a significant contribution to the total number of registered events. The filter caps only absorb a small percentage of photons of the incoming photon field, and most importantly, no beam hardening occurs for these energies. Consequently, all three detectors have the same impinging photon fields. The filter caps and the plastic cover are sufficient to stop the β radiation in a way that only a few particles impinge onto the sensor elements of Slots 2 and 3. Calculating the ratios of the total number of registered events between all three detectors will establish which radiation field is present. With these energy histograms, it is apparent that for photon fields the ratios $r_{2,1}$ and $r_{3,1}$ between the total number of registered events between Slots 2 and 1, and Slots 3 and 1 are much larger than for β radiation fields. Such discrimination is viable for β energies up to several MeV until the energy loss in the filter caps is insufficient to yield differences in the energy deposition spectra of the three detectors.

Photon fields must be differentiated between low-energy photon fields and ones with larger energies. Low-energy photon fields correspond to the measuring capabilities of Slot 1 as it obtains energy histograms for photon fields from 12 keV upwards. Compared to Slot 2, which also has its energy threshold at 12 keV, a larger event rate is observed in Slot 1 since the 2 mm aluminum beam harden the photon field. The ratio $r_{2,1}$ will be small. In the case of Slot 3, the ratio $r_{3,1}$ will also be small or even zero for those low-energy fields due to its energy threshold at 32 keV. This results in difficulties discriminating between low energy fields and electron fields. Therefore, another condition is needed to discriminate between both fields. To counteract the wrong classification of the radiation field, Slot 1 is used as a binary classifier to filter out low-energy photon fields. The number of registered events above certain energy (represented by the energy bin edge) is compared to the total number of registered events. This is called the ratio r_1 in the following. A low-energy photon field is assumed when the ratio is below a to be determined threshold. If it is above that threshold, either a photon or electron field is assumed. As the event rate between Slots 1 and 2 become similar for deposited energies greater 50 keV (see Figure 4.4), an upper limit for energy bin edge equal to that energy is viable for the threshold, which is represented via an energy bin in the following. Measurements for reference photon and β fields are used to determine ratios that allow correct classification of the particle type. Simulation data from [19] is used to validate the conditions for photons. Figure 4.21 shows the ratios for the reference fields in (a) and (b) together with dashed lines indicating the values for the ratios $r_1 = 15\%$, $r_{2,1} = 26\%$, and $r_{3,1} = 8\%$. They are determined for the measured ratios of the reference fields. The ratios of the simulation data in (d) show that a lower threshold of 22 keV is sufficient to classify the two types of photon fields correctly. The threshold bin of Slot 1 is set to the fifth bin, corresponding to 33.5 keV. Otherwise, N-25 is recognized as an electron

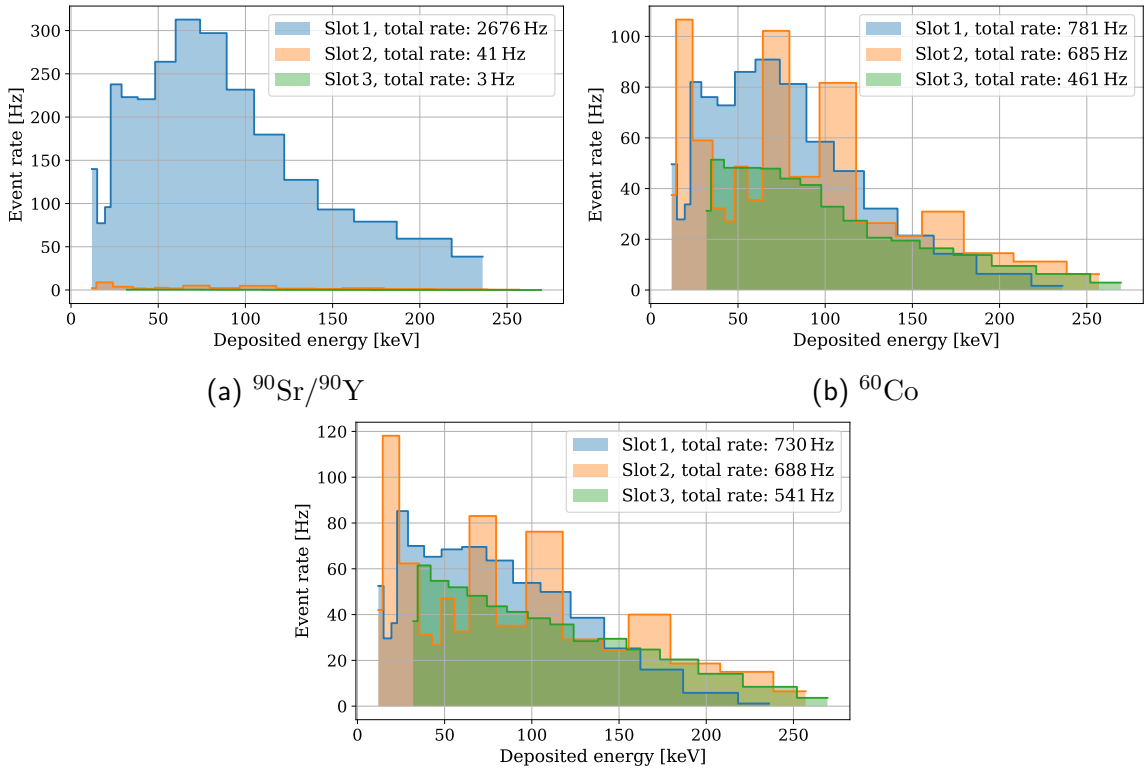

(a) ^{90}Sr/^{90}Y (b) ^{60}Co

(c) ^{137}Cs

Figure 4.20.: Energy deposition spectra recorded in the Dosi-mode for three different radionuclides. They are ^{90}Sr/^{90}Y (a), ^{60}Co (b), and ^{137}Cs (c). The registered number of events is normalized to the exposure time to yield the event rate. It is to be noted that different reference doses for different particle types are applied.

field, which is shown by choosing a threshold bin of 24.5 keV. It is also verified with the simulated data presented in (c). It also shows why setting the energy condition for Slot 1 is necessary as photon fields with energies below 20 keV satisfy the ratio conditions for $r_{2,1}$, and $r_{3,1}$ and would be classified as electron fields without the usage of r_1.

The complete process of the branching algorithm is illustrated in a flowchart in Figure 4.22. A branching algorithm categorizes the radiation fields into low-energy photon fields, photon fields, and electron radiation fields of mean energies larger than 71 keV. This energy corresponds to the mean value of the spectrum of the ^{147}Pm reference field. A low-energy photon field has a ratio $r_1 < 15\%$ in the scope of this analysis, while photon fields exceed the value. A threshold equal to 33.5 keV is chosen to calculate ratio r_1, which guarantees that low-energy photon fields are classified correctly. The threshold value limits the possible energy range of β radiation, which requires registered events with deposited energies greater than 33.5 keV to be classified

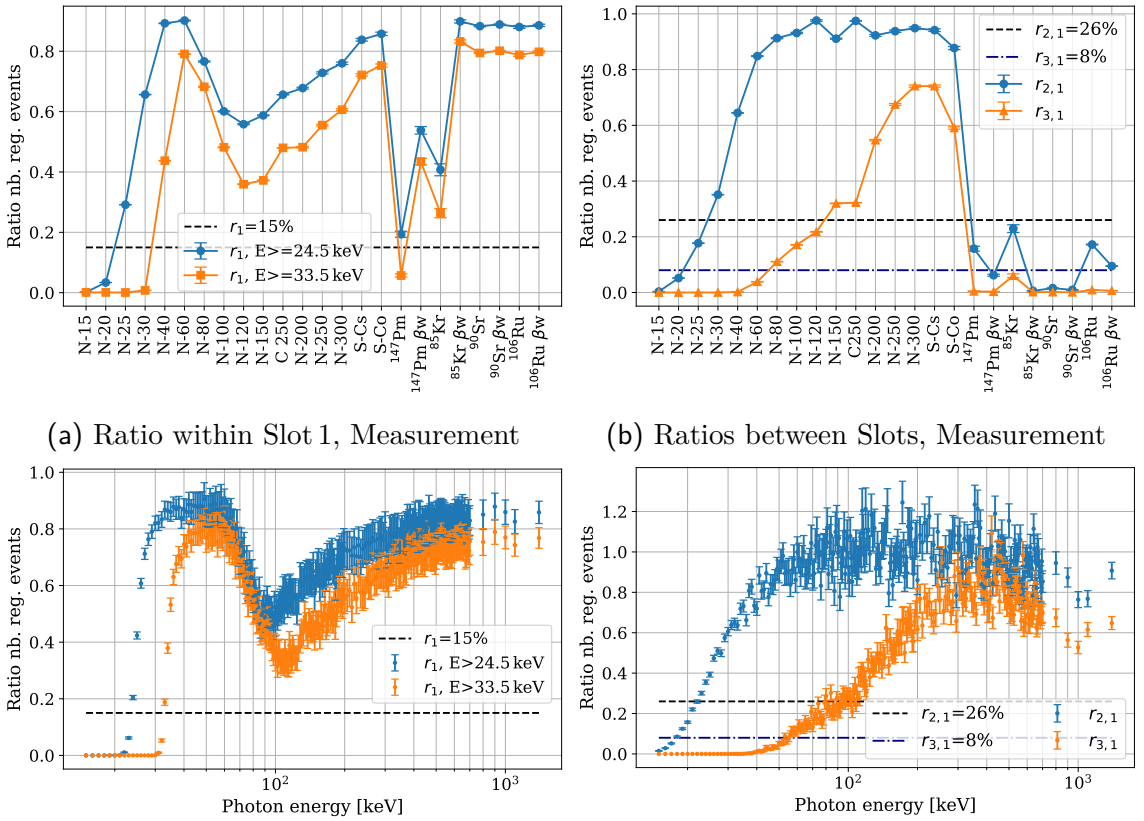

(a) Ratio within Slot 1, Measurement

(b) Ratios between Slots, Measurement

(c) Ratio within Slot 1, Simulation

(d) Ratios between Slots, Simulation

Figure 4.21.: Ratios of the number of registered events within Slot 1 above an energy threshold r_1, and Slots 2 and 1 $r_{2,1}$, and Slots 3 and 1 $r_{3,1}$. Those ratios are calculated for measurements of photon and electron reference fields according to ISO 4037-1 [67] and ISO 6980-1 [85] in (a), (b), and simulation data taken from [19] in (c),(d). The uncertainty bars denote the uncertainty propagation of the ratios, where Poisson statistics is assumed for the input number of registered events.

as an electron field. The target personal dose equivalents are $H_\mathrm{p}(10)$, $H_\mathrm{p}(0.07)$, $H_\mathrm{p}(3)$ for photons, and additionally the $H_\mathrm{p}(0.07)$ for electrons. It is assumed that the current stage in the flow of the dosemeter is a complete readout of all three detectors and that the dose value of the exposure is calculated next. Conversion factors for all four dose quantities are stored in the memory of the dosemeter. Before determining the appropriate dose equivalent, discrimination of the particle type of the incident radiation fields is necessary. The queries applied in the branching process to decide which conversion factors to use consist of the following conditions:

First, the combined number of registered events in the energy bins greater than 33.5 keV of Slot 1 are compared to the total number of registered events of the complete detector. It is assumed that either a photon or electron interacted in the

detector if $r_1 > 15\%$; otherwise, a low-energy photon field is present. In this case, conversion factors for a personal dose equivalent of interest are used to calculate the photon dose of the exposure, and the displayed dose is accumulated by it.

The next step is to discriminate between electron and photon fields if $r_1 > 15\%$. In the case of electrons below several MeV, a low number of registered events is expected in Slots 2, and 3. A lower threshold for the maximum value of electron energy corresponds to the mean energy of the ^{106}Ru/^{106}Rh reference field since this is the largest energy investigated so far. The ratios of the number of registered events in the detectors are compared. It is classified that the impinging field consists of electrons if those ratios are below a certain threshold. After deciding which type of radiation is present in the field, the corresponding personal dose equivalent is calculated, and its displayed dose value is accumulated.

An attempt of classification is made to decide if a photon or electron field is present in measurements. Data for reference photon fields between N-15 to N-300, S-Cs, and S-Co from PTBs photon radiation facilities and the β reference fields measured at PTBs BSS2 with and without Kapton window are utilized. The ratios used to classify a radiation field are r_1 =15% with an energy threshold of 33.5 keV, $r_{2,1}$ =26%, and $r_{3,1}$ =8%. Table 4.8 summarizes the application of the three conditions to the complete data set. The output labels correspond to low-energy photon fields (γ_{low}), photon fields (γ), and electron fields (e^-). Both types of photon fields are classified correctly as such. Due to the threshold for condition 1 of 33.5 keV, reference photon fields with mean energies equal and smaller N-30 are classified as low-energy photon fields. ^{147}Pm is classified as low energy photon field without the β window due to the stopping of its β particles in the ABS plastic cover. Using the β window allows correct classification of ^{147}Pm. ^{85}Kr, ^{90}Sr/^{90}Y, and ^{106}Ru/^{106}Rh are classified as electron fields with and without utilizing the β window.

The current number of measurements is not sufficient to determine conversion factors for the upper twelve energy bins of Slot 1 for $H_{\text{p}}(0.07)$ electron dosimetry since only four β reference fields are measured. The recorded energy deposition spectra of Slot 1 with the Kapton window shows a significantly lower number of entries for ^{85}Kr compared to ^{90}Sr/^{90}Y, even though both spectra correspond to a reference dose of 1 mSv. Any set of any given conversion factors will underestimate the dose of ^{85}Kr as it shows a low number of registered events in each energy bin and will therefore underestimate the electron dose severely. A key distinction between both reference fields is the Landau distribution for ^{90}Sr/^{90}Y. A search for this distribution is needed before the dose is determined. Different sets of conversion factors are required for different electron energy ranges. If a Landau distribution is detected, a high-energy electron field is assumed. Investigations into the ratios $r_{2,1}$ and $r_{3,1}$ are needed to estimate the maximum electron energy since the ratios increase with increasing electron energy. With that, a suitable set of conversion factors is chosen to determine the dose. For electron dosimetry where an energy deposition spectrum unequal to the

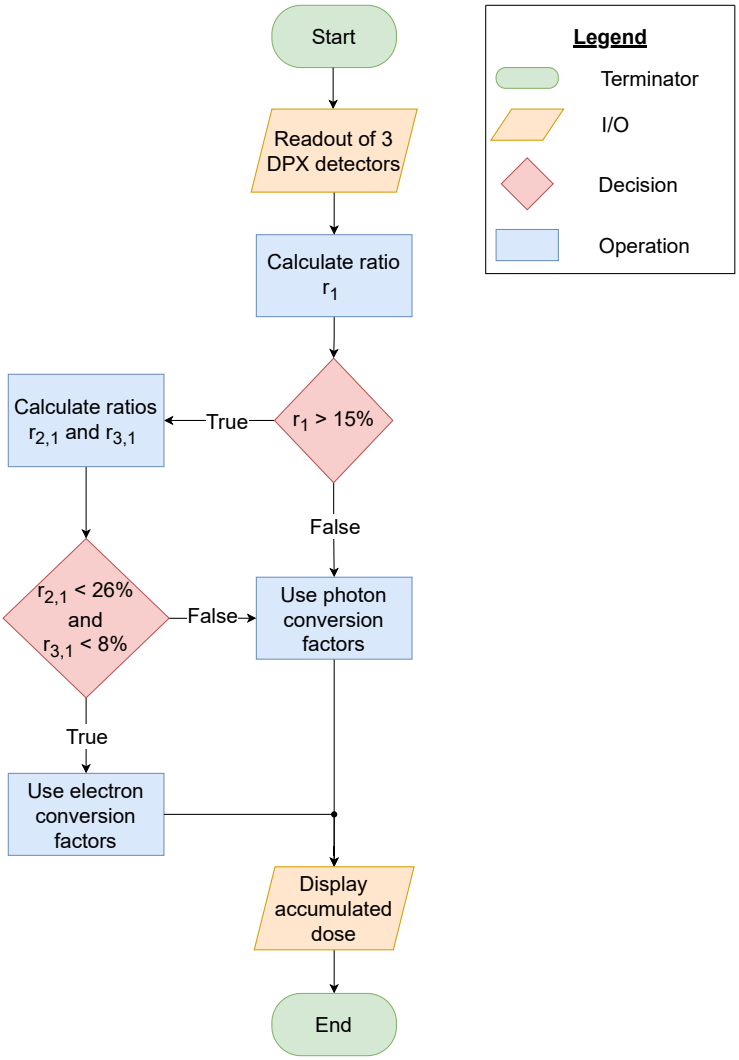

Figure 4.22.: Flowchart of the branching algorithm. All three detectors are read out, and their energy histograms are analyzed. First, Slot 1 is compared to itself if the ratio of its number of registered events greater than 33.5 keV and its total number of registered events r_1 is larger than 15%. If that is the case, a second query into the ratios between the number of registered events in Slots 2 and 1, $r_{2,1}$, and Slots 3 and 1, $r_{3,1}$, is started. If $r_{2,1}$ is lower than 26% and $r_{3,1}$ lower than 8%, an electron field is assumed, and its corresponding conversion factors are used. In all other cases, the radiation field is classified to consist of photons, and the corresponding conversion factors are utilized. Depending on the outcome, a personal dose equivalent is calculated, and the accumulated dose is displayed.

Photon quality	Output label	Photon quality	Output label	β quality	Output label
N-15	γ_{low}	N-120	γ	^{147}Pm	γ_{low}
N-20	γ_{low}	N-150	γ	^{147}Pm, βw	e^-
N-25	γ_{low}	N-200	γ	^{85}Kr	e^-
N-30	γ_{low}	C 250	γ	^{85}Kr, βw	e^-
N-40	γ	N-250	γ	^{90}Sr/^{90}Y	e^-
N-60	γ	N-300	γ	^{90}Sr/^{90}Y, βw	e^-
N-80	γ	S-Cs	γ	^{106}Ru/^{106}Rh	e^-
N-100	γ	S-Co	γ	^{106}Ru/^{106}Rh, βw	e^-

Table 4.8.: Classification output of the branching algorithm. Measurements of photon and β reference fields are used for the analysis. The conditions for the ratios are r_1 =15%, $r_{2,1}$ =26%, and $r_{3,1}$ =8%. The output labels denote the type of radiation field. These are γ_{low} for low energy photon fields, γ for photon fields, and e^- for β radiation fields. The usage of the β window is indicated by βw.

Landau distribution is recorded, extensive studies with electron beams and other β radiation sources are necessary to determine conversion factors.

Since determining the electron dose is a very extensive procedure, another approach is more feasible. Dosimetry of electrons relies on the knowledge of the absolute electron fluence. A reconstruction algorithm must be employed for the energy deposition spectrum of electrons interacting in Dosepix to yield the incident absolute electron fluence spectrum. Such algorithms require extensive simulations and optimizations of the current design of the dosemeter, especially of the filter caps. There is potentially even the need for more Dosepix detectors to determine the incident electron fluence spectrum reliably. The determination of the electron dose with Dosepix will not be further investigated, as it is beyond the scope of this chapter.

Assuming one or more sets of conversion factors exist for different radiation fields, it is still difficult to apply branching algorithms correctly. Mixed radiation fields are the main problem. They consist, for example, of a combination of photon and electron radiation. A comprehensive overview regarding dosimetry in mixed radiation fields is given in [94]. Usually, most radiation fields consist of a mixed radiation field, but typically the dose contribution of one particle type is negligible. For instance, all β-radiation sources are accompanied by Bremsstrahlung and typically γ-decay photons. On the other hand, high-energy photons ionize electrons in the air, leading to small electron contributions. If the dose contributions of photons and electrons are both non-negligible and the branching algorithm only detects one particle type, then severe overestimation or, even worse, underestimation of the dose can occur because, depending on the particle type, stronger or weaker weighting is required. For such a mixed radiation field, a potential solution utilizes the Dosepix detectors

in Slot 1 and Slot 2. Both need to be equipped with identical energy bin edges for energy bin indices 0 to 11, i.e., the energetically upper twelve energy bins. The difference in the number of registered events between the energetically upper bins of both detectors is calculated. This method is only applicable if the electron is fully stopped in the aluminum filter-cap, i.e., below about 1 MeV. Adjustments to the thickness of the aluminum filter cap or potential change of its material are ways to increase the maximum detectable electron energy. The energetically lower energy bins are not utilized as they will result in different count rates, especially for low energies due to beam hardening of the aluminum filter-cap. However, the aluminum filter will attenuate the radiation beam also at larger energies, which is why a proportionality factor for said attenuation by aluminum half-sphere and potential fixed-count rate discrepancies must be considered. The photon dose is calculated via:

$$D_\gamma = \sum_{i=1}^{4} \gamma_i^{\text{Free}} N_i^{\text{Free}} + \sum_{i=1}^{16} \gamma_i^{\text{Al}} \cdot N_i^{\text{Al}} + \sum_{i=1}^{16} \gamma_i^{\text{Sn}} \cdot N_i^{\text{Sn}} \tag{4.2}$$

where γ_i^x and N_i^x denote the conversion factors for photons and the number of events in bin i of detector x. The sorting of the index follows the description of energetically ascending, where every single detector has 16 energy bins labeled from 1 to 16. The superscripts Free, Al, and Sn denote Slot 1, Slot 2, and Slot 3 respectively. The electron dose is calculated via

$$D_\epsilon = \sum_{i=5}^{16} \epsilon_i^{\text{Free}} \cdot N_i^{\text{Free}} \tag{4.3}$$

where ϵ_i^{Free} denotes the conversion factors for electrons in Slot 1 in bin i. Here, N_i^{Free} is defined as

$$N_i^{Free} = \begin{cases} N_i^{\text{Free,meas}}, & \text{for } j = 1,2,3,4 \\ N_i^{\text{Free,meas}} - \alpha^i \cdot N_i^{\text{Al}}, & \text{for } j = 5,...,16 \end{cases} \tag{4.4}$$

where α^i denotes the aforementioned proportionality factor, and $N_i^{\text{Free,meas}}$ the measured energy histogram in Slot 1. This method demands high calibration efforts since the bin edges between Slots 1 and 2 must align in high precision with each other and the proportionality factor must be correctly determined. Furthermore a precise detector simulations for different radiation sources, especially for mixed

radiation fields is required. The electron interaction in Dosepix has to be further investigated, especially at facilities with monoenergetic electron beams, to study and optimize branching algorithms. In closing, the only reasonable solution which includes dosimetry of electron fields is a more sophisticated dosemeter consisting of a higher number of Dosepix detectors, each with its optimized filter cap. Measurements of the DPX detectors are then used to determine the spectrum of the incident radiation field, resolved into its photon and electron contributions. Knowing the incident spectrum allows precise calculation of the personal dose equivalent because fluence to dose equivalent conversion coefficients can directly be applied to the reconstructed spectrum.

4.5. Eye Lens Dosimetry with Dosepix

4.5.1. Importance of Eye Lens Dose Monitoring

Studies regarding the radiosensitivity of the eye lens suggested that the threshold dose for radiation-induced cataract formation is lower than previously assumed. Its value is considered around 0.5-2 Gy for acute, and 5-6 Gy for prolonged exposure [8]. For instance, epidemiological studies into Chernobyl clean-up workers and a 20-year cohort study into cataract risk among radiological technologists indicated that the threshold value for cataract formation is below those values [95, 96]. Investigations in [10] concluded that a dose-dependent increased risk of posterior lens opacities for interventional cardiologists and radiological technologists exists if radiation protection equipment is not utilized. Further studies confirmed an increased rate of cataract formation induced by radiation [5, 97, 98]. Therefore, it was deduced that the real threshold dose of radiation cataractogenesis must be smaller than previously thought of. Also, the question was posed if a reliable value even exists [8]. In the course of this, the equivalent dose limit to the lens of the eye was severely restricted. In 2011 ICRP issued the following recommendation: "For occupational exposure, a dose limit for the equivalent dose to the lens of the eye of 20 mSv/year, averaged over defined periods of 5 years, with no annual dose in a single year exceeding 50 mSv. Previously, this dose limit had been 150 mSv/year" [77].

In 2019, the previous findings were put to German radiation protection law to prevent radiation-induced cataract formation for occupationally exposed workers. The threshold of the organ equivalent dose of the eye lens was reduced from 150 mSv per year to 20 mSv per year (under section §78 (2) 1 of StrlSchG). The eye lens dose $H_{\mathrm{p}}(3)$ is used as the operational quantity of the organ equivalent dose of the eye lens.

The ORAMED (Optimization of RAdiation protection for MEDical staff) project [99] was carried out to optimize working procedures of staff in medical applications regarding radiation protection. It was the driving force in defining an appropriate set of conventions and procedures in eye lens dosimetry within its work package 2. In the course of this project, the water cylinder phantom was proposed, and conversion

coefficients between air kerma and eye lens dose on said phantom were determined [100, 58]. The executive summary of the ORAMED project states that very few active personal dosemeters can detect low energy fields, and none of them are really designed for working in pulsed radiation fields [99]. Note that the investigations into APDs were carried out for whole-body dosemeters measuring the $H_{\mathrm{p}}(10)$ as currently, no active personal eye lens dosemeter exists. At the end of 2021, only two passive personal dosemeters for individual monitoring of $H_{\mathrm{p}}(3)$ are assessed in their conformity [101]. Studies have identified that interventional radiology and cardiology are among the workplaces with the highest radiation exposure to the lens of the eye [8, 102, 103]. The eye lens dose for staff in radiological interventions might even exceed the annual dose limit of 20 mSv [4]. Another conclusion of the authors is that their results indicate the importance of an existing real-time dose monitoring system that makes the staff instantly aware of the exposure [4]. The ORAMED work package 2 was finalized with the development of a passive dosemeter for measurements of the eye lens dose specifically for members of medical staff [104, 105].

A prototype comprised of one Dosepix detector with the use case as a real-time active personal dosemeter for monitoring of the eye lens dose $H_{\mathrm{p}}(3)$ is presented in the remainder of this chapter. Its specifications aim to achieve correct determination of the eye lens dose in continuous photon fields, especially for low energies and in pulsed photon fields with pulse durations of several milliseconds and dose rates in the pulse of several Sievert per hour.

4.5.2. Eye Lens Dosimetry with a Single Dosepix

So far, three Dosepix detectors have been utilized for personal dosimetry in the energy range between 12.4 keV and 1250 keV. Such a dosemeter is not sufficiently small and compact enough to be placed in the vicinity of the eye as it takes up too much space. This section investigates the reduction of the number of Dosepix detectors from three to one. In particular, a single Dosepix detector is utilized for measurements of the eye lens dose $H_{\mathrm{p}}(3)$. In the beginning, the readout electronics used for the Dosepix dosimetry demonstrator with three detectors are utilized to test Dosepix's energy dependence of the response, i.e., the ratio of the measured $H_{\mathrm{p}}^{\mathrm{DPX}}(3)$ and the reference $H_{\mathrm{p}}^{\mathrm{ref}}(3)$. The Dosepix detector is placed in the central slot with a 2 mm thick plastic cap in front of the sensor element. The readout electronics are attached to the water cylinder phantom, which emulates the scattering properties of the human head. Its center is placed in 2 m distance to the focus of a MEGALIX Cat X-ray tube [70] on a turntable to allow rotation and consequently irradiations at different angles of radiation incidence. The reference point is the center of the phantom through which the axis of rotation is drawn. It is perpendicular to the top and bottom cylinder disk faces.

Reference dose measurements of air kerma are performed with the RQX sensor of the Dosimax plus A. It is positioned in close proximity to the Dosepix on the readout PCB during the exposure. Twenty reference spectra as previously defined in Section 3.6 are used to determine the conversion factors. These factors convert a registered number of events in an energy bin into a contribution of the total measured $H_\mathrm{p}(3)$. The reference fields are chosen to comprehensively represent the mean energy range between 30 and 105 keV. Several different incident spectra with varying mean energies allow the investigation of the energy dependence of Dosepix since different energy deposition spectra are registered. Compared to Section 3.6, the distance between the Dosepix detector and the X-ray tube focus is increased to 2 m. The reference spectra are simulated with xpecgen [72] to take the additional attenuation of the air into account. The conversion coefficients between air kerma and $H_\mathrm{p}(3)$ are determined via Equation (3.14) and the corresponding mean energies calculated according to Equation (3.15). Figure 4.23(a) shows the energy spectra of the simulated incident reference fields. The color code indicates the kVp value. Figure 4.23(b) illustrates the conversion coefficients between air kerma and $H_\mathrm{p}(3)$ and the reference dose values of the measurements. The irradiations of the Dosepix detector are performed with a fixed exposure time of 20 s and a constant tube current of 10 mA. The reference spectra are created by choosing a combination of beam hardening filter and successive increase of the tube voltage, which explains the groups of increasing reference dose in Figure 4.23(b).

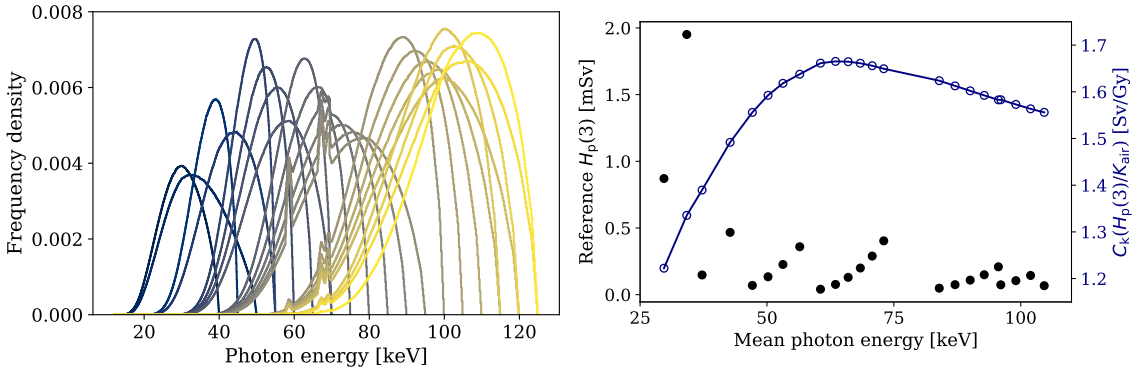

(a) Simulated reference fields

(b) Reference dose and conversion coefficients

Figure 4.23.: Simulated reference spectra (a) at 2 m distance. The color code indicates the kVp range, which lies between 40 and 125 kVp. They are used to determine the spectrum-specific conversion coefficients which are used to calculate the corresponding applied reference eye lens dose of the measurement, both seen in (b).

The energy thresholds are set to values between 12 keV and 150 keV. Events with a deposited energy above 150 keV increment the counter of bin index 0. Table 4.9 lists the utilized energy bin edges. They are identical for the large and the small pixels

Bin index	Bin edge [keV]
15	12
14	15
13	20
12	25
11	30
10	35
9	40
8	50
7	60
6	70
5	80
4	90
3	100
2	110
1	130
0	150

Table 4.9.: Energy bin edges used for measurements in Dosi-mode. These bin edges are used for both the large and small pixels. Bin index numbering is in reversed order to the increasing energies of the bin edges.

and are chosen to represent the energy deposition in the energy range of interest appropriately. For smaller energies, a bin width of 5 keV is chosen as the detection efficiency is high at low energies. Large bin widths for these energies increase the potential of digital pile-up, i.e., an overflow of the bin register. The bin width is increased as the energy increases. 150 keV marks the value of the bin edge for the last energy bin. For the small pixels, no significant energy deposition is expected for these energies, while the large pixels will register events in the highest energy bin. The number of events in the highest energy bin is not expected to be significant in the energy range of the radiation qualities of interest. Conversion factors between the number of registered events in an energy bin and the dose measured by Dosepix are determined for these energy bins. Energy histograms are recorded in the Dosi-mode with an I_{Krum} of 11 DACs. Section 3.8 describes the method to determine conversion factors via measurement, which is utilized in the following. Because of the maximum kVp of 125 kV, no entries in the energy bins of bin indices 0 and 1 are expected. Therefore, the conversion factors of the upper (energetically) two bins are set to zero. The remaining 14 energy bins are utilized for dose determination. Conversion factors are optimized via a least-squares fit for both the large and the small pixels. The corresponding conversion factors are shown in Figure 4.24(a) and (b). The large pixels follow a smooth exponential trend between bin indices 2 and 10. Energy bins of indices 11 to 13 deviate from this trend. These bins are in an energy range with sufficiently high detection efficiency, which are therefore the entries with the highest

contribution to the total event rate. The exponential increase of the conversion factors is a combination of the decreasing detection efficiency in Dosepix, which leads to a stronger weighting of entries in high energy bins, and the continuous increase of the $H_\mathrm{p}(3)/\Phi$. The small pixels show an exponential trend with large fluctuations and conversion factors that are running into the lower boundary for bin indices 10,12,13, and 15. The energy dependence of the response is shown in Figure 4.24(c) and (d) for the large and small pixels, respectively. The uncertainty bars denote the calculated uncertainty on the dose divided by the reference dose. The uncertainty on the number of events in an energy bin is assumed to follow Poisson statistics. Both pixel types exhibit a flat response around 1 over the complete energy range. The legal limits are indicated by the red dashed line. All values stay within those limits. The number of measurements exceeds the number of free parameters and is therefore large enough to sufficiently determine the conversion factors. For the small pixels, even ten conversion factors are sufficient to determine the dose as two factors are set to zero, and four are converging into the lower boundary, which indicates that those conversion factors are negligible. Figure 4.24(e) and (f) show the relative statistical uncertainty F_stat. The limits are calculated using the reference dose according to [69] as described in section 4.2. F_stat is below 1 % for the large and below 8 % for the small pixels for all energies. It, therefore, stays way within limits for both pixel types. A pattern of groups of decreasing relative statistical uncertainty is observed. It corresponds to the groups of increasing dose in Figure 4.23, i.e., increased statistics reduce the uncertainty. The higher dose is attributable to the reference fields. They are prepared by placing a combination of beam hardening filters in front of the X-ray tube exit and by varying the kVp value of said X-ray tube. Increasing the tube voltage also increases the flux approximately by square [41]. The interaction probability in a material decreases with increasing energy. If the kVp increases, a relatively larger amount of photons at the tail towards larger photon energies will pass the material without interaction. Combining both facts results in an increased registered event rate, which reduces the statistical uncertainty.

The conversion factors are validated by reference spectra, which are not used in the dose calibration procedure, i.e., the determination of the conversion factors. Five reference fields of the N-series in the kVp range of the used X-ray tube, i.e., N-40 to N-120, are used. The axis of rotation is the center of the phantom, which itself is placed on a rotary table. The response and angular dependence are shown in Figure 4.25. The energy and angular responses are close to 1, which demonstrates usability of the conversion factors. It is shown that a single Dosepix is able to correctly determine the eye lens dose between 30 and 105 keV. This allows the application of Dosepix in dosimetry of a reduced energy range. Using only one Dosepix detector reduces the size of the dosemeter compared to the Dosepix dosimetry demonstrator. This opens the door for applications with the need of small and compact dose monitoring devices. The acquired knowledge is utilized for the development and the testing of an eye lens dosemeter prototype in the following.

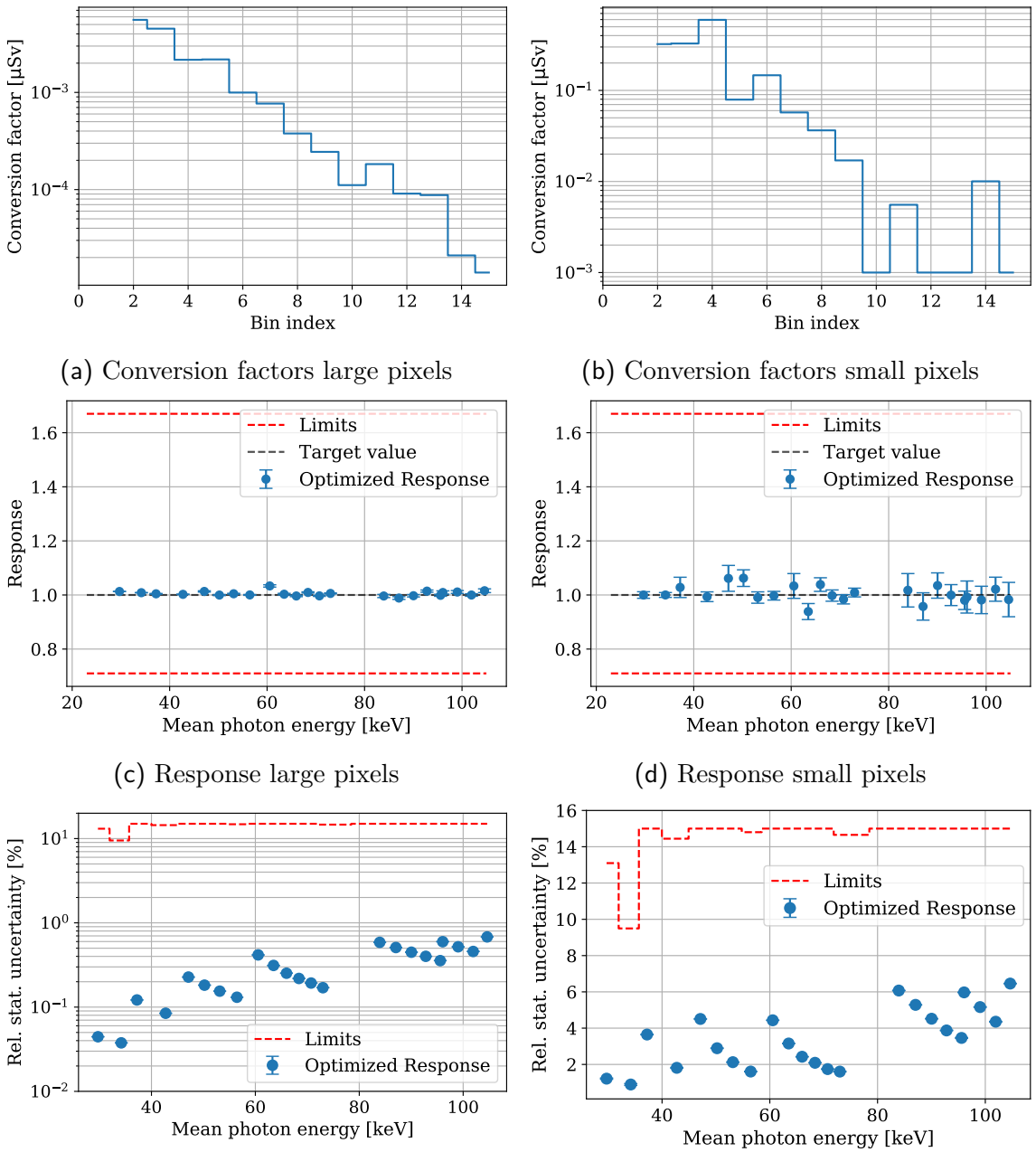

(a) Conversion factors large pixels

(b) Conversion factors small pixels

(c) Response large pixels

(d) Response small pixels

(e) F_{stat} large pixels

(f) F_{stat} small pixels

Figure 4.24.: Conversion factors for the determination of $H_{\text{p}}(3)$ via a single Dosepix detector for the large and small pixels in (a), (b). The energy dependence of the response of the data used to determine the conversion factors is shown in (c), (d). The dashed black lines represent the target response of 1 for the optimization. The relative statistical uncertainty F_{stat} for the large (e) and small pixels (f) is determined as the ratio of the uncertainty of the measured dose and the measured dose. All limits according to [69] are drawn in dashed red lines.

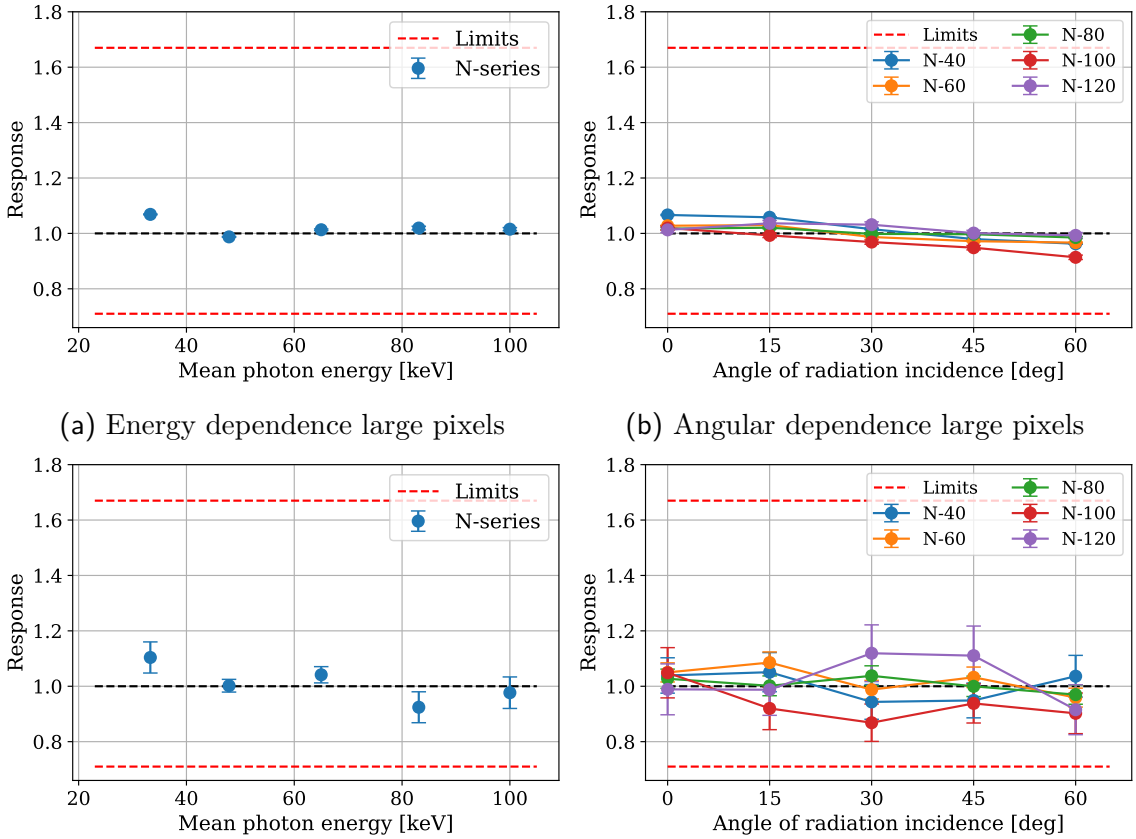

(a) Energy dependence large pixels

(b) Angular dependence large pixels

(c) Energy dependence small pixels

(d) Angular dependence small pixels

Figure 4.25.: Verification of the conversion factors via measurements of the N-series, which is not used for the optimization. The red dashed lines indicate the limits according to [83, 84].

4.6. Eye Lens Dosemeter Prototype

The measurements in continuous and pulsed photon fields with the eye lens dosemeter prototype presented in the following were performed by Florian Beißer during his master's thesis, which was supervised by me.

A prototype of the first active personal dosemeter for monitoring of the eye lens dose $H_p(3)$ is developed in the scope of the project EXTRA (Electronic X-ray Tracker), which won the Medical Valley Award 2018. The design consists of a real-time dosimetry system comprised of a single Dosepix detector per dosemeter module for application in continuous and pulsed radiation fields. A smaller energy range of 12.4-248 keV is aimed for, compared to the previously presented Dosepix dosimetry demonstrator. This energy range is sufficient to fulfill type test requirements according to PTB-A 23.2 [83, 69]. No active system exists to this day, only two passive dosemeters have passed the conformity assessment for a $H_p(3)$ dosemeter in Germany [101]. Especially

problems of active electronic personal dosemeters due to the pulsed nature of the radiation beams at medical facilities are nonexistent for Dosepix since its dead-time free data readout. An eye lens dosemeter might be used in various applications where significant exposure to the eye is observed and low photon energies are expected. This is realized in, e.g., in applications in the medical field. A potential field of applications is interventional procedures in medicine that would profit from an active personal dosemeter that detects low energy photons and pulsed photon radiation [12]. In interventional medicine, photon energies up to 150 keV, pulse durations of 1-20 ms, dose rates in the direct beam of 2-360 Sv/h, and dose rates of 5 mSv/h to 10 Sv/h in the scattered radiation field are possible [81]. Furthermore, monitoring of the eye lens in interventional radiology and cardiology is important since these fields were identified among the workplaces with the largest exposure of the eye lens to radiation [4].

The eye lens dosemeter is attached to the head of the user. The representative position of a $H_p(3)$ dosemeter is in the proximity to the eye [106]. Possible positions are on the forehead or a headband above the eyes. In applications with a known radiation source position, the dosemeter should be oriented towards it. The Dosepix detector is mounted in a 3D printed case attached to a headband. This case is attached to the side of the head, which is exposed to the radiation source. Furthermore, the position of the sensor element surface is parallel to a plane through the eye lens, i.e., the dosemeter looks in forward direction. The interior of the dosemeter case carries readout electronics, a battery pack, and the Dosepix detector. A small lead glass filter can be placed in front of the dosemeter case to take into account the attenuation of the radiation protection glasses. For the metrological characterization of Dosepix, no lead glass filters are used as these characterizations intend to demonstrate that the dose of the photon field is correctly determined. Tests into the attenuation of the photon field by the lead glass filter must be performed in the future.

The Dosepix detector has no additional filter in front of its sensor element as it is sufficient in the medical X-ray energy range as shown in [19]. The material of the case is photopolymer resin. The case is important for the energy characteristics of the system, especially the front side, which is directly above the sensor element of Dosepix at a distance of 1.5 mm. The material attenuates low-energy photons predominantly. Its thickness must be chosen such that β-radiation of ^{85}Kr is fully stopped in the material. This β reference field is used to investigate the influence of β-radiation on the eye lens dose indication. A thickness of 2 mm is chosen for the prototype, which should be sufficient to fully stop β-radiation of ^{85}Kr. The total weight of the prototype is approximately 60 g. Its dimensions are about 8.9 cm in length, 2.8 cm in-depth, and 3 cm height. The depth dimension is leaning towards the head of the wearer. A homogeneous weight distribution of the dosemeter is achieved due to its length. All in all, no discomfort in wearing the dosemeter should occur due to its light weight and compact dimensions.

The dosemeter housing is also supposed to be equipped with a display that is necessary when circumstances do not allow a tablet or other monitor devices. This display is the main carrier of the dose information and supersedes other display methods, which only exist for convenience and user-friendliness. The dose measured by Dosepix can be sent to a tablet via Bluetooth, which displays the accumulated dose in real-time to the user. Such a system allows direct response to situations with increased dose exposure. In this case, additional radiation protection equipment such as lead glass shields might be installed, or even a re-positioning of the staff member could be sufficient. Most importantly, a real-time dosimetry system accomplishes training of the user to teach themselves correct behavior to reduce the dose exposure. An active warning is enabled using a flashing LED and an alarm sound if dose/dose rate thresholds are surpassed. A picture of the prototype is shown in Figure 4.26. It is attached via a headband to a head model. It wears glasses to emulate the radiation protection glasses.

It must be mentioned that a monitoring system for clinical applications, e.g., for interventional procedures, is available. The RaySafe i2 real-time dosimetry system monitors the personal dose equivalent $H_\mathrm{p}(10)$. The dosemeter is worn on the upper trunk and is connected wirelessly to a display station. Multiple users can see their accumulated dose in real-time on said display station. Its technical specifications according to the manufacturer are an energy range of 33 keV to 101 keV and a dose rate range between 40 µSv/h to 300 mSv/h [107]. It is investigated in its metrological properties, and published results confirm its energy range specifications [108] and its upper dose rate limit [7]. Its successor system RaySafe i3 states an extended energy range up to 117.7 keV (N-150) and an extended dose rate range of up to 500 mSv as technical specifications [109]. In both cases, low-energy dose contributions are underestimated as shown for the RaySafe i2 (normalized response of 0.27 for N-30) and inferred for the RaySafe i3 as the lower energy specifications did not change. Energy contributions below 30 keV are also relevant in interventional procedures as the staff is predominantly exposed to the scattered radiation beam, and scattering with the patient softens the X-ray field.

The combined influence of the mean photon energy and angular dependence and the dependence of the dose rate and pulse duration of the normalized response of the prototype is presented in the following section. Two different positions on the water cylinder phantom are investigated. It is necessary to study the differences between both positions due to lack of definition within international standards for a long dosemeter system. The eye lens dose is defined in 3 mm depth of the ICRU 4-element tissue cylinder phantom. The radius vector of the cylinder antiparallel to the radiation field denotes 0°. It is reasonable to assume that the position of the dosemeter should be on the center front of the phantom as the dose is defined in 3 mm depth on the front face of the ICRU cylinder phantom. Usually, the reference point of the dosemeter coincides well with the surface of the ISO calibration phantoms because of the small widths of the dosemeters. The reference point of the $H_\mathrm{p}(3)$ dosemeter prototype is the sensor element which is 1.5 mm below the inner case front side.

Placing the dosemeter prototype on the center front of the phantom puts the reference point in a relatively large distance to the phantom. This means that backscattering contributions are significantly reduced. The tests are performed without Bluetooth but with a USB cable attached to the dosemeter. The system aims to achieve type test conformity according to PTB, and IEC standards [83, 84] and is tested according to these requirements.

Figure 4.26.: Prototype of the $H_p(3)$ dosemeter with one Dosepix detector. The case material consists of white photopolymer resin. The notches in the cover indicate the position for lead glass filters. Those filters will resemble the attenuation of radiation protection glasses worn by the user. The prototype is fixed to a headband which is attached to the head of the user. The position of the sensor element of Dosepix is as close to the eye as possible. The normal vector of the sensor element is parallel to the viewing direction of the user, i.e., the dosemeter looks in forward direction.

4.6.1. Continuous Photon Fields

Measurement Data

The dosemeter prototype is attached to the center front of the water cylinder phantom. Dosepix's energy bin edges are consistent with the settings used for the previous measurements with a single Dosepix detector presented in Section 4.5.2. Table 4.10 summarizes the used reference fields and the angles of radiation incidence per radiation quality. Typically, only radiation qualities of the N-series are used to scan the energy range and determine the dosemeter's energy dependence. These measurements are used to optimize the conversion factors. In addition to the N-series, radiation qualities according to DIN 6818-1 [110] are measured to test broader spectra with mean energies in between the typically tested energies and to validate the determined conversion factors. All irradiations are performed at a dose rate of 10 mSv/h, with an exposure time of 60 s. This results in a reference dose of 167 µSv. The corresponding limit for the coefficient of variation is therefore 15% [83, 69, 84].

DIN 6818-1	ISO 4037-1	$\langle E \rangle$ [keV]	α [°]
	N-15	12.4	0; ±60
C 20		13.7	0
	N-20	16.3	0; ±60
C 30		20.1	0
	N-25	20.3	0; ±60
B 30		23	0
	N-30	24.6	0; ±60
C 40		25.7	0
B 40		29.8	0
	N-40	33.3	0; ±60
	N-60	47.9	0; ±60
	N-80	65.2	0
	N-100	83.3	0
	N-120	100	0; ±60
	N-150	118	0; ±60
	N-200	165	0
	N-250	207	0
	N-300	248	0; ±60

Table 4.10.: X-ray reference fields according to DIN 6818-1 [110] for the B- and C-series, and ISO 4037-1 [67] for the N-series used for measurements with the eye lens dosemeter prototype at PTB. These radiation qualities are associated by their mean energy $\langle E \rangle$. Additionally, the angles of radiation incidence α at which the irradiations are performed is stated.

Figure 4.27 shows an excerpt of the recorded energy histograms for the large (a) and the small pixels (b). Similar to the measurements of Slot 1 of the Dosepix dosimetry demonstrator, a small number of analog pile-up events are observed for the large pixels at low energies. They are assumed to be accidental occurrences, which do not significantly impact dose determination since their amount is small. Overall, the energy deposition spectra show the expected shape. N-300 would theoretically deposit energies up to 248 keV in a large pixel as shown for Slot 1 for the Dosepix dosimetry demonstrator. Due to the focus on the low energy range, a trade-off is made for the upper energy bin. The response will be skewed slightly for N-300 due to large energy depositions. This is no problem for the small pixels, which usually have energy depositions below 160 keV. The small pixels exhibit the kVp cut-off criteria well, i.e., an abrupt ending of the energy deposition spectrum at the kVp value of the radiation quality is observed.

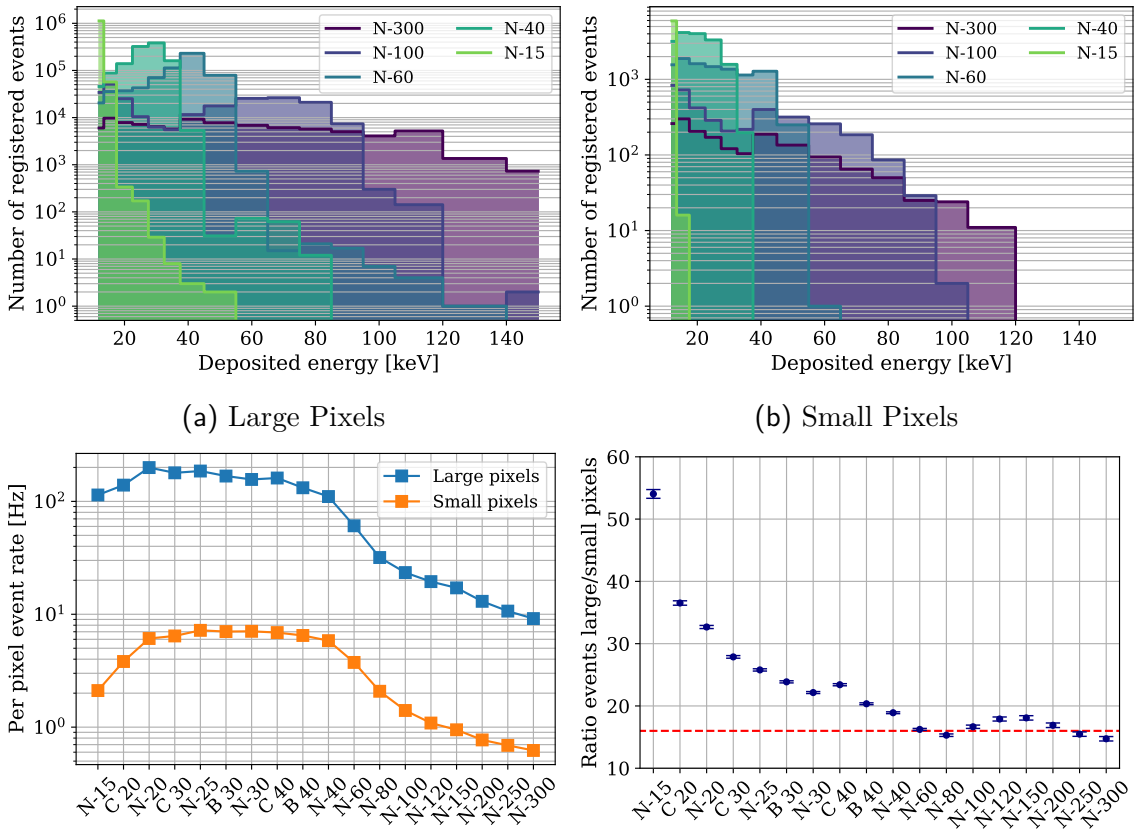

(a) Large Pixels

(b) Small Pixels

(c) Per-pixel event rate

(d) Event ratio large/small pixels

Figure 4.27.: Energy histograms of selected radiation qualities of the N-series for the large and the small pixels in (a) and (b). The per pixel event rate for all measured radiation fields is shown in (c). These values are used to calculate the event ratio between large and small pixels in (d).

The per-pixel event rate for both pixel types and the ratio between the event rate of large and small pixels are shown in Figure 4.27(c) and Figure 4.27(d). Here, all uncertainties denote uncertainty propagation of the Poisson uncertainty on the number of registered events. N-15 and C 20 radiation qualities have contributions of the spectrum below the energy threshold, which means part of the spectrum is cut off. At the energy threshold, the small pixels register an even lower number of events compared to the large pixels due to diffusion losses as described earlier. The event ratio between large and small pixels converges towards a value of 16 with increasing energy starting at N-60.

Conversion Factors

The recorded energy histograms of the N-series are used to determine a set of conversion factors translating the number of registered events in an energy bin into the eye lens dose $H_\mathrm{p}(3)$. This additional optimization is necessary to determine a set of conversion factors over the whole energy range since the previous optimization is performed for the energy range of 30-105 keV. Each pixel type has its individual conversion factors. At least four values of conversion factors must be held constant as only 13 reference fields of the N-series are available. The optimization routine is described in more detail in Section 3.8. The lower and upper boundaries are 10^{-5} µSv, and 0.9 µSv for the large and 10^{-3} µSv to 7 µSv for the small pixels. The radiation quality N-300 is excluded from the fit due to fluctuations of the response for the large pixels as the high-energy parts of this radiation field are accumulated in the last energy bins. The radiation quality N-15 is excluded from the fit for the small pixels because the majority of registered events is condensed in one energy bin. The second energy bin only registers 16 entries resulting in a ratio of about 370 compared to the first bin. In comparison: The ratio between the bins with the same bin indices is around 20 for the large pixels, where no problems arise in the optimization procedure. Fewer events are registered in the small pixels due to the cut into the energy spectrum via the energy threshold and diffusion losses for energies at the threshold. These missing events result in underestimating the dose contribution of the particular energy bin. Consequently, this radiation quality must be excluded from the optimization for the small pixels.

The input conversion factors are determined in Section 4.5.2 for eye lens dosimetry with a single Dosepix detector. The same detector is used for these investigations. In building the prototype, several pixels became damaged, so they are excluded in the following. A correction factor for the smaller effective area adapts the conversion factors to the lower number of pixels. This factor is 192/173 for the large and 64/47 for the small pixels. As the conversion factors of bin indices 0 and 1 are set to zero in the previous investigations, an exponential extrapolation of those is performed to determine start parameters for the corresponding energy bins. Six values of the conversion factors for the large and seven for the small pixels are held constant during the optimization to stabilize the overall trend.

Figure 4.28 shows the conversion factors between the number of registered events per bin to eye lens dose $H_p(3)$ for the large and the small pixels. None of the conversion factors runs into its lower boundary. Between adjacent conversion factors, fluctuations are observed, which are more prevalent for the small pixels. An exponential trend of the conversion factors is seen for the higher energy bins (lower bin index number). It becomes flat for energy bins with a large bin index, i.e., small energy. A trade-off between accuracy and stability must always be made when determining conversion factors. A smoother trend corresponds to a larger systematic uncertainty of the dose measurement for the influence quantity mean photon energy, while larger fluctuations of the conversion factors are observed for a low systematic uncertainty.

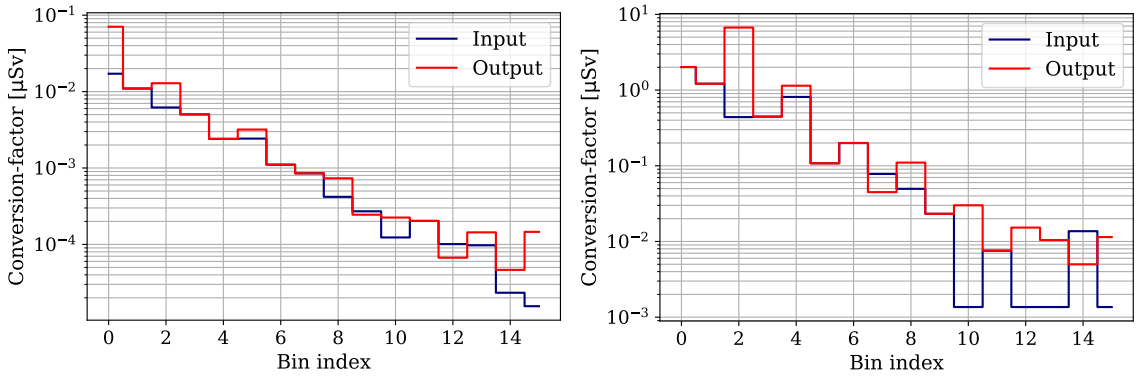

(a) Large Pixels (b) Small Pixels

Figure 4.28.: Conversion factors from total number of registered events in an energy bin of Dosepix to the personal dose equivalent $H_p(3)$ for the large and the small pixels. The input conversion factors (blue) are determined via recorded energy histograms of arbitrarily defined photon fields. The output conversion factors (red) are optimized with respect to recorded energy histograms of the N-series at facilities of PTB.

Results and Discussion

The combined influence of the quantities mean photon energy and angle of radiation incidence are investigated at facilities of PTB. All response values of both influence quantities are normalized to the response of the radiation quality N-80 at 0 ° angle of radiation incidence and have to stay within the range of 0.71 and 1.67 [83, 84]. The corresponding results are presented in Figure 4.29(a,b) for the large and small pixels. Both pixel types show a flat response around one for the optimized energy range within their uncertainties. The uncertainty increases with the energy for the small pixels as the value of the conversion factor increases significantly, and the number of registered events decreases. The normalized responses of the validation radiation qualities are all close to one except for C 20 due to its low energy contributions.

It is still within limits for the large pixels but deviates strongly compared to N-15, which also has low energy contributions that are below the energy threshold. For this particular type of radiation qualities, the optimized conversion factors must be taken with caution. For radiation qualities with energies within the range of energy bins, no significant deviations are seen and expected since the response gradients between adjacent energies are small. This means that mean photon energies between the energy grid points used for the optimization will result in a response close to 1. For the small pixels, the trend between N-15 and C 20 is visible. Overall, the response of the small pixels deviates more from one than the response for the large pixels.

The relative statistical uncertainty F_{stat} and the coefficient of variation v are shown for both pixel types in Figure 4.29(c),(d). Measurements of five selected radiation qualities are repeated four times, where the irradiations for N-150 are performed with the phantom behind the detector and for the remaining four (N-30, N-80, N-120, and N-300) on the side of the phantom. The energies are sampled to represent the complete energy range. Both v and F_{stat} coincide well with each other within their uncertainties for N-30 and N-150 for the large and all except N-30 for the small pixels. A tendency towards a lower v is observed for the large pixels. For N-30, a larger v is determined. At N-80, a much smaller coefficient of variation is measured for the large pixels. For the small pixels, F_{stat} and v exceed the limit for N-200 and N-300 respectively. Those values will be within the limits when using a sensor with all 64 small pixels working. Pure correction of the number of events yields a factor $\sqrt{47/64}$ which reduces the coefficient of variation to 14.6% at N-300. Therefore, all values are within limits. The coefficient of variation is well represented via the relative statistical uncertainty and even overestimated by it in the investigated energy range. This finding is counterintuitive and contradicts previous findings at the beginning of the chapter. The coefficient of variation must be larger than F_{stat} since F_{stat} assumes the number of registered events Poisson distributed and independent among pixels and energy bins. In reality, one photon can trigger several pixels with registered energy contributions in different energy bins. Further investigations into this matter are necessary for the future. A possible explanation is the utilized set of conversion factors. A different set must be determined to validate the results.

The combined influence of the energy and angular dependence is shown in Figure 4.30. Certain radiation qualities are not utilized for the tests at angular irradiation. This is due to the decrease of the angular dependence with increasing energy, as shown for the Dosepix dosimetry demonstrator. Low-energy fields are interesting as these photons are prone to absorption in the dosemeter case and are sensitive to changes. The symmetry of the prototype is tested with angles of radiation incidence of $\pm 60°$. At these angles, the focus point lies at the edge of the front side of the case, which maximizes the effective material thickness. The measured dose is underestimated for energies below 25 keV. Increasing the effective thickness of the cover by changing the angle of radiation incidence results in stronger absorption of the photon field. A small asymmetry is observed for $+60°$ which is the backside of the dosemeter and is

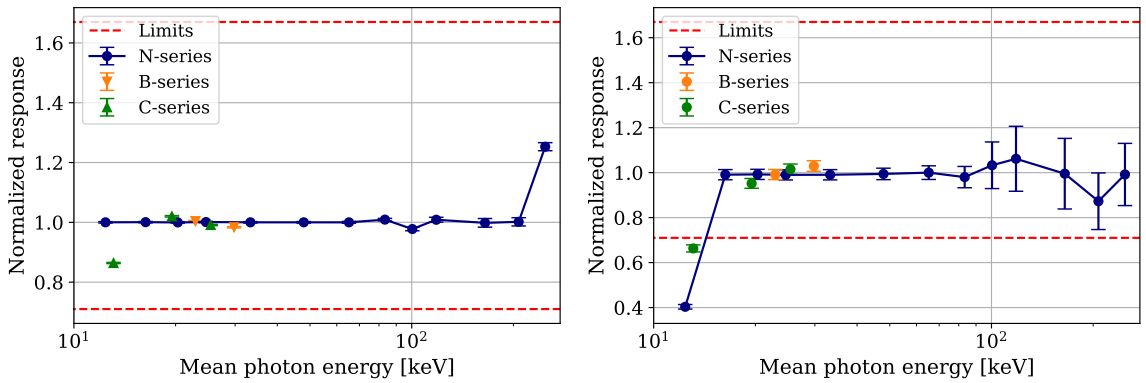

(a) Normalized response large pixels

(b) Normalized response small pixels

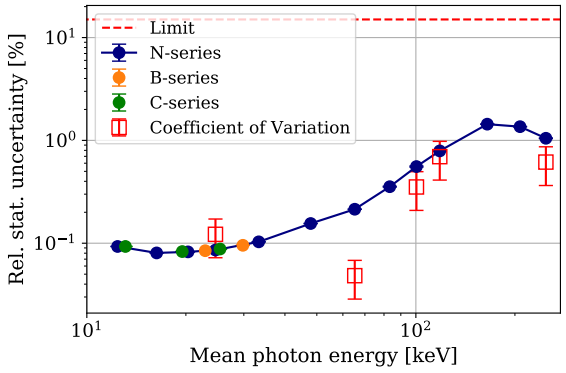

(c) F_{stat} and v large pixels

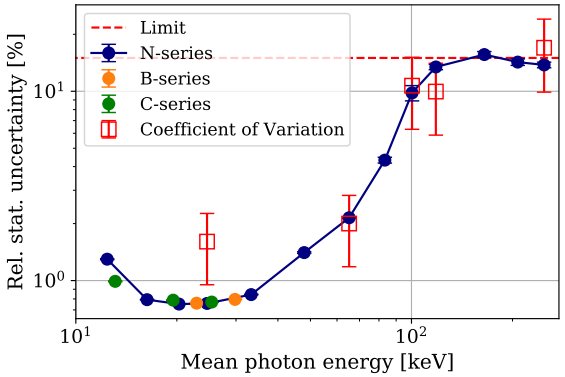

(d) F_{stat} and v small pixels

Figure 4.29.: Energy dependence of the response normalized to N-80 for the large and N-60 for the small pixels in (a) and (b). Reference photon fields of the B-, C-, and N-series are used. The energy dependence of the relative statistical uncertainty F_{stat} for the investigated radiation fields is shown in (c) and (d) for the large and small pixels. The red square denotes selected radiation qualities that are used for the determination of the coefficient of variation for a sample size of four measurements.

adjacent to the head. N-120 and N-150 show larger discrepancies for the small pixels. It is due a fluctuating number of events in energy bins with a large value which skews the response. Overall, a rated range of use between 12.4 keV and 248 keV for the large and 16.3 keV and 248 keV for the small pixels.

The radiation qualities with the largest back-scattering contributions are used to determine the back-scatter factor for the eye lens dosemeter prototype. The three utilized reference photon fields are N-60, N-80, and N-100. Contributions arise from the phantom and the prototype's interior, such as the readout electronics and the battery pack. Table 4.11 shows the back-scatter factor. It is calculated by performing two measurements, one with and another without the water cylinder phantom. The dose is determined for each individual exposure, and the ratio between the dose with

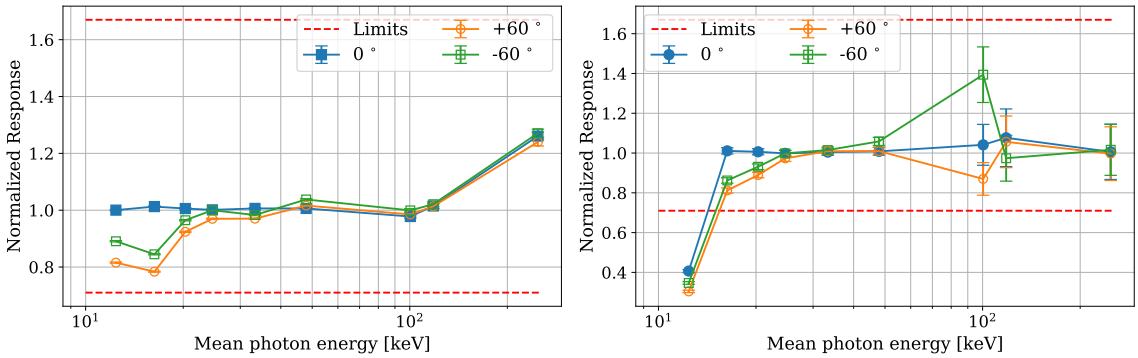

(a) Large pixels (b) Small pixels

Figure 4.30.: Combined influence of the dependence of the normalized response on the mean photon energy and the angle of radiation incidence for the large and the small pixels. The investigations are carried out in reference photon fields of the N-series. The uncertainty bars denote the uncertainty on the normalized response calculated via Equation (3.5).

and without phantom is calculated. Uncertainty propagation of the uncertainty of the dose yields the declared uncertainties. The largest back-scattering contribution is determined for N-100. All back-scatter factors between small and large pixels coincide well within their uncertainties. Overall, the back-scattering contribution is small due to the large distance between the phantom surface and detector position.

Radiation quality	Pixel size [µm]	Back-scatter factor
N-60	55	1.003±0.020
	220	1.006±0.003
N-80	55	1.020±0.031
	220	1.006±0.003
N-100	55	1.058±0.068
	220	1.016±0.006

Table 4.11.: The back-scatter factor (ratio dose w/ and w/o phantom) is summarized for three different radiation qualities for both pixel types. The radiation qualities are chosen in the energy range where the highest contribution is expected. The prototype is placed on the center front of the water cylinder phantom.

Next, the influence of the position of the prototype with respect to the phantom is examined. The final dosemeter will be attached to the side of the head in future applications. However, it has been positioned in front of the water cylinder phantom so far, which is equivalent to wearing the dosemeter on the forehead. This is necessary, as the eye lens dose quantity is defined on the center front of the phantom. Now, the

dosemeter prototype is attached to the side of the phantom to estimate the additional phantom scattering component. All irradiations are performed at 0° angle of radiation incidence with a reference dose rate of 10 mSv/h. As for the reference dose quantity: It is assumed that conditions for $H_p(3)$ irradiations are fulfilled, i.e., the dosemeter is positioned on the center front of the water cylinder phantom. This is necessary to use the eye lens dose as conversion coefficients between air kerma and $H_p(3)$ exist only for this case. Using the same dose equivalent allows comparability between both dosemeter positions. So far, there is no detection system with its reference point at a large distance to the front face of the cylinder phantom surface. Furthermore, no long detection system attached to the side of the head is existing. Therefore, there is no need for consideration of different definitions of the eye lens dose to assess the dosemeter system. Regulators must determine a coherent approach for the testing procedure of eye lens dosemeters that are worn on the side of the head and especially of a long detection system. Figure 4.31 shows the energy dependence of the response in comparison to the aforementioned dosemeter positions. The back-scatter factor is small when the prototype is attached to the center front of the water cylinder phantom. The conversion factors are optimized for this dosemeter position. When placing the prototype on the side of the phantom, a significantly larger proportion of phantom back-scattering (in this case, to the side) is observed since the response is larger than one. It results from the detector being spatially closer to the phantom. An up to 20% larger dose is calculated with the prototype attached to the side of the phantom. Turning this around: Determining conversion factors for the use case will result in 20% underestimation of the dose when the conformity assessment is performed for center front irradiations. A small deviation of the response between both positions is observed for N-30 as the scattering contribution is small for low energies. For future investigations, a consistent testing routine for a long dosemeter system that is worn on the side of the head must be formulated. Until then, the irradiations are performed according to $H_p(3)$ calibration conditions.

The position of the dosemeter on the side of the water cylinder phantom is further investigated. The reference point is the center of Dosepix's sensor matrix. The normal vector on the surface of the sensor element points along the long axis of the prototype. This design reproduces the reality for irradiations of the eye lens. The incidence direction of the radiation field will span angles of radiation incidence larger than 0° to the normal vector of Dosepix with respect to the use case. Therefore, it is necessary to perform irradiation for angles of radiation incidence of up to 90° to understand how the response behaves. The complete range of angles of radiation incidence is ±90°, which takes the possibility into account of the dosemeter being placed on the wrong side of the head. Here +90° denotes the case where the dosemeter is positioned behind the phantom and -90° the case where the dosemeter is positioned in front of the phantom.

Figure 4.32 shows the angular dependence of the response scanned in 15° steps. The red dashed lines indicate the limits of the minimum rated range of use for the angle of radiation incidence which is ±60° with the limits of 0.71 and 1.67 [67]. The response

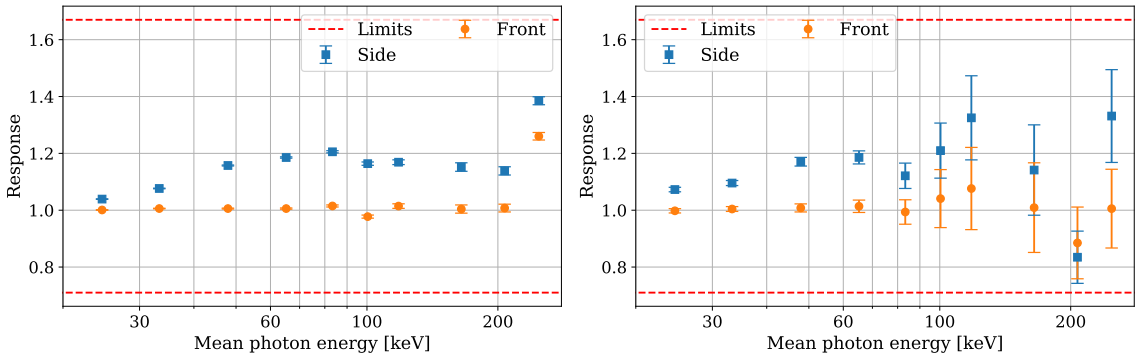

(a) Large pixels (b) Small pixels

Figure 4.31.: Energy dependence of the normalized response for two different positions of the prototype for the large (a) and the small pixels (b). When attached to the side of the water cylinder phantom, a larger scattering contribution is measured. The uncertainty bars denote the uncertainty of the dose measured by Dosepix divided by the reference dose.

is above one as the conversion factors are determined for center front irradiations. When the phantom covers the dosemeter, an underestimation of the dose is observed. The response to N-30 is nearly flat over the complete range of angles of radiation incidence. When the sensor element stands orthogonal to the direction of the incident radiation field, an underestimation is observed for N-30, as the effective area of the sensor element is minimized to $16 \times 220\,\mu m \times 300\,\mu m$. Interestingly, N-80 does not show this behavior. Since N-80 is one of the radiation qualities of the N-series with the largest back-scattering contribution (highest at N-100), it is apparent that those extra events are due to scattering in the case, its interior components, and the phantom. The dose increases for N-80 with increasing angle of radiation incidence. The response is symmetric around 0° except for the fringes at ±90°. Consequently, only a small dependence on the choice of the side of the head exists for angles of radiation incidence of ±75°.

4.6.2. Pulsed Photon Fields

The irradiations in pulsed photon fields are performed at PTBs X-ray unit for pulsed radiation GESA (GEpulste Strahlungs Anlage) presented in [6]. The eye lens dosemeter prototype is attached to the center front of the water cylinder phantom. It is irradiated with the two reference photon fields RQR 5 and RQR 8 which are defined according to international standard IEC 61267 [76]. These medical radiation qualities RQR 5 (70 kVp, filtered with 2.83 mm Al) and RQR 8 (100 kVp, filtered with 3.36 mm Al) have mean energies (fluence) of 40.4 keV and 50.9 keV respectively. Both are used for the investigation of the dose rate dependence of the normalized response. Only the RQR 8 quality is used for the investigations of the dependence on the pulse

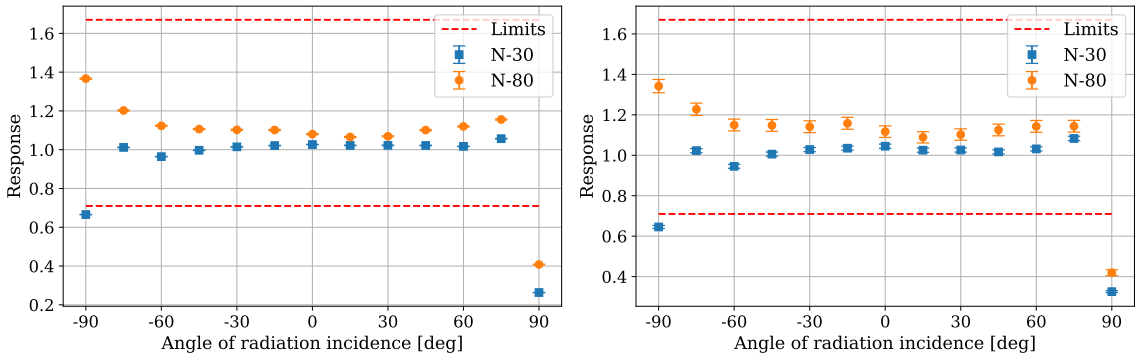

(a) Large pixels (b) Small pixels

Figure 4.32.: Angular dependence of the response for radiation qualities N-30 and N-80. The prototype is attached to the side of the water cylinder phantom. The dosemeter is behind the phantom at an angle of radiation incidence of +90° and in front of it at an angle of radiation incidence -90°.

duration. Each irradiation at a specific pulse duration is repeated four times for statistical purposes. The measured dose is determined for every single irradiation and the corresponding response is calculated and the mean response over all four irradiations is then used for further analysis. Its uncertainty denotes the standard uncertainty of the mean. As for the nomenclature: Dose rate means the dose rate in the pulse and pulse duration the pulse width of a single pulse.

Dependence on the pulse duration

Pulse durations between 400 µs and 10 s are utilized for a RQR 8 reference photon field. All irradiations are performed with a constant dose rate of 4 Sv/h, except at 400 µs with a dose rate of about 1.73 Sv/h. The range of the normalized response is limited to 0.8 and 1.2 [83], where the reference pulse duration is at continuous radiation, i.e., a pulse duration of 10 s.

Dosepix is read out once per irradiation. All recorded energy histograms are shown together with the per-pixel event rate and the event rate ratio between large and small pixels in Figure 4.33. An increase of the number of registered events with increasing pulse duration is observed which corresponds to a larger reference dose since a constant dose rate is applied. A larger reference dose results in a larger photon fluence and therefore a larger number of registered events. An increase of the pulse duration is accompanied by a prolongation of the tail of the energy deposition spectrum. Events are registered in energy bins where none are expected for the large pixels. As a tube voltage of 100 kVp is applied, a maximum energy of 100 keV is possible. Due to the detector resolution, events will also be registered in the energy bin above (bin index 2 with a threshold energy of 110 keV). All registered events in the energy bins above 130 keV (i.e., bin indices 0 and 1) are subsequently pile-up

events. They occur accidentally at a constant rate for a given dose rate as seen in Figure 4.33(a). The per-pixel event rate is nearly constant over the complete pulse duration range for the large pixels and small pixels, except for 400 µs. The event rate ratio is between 17 and 18 which corresponds well to the energy dependence of the event rate ratio as previously demonstrated in continuous photon fields.

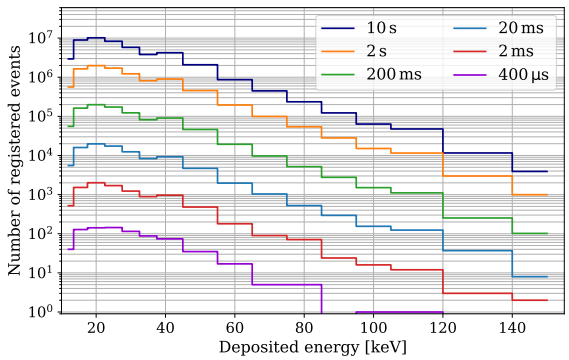

(a) Energy histograms large pixels

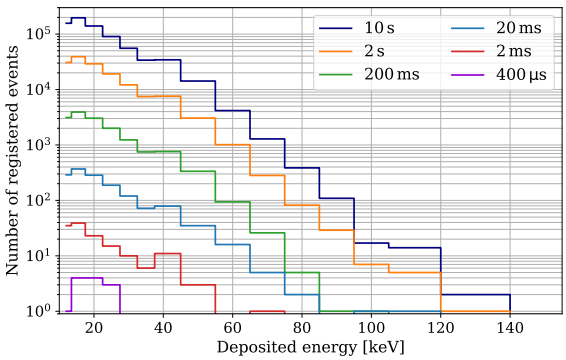

(b) Energy histograms small pixels

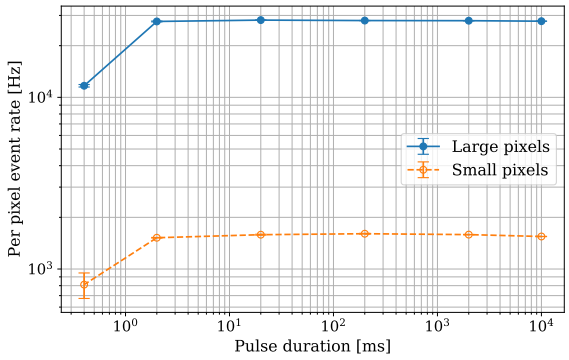

(c) Per pixel event rate

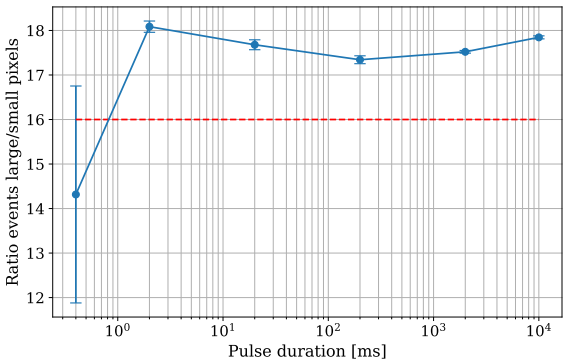

(d) Event rate ratio large/small pixels

Figure 4.33.: Energy histograms of the large (a) and small (b) pixels for different pulse durations in a RQR 8 reference photon field. For the sake of clarity only one of four histograms is shown for each pulse duration. Summation over such an energy histogram yields the total number of registered events which is divided by the number of pixels and the exposure time to yield the per pixel event rate (c). The data points denote the mean total number of registered events over the four irradiations. Its uncertainty corresponds to the standard uncertainty of the mean. The ratio of the per-pixel event rates between large and small pixels (d) results in values larger than the expected volume ratio of 16 indicated by the red dashed line.

Figure 4.34(a) shows the pulse duration dependence of the normalized response R_{Norm} for the large and small pixels. The limits of R_{Norm} are 0.8 and 1.2 according to PTB-23.2 and are indicated via the red dashed lines. For the large pixels, all values

are within limits, whereas for the small pixels R_{Norm} exceeds the upper limit at a pulse duration of 20 ms.

The reference response at continuous radiation is about 1 without applying of normalization. In a pulsed radiation field, an overestimation of the dose compared to the response at continuous radiation is observed for both pixel types. The data does not indicate why the measured dose is larger for pulsed radiation. At continuous radiation, five large pixels experience digital pile up, i.e., an overflow of their register. However, this does not account for the deviation of the dose compared to pulsed radiation. Digital pile-up is corrected in the analysis by adding 2^{16} to the number of registered events in the corresponding bin. Furthermore, no digital pile-up occurs in the small pixels that also overestimate the dose in pulsed radiation fields. The exposure time of 10 s is a borderline value for the readout of the detector. For the operation of a dosemeter, a shorter readout time such as 1 s is preferable to prevent digital pile-up.

All data points are about 1.1 within their uncertainties in the range of pulse durations from 4 µs to 2 s. They denote the standard uncertainty of the mean. The uncertainty increases with shorter pulse durations as the number of registered events decreases. R_{Norm} for the large and small pixels are in good agreement to each other between 200 ms and 10 s, i.e. the ASIC is operating correctly indifferent to the sensor pixel size. Deviations arise due to statistics and the choice of pixel type specific dose conversion factors. The largest deviation between large and small pixels is observed for a pulse duration of 20 ms. Here, 2 out of 4 measurements deviate strongly from the expected dose, as seen by the large uncertainty bar. Therefore, the mean is skewed towards a larger value. Events are registered for two of the four measurements in the energy bin with bin index 2, whose conversion factor is large with 6.7 µSv. This leads to an overestimation the dose at those irradiations since the reference dose is 22.2 µSv. This is problematic as photon fields with high energies deposit energy in this bin. A strong overestimation will be observed if the reference dose is small compared to this value and if the number of exposures is also small. In this case, a smooth trend of the conversion factors is preferable as the conversion factor for that particular energy bin would be smaller. Such a change would impact the energy dependence negatively. However, over several exposures, i.e., increasing statistics, this large conversion factor does not impact dosimetry with the small pixels. For them at 200 µs, the uncertainty extends over the complete range of the limits, with the possibility of even exceeding them. At this pulse duration, the total number of registered events is 12, 14, 11, and 24 for each irradiation at a mean reference dose of 0.192 µSv.

Figure 4.34(b) shows the dependence of the coefficient of variation on the pulse duration. The limit is calculated according to [69] using the reference dose of each irradiation and is indicated via the red dashed line. Its value increases with a decreasing pulse duration since the number of registered events decreases. Deviations between large and small pixels are smaller than for the energy dependence of the normalized response.

Overall, small dependencies of the normalized response are observed in pulsed fields. The statistical uncertainty of the small pixels is dangerously high and potentially deal-breaking when conformity is assessed. One data point is even above the upper limit. Medical applications are performed with pulse durations of several milliseconds [81]. A stable normalized response is observed for the large pixels in this range. The large pixels are flat around 1.1 in pulsed fields. The reason for the independence from the pulse duration is the dead-time-free measurement of the Dosepix. Neither dead-time correction factors nor a dead-time itself, during which a pulse might be missed have to be considered. This lead to a stable behavior of the large pixels of Dosepix. The discrepancies between pulsed and continuous fields must be investigated further. The trend of the small pixels between 200 ms and 10 s suggests an increase of the response with decreasing pulse duration. More sample points in between will potentially help resolve the issue.

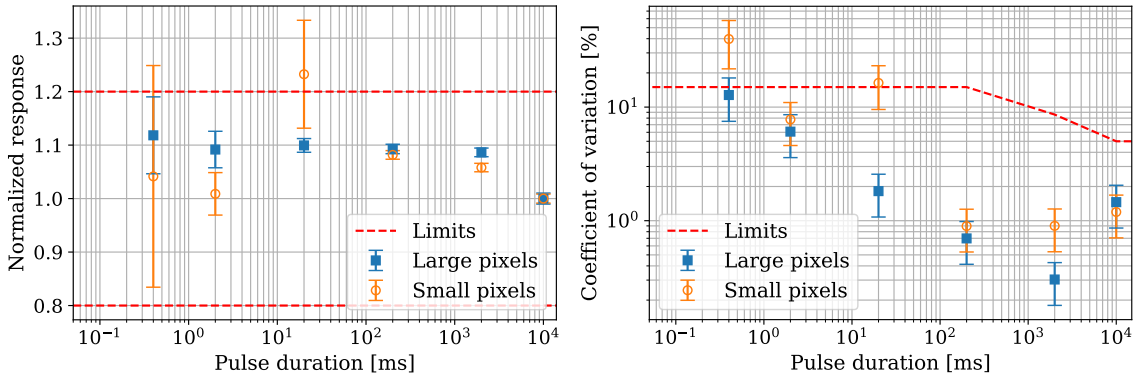

(a) Normalized Response (b) Coefficient of variation

Figure 4.34.: Pulse duration dependence of the normalized response (a) and the coefficient of variation (b). The irradiations are performed with a RQR 8 reference field according to IEC 61267 [76]. The limits according to PTB-A 23.2 [83] are indicated by the red dashed lines. The limits for the coefficient of variation are calculated utilizing the reference dose.

Dependence on the dose rate

The dose rate dependence of the normalized response is investigated at a constant pulse duration of 200 ms. Dose rates from 0.1 Sv/h up to 583 Sv/h for the RQR 5 and up to 592 Sv/h for the RQR 8 radiation qualities are applied. The recorded energy histograms are shown in Figure 4.35 for both reference fields and pixel types. At the lowest dose rate of 0.1 Sv/h, the energy deposition spectra look as expected. A cutoff is observed at the respective kVp values. Larger dose rates increase the pile-up probability, which leads to changes in the shape of the energy deposition spectra. With increasing dose rate a higher number of events is registered in the tail. Effectively, a broader and flatter energy deposition spectrum is recorded as several

low-energy photons are converted into a single high-energy event. Moreover, a shift of the spectrum below the energy threshold is observed as only an exponential decrease of the number of registered events is seen for the lowest energy bins at the highest dose rates. The large pixels are stronger affected than the small pixels due to the larger detection volume.

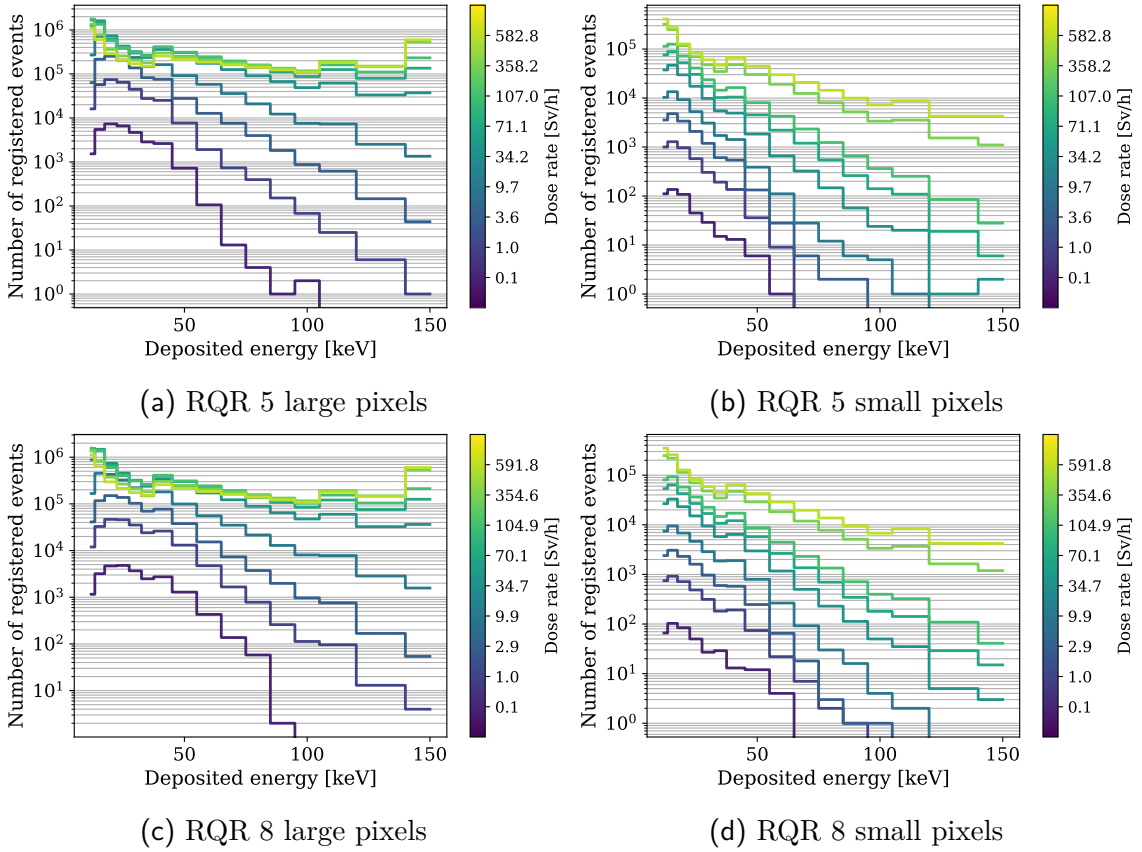

(a) RQR 5 large pixels

(b) RQR 5 small pixels

(c) RQR 8 large pixels

(d) RQR 8 small pixels

Figure 4.35.: Energy histograms of the large and small pixels for irradiations with RQR 5 and RQR 8 reference photon fields. The varied influence quantity is the dose rate. A significant change of the energy deposition spectrum is observed with increasing dose rate as pile up occurs.

Figure 4.36(a) shows the per-pixel event rate and the event rate ratio between large and small pixels. The event rate increases linearly with the dose rate up to 10 Sv/h for the large and up to about 100 Sv/h for the small pixels. These values correspond well with the increased pile-up occurrence observed for the energy deposition spectra. Analog pile-up is increasing with an increasing dose rate which is equal to an increase of the photon fluence. A decreasing ratio of the event rates between large and small pixels is observed as seen in Figure 4.36(b) as the event rate of the large pixels decreases for lower dose rates compared to the small pixels. At the smallest investigated dose rate a ratio above 16 is observed, which differs for both reference photon fields. This

corresponds well with the previously presented energy dependence of the event rate ratio as it increases for smaller energies.

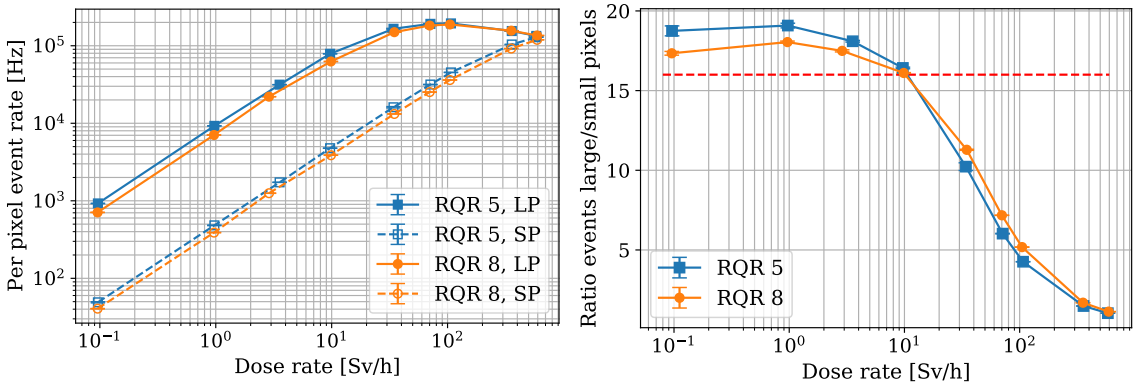

(a) Per-pixel event rate

(b) Event rate ratio large/small pixels

Figure 4.36.: Per-pixel event rate of the large and small pixels for two different radiation qualities (a). These data points are used to calculate the event rate ratio between large and small pixels (b).

The distance the X-ray tube and the eye lens dosemeter prototype is 2.5 m. High dose rates require a reduction of the distance down to 0.5 m, which results in a smaller field diameter. It is decreased from 42 cm down to 8.6 cm. The water cylinder phantom is no longer completely irradiated due to the smaller field diameter. Consequently, two correction factors must be determined to mitigate that influence. The first one considers the back-scatter percentage of the phantom. Irradiations with and without phantom are performed for this. The ratio of both mean response values yields the back-scatter factor. The corresponding uncertainty is calculated via uncertainty propagation. Furthermore, the influence of the field diameter is corrected similarly by calculating the ratio of the mean responses at the large and the small field diameter. These corrections are determined for both pixel types and radiation qualities. Another correction factor is determined for the placement of the prototype on the side of the phantom. All values are summarized in Table 4.12. A large field diameter and the water cylinder phantom behind the prototype is defined as the reference condition to which each response is corrected. At the time of the measurement campaign, it is not anticipated that the large pixels would be influenced by analog pile-up as early as 1 Sv/h. Therefore, no back-scatter factor for the prototype on the side of the phantom is used for the data points at dose rates of 2.88 Sv/h and 3.55 Sv/h for RQR 8 and RQR 5 reference fields. Analog pile-up will result in an overestimation of the measured dose which results in incorrect values of the calculated ratios at different dose rates. Especially for the RQR 8 reference field, where correction factors are determined for 10 Sv/h, a significant overestimation of the dose occurs, which skews the correction factor for the prototype on the side of the phantom. For the small pixels, all correction factors are used as the dose rates are sufficiently low and do not result in a significant amount of analog pile-up.

Radiation quality	Pixel size [µm]	Field-diameter influence	Back-scatter factor (back)	Back-scatter factor (side)
RQR 5	55	0.988 ± 0.011	1.014 ± 0.018	1.006 ± 0.011
	220	0.982 ± 0.004	0.991 ± 0.004	1.075 ± 0.006
RQR 8	55	0.973 ± 0.013	1.003 ± 0.011	1.060 ± 0.012
	220	0.935 ± 0.016	1.016 ± 0.018	0.819 ± 0.013

Table 4.12.: Correction factors applied for investigations of the dose rate dependence of the normalized response. For RQR 5 and RQR 8, dose rates of 1 Sv/h and 10 Sv/h are used to determine the correction factors. The irradiations on the side of the phantom are performed at 3.55 Sv/h and 2.88 Sv/h for RQR 5 and RQR 8 respectively.

Figure 4.37(a,b) shows the dose rate dependence of the normalized response. The normalized response must stay within the range of 0.87 to 1.18 which is indicated by the red dashed lines [83]. The reference dose rate is 0.1 Sv/h. An energy dependence is observed since differences between the normalized response values for the RQR 5 and RQR 8 reference fields occur. This energy dependence is small at the lower end of the investigated dose rates. For the small pixels, all data points coincide well within their uncertainties as long as no strong influence of analog pile-up is observed beginning at about 100 Sv/h. The detection efficiency of Dosepix is larger for lower energies and therefore impacts analog pile-up stronger. The discrepancy of the normalized response between both reference fields increases with the dose rate since the RQR 5 radiation quality has a lower mean energy. This observation is true for both pixel types.

The data point at a dose rate of 2.88 Sv/h for the large pixels slightly exceeds the limit of 1.18. For this value, no correction is calculated due to the aforementioned reasons. Assuming a correction factor with a value of 6% as for the small pixels and applying it on the normalized response will result in a response in accordance with the limits. A correction factor must be at least larger than 4% so that this value remains within the limits. Furthermore, the response calculated for the pulse duration variation in an RQR 8 reference field at 4 Sv/h for 200 ms results in a response of 1.075±0.004, which is within the limits. It is therefore inferred, that the value at 2.88 Sv/h is within the limits after application of a correction factor.

At the highest dose rates, the overflow flag is set for the large pixels. The affected bins are corrected by subtracting a value of 2^{15} from the number of registered events in highest energy bin. This correction explains the drop of the normalized response above 100 Sv/h. Overall, a rated range of use for the large pixels extends up to at least 4 Sv/h (RQR 8) and 3.55 Sv/h (RQR 5). For the small pixels a rated range of use extends up to at least 34.2 Sv/h (RQR 5) and 34.7 Sv/h (RQR 8).

Figure 4.37(c) and (d) show the coefficient of variation for the large and the small pixels respectively. Four measurements per dose rate are measured. It is calculated as the ratio between the standard deviation and the mean response. The response is used as the reference dose value fluctuates between irradiation. It is overall larger for the small pixels and below the limit for all data points.

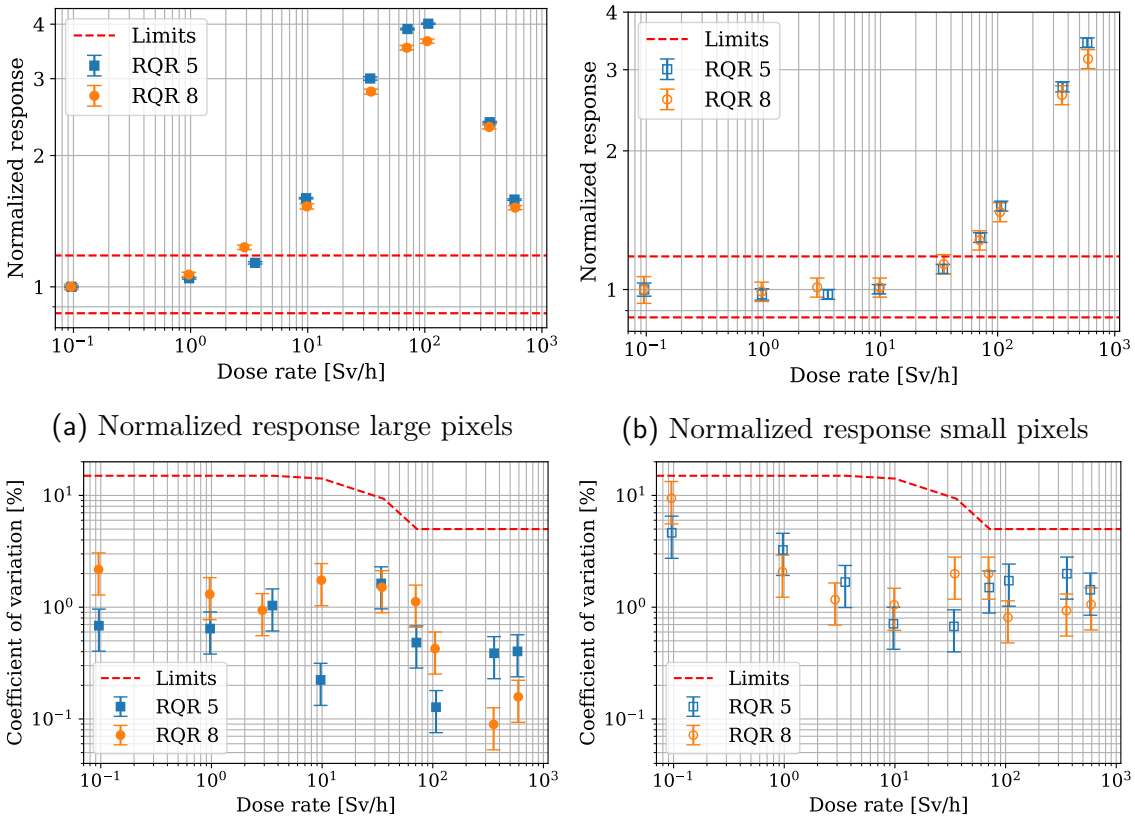

(a) Normalized response large pixels

(b) Normalized response small pixels

(c) Coefficient of variation large pixels

(d) Coefficient of variation small pixels

Figure 4.37.: Dose rate dependence of the normalized response (a) and the coefficient of variation (b) for the large (LP) and the small pixels (SP). The radiation qualities RQR 5 and RQR 8 according to IEC 61267 [76] are used. The limits according to PTB-A 23.2 and IEC 61526 [83, 84] are indicated by the red dashed lines. The limits for the coefficient of variation are calculated using the reference dose.

4.6.3. Comparison of the Results to Literature

This section gives a comprehensive overview of current eye lens dosemeter systems. Their energy dependencies are compared to the presented results for the Dosepix eye lens dosemeter prototype. Results of active personal dosemeters are used to compare the dose rate dependence of the normalized response.

A much smaller rated range of use of the eye lens dosemeter prototype for the dose rate dependence compared to results of the Dosepix dosimetry demonstrator consisting of three Dosepix detectors is observed [82]. This is due to the reduced number of detectors. A lower number of detectors implies larger values of the conversion factors, which leads to a stronger overestimation of the dose at relatively lower dose rates due to analog pile-up. Furthermore, one of the three detectors is covered with 1 mm tin, resulting in a low event rate and an insignificantly small number of pile-up occurrences. The contribution to the dose of such a detector will yield correct results over the whole dose rate range and therefore stabilize the dosemeter system. Correct results at such large dose rates are impossible to achieve when utilizing only one unfiltered detector. A filter is not to be recommended for the $H_{\mathrm{p}}(3)$ dosemeter prototype as it will decrease the rated energy range of use at the lower photon energies. As the current specifications are within the legal limits for dose rates, no modifications are necessary. Nonetheless, if a higher dose rate range is desired, the energy bin edges must be changed towards larger energies to compensate for analog pile-up events. Algorithms to determine new energy bin edges as presented in [35] must be implemented and fed with simulation data to determine more suitable energy bin edges. This will compensate for the overestimation due to analog pile-up since the complete bin edge distribution is changed, and potentially more energy bins are utilized for large energy contributions. However, this requires adjustment of the conversion factors in a way that the highest energy bins do not yield a significantly large dose contribution. This proposition must be verified in future investigations into the eye lens dosemeter prototype.

Comparisons regarding the pulsed radiation must be made with $H_{\mathrm{p}}(10)$ for widely distributed active personal dosemeters. A survey regarding the use of active personal dosemeters in hospitals showed that silicon diodes are the predominantly used detector type [11]. Tests in pulsed photon fields are performed in [7] investigating commonly used APDs in European hospitals. The radiation quality used is RQR 8. Only 3 of 10 APDs fulfilled the authors' requirements of a dose rate above 1 Sv/h within the margin of ±20% for the response: EPD Mk 2.3 (1.5 Sv/h), DMC 3000(3 Sv/h) and Rad-60SE (4 Sv/h). The latter has a rated range of use starting at 60 keV. Therefore, the authors concluded that only EPD Mk 2.3 and DMC 3000 are acceptable for pulsed radiation and that they are the best-tested dosemeters to cover energies found in hospitals. The results for the large pixels of Dosepix are within limits until 4 Sv/h. They are on par with the state-of-the-art active personal dosemeters. The small pixels will extend the dose rate range to around 36 Sv/h and allow an active warning for much larger dose rates than the state-of-the-art APDs.
The previously mentioned RaySafe I2 is also tested in [9]. Its maximum dose rate is 300 mSv/h. Additionally, its energy dependence is presented for radiation qualities of the N-series in [108]. Its response for low-energy photon fields is worse than that of Dosepix. In totality, Dosepix performs better than this currently available monitoring system for interventional procedures. Furthermore, Dosepix delivers the possibility of measuring the eye lens dose, which is measured by none of the aforementioned

active personal dosemeters. Another advantage of Dosepix is its performance in the low energy range. The presented dosemeter begin their rated range of use at 16 keV (EPD Mk 2.3), 15 keV (DMC 3000) and 33 keV (RaySafeI2) [7, 108]. The large pixels can correctly determine the eye lens dose down to a mean photon energy of 12.4 keV.

Eye lens dosimetry is currently conducted with passive dosemeters. EYE-D utilizing a TLD was shown to have a rated range of use for the energy range of 16.4 keV to 662 keV (N-20 to S-Cs). It coincides with the lower energy limit of the small pixels. However, its energy dependence is fluctuating largely and underestimating the dose strongly between 100-200 keV with a minimum response at 100 keV [105]. The authors do not explicitly state the minimum value, which lies by a measure of the eye at around 0.75.

Another passive dosemeter with peer-reviewed results is published in [111]. The BeOSL eye lens dosemeter can be integrated into radiation protection glasses. Latter ones are specifically designed to include the dosemeter. They are placed on the side of the glasses and therefore closer to the eye than the Dosepix eye lens dosemeter prototype. Its big advantage compared to other passive dosemeters is the readout station, which allows the determination of the dose after the intervention. Nonetheless, no active warning and real-time monitoring is possible with this eye lens dosemeter. Its energy dependence of the normalized response was compared to EYE-D eye lens dosemeter [111]. The normalized response of BeOSL is closer to one than the normalized response of the EYE-D. The rated range of use for the combined influence of energy and angle of radiation incidence is between N-20 and S-Co. The response increases for lower photon energies.

Comparing the presented eye lens dosemeter prototype comprised of one Dosepix detector to the aforementioned passive dosemeters shows a more accurate dose determination via Dosepix due to its spectroscopic ability. The large pixels correctly determine the dose down to 12.4 keV, which is lower than the minimum energy of the passive eye lens dosemeters. Towards larger photon energies, an overestimation of the measured dose is possible as the response increases rapidly with N-300. BeOSL, for instance, correctly determines the eye lens dose up to 7 MeV as inferred by the authors of [111]. The Dosepix eye lens dosemeter prototype is not designed for large energies.

Overall, Dosepix performs at least on par with the state-of-the-art active personal dosemeters that are currently available. It delivers a more accurate normalized response for both the energy and the dose rate dependence than the Raysafe I2 dosemeter. A comparison to passive eye lens dosemeters shows that Dosepix has an overall much flatter energy response in its rated range of use of 12.4-248 keV and only shows dependencies of the angle of radiation incidence at low photon energies. Its maximum energy range is nevertheless smaller than its passive counterparts. In conclusion, it is to be noted that several tests into the reproducibility of the results for a set of several prototypes must be conducted to investigate the stability of conversion factors across different dosemeters before large-scale comparisons to other dosemeters

can be performed. Nevertheless, the presented results are very promising and show the potential of Dosepix to be the first and possibly one of the best active personal dosemeters for monitoring the eye lens dose $H_p(3)$.

4.7. Conclusion

In this chapter, the metrological properties of the Dosepix detector regarding personal dose equivalents were investigated. At first, the combined influence of the dependence of the normalized response on the mean photon energy and the angle of radiation incidence was determined. It was presented for the personal dose equivalents $H_p(10)$, $H_p(0.07)$, and the eye lens dose $H_p(3)$. A system of three Dosepix detectors referred to as the Dosepix dosimetry demonstrator was utilized for this purpose. Since the primary reference dose quantity was $H_p(10)$, an ISO water slab phantom was used. The Dosepix dosimetry demonstrator was attached to this phantom. Its orientation was orthogonal to the axis of rotation and parallel to the surface of the ISO water slab phantom. The normalized response remains flat around 1 for all three personal dose equivalents at 0 ° angle of radiation incidence for the large (220 µm) and the small (55 µm) pixels. Such a flat response implies that mean photon energies between the investigated energy grid points will result close to 1 as well since no significant response gradients are observed.

Additionally, different angles of radiation incidence were investigated. It was shown that no asymmetry of the normalized response exists by rotating and irradiating the Dosepix dosimetry demonstrator at ±60 °. The measured dose is underestimated for $H_p(0.07)$ and $H_p(3)$ at ±60 ° in low-energy X-ray fields. Such an underestimation results from the definition of the dose equivalents as the reference dose becomes too large under angular irradiation to be compensated by the conversion factors of Dosepix. Nevertheless, all minimum requirements are fulfilled for all three personal dose equivalents. The effective range of use is determined according to these results from 12.4 keV to 1250 keV for angles of radiation incidence of ±60 ° for the $H_p(10)$, 24.6 keV to 1250 keV for the $H_p(0.07)$, and 20.3 keV to 1250 keV for the $H_p(3)$. The energy ranges are viable for both the large and the small pixels. For $H_p(0.07)$ S-Co for -60 ° is slightly above the limit but potentially outside the limit within its uncertainty. A safe rated range of use for the $H_p(0.07)$ of small pixels is 24 keV to 662 keV.

The energy dependence of the relative statistical uncertainty was investigated, and the coefficient of variation was sampled for N-300 and S-Co. It was shown that both stay below 1% for the large pixels and below 5% for the $H_p(10)$ and below 7% for the $H_p(0.07)$ and $H_p(3)$ for the small pixels. Therefore, both pixel types are viable for individual monitoring, i.e., dosimetry of the personal dose equivalent for photon radiation. Overall, the measured coefficient of variation is larger than the relative statistical uncertainty. However, a conservative estimation factor of 1.45 for the large pixels allows the use of the relative statistical uncertainty as a measure of the

uncertainty as already presented in [20]. For the small pixels, a conservative estimate of 1.75 must be applied.

Another discussed topic was the influence of β-radiation on the indication of the $H_{\mathrm{p}}(10)$ in the case of photon dosimetry. Such a test is necessary as electrons will deposit energy when passing the Dosepix detector leading to a number of events in the measured energy histograms and, therefore, a measured dose. The influence was above 10% for the standard conversion factors also presented in [20]. To circumvent this, only 4 of the 16 energy bins of Slot 1 were used for dosimetry with the Dosepix. This reduces the influence to below 2% for the large and 3% for the small pixels. A branching algorithm was presented and applied for photon and β-radiation fields. The mean photon energies range from 12.4 keV to 1250 keV, whereas the mean β energies are from 71 keV to at least 1.3 MeV. All β-radiation fields were correctly classified when using a β-window in front of Slot 1. Dosimetry of β-radiation fields could not be investigated since the number of measurements was lower than the 12 conversion factors available. Determining the electron dose $H_{\mathrm{p}}(0.07)$ is unfeasible with the current setup. Measurements of ^{85}Kr and ^{90}Sr/^{90}Y had the same reference dose, while ^{90}Sr/^{90}Y registered a significantly larger number of events in all available energy bins. No set of conversion factors exists to determine the dose correctly in this case. Further investigations into the discrimination between electron fields must be performed. Even with improved branching algorithms, problems for the classification will occur in mixed radiation fields, which will lead to significant errors in the dose determination. Therefore, the cleanest version for determining the electron dose is an approach of reconstructing the electron fluence spectrum with the Dosepix detector. More sophisticated investigations must be carried out in the future for this purpose to determine the number of necessary Dosepix detectors and new shapes and materials of filter-caps.

In the last part of the chapter, a prototype of the first active dosemeter for individual monitoring of the eye lens dose consisting of a single Dosepix detector was presented. This prototype consists of one unfiltered Dosepix detector in a 3D printed dosemeter case. Such a dosemeter is attached to the side of the head, and its sensor surface normal points in the forward direction. It is designed for the use case as a complete dosemeter system that sends the dose information via BlueTooth to a tablet. This tablet displays the accumulated dose in real-time. At all times, a display is integrated into the case of the dosemeter to allow a wide variety of applications. Its combined influence of the energy and angular dependence, the dose rate dependence, and the pulse duration dependence of the normalized response were investigated. Facilities of the PTB were utilized for those tests as they deliver precise reference photon fields with accurate reference dose values. Since only one Dosepix detector was used, the energy range was reduced to 12.4 keV up to 248 keV. The required minimum rated range of use extends to the radiation quality N-300 (mean photon energy of 248 keV). The determined rated range of use is 12.4 keV to 248 keV for the large and 16.3 keV to 248 keV for the small pixels. Comparisons to passive eye lens dosemeters showed an unparalleled energy dependence of Dosepix. The dependence of the normalized

response on the pulse duration is small for the large pixels, and the response in pulsed fields is flat between 400 µs to 2 s and within limits up to 10 s. Several issues due to event statistics of the small pixels and large values of conversion coefficient resulted in large statistical uncertainties. Further investigation into the stability of the small pixels and the roll of their conversion factors must be conducted. Nevertheless, all data points between 400 µs to 10 s, except 20 ms, are within limits. Dependencies of the normalized response of the dose rate were within limits up to around 4 Sv/h (RQR 8, for variation of pulse duration) and 3.55 Sv/h (RQR 5) for the large, and 34.7 Sv/h (RQR 8) and 34.2 Sv/h (RQR 5) for the small pixels. Investigation into two different reference photon fields (RQR 5,8) showed small differences at low dose rates and significant differences when analog pile-up occurred. The rated range of use for the dose rates is nevertheless not impacted by the energy dependence. Comparing Dosepix to the dose rate dependence of the state-of-the-art active personal dosemeters showed that Dosepix is at least on par with the best dosemeters and shows correct dose determination for slightly larger dose rate values.

5. X-ray Polarimetry with Timepix3

Contents

The capacity of the Timepix3 detector for polarimetry of linearly polarized X-rays is studied in this chapter. Pioneer work into X-ray polarimetry with the Timepix detector - the predecessor to Timepix3 - was previously demonstrated in [21, 22, 112]. The advantages of Timepix3 are its small time resolution of 1.56 ns, the simultaneous measurement of time and energy, and an event-by-event data-driven readout with a small per-pixel dead-time of 475 ns. All these features are utilized together with the pixelation of the detector to determine the angular distribution of coincident event cluster pairs by means of Compton scattering of X-rays in the sensor element of Timepix3. At first, fundamental considerations regarding X-ray polarimetry are stated. Afterward, an analysis is presented to determine the azimuth angle of two coincident event cluster pairs in the sensor element. It is tested by applying it to a toy simulation and measurement data of unpolarized and polarized X-ray fields. Unpolarized X-rays become linearly polarized after Compton scattering with a PMMA target. The setup used for the investigations is presented and simulated to determine the energy spectrum incident on the detector and the accepted scattering angles. Furthermore, measurements for a rotation of 90° of the detector are performed to confirm that linearly polarized X-rays are present. The azimuth angle distribution of unpolarized and linearly polarized X-rays is determined for X-rays that Compton scatter in the sensor element of Timepix3.

5.1. Studying Polarization of X-rays

Studies on the linear polarization of X-rays have been increasing in recent decades due to growing interest in the subject. In particular, there has been an increase in polarization measurements in astronomy and astroparticle physics. Polarization measurements help understand emission mechanisms, physical conditions, and emission geometries of astrophysical sources [14]. There are several ways to create polarized X-rays in the astrophysical environment, which are cyclotron radiation, synchrotron radiation, curvature radiation, bremsstrahlung, and Compton scattering [113]. The orientation of the X-ray polarization will depend on the orientation of the magnetic field [114], which makes polarization measurements an effective tool in studying magnetic fields of astrophysical objects [115].

Pioneer measurements into the polarization of the Crab nebula were conducted via an X-ray polarimeter on the OSO-8 satellite. The observed energies were 2.6 keV and 5.2 keV with a measured degree of polarization of (19.2±1)% [116, 117]. This finding proved that the X-rays emitted from the Crab nebula are of synchrotron origin. Other polarization studies were performed by RHESSI of polarized emission of a gamma-ray burst [118], and the IBIS and SPI instruments on board of INTEGRAL for galactic X-ray sources Cygnus X-1 [119, 120] and the Crab nebula [121].

In December of 2021, the Imaging X-ray Polarimetry Explorer (IXPE) space observatory dedicated to X-ray polarimetry was launched. It is equipped with three gas pixel detectors [45] that measure the anisotropy of the emission direction of photoelectrons produced by polarized photons [122]. These detectors allow simultaneously energy, time, and position resolved measurement of polarized sources [13]. Its energy range is between 2 keV and 8 keV [122].

Other missions employ CZT (Cadmium-Zinc-Telluride) detectors for polarization studies of hard X-rays. The CZT-imager onboard of Astrosat is designed for hard X-ray imaging, and spectroscopy [14]. It also allows polarization studies of X-rays in the energy range of 100-300 keV by utilizing Compton scattering in the detector plane. The NuSTAR mission operating in the low earth orbit since 2012 also studies polarization with a pixelated CZT detector employing Compton scattering. Their sensitive energy range is stated as 3 keV to 80 keV [115].

X-ray polarimetry is a very active field of research in which many different detection methods and detector systems are used. All utilize a different physical interaction to determine the degree of linear polarization of X-rays. The instrument on OSO-8 used a Bragg polarimeter, the gas pixel detectors of IXPE utilize the photoelectric effect, and CZT (Cadmium-Zinc-Telluride) detectors on board of NuSTAR and Astrosat employ Compton scattering. In the following sections, measurements of unpolarized and polarized sources in the laboratory are performed with the Timepix3. The interaction used to study linear polarization of X-rays is Compton scattering, and the tested energy range is between about 20 keV to about 80 keV.

5.2. Polarimetry by Means of Compton Scattering

The cross-sections of the photoelectric effect and Compton scattering exhibit a dependence of their angular distributions relating it to the electric field vector of the incident electromagnetic radiation. It makes both interactions accessible for studies of linear polarized X-rays. The azimuth angle distribution is accessible for a position, time resolving detector such as the Timepix3 if the X-ray is linearly polarized. The azimuth angle is measured in the detector plane and determined via utilizing its pixelation, while the events are correlated via their time of occurrence and their energy. Depending on the energy of the investigated source, a different interaction can be used to study the polarization. For the photoelectric effect, the direction of the photoelectron gives insights into the degree of linear polarization of the X-ray. It is viable at the lower energy range, which in the case of silicon is of up to 60 keV [44]. Above that, Compton scattering becomes the dominant interaction type, making it preferable for energies larger than 60 keV. The X-ray band between 3-100 keV is the potential rated energy range of use for applications of Timepix3 in polarimetry. Extensions of the energy range are possible by changing the sensor material, increasing the photoelectric yield, and extending the efficiency of the detection system. X-ray polarimetry employing Compton scattering in the sensor element of Timepix3 is investigated in this chapter. For polarimetry with the Timepix detector utilizing photoelectric effect, it is referred to [21] and tests into the capability of Timepix3 must be performed in the future. Basic considerations with respect to Compton scattering in Timepix3 are stated in the following.

The Klein-Nishina cross-section for Compton scattering shows a $\cos^2(\phi)$ dependency of the azimuth angle. Assuming an 80 keV photon, the Klein-Nishina cross-section computes to the data visualized in Figure 5.1. Drawing the line at a scattering angle of 90° shows a $\sin^2(\phi)$ distribution, which results from inserting $\theta = 90°$ in the Klein-Nishina cross-section. These azimuth modulation curves are the distributions of interest of the remainder of this chapter. Such a modulation curve is only observed when the incident photon field is polarized. It shows that scattering parallel to the direction of the polarization vector is suppressed. If the source's linear polarization has no defined orientation, i.e., it is unpolarized, a uniform distribution will be observed since no defined axis exists around which the scattering anisotropy can be observed. The top and valley values of the modulation curve provide information about the degree of polarization, which is further described later on.

The utilized Timepix3 detector is equipped with a 300 µm thick silicon sensor element with a sensitive area of 14.08 mm×14.08 mm. Silicon as sensor material has a sufficiently high interaction probability via Compton scattering in the investigated energy regime (photon energies of up to 100 keV). The sensor surface is defined in the x-y plane, and the polarized field propagates dominantly in the z-direction. The source of the polarized photon field is assumed at a large distance, i.e., the radiation field is parallel. The electric field components of the linear polarized incident photon are pointing in the x-, y-direction. If the photon field is polarized, a predominant orienta-

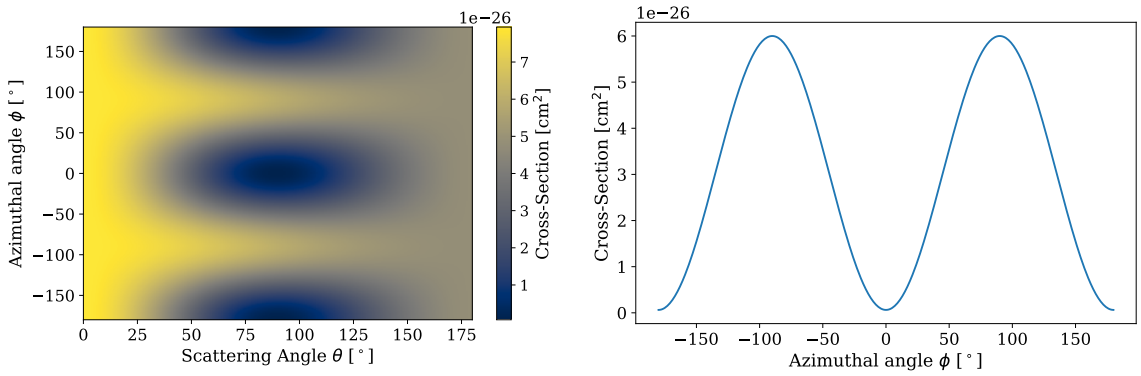

(a) Klein-Nishina cross-section.

(b) Modulation curve at θ=90°.

Figure 5.1.: Klein-Nishina cross-section in dependence of the scattering angle and the azimuth angle for an incident photon with an energy of 80 keV . A cut along θ=90° shows a typical modulation curve.

tion of the electric field exists. This predominant orientation defines the reference axis around which the azimuth angle dependence is observed. Using a thin sensor leads to the observation of two event clusters with a scattering angle of predominantly 90° in the sensor plane due to larger extension in the x,y direction compared to the thickness in the z-direction, which is equal to the sensor thickness. The thin sensor has a lower total interaction probability, i.e., a smaller detection efficiency as a consequence.

The determination of modulation curves is realized by observing two event clusters coincident in time in the sensor element at different pixel positions. An event is triggered when the deposited energy in the pixel surpasses the detector's energy threshold of 3 keV. The possible combinations of interaction channels with energy deposition in the X-ray regime are Compton scattering followed by Compton scattering or Compton scattering followed by the photoelectric effect. Both combinations show different energy signatures. The first event (Compton scattering) will deposit a small amount of energy onto the recoil electron. The second event can either absorb the remaining energy (photoelectric effect) or only deposit an even smaller amount of energy to another recoil electron (Compton scattering). These interaction channels limit the energy rated range of use since the incident photon fields must have energies large enough to deposit at least 3 keV for the second Compton scattering. In the case of the photoelectric effect, the second interaction point must have an energy below 60 keV that the interaction probability is sufficient to observe it. The Compton scattering energy transfer depends on the incident photon energy and the scattering angle and is shown in Figure 5.2 and calculated via Equation (2.7). The maximum energy transfer occurs at the backscattering of the photon. At the estimated mean scattering angle of 90° (270°), the energy deposition via Compton scattering is 10.829 keV for an incident photon with 80 keV. Rayleigh scattering in the sensor element yields a distortion of the angular distribution because this interaction type does not deposit energy in the detector. A possible interaction combination for this is Compton scattering

followed by Rayleigh scattering followed by photoelectric effect. However, the rate of occurrence is low since three interactions are involved. In the following section, an analysis of Timepix3 data is presented that is specified to determine the azimuth angle of Compton scattering followed by the photoelectric effect in the plane of the sensor element.

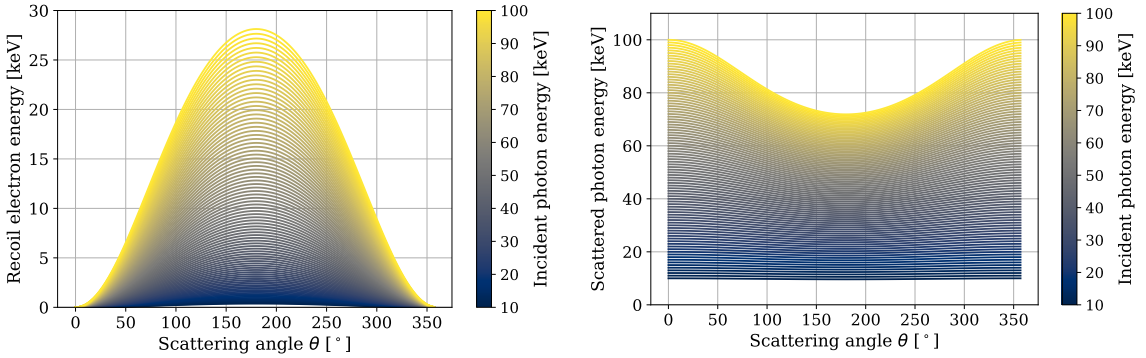

(a) Recoil electron energy in dependence of the energy of the incident photon and the scattering angle.

(b) Scattered photon energy in dependence of the energy of the incident photon and the scattering angle.

Figure 5.2.: Energy transfer of the incident photon to (a) the recoil electron and (b) the scattered photon. The color code states the different incident photon energies. The highest energy transfer to the recoil electron occurs at a scattering angle of 180°.

5.3. Data Analysis

The Timepix3 allows simultaneous measurement of time (ToA), energy (ToT), and position of the interaction of the ionizing particle with the sensor element. The position is stored as a matrix index, which corresponds to a number between 0 and 2^{16}-1. The time information is utilized to analyze coincidences between events. The dead time for a triggered pixel is 475 ns. The deposited energy is used for increased position resolution and for the setting of energy cuts depending on estimations of the expected energy distributions. An analysis is developed that searches for coincident event pairs and determines their azimuth angle in the detector plane.

The Timepix3 data delivers the information about the matrix index, ToA, FToA, and ToT, which are further processed in the analysis. The matrix index is utilized to determine the 2D pixel coordinate (x,y). The y-axis is inverted, i.e., it points to the bottom. ToA and FToA are used to calculate the timestamp of the event in [ns] via

$$t[\text{ns}] = 25 \cdot \text{ToA} - 1.56 \cdot \text{FToA}. \tag{5.1}$$

The energy deposited in [keV] in the pixel is calculated via

$$E[\text{keV}] = \frac{ad + \text{ToT} - b + \sqrt{(b + ad - \text{ToT})^2 + 4ac}}{2a} \tag{5.2}$$

where a,b,c,d denotes the calibration parameters determined according to standard Timepix calibration procedures (see [123]). These units are used in the following as input for the data clustering, which is necessary since charge sharing is predominant in Timepix3 due to its small pixels. The clustering utilizes a nearest neighbor search, which takes place in a 3d parameter space with the coordinates x,y, and timestamp as input. The search categorizes a cluster for the clustering radius r_{clust} and the clustering time t_{clust}. Typically, the parameter for the clustering time is between 100 ns, and 400 ns, depending on the application. The standard parameter for r_{clust} is diagonal pixel pitches ($\sqrt{2}$) for X-rays. It stems from the typical cluster size as described in [124], where photon events in the X-ray regime usually only trigger a center pixel and its direct neighbors due to small track lengths of the secondary electron. Track lengths are approximated by $(E_{\text{e}}/10)^{1.75}$ with E_{e} in keV and the result in microns [125]. For a 80 keV photon a track length of 38.05 µm is expected. It is in the magnitude of the pixel pitch, which implies that only adjacent pixels are potentially triggered as well. If two or more events have been deemed a cluster, then an energy-dependent weighting of the position is performed, resulting in higher spatial accuracy. The position (x,y) of a cluster is calculated as the weighted sum, with the energy in the pixel as the weights:

$$x_{\text{Cl}} = \frac{\sum_i x_i E_i}{E_{\text{Cl}}} \tag{5.3}$$

where the index i denotes pixel i and E_{Cl} the summed energy over all pixel in the cluster. An analogous calculation is performed for the y coordinate. The time of the event with the largest energy is used as the output time t_{Cl}. The output energy of the event is the sum over the energies per pixel E_{Cl}.

After the clustering, another nearest neighbor search is performed with the opposite intention, i.e., the search for spatially separated event pairs. At first, the analysis searches for two coincident event clusters on the pixel matrix. At a certain point in the analysis, a query into the distance between the coincidence events is started. Its clustering time is called the coincidence time window t_{coinc} in the following, and its value is identical to the data clustering. It is varied for estimates of random coincidences since these increase proportional to the time, while real events will reach

their maximum and stay constant from thereon. The nearest neighbor search will output exactly two coincident cluster pairs. Their positions are further processed to apply distance and position cuts in the analysis.

A fiducial area is defined, which is a circular area of radius 127.5 around the center of the pixel matrix. Events in the pixel matrix corners are discarded as they will lead to distance asymmetries. The next decision is made for the distance between the two event points. The event pair must be separated by the distance r_{min}. Events are viable if the length of the connection vector of the coincident event cluster pair is larger or equal to 8-pixel pitches (440 µm). This cut is needed to reduce the systematic uncertainty on the azimuth angle due to pixelation. The systematic uncertainty on the azimuth angle is approximated by $\arctan(0.5/8) = 3.57\,^\circ$ [112], where 0.5 times the pixel pitch is the distance between a pixel center to its edge and eight the minimum cluster distance r_{min} in multiples of the pixel pitch. An azimuth angle bin width of down to about 3.6° is possible. It requires a larger amount of statistics so that all azimuth angle bins are sufficiently filled up. Therefore, the use of larger angle bin widths is more practicable. A bin width of 10 ° is used in the following.

The maximum spread of the scattering angle θ is determined via geometrical considerations. A scattering angle of predominantly 90 ° is expected since the extension of the pixel matrix is much larger than the sensor thickness. Due to the minimum spatial distance between two-pixel clusters, the scattering angle deviation to 90 ° in the sensor computes to $\arctan(300/(8\times55)) = 34.29\,^\circ$, where 300 denotes the sensor thickness in microns and 8×55 the pixel pitch times r_{min}. The expected scattering angle range is therefore $90\,^\circ \pm 34.29\,^\circ$. This range is calculated under the assumption of incidence of the X-ray orthogonal to the sensor element. In reality, the spread will be larger due to different angles of radiation incidence. It can be reduced by increasing the distance between the source and the detector. The spread of the scattering angle and the systematic uncertainty on the angle binning can be further reduced by choosing a larger minimum distance between two pixels. This, in turn, leads to a decrease in the event rate.

The polarization orientation of the impinging X-ray is unknown. Hence, a fixed detector axis is used to calculate the azimuth angle, which allows the determination of the polarization orientation. The reference axis is chosen as the axis orthogonal to the axis of the readout area of the ASIC of Timepix3. In the experiments, it is parallel to the horizontal axis of the laboratory. It is calculated via knowledge of the first interaction point. The event cluster with the smaller energy is chosen as the first interaction point in the following. It results from previous consideration regarding the energy deposition in the sensor via Compton scattering. The second event cluster must carry the remaining energy since coincident event cluster pairs of Compton scattering, and photo-effect are of interest for the analysis. The event that suffices the condition for the first event defines the zero point coordinate of the crossing with the x-axis and the reference axis. A third point is therefore defined with the coordinates $\vec{p_0} = (x_1, 0)^T$. Also, the first point is $\vec{p_1} = (x_1, y_1)^T$, and the

second point is $\vec{p_2} = (x_2, y_2)^T$. The vectors between the first point and the reference axis point $\vec{v_0} = \vec{p_0} - \vec{p_1}$ and the first point to the second point $\vec{v_1} = \vec{p_2} - \vec{p_1}$ are used in the calculation of the azimuth angle. This is illustrated in Figure 5.3. It shows the three points along with the definition of the reference axis and the azimuth angle. It is calculated utilizing the arctan2() function. It takes two inputs which are the determinant $\det(\vec{v_0},\vec{v_1})$ and the dot product of both vectors $\mathrm{dot}(\vec{v_0},\vec{v_1})$. It holds:

$$\phi = \mathrm{arctan2}(\det(\vec{v_0}, \vec{v_1}), \mathrm{dot}(\vec{v_0}, \vec{v_1})). \tag{5.4}$$

Histogramming the calculated azimuth angles ϕ yields a modulation curve similar to Figure 5.1(b). They are typically approximated by a cosine squared distribution in the literature [22]

$$M(\phi) = A\ \cos(\phi - \phi_0)^2 + B \tag{5.5}$$

where ϕ_0 denotes the azimuth displacement with respect to the reference axis, A represents the amplitude (top), and B the offset (valley) of the modulation curve. These two parameters are used to determine the modulation factor μ:

$$\mu = \frac{A}{A + 2B}. \tag{5.6}$$

Its corresponding uncertainty is calculated via uncertainty propagation of the fit parameters and their corresponding fit uncertainties

$$u(\mu) = \frac{2}{(A + 2B)^2}\sqrt{(A\,u(B))^2 + (B\,u(A))^2}. \tag{5.7}$$

The flowchart summarizing the complete data analysis is shown in Figure 5.4.

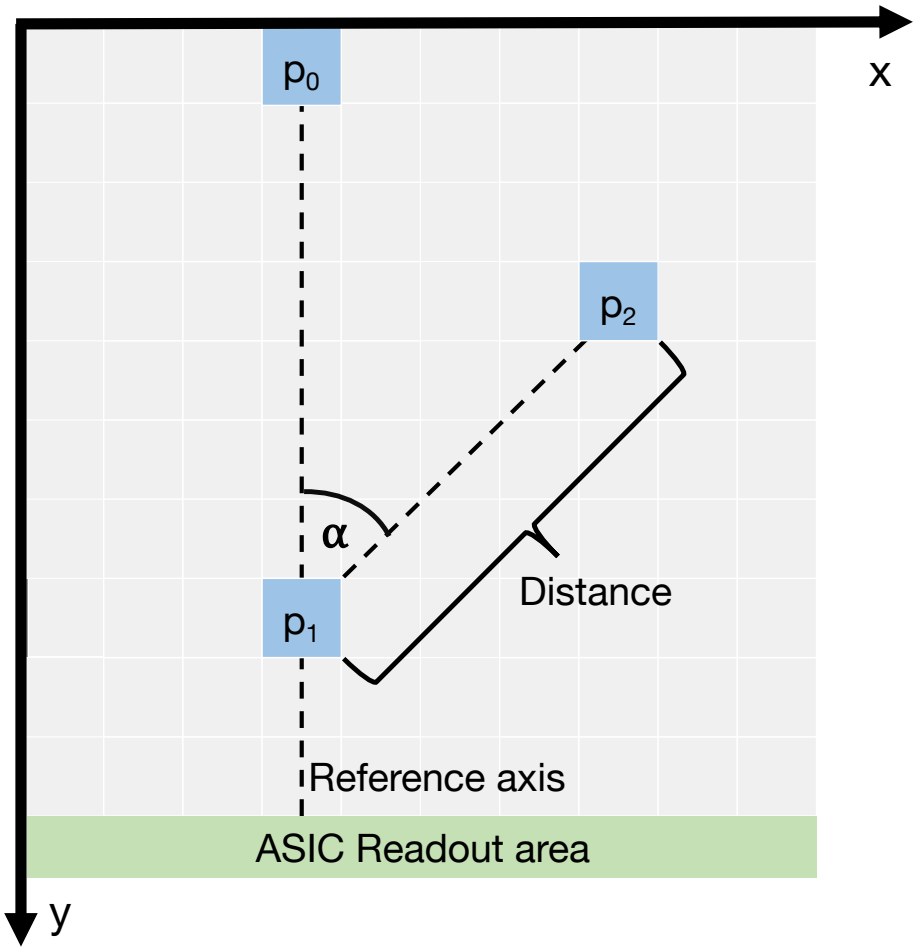

Figure 5.3.: Schematic illustration of the pixel matrix. The two coincident events are stated as positions p_1 and p_2. p_1 additionally defines the point p_0 for the reference axis. These three positions allow calculation of the azimuth angle, here indicated by α. An angle is tolerated if the distance between the coincident events is at least 8 pixels.

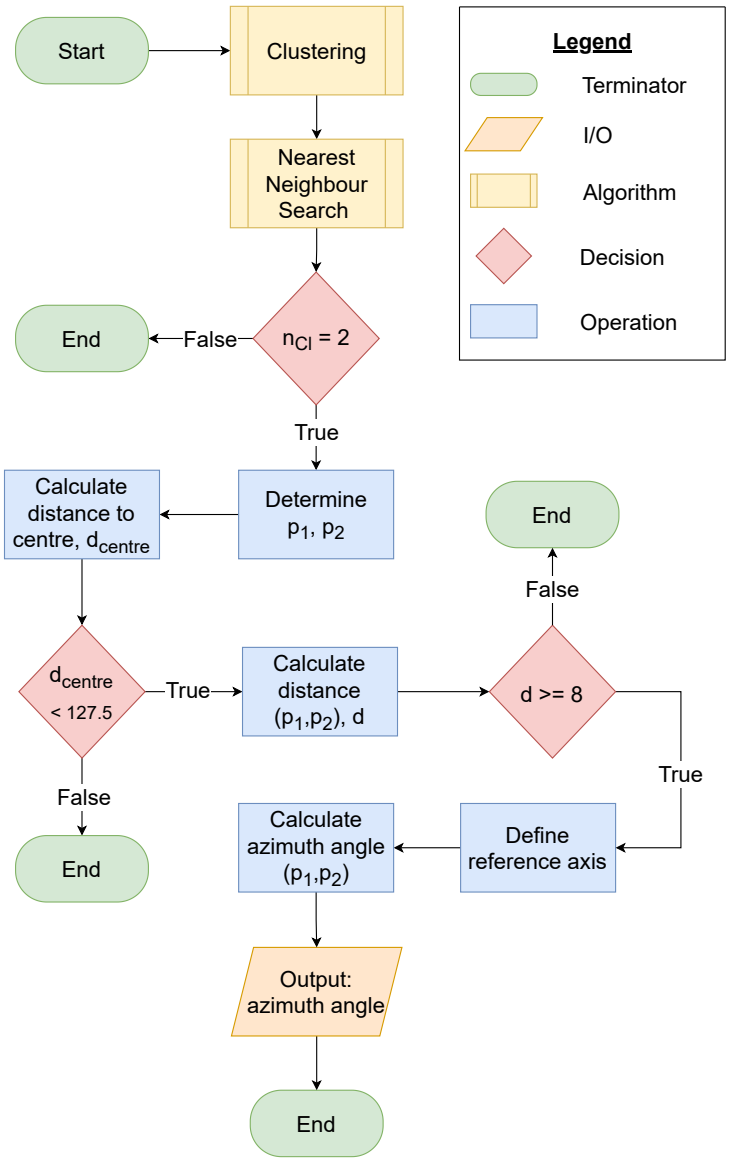

Figure 5.4.: Flowchart illustrating the processes to determine the azimuth angle between two coincident events. Coincident event pairs of a number n_{Cl} equal to 2 are determined via a nearest neighbor search. The positions of both event clusters are utilized to determine the azimuth angle.

5.4. Application of the Analysis to a Toy Simulation

The analysis described in the previous section is tested with random data created by a toy simulation. The aim is to show that the analysis returns the input distribution of the azimuth angle without large deviations.

For this purpose, the time differences are chosen as coincident, and the energy values are random so that both values fulfill the conditions stated by the algorithm. The random parameters are the x and y coordinates of the first event on the pixel matrix, the distance between the positions of the coincident events, and the azimuth angle between the vector of the coincident positions and the vector between the first event and the reference axis. The starting point is a random number between 0 and $2^{16} - 1$ chosen from a uniform distribution. This number corresponds to x and y coordinates on the pixel matrix. The second interaction point is calculated via a distance generated from an exponential distribution and the azimuth angle. The latter one is drawn from different distributions for testing purposes. These are a $\cos^2(\phi)$ and a uniform distribution. All three input distributions are shown in Figure 5.5. The second position is rounded to an integer to recreate the pixelation of the sensor by placing the event in the center of a pixel. The determined azimuth output distribution is shown in Figure 5.6. Additionally, the residuals between the input and output distributions are shown. The histograms of the azimuth distributions have a bin width of 10 °. The number of entries per bin is normalized to the total number of events. This normalization is necessary due to dismissing event positions exceeding the pixel matrix and, therefore, a lower number of reconstructed event pairs than the input number of event pairs. In Figure 5.6(a), a high gradient is found for multiples of 90° between two neighboring bins, which each show large residuals compared to the mean over all values. The uniform distribution approximates unpolarized X-rays. These X-rays will result in a 1D fixed pattern noise of the azimuth distribution. This pattern corresponds to a systematic uncertainty on the angular binning due to the pixelation of the detector. It is canceled in the following by using a correction factor, which is interpreted as the detector's relative geometrical acceptance κ. It corresponds to the mean over all points divided by the point's value per azimuth angle bin.

This 1D fixed pattern noise is also seen in Figure 5.6(b) with the difference that at ±90 ° none is observed because of the zero points of the angular distribution. The relative geometrical acceptance found from the uniform distribution is applied to the $\cos^2(\phi)$ output. It yields a curve corrected to the input distribution with small residuals to said input distribution. Overall, it is shown that the analysis can fully reconstruct input angular distributions. The geometrical acceptance is determined and applied to the output of the analysis to counteract the 1D fixed pattern noise induced by the detector's pixelation. In the next section, the response of Timepix3 to unpolarized X-rays is measured, and the relative geometrical acceptance for real measurements is determined.

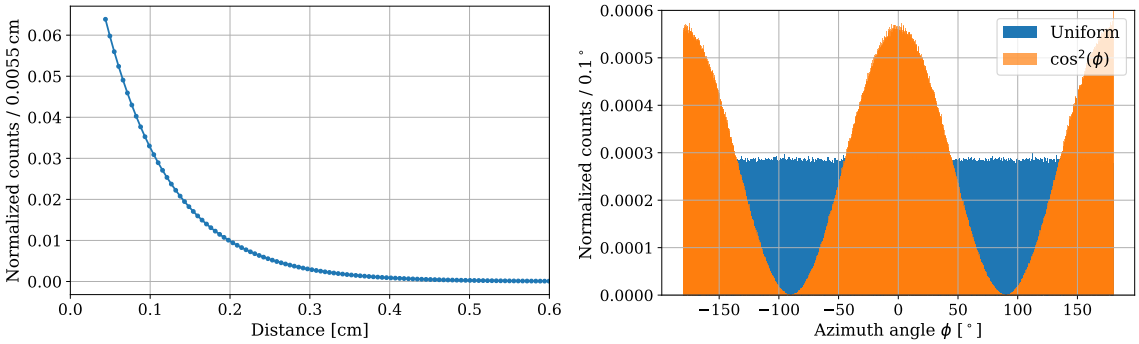

(a) Distance distribution (b) Angular distributions

Figure 5.5.: Input distributions for the toy simulation which are used to draw the randomized event pairs. (a) shows the distance distributions which is assumed as exponentially attenuating. (b) displays the input angular distributions with an uniform and a $\cos^2(\phi)$ distribution. The uniform distribution approximates an unpolarized X-ray beam which shows no preference with respect to the reference axis in the detector, while the $\cos^2(\phi)$ distribution approximates a polarized X-ray beam with a polarization orientation orthogonal to the reference axis.

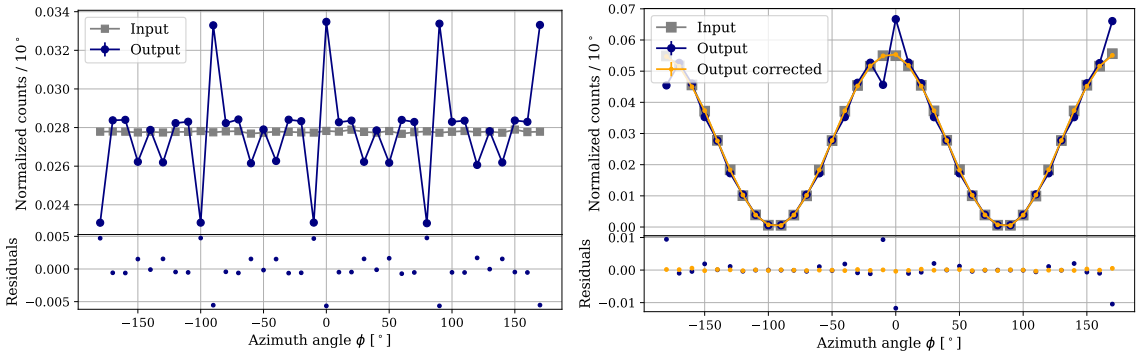

(a) Uniform (b) $\cos^2(\phi)$

Figure 5.6.: Validation of the analysis with well-defined input distributions. The uniform input distribution is reconstructed with a 1D fixed pattern noise due to the pixelation of the detector. The input clusters are always positioned in the center of a pixel. The output of the uniform distribution allows calculation of a relative geometrical acceptance κ for correction per azimuth angle bin. The output (blue) of a $\cos^2(\phi)$ input (b) also shows the systematic uncertainty which is corrected via κ (orange). The correction minimizes the fluctuation of the residual between the input and corrected output distributions.

5.5. Measurement of Unpolarized X-rays

Due to the pixelation of the Timepix3, certain angles are preferred when determining the azimuth angle. This means that a non-uniform geometrical acceptance in the azimuth angle is observed when binning a uniform angular distribution. The effect was already demonstrated and corrected for a toy simulation. Latter assumes a perfect detector without dead pixels, no real energy correlations between the coincident events, no charge carrier transport, and no temperature dependence. All events are assigned to the pixel center, equal to an event cluster of size 1. Since charge sharing exists in the real detector, cluster sizes larger than one are observed. These event clusters are utilized to improve the position resolution in the following.

A real photon field is now used to determine the geometrical acceptance of the azimuth angle binning. An unpolarized photon field shows no preference axis of the electric field and, therefore, no preference of the azimuth angle. The lack of a preference orientation results in a uniform azimuth distribution in the detector, optimal for determining the geometrical acceptance. The Timepix3 is irradiated by an ^{241}Am source with an activity of 1.1 GBq. Its energy observed by the detector is the predominant γ-decay radiation of 59.54 keV [126].

When dealing with monoenergetic photons, a viable option for the analysis is employing energy cuts. The first event is Compton scattering, i.e., the energy of the first event cannot exceed 11.25 keV, which corresponds to the Compton edge for 59.54 keV. With this information, an energy cut can be applied to the first interaction, which stays below the Compton edge. As Compton scattering followed by photoelectric effect interaction pairs are searched, a second condition states that the sum of the coincident event cluster pair must be 59.54 keV. The detector resolution has to be taken into account when applying the cuts. One possible way to state the conditions is also 14.5 keV for the first condition and the range of 56-63 keV for the second. Finding the correct conditions depends on precise knowledge of the detector parameters and the ambient conditions. The energy calibration must be precise, measurements must be performed at the temperature of the calibration, and the energy dependence of the detector resolution must be known for this approach to be feasible. Furthermore, it is easy to state conditions for monoenergetic photons, but it becomes more sophisticated for broad spectra, typically occurring. The energy threshold of 3 keV limits the lower energy range for the polarimeter since the incident photon must have an energy sufficient to deposit at least said 3 keV in a pixel.

Another approach used for the remainder of the chapter is calculating the Compton scattering angle θ. The information used is the sum of energies of both event clusters, which corresponds to the energy of the incident particle, and the energy of the scattered photon, which corresponds to the energy of the second event cluster since this is the event of the photoelectric effect. Knowing the energy of the incident photon and the energy of the scattered photon allows the calculation of the Compton scattering angle θ. The equation used is

$$\cos(\theta) = 1 - m_e(1/E'_\gamma - 1/E_\gamma) \tag{5.8}$$

where m_e=511 keV denotes the electrons rest mass, E_γ the energy of the incident photon and E'_γ the energy of the scattered photon. Event pairs are discarded whose energy correlation results outside the definition domain of the arccos(x) function, which is $[-1, 1]$. The distribution for the Compton scattering angle is calculated for the ^{241}Am measurement and is shown in Figure 5.7. The analysis parameters are a clustering time and a coincidence window of 202.8 ns, and a minimal pixel distance of 8 pixels. As previously estimated, the scattering predominantly occurs at 90° in the 300 µm silicon sensor. The distribution is skewed towards backscattering (180°) and ends abruptly below 55° The scattering angle range previously estimated via purely geometrical assumptions is between 55.71° and 124.29° which corresponds well with the measurement. The geometrical estimation assumes a normal incidence of the incoming X-ray. This is not the case in the underlying measurements, which results in a larger acceptance range of Compton scattering angles and explains the tail toward larger scattering angles. Since energies are used to calculate the scattering angle, a broadening of the distributions is expected due to the detector's energy resolution, which is the major influence on the observed shape. For this particular energy, it is to be noted that the 3 keV recoil electron energy is achieved for a scattering angle of around 57° which corresponds to the observation of the cut off towards lower scattering angles. Therefore, the energy threshold and the incident photon energy limit the range towards lower Compton scattering angles.

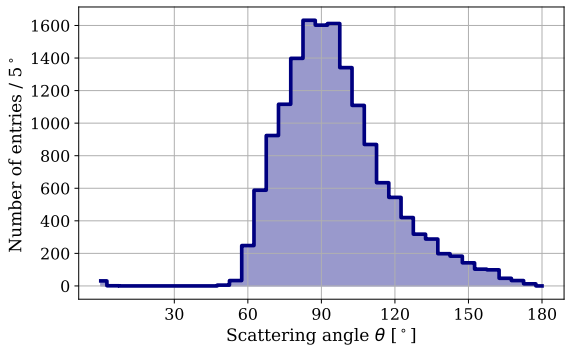

Figure 5.7.: Distribution of the Compton scattering angle in the 300 µm silicon sensor of Timepix3. The scattering angle is calculated according to Equation (5.8).

The corresponding energy histograms of each event cluster and their sum are shown in Figure 5.8. It represents well the previously mentioned assumptions towards the energy cuts, which are realized by restriction of the Compton scattering angle to valid energy correlations between the events. All energies for the first event cluster are

below the energy of the Compton-edge. The second event represents the scattering peak. The total energy is well around the theoretical energy of 59.54 keV.

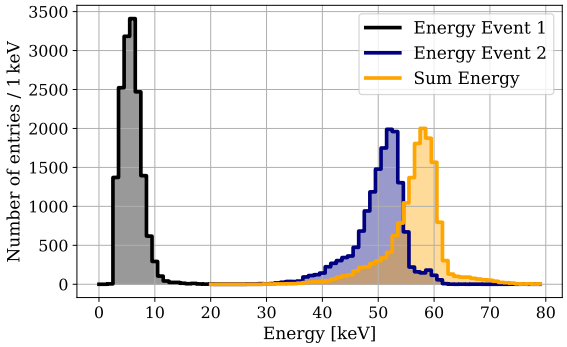

Figure 5.8.: Energy histograms of the first and second event cluster and their summed energy for the irradiation with unpolarized photons of ^{241}Am. It represents the interaction sequence Compton scattering followed by photoelectric effect in the sensor volume of Timepix3.

The contribution of random coincidences (accidentals) to the event rate is determined next. This procedure is used in the following for all presented measurements. The rate of accidentals is assumed as constant. Increasing the coincidence window will increase the number of accidentals linearly. Above a saturation coincidence time, the contribution of real coincidences to the event rate will remain constant, which allows the determination of the rate of accidentals via a linear fit. The analysis is performed with different coincidence time windows, sampled between 0 ns, and 474.24 ns. The event rate of coincident cluster pairs in dependence of the coincidence time window is shown in Figure 5.9. A linear fit is performed for coincidence time windows above 102.96 ns. The event rate is subtracted by the determined rate of accidentals. A constant coincidence rate is observed after corrections. The best choice for the value of the coincidence time window is a multiple of the time resolution (1.56 ns) between 102.96 ns and 202.8 ns. In this range, the constant coincidence rate is achieved, i.e., all values above 102.96 ns can be chosen, as long as a correction is performed. The rate of accidentals in the case of this measurement is determined to (0.0040±0.0002) Hz/ns.

The data clustering is performed for a clustering time of t_{clus}=202.8 ns. The clustering is used once with and without an energy-weighted position determination. When the position is not energy weighted, the center of the pixel with the highest energy is assumed as the pixel position. The relative geometrical acceptance κ is calculated to correct the 1D fixed pattern noise. It is the ratio between the mean number of coincident cluster pairs in all bins and the number of coincident cluster pairs in the azimuth angle bins. Figure 5.10 shows the azimuth distribution for the measurement of ^{241}Am. The angular distribution is corrected by κ, which results in the mean. The azimuth angle bins have a bin width of 10 °. No distinct modulation curve is observed, which implies unpolarized X-rays. The residuals of the mean, to which the angles bins are corrected, and the measured distribution is calculated and shown in the

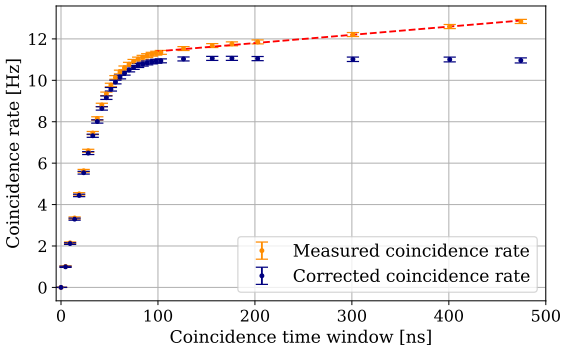

Figure 5.9.: Determination of the rate of random coincidences (accidentals). The measured coincidence rate is shown in orange and the corrected one in blue. After saturation of the event rate of coincidence cluster pairs is is assumed that every further contribution is attributed to accidentals. The rate of accidentals is constant. Increasing the coincidence window increases the number of detected accidentals. A linear fit (red dashed line) is used to determine the accidental rate, which is utilized for the correction of the event rate. The determined rate of accidentals is (0.0040±0.0002) Hz/ns.

lower panel of the plot for each measurement. Their fluctuation around zero becomes smaller for the energy-weighted analysis. The standard deviations of the residuals are 0.085 and 0.074 for the unweighted and weighted analysis, respectively. This shows that the energy-weighted analysis reduces the systematic uncertainty of the angular binning. The relative geometrical acceptance depends on the analysis parameters. If these are changed, a new relative geometrical acceptance must be calculated. For the relative geometrical acceptance shown in Figure 5.11, the analysis conditions are of r_{min}=8, t_{coinc}=202.8 ns, t_{clust}=202.8 ns, energy weighting on, minimum energy as primary interaction point, and binning of 10 °. The maximum and minimum of κ are 1.23±0.07 and 0.85±0.04, respectively. The introduction of the geometrical acceptance and knowledge of the random coincidence rate allows performing corrections to the azimuth angle bins. The correction factor for accidentals c_i for azimuth bin i is given as

$$c_i = \frac{\dot{N}_{\mathrm{acc}}}{\kappa_i \cdot n_{\mathrm{bins}}} \tag{5.9}$$

where $\dot{N}_{\mathrm{acc}}$ denotes the event rate of accidentals, κ_i the relative geometrical acceptance for azimuth bin i, and n_{bins} the number of azimuth angle bins.

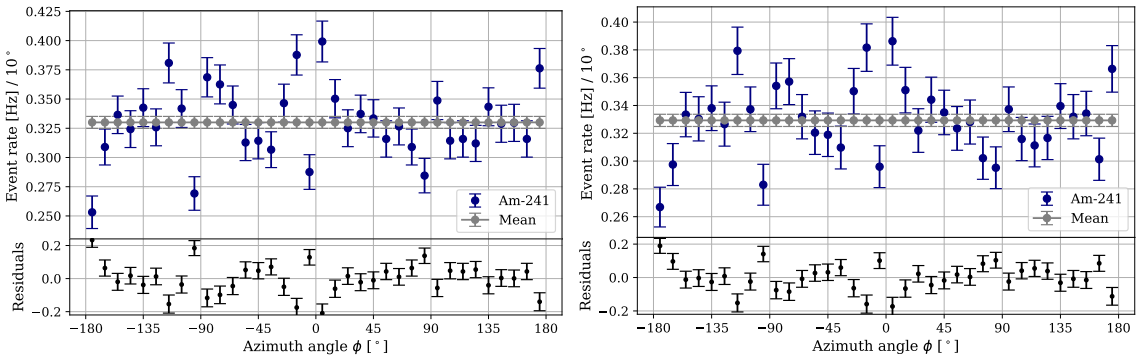

(a) Unweighted clustering (b) Energy weighted clustering

Figure 5.10.: Modulation curve for unpolarized X-rays isotropically emitted by an ^{241}Am source. The uncertainty is the Poisson uncertainty on the counted events. The mean is shown as the value to which the curve is corrected by the correction factor. Its uncertainty is the uncertainty on the mean. In (a) the pixel position with the highest energy is chosen as event point and in (b) energy weighting is performed. The fluctuation decreases with the energy weighting which counteracts the 1D fixed pattern noise introduced by the pixelation.

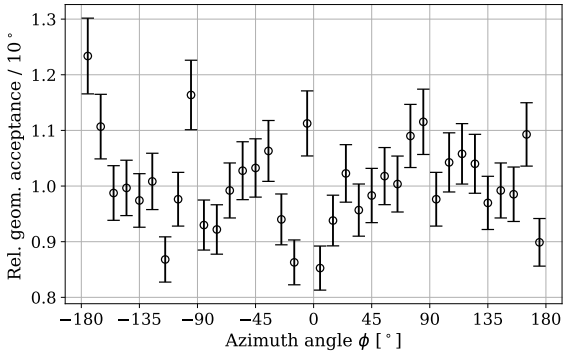

Figure 5.11.: Relative geometrical acceptance κ determined for the measurement of unpolarized X-rays of ^{241}Am. The analysis parameters are r_{min}=8, t_{coinc}=202.8 ns, t_{clust}=202.8 ns, energy weighting on, and binning of 10 °. Maximum and minimum values of κ are 1.23±0.07 and 0.85±0.04.

5.6. Proof of Polarization Measurements

The method of creating a polarized field, determining if it is polarized and calculating its modulation factor μ is performed in this section. The polarized X-rays are created by scattering an unpolarized photon beam with a PMMA target. A cuboid of 1 cm diameter is used for this purpose. The incident photon field is a 100 kV X-ray spectrum of a MEGALIX Cat [70] tungsten anode X-ray tube filtered with 1 mm iron and 1.5 mm aluminum applying a tube current of 10 mA. Its beam spread is confined by a lead collimator of 1 mm diameter. The detector is positioned on an optical table at the same height as the collimator exit at a 90° degree to the connection line between the source focus and the target center. Its detection plane is rotated by 90° around the connection line between the target center and detector surface center. This rotation is needed to verify if the observed modulation is detector and algorithm induced or due to the polarization of the detected X-rays. If the photon field is linearly polarized, then the electric field will show a predominant axis in the detector plane. Rotating the detector by 90° should displace the modulation curve by 90° due to the fixed reference axis of the detector. With that, the capability of polarimetry is demonstrated, and the proof of polarization is provided.

Figure 5.12 shows the measurements for horizontal (0° rotation, reference axis parallel to the horizontal axis in the laboratory) and vertical (90° rotation) detector orientation. The uncertainties denote the Poisson uncertainty on the number of measured coincident events in an azimuth angle bin. The utilized analysis parameters are a minimum pixel radius of r_{min}=8, a coincidence time window of t_{coinc}=202.8 ns, a data clustering time of t_{clust}=202.8 ns, energy weighting on, and a binning of 10 °. The correction of the geometrical acceptance of the detector is applied to the azimuth angle bins. Furthermore, no background subtraction is performed. This means that X-rays coming directly from the tube or X-rays scattered in the measurements chamber with a unknown degree of polarization interact in the detector and lower the determined modulation factor. The curve is displaced after the detector is rotated. The calculated azimuth displacement is 92.17°±1.60° and -1.32°±1.54° for the measurements of the horizontal and vertical orientations, respectively. The uncertainties are the uncertainties of the fit. The horizontal orientation displays a $\sin^2(\phi)$ distribution with small azimuth displacement. The azimuth displacement for the vertical orientation is 0° within its uncertainty. The rotation of the detector by 90° results in a 90° rotation of the modulation curve within its uncertainties. Small deviations within several degrees are acceptable since systematic uncertainties arise due to the rotation of the detector and an associated misalignment of the sensor plane. The expected result is observed, which proves a linear polarized photon field. Modulation factors of this linearly polarized X-ray field are 0.63±0.03 and 0.69±0.03 for the horizontal and vertical orientation, respectively. Both modulation factors deviate noticeably from each other and only agree within their uncertainties at an extreme case. The horizontal measurement is slightly asymmetric and shows an excess of events at about

90°. In Section 5.8 it will be shown that this excess results from the background rate of the measurement, which is not determined for this set of measurements.

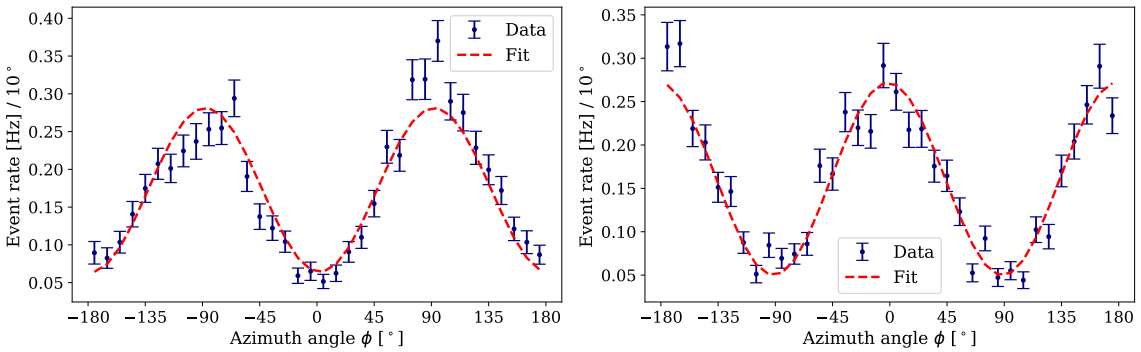

(a) Horizontal orientation

(b) Vertical orientation

Figure 5.12.: Proof of polarization measurements with horizontal (0° rotation, reference axis parallel to the optical table) and vertical (90° rotation) orientation of the detector.

The setup is optimized in the following section to study different target diameters, which correspond to different source extensions. Furthermore, background measurements are performed to correct diffuse scattering in the measurement chamber. It is concluded from these measurements that Timepix3 detects polarized X-rays. Therefore, the following measurements will take place without rotation of the detector.

5.7. Optimized Polarization Setup

The X-ray source used is a MEGALIX Cat [70] with a tungsten anode for application in angiography. Photons emitted by an X-ray tube are unpolarized. A linear polarized photon field is produced by scattering off a target. The scattering targets are PMMA round bars (cylinders) of different diameters. The different diameters emulate different source extensions as the acceptance range of the angle incident to the detector increases with the target diameter. Moreover, having different diameters allows using a single setting of the X-ray tube while the photon flux increases via the target diameter. With that, only a single measurement of the background rate, i.e., without a target, is necessary. This minimizes the exposure time with the X-ray tube since the background measurements are time-consuming. The used diameters are 5 mm to 20 mm in 5 mm steps. PMMA has a low Z and consequently a high interaction probability of Compton scattering in the investigated X-ray regime. To yield sufficiently high contributions of photons interacting via Compton scattering in silicon, a 100 kV tube voltage is used. The photon field is beam-hardened to suppress low energy contributions. A total filtration of 4.4 mm aluminum is used. The tube current is set to 3 mA.

The degree of linear polarization states which percentage of the ensemble are linearly polarized and is calculated using the Compton scattering angle according to [113]:

$$P_{\mathrm{DOP}} = \frac{\sin^2\theta}{E/E' + E'/E - \sin^2\theta}. \tag{5.10}$$

where θ denotes the scattering angle, E the energy of the incident photon, and E' the energy of the scattered photon. Figure 5.13 shows the incident photon spectrum and its corresponding degree of polarization for different photon energies. Scattering the incident photon field at 90° will result in a fully linear polarized photon field for the investigated energies. Increasing the angular acceptance, i.e., allowing an increased range of scattering angles, decreases the degree of polarization. This means that the angular acceptance of the scattered photons impinging onto the Timepix3 must be small. This is realized by a large distance between target and detector.

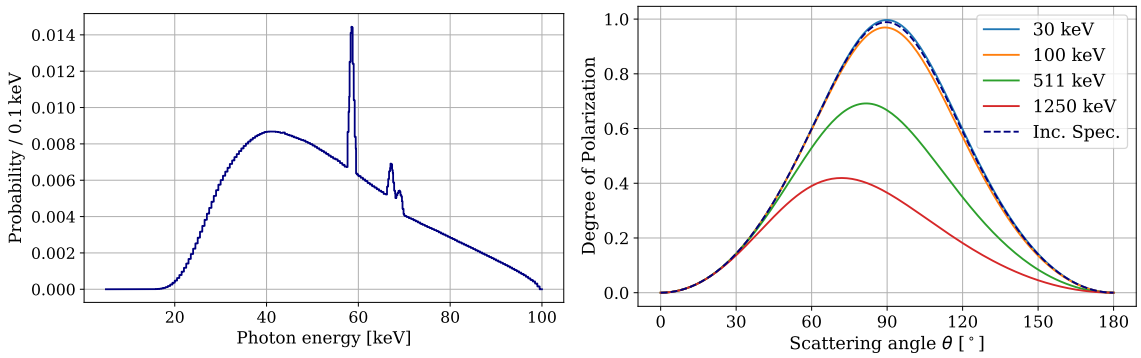

(a) Incident spectrum.

(b) Degree of Polarization.

Figure 5.13.: The incident photon spectrum for the following investigations in (a). This spectrum is used to calculate the degree of linear polarization in dependence of the scattering angle according to Equation (5.10). Other energies are used for comparison.

The Timepix3 is positioned at a distance of 22 cm at an angle of 90° to the target, fixed to an aluminum rail. This allows positioning the target in and outside of the beam. Every measurement with a target needs a measurement without the target to estimate the background rate. A lead brick collimator (10 cm × 10 cm × 5 cm) with a hole of 1.6 cm in diameter is used to minimize the background scattering rate. This lead brick is additionally equipped with a tungsten collimator ($\varnothing$= 1.6 cm , thickness = 2 mm) with a hole of 2 mm in diameter. The collimator system is used to narrow the photon beam impinging on the PMMA target. The distance between the collimator exit and the target center is 10 cm. Additionally, several lead bricks are positioned along

the beam path on the side of the detector to suppress the background rate further. The collimator-target and target-detector axes are aligned via adjustment lasers. Both laser beams penetrate through the center axis of the cylinders. The X-ray beam impinging onto the sensor element of the Timepix3 is softened due to Compton scattering off the target. The complete setup is schematically illustrated in Figure 5.14.

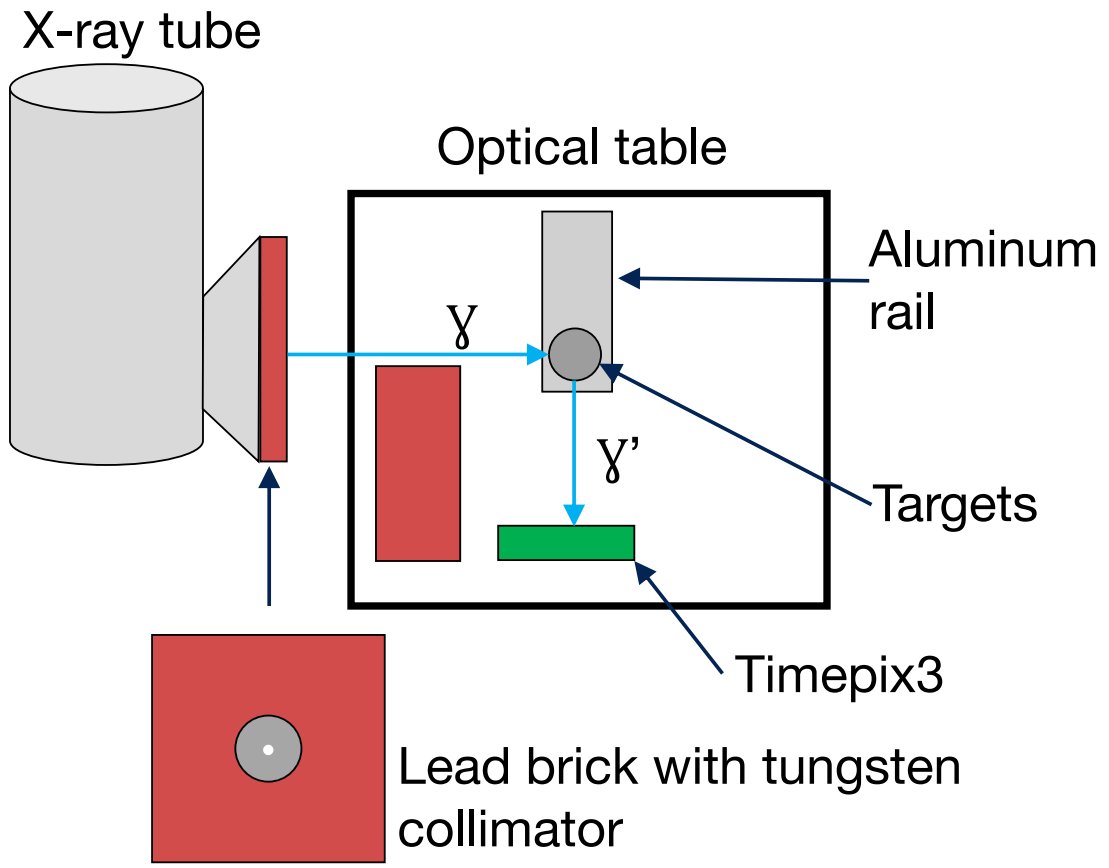

Figure 5.14.: Schematic illustration of the polarization setup. A beam hardened and collimated unpolarized X-ray beam scatters off a PMMA target to polarize it. The beam is linearly polarized post scattering. This polarization allows the investigation of the azimuth angle dependence in the sensor element. The angular dependence is described by the Klein-Nishina cross-section. Lead bricks are used to suppress background rate of direct radiation and multiple scattering exposure of the tube X-rays.

The setup is simulated with Geant4. It is a software toolkit that simulates the passage of particles through matter [127, 128, 129] and is utilized to interpret the measurements and assess the setup in the laboratory. First, the angular distribution of the collimator system is simulated. The used physics list is polarized Low Energy Liv-

ermore. It takes all photon interactions with respect to polarization into account. The source behind the collimator is positioned at the representative position of the setup, equal to the X-ray tube's focus point. It is positioned at x =-23.3 cm relative to the center of the target position. The photon beam travels along the x-axis in a positive direction. A plane is spanned over the y-z plane at $x = 0$, used as the detection plane, also called ghost volume. The material of the plane is vacuum. The photon is killed if it hits this plane. Its position, energy, and angular distribution impinging on the ghost volume are stored. The source emits photons isotropically with the limitation of the direction of the collimator to reduce computation time. Figure 5.13(a) already showed the incident spectrum. Furthermore, the position and angular distribution are shown in Figure 5.15. The radius of the irradiated spot is 1.75 mm and a small full opening angle of 0.8°. Such a small spot allows a low background rate and precise irradiation of small targets. An optimal target, in this case, would have a diameter of 3.5 mm.

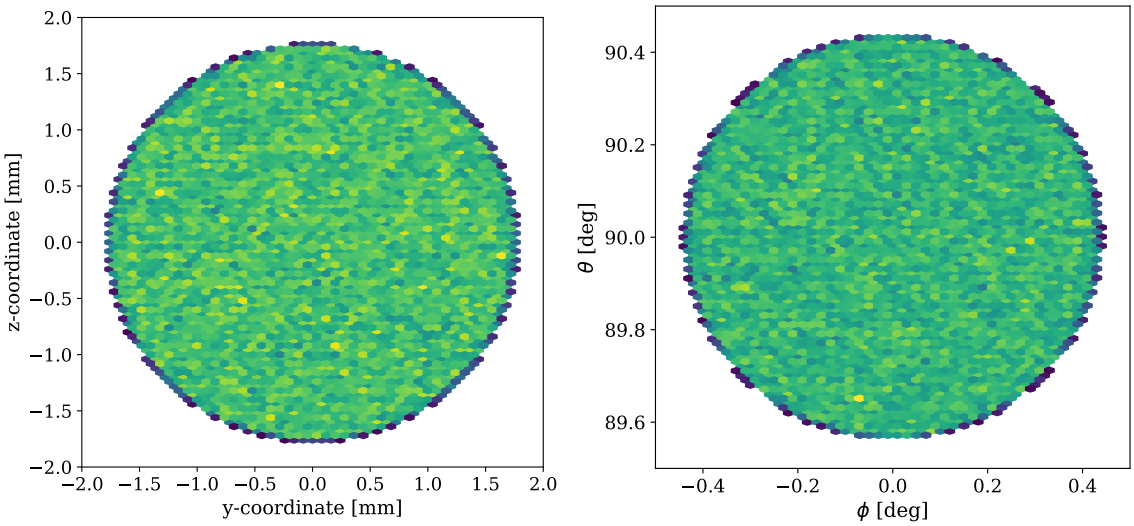

(a) Position distribution

(b) Angular distribution

Figure 5.15.: Collimator distributions at the center plane of the targets. The collimated spot is small compared to the diameter of the targets.

In the second step, the scattering in the PMMA targets is simulated. The source is the previously stated collimator, and the determined angular distribution is used to irradiate the targets. Latter ones are positioned in the center of the world volume, and their thicknesses are varied. The detector is a ghost volume at the position and size of the Timepix3 in the measurement, which is at a distance of 22 cm. All events impinging in the ghost volume are killed, and the Compton scattering angle and the energy are stored. Figure 5.16 shows the distribution of the accepted Compton scattering angle and the scattered energy spectrum for each target diameter. Since the collimator is confining the incident distribution and the target detector distance is large with 22 cm, the scattering angle is around 90 °. The width of the distribution

increases with the target diameter since the interaction positions along the direction of the incident X-ray span a wider range. This skews the mean of the distribution to lower values since the incident beam is attenuated along its trajectory by the scattering target. The expected energy range of scattered events impinging onto Timepix3 is about 20 keV to 80 keV. This, together with the energy of the primary photon, allows the calculation of the degree of linear polarization according to Equation (5.10). The average degrees of linear polarization are 0.987±0.014 for 5 mm, 0.985±0.018 for 10 mm, 0.983±0.022 for 15 mm, 0.980±0.027 for 20 mm. The uncertainty denotes the standard deviation. These values serve as orientation.

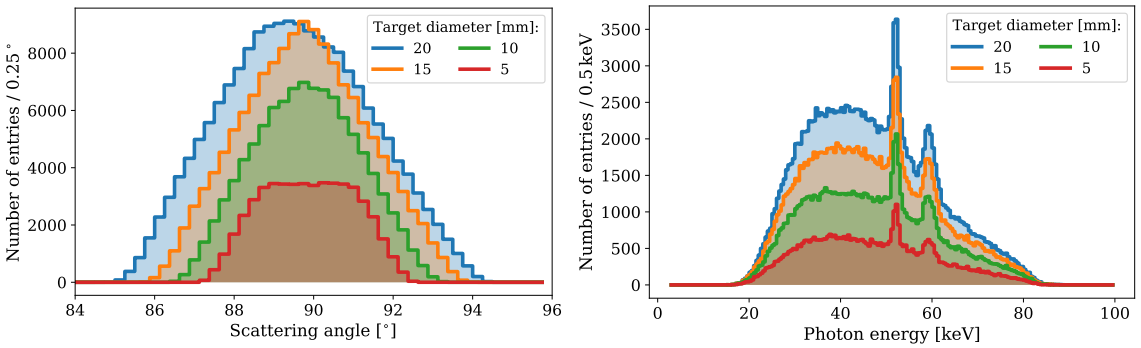

(a) Scattering angle

(b) Energy spectra

Figure 5.16.: Distributions of the accepted Compton scattering angle θ in the PMMA target (a) and the energy distribution of the scattered X-ray (b) for the for different target diameters.

5.8. Measurement of Polarized X-rays with Background Subtraction

This section presents the measurements with the four different target diameters. Additionally, a background measurement without a target is performed, missing for the proof of polarization measurements. It is used to subtract the background contribution for every azimuth angle bin. The analysis parameters are a minimum pixel distance of r_{min}=8, a data clustering time of t_{clust}=202.8 ns, energy weighting on, and an azimuth angle binning of 10 °. All measurements are analyzed with the same parameters. The first interaction point is important since it defines the crossing point of the reference axis with the x-axis on the pixel matrix. The event with the smaller energy E_{min} is used. A cut via the determination of the scattering angle is applied to the data. The base assumption is that the energy correlation between the second event and the sum energy of both events used to calculate the Compton scattering angle via Equation (5.8) is within the definition domain of the arccos(x) function. This cut is called θ cut in the following. All uncertainties declared in the

scope of this section are assumed as the Poisson uncertainty $\sqrt{n_i}$ on the number of measured coincident event cluster pairs n_i in the azimuth angle bin i. Appropriate uncertainty propagation is performed whenever a new quantity is calculated.

The background measurement is analyzed first. The coincidence time window between the event cluster pairs used to calculate the azimuth angle is sampled between 0 ns, and 474.24 ns. The coincidence event rate is determined for every coincidence time window by taking the sum over all azimuth angle bins and dividing it by the exposure time. The coincidence rate in dependence of the coincidence time window of the background measurement is shown in Figure 5.17. It illustrates the coincidence rate with and without θ cut. After applying the cut, the measured coincidence rate is reduced by 2.33±0.2. The linear correction fit for the accidental rate is already applied the same way as previously demonstrated for the measurement of the unpolarized X-ray source. A linear increase of the event rate is observed between 0 ns, and about 50 ns. After this, it begins to saturate and becomes constant at about 126.36 ns. A coincidence time window of 202.8 ns with the application of appropriate corrections for the accidental rate is used in the following. Accidental rates of $(9.1\pm0.8)\cdot10^{-6}$ Hz/ns and $(1.0\pm0.6)\cdot10^{-6}$ Hz/ns are determined for the analysis conditions without and with the application of the θ cut respectively. The event rate of accidentals is reduced by a factor of 9±5 after applying the θ cut. It is, therefore, a strong tool in the rejection of random coincidences in the detector. Random coincidences will have an arbitrary energy correlation, which is rejected by restricting the analysis on coincident event cluster pairs with an energy correlation defined by Compton scattering.

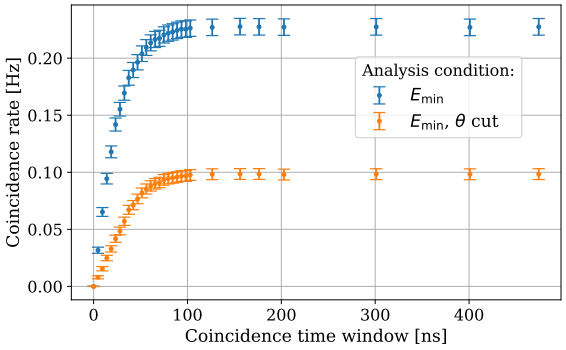

Figure 5.17.: Coincident rate in dependence of the coincidence time window for the two event cluster pairs. The underlying measurement is a background measurement, i.e., without target. The two different analysis conditions are the minimum energy and the minimum energy with application of the θ cut, which is determined via the energy correlations of the two coincident event cluster pairs.

With a coincidence time window of 202.8 ns, the analysis is performed for the background measurement. Figure 5.18 shows the determined Compton scattering angle, the energy distribution of the coincident event cluster pairs, the recorded modulation curve, and a 2D histogram of the Compton scattering angle and the azimuth

angle. The Compton scattering angle shown in (a) is broader than the one seen for the unpolarized X-ray source. The left flank is appropriately positioned and cuts off at about 60°. Moreover, scattering angles of up to 170° are observed on the right flank. According to the geometrical estimation for irradiation on the front side of the detector, such angles should occur only in a moderate amount due to the detector's energy resolution. The bulk of events at around 90° indicates that the source of irradiation partially stems from scattered radiation whose direction is normal to the front side of the detector. Another contribution explaining the right flank of the distribution stems potentially from irradiation of the side of the detector. This is reinforced by the modulation curve shown in (c), which shows an asymmetry for positive azimuth angles. The modulation curves asymmetry indicates preferred irradiation of one part of the sensor element. In this case, the X-rays must stem from above of the setup. This means that the direct X-ray beam is scattered on the ceiling or the chamber walls and detected by Timepix3. This would mean that the collimator did not fully cover the tube exit, and gaps were present. The 2D histogram shown in (d) indicates that the events at larger scattering angles θ correlate with the excess events at positive azimuth angles ϕ. This observation is not significant enough since the number of events is small, corresponding to large uncertainties. A modulation factor is measured, which corresponds to the scattering of the primary X-ray beam in the measurement chamber. Its modulation curve is fitted via Equation (5.5). The parameters A and B are used to calculate the modulation factor and its corresponding uncertainty via Equation (5.6) and Equation (5.7) as 0.35±0.07. The modulation is rather high for background radiation. This means that the source of the X-ray background is a combination of diffuse scattering and distinct scattering at an element in the measurement chamber. Furthermore, the fit determines the parameter ϕ_0 representing the azimuth displacement with respect to the reference axis. Its is $\phi_0 = 80.51° \pm 7.27°$. The large uncertainty is explained by the asymmetry of the modulation curve, which favors azimuth angles of $\phi > 0°$, and the low statistics. The energy distributions shown in (b) display the expected energy ranges for the first and the second event. Also, the sum energy is within the expected range of scattered X-rays emitted by the 100 kVp primary X-ray spectrum.

Now, the data from the measurements of polarized X-rays for different PMMA targets is investigated. Their coincidence rate is calculated as the difference between the coincidence rate of the target and the coincidence rate of the background. Figure 5.19 shows the corresponding coincidence rates in dependence of the coincidence time window in (a) without cuts and the minimum energy of the event as the initial condition, and in (b) after application of the θ cut. The linear correction fit for the accidental rate is already applied for all curves. The corresponding accidental event rates and the ratios are summarized in Table 5.1. It shows a reduction of the accidental rate between 6.5±1.5 and 18.7±2.2 depending on the target. After applying the θ cut the coincidence rate is reduced by the factors of 2.8±0.1, 2.4±0.1, 2.3±0.1, 2.4±0.2 for the 2.0 cm, 1.5 cm, 1.0 cm, and 0.5 cm target diameters respectively.

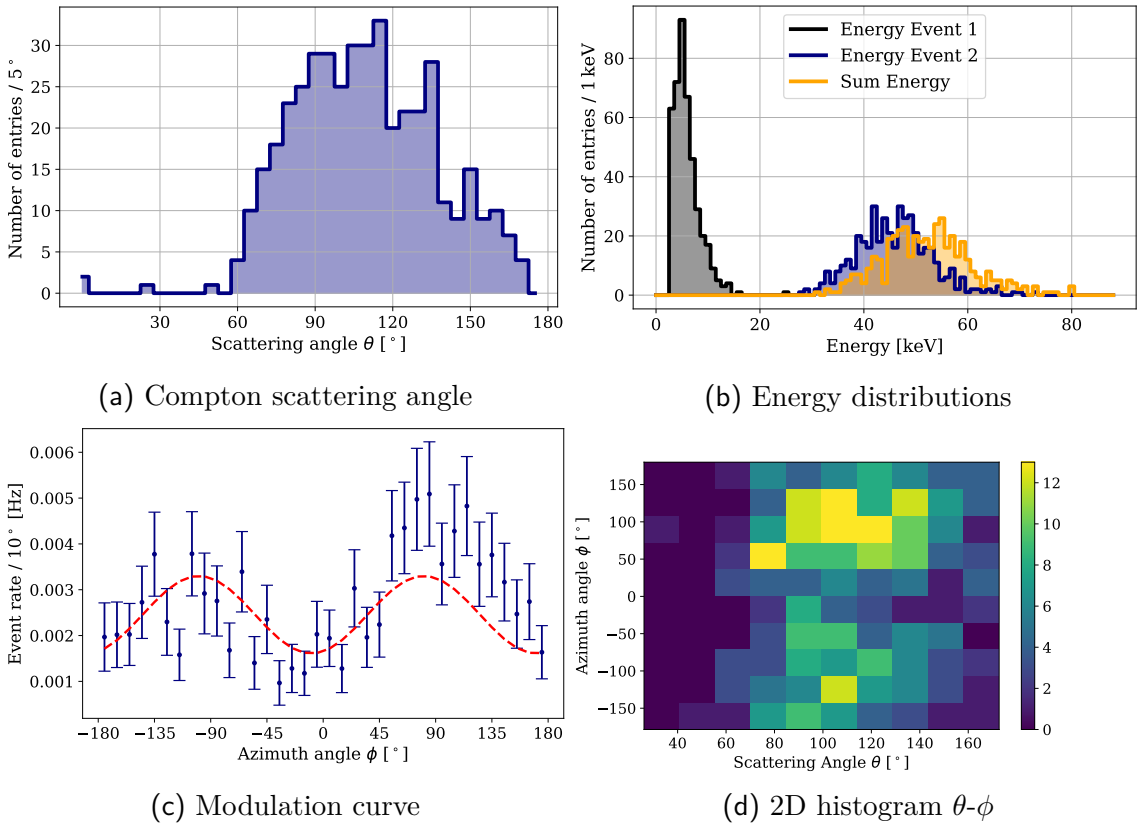

(a) Compton scattering angle

(b) Energy distributions

(c) Modulation curve

(d) 2D histogram θ-ϕ

Figure 5.18.: Distributions of the Compton scattering angle θ in the sensor element of Timepix3 in (a), the energy distributions for the coincident event cluster pairs and their sum energy in (b), the recorded modulation curve of the azimuth angle ϕ in (c), and the corresponding 2D histogram for the Compton scattering angle θ and the azimuth angle ϕ in (d) for the background measurement.

Target ⌀[cm]	$\dot{N}_{\text{acc}}$ [Hz/ns]	$\dot{N}_{\text{acc}}$, θ cut [Hz/ns]	Ratio
2.0	$(13.2\pm0.2)\cdot10^{-3}$	$(1.2\pm0.1)\cdot10^{-3}$	11.2±0.5
1.5	$(3.4\pm0.1)\cdot10^{-3}$	$(3.5\pm0.3)\cdot10^{-4}$	9.9±0.8
1.0	$(9.7\pm0.2)\cdot10^{-4}$	$(5.2\pm0.6)\cdot10^{-5}$	18.7±2.2
0.5	$(1.8\pm0.1)\cdot10^{-4}$	$(2.8\pm0.7)\cdot10^{-5}$	6.5±1.5

Table 5.1.: Accidental event rates for the different target diameters. It is determined for the minimum energy as a condition for the first interaction points with and without applying the θ cut. Uncertainties denote the corresponding uncertainty of the fit. For the uncertainty of the ratio, uncertainty propagation is performed.

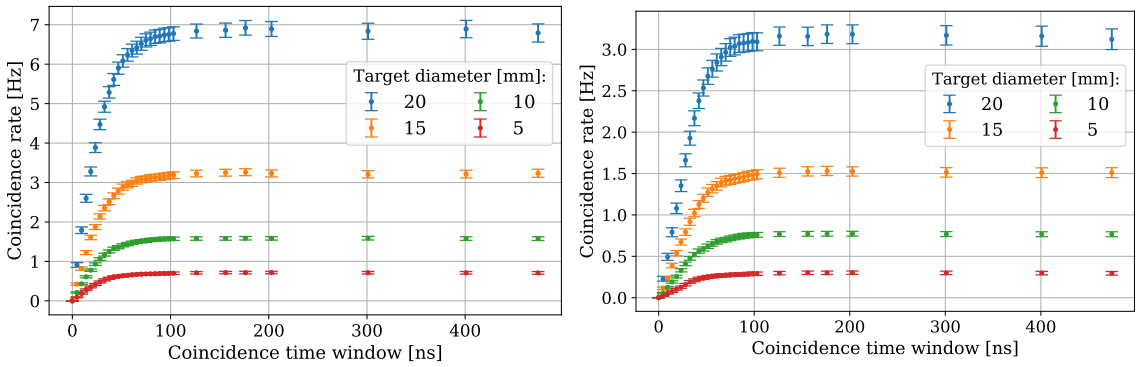

(a) No cuts (b) θ cut

Figure 5.19.: Coincident rate in dependence of the coincidence time window for the two event cluster pairs. The underlying measurements are for the different target diameters. The coincidence rate is shown in (a) without cuts and the minimum energy as condition for the first interaction points and in (b) with application of the θ cut, which is determined via the energy correlations of the two coincident event cluster pair.

Figure 5.20 shows the Compton scattering angle in the sensor element of Timepix3 (a), the energy distribution of the coincident event cluster pairs (b), the recorded modulation curve (c), and a 2D histogram of the Compton scattering angle and the azimuth angle (d) exemplary for the measurement with the PMMA target of 2 cm in diameter. The Compton scattering angle shown in (a) lies well around 90°. The estimated range via geometrical considerations due to a minimum distance of 8 pixels is 90 °±34.29 °. The distribution lies well within the estimation considering the broadening due to the detector's resolution. The left flank cuts off due to the energy threshold of the detector. Moreover, diffuse scattering with the optical table, the readout board on which the detector is mounted, or the cooling ripple attached on the backside of the readout board right behind the sensor element, and the previously shown background contribution that is only subtracted for the azimuth angle bins, result in contributions outside the estimated range.

The energy contributions of each coincident event and their sum shown in (b) result in similar results as the background measurement. For a Compton scattering angle of 90 °-34.29 °, the incident X-ray must have at least about 61 keV to surpass the energy threshold of the detector, while for the upper scattering angle range of 90 °+34.29 ° the energy of the incident X-ray must be of at least about 33 keV. Latter value explains the lower range of the measured energy spectrum. Towards larger energies, the only restriction is the maximum energy of the incident X-ray, which is about 80 keV. Energies between about 30 keV to 80 keV are reconstructed with the presented approach. Therefore, the minimum rated range of use of the X-ray Compton polarimeter is stated as said range.

The modulation curve is shown in (c). It is calculated as the measured entries in the angle bins normalized to the exposure time, times the geometrical acceptance of the detector determined from the measurements with an unpolarized X-ray source. This azimuth angle bin rate is subtracted by the background rate shown in Figure 5.18(c). Also, the accidental rate at 202.8 ns (as defined in Equation (5.9)) is subtracted from the measured event rate per azimuth angle bin. The resulting modulation curve is fitted via Equation (5.5), and the modulation factor and its corresponding uncertainty are calculated via Equation (5.6) and Equation (5.7) to $\mu = 0.77 \pm 0.04$. Also, the azimuth displacement with respect to the reference axis ϕ_0 is determined as $88.97° \pm 1.93°$. It is 90° within its uncertainty, which means a $\sin(\phi)^2$ distribution is observed. This indicates that the linear polarization orientations of the X-ray aligns with the reference axis. It lies in the scattering plane, i.e., the plane parallel to the optical table the detector is placed on. Table 5.2 summarizes the calculated μ and ϕ_0 for all four targets. An increasing target diameter reduces the calculated modulation factor. The decrease of modulation is significant and much stronger than determined in the simulation of the setup in Section 5.7. One reason is the larger range of acceptance angles of Compton scattering in the PMMA target incident to the sensor surface. This decreases the measured polarization. Moreover, the simulation of the setup did not directly compute the polarization. The degree of linear polarization can therefore deviate in reality. Increasing the target thickness increases the probability of multiple Compton scattering in the PMMA target. Especially the z-direction of the PMMA round bar is affected since it is 6 cm long. This multiple Compton scattering decreases the overall degree of linear polarization in the measurement, which in turn decreases the measured modulation factor. For the target diameter of 0.5 cm, a modulation factor above 1.0 is calculated. It is due to negative values in the azimuth angle bins after correction. Since the modulation is a positive definite quantity, this will result in incorrect modulation factors. This measurement must be discarded.

Figure 5.20(d) shows the 2D histogram of the Compton scattering angle θ and the azimuth angle in the sensor element ϕ. It shows no extensive asymmetries, which indicates that primarily signal was measured.

Target ⌀[cm]	2.0	1.5	1.0	0.5
μ	0.77±0.04	0.81±0.04	0.85±0.04	1.16±0.06
ϕ_0 [°]	88.98±1.94	90.48±1.59	90.42±1.90	90.99±1.90

Table 5.2.: Modulation factors μ and the azimuth displacements with respect to the reference axis ϕ_0 for the different target diameters. The modulation factor and its corresponding uncertainty are calculated via Equation (5.6) and Equation (5.7).

At this stage, no comparison to other Compton X-ray polarimeters can be made. The performance of an X-ray polarimeter comprised of a Timepix3 detector must be

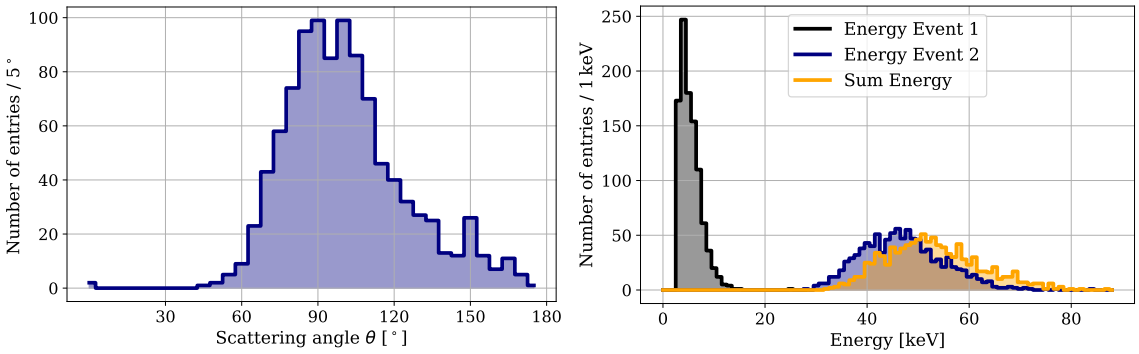

(a) Compton scattering angle

(b) Energy distributions

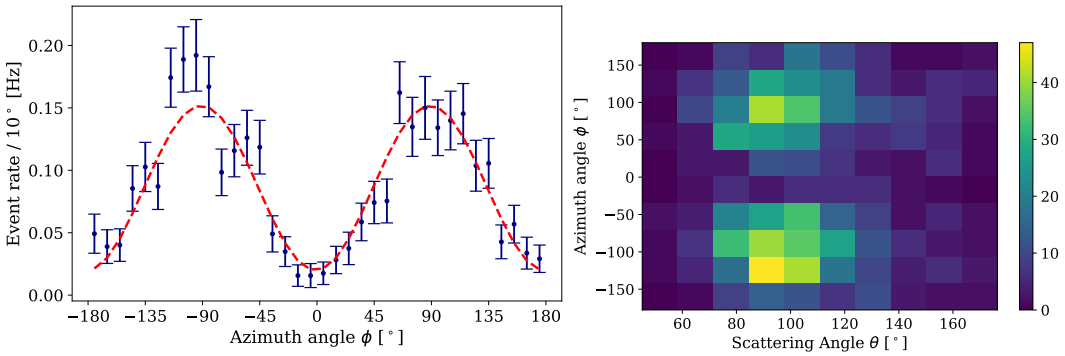

(c) Modulation curve

(d) 2D histogram θ-ϕ

Figure 5.20.: Distributions of the Compton scattering angle θ in the sensor element of Timepix3 in (a), the energy distributions for the coincident event cluster pairs and their sum energy in (b), the recorded modulation curve of the azimuth angle ϕ in (c), and the corresponding 2D histogram for the Compton scattering angle θ and the azimuth angle ϕ in (d) for the measurement with the PMMA target of 2 cm in diameter.

studied in the future via detector simulations or measurements in X-ray fields with known degree of linear polarization. These will help calculating figures of merit like the μ_{100}, which is used to calculate the degree of linear polarization in a measurement via [22]:

$$P_{\mathrm{DOP}} = \frac{\mu}{\mu_{100}}. \tag{5.11}$$

The value of μ_{100} is typically determined via a simulation of a 100% linearly polarized X-ray source and an analysis identical to the one of the measurement. Furthermore, simulations must determine the efficiency ϵ of the polarimeter, i.e., the ratio between the number of coincident event cluster pairs and the number of incident X-rays.

The efficiency ϵ, together with μ_{100} allows calculation of another important figure of merit - the Minimum Detectable Polarization (MDP), which describes the sensitivity of the detector. It is the measurable degree of linear polarization of an polarized X-ray source that arises not from measurement of an unpolarized source. For a confidence interval of 99% it holds [22]:

$$MDP_{99} = \frac{4.29}{\mu_{100} \cdot \epsilon \cdot S} \cdot \sqrt{\frac{(S+B) \cdot \epsilon}{T}} \tag{5.12}$$

where S denotes the photon flux impinging on the detector, B the corresponding background rate, and T the exposure time. Knowing μ_{100} and ϵ allows calculating estimates for MDP_{99} for different astrophysical sources such as the Crab nebula, as performed in [22]. It will allow comparison to other instruments dedicated for X-ray polarimetry.

5.9. Conclusion

The application of the Timepix3 detector as an X-ray polarimeter was demonstrated in this chapter. For this purpose, an algorithm was developed to determine the azimuth angle between two coincident events clusters on the pixel matrix. Their minimum distance to each other is 8 pixels. The clustering time and coincidence window are set to 202.8 ns. The event clusters are cut to the inner radius of 127.5 pixel pitches from the center point of the pixel matrix. Choosing such a fiducial area is necessary to negate asymmetries due to the square shape of the pixel matrix. It is searched for interactions pairs consisting first Compton scattering followed by photoelectric effect. Energy deposition in the sensor via the Compton effect is small in the investigated energy range of 20-80 keV, and therefore the cluster with the lowest energy is chosen as the first interaction point. This defines the reference axis of the analysis. In the next step, the Compton scattering angle is calculated via the energy correlations of the sum of energies of both event clusters (incident photon energy) and the energy of the second event cluster (scattered photon energy). Applying such a cut improves the rejection of accidentals by factors between 6.5±1.5 to 18.7±2.2, while the event rate is reduced by on average 2.5 with a standard deviation of 0.2, depending on the used target.

Unpolarized and polarized X-ray beams were utilized for the irradiations. In the case of unpolarized X-rays, no distinct modulation was found. This measurement was used to determine the relative geometrical acceptance used to correct the detector's 1D fixed pattern noise due to its pixelation. Modulation curves were shown for a Compton scattering experiment where an unpolarized photon beam is incident to a PMMA cylinder target. Scattering of the X-ray with this target polarizes it. For an angle of

90 ° an almost 100% polarized beam is expected. In a first experiment, the detector was rotated by 90 ° to prove that the measured modulation stems from polarized X-rays. It was shown that the measured modulation indeed stems from polarized X-rays. Measurements with and without targets were performed. The latter are background measurements, which are employed for background subtraction. Modulation factors were determined for all target diameters of 2.0 cm 1.5 cm 1.0 cm, and 0.5 cm as 0.77±0.04, 0.81±0.04, 0.85±0.04, and 1.16±0.06 respectively. A significant loss of polarization is measured with increasing target diameter. As the reason for this, multiple Compton scattering in the PMMA target was stated. It effectively decreases the degree of linear polarization of the accepted photons incident on the detector. The measurement of the 0.5 cm target diameter must be discarded since a modulation factor above 1.0 was measured due to negative entries in the azimuth angle histogram.

Application of Timepix3 for X-ray polarimetry by means of Compton scattering is a viable option in the energy range of 30-80 keV when utilizing Compton scattering followed by photoelectric effect event chains. The combination of energy, position and time-resolved measurement of X-rays allows in-depth analysis of the basic nature of X-rays interacting in the sensor material of Timepix3. Future investigations into Compton scattering followed by Compton scattering event pairs will increase the rated range of use of the polarimeter significantly. So far, it is limited since the probability of the photoelectric effect in silicon decreases drastically with increasing energies. For precise determinations of the degree of polarization of an X-ray source requires the knowledge of the modulation factor for a 100% polarized X-ray beam μ_{100}. For this purpose, a detector simulation is needed in the future. Such a simulation will also determine the efficiency of the polarimeter, which in turn allows calculation of MDP_{99} an important figure of merit. With that, the performance of observations of astrophysical sources can be estimated, and comparisons to existing polarimetry systems drawn.

6. Summary

The applications of hybrid pixel detectors in two different research fields were successfully demonstrated in this thesis. One of these is Dosepix, which is an energy-resolving, photon-counting detector. Its sensor element employs two different pixel types, which were investigated in their metrological properties separately. For dosimetry, a system comprised of three differently filtered Dosepix detectors is utilized.

The ambient dose equivalent $H^*(10)$, and the directional dose equivalents $H'(3, \Omega)$, and $H'(0.07, \Omega)$ are the operational quantities of interest in Chapter 3. Additionally, the determination of the air kerma of a photon field was carried out with the same dataset since the area dose equivalents are measured free in air. National and international requirements define limits and minimum rated ranges of use for area dosemeters in PTB-A 23.3 and its complement, IEC 60846-1 [64, 65, 66], and for semiconductor detectors as used in X-ray diagnostic imaging as stated in and IEC 61674 [68]. These limits were compared to the results of the combined influence of the dependence of the normalized response on the mean photon energy and the angle of radiation incidence. Measurements were performed at facilities of PTB with the Dosepix dosimetry demonstrator. Overall, the rated range of use for the combined influence of energy and angular dependence is determined as 16.3 keV to 1250 keV up to 45 ° for the ambient dose equivalent $H^*(10)$ and the directional dose equivalent $H'(3, \Omega)$ for the large and the small pixels, and from 20.3 keV to 1250 keV up to 45 ° for the small pixels and from 24.6 keV to 1250 keV up to 45 ° for the large pixels for the directional dose equivalent $H'(0.07, \Omega)$. The range of the angle of radiation incidence can be expanded with the cost of a reduced range of mean photon energies. For air kerma an energy range from 24.6 keV to 1250 keV is within the limits of $\pm 5\%$ for the large pixels. For the small pixels the relative statistical uncertainty exceeds its limits above 100 keV, which makes their use unfeasible. Further tests in RQR and RQA reference fields as required by [68] must be performed to verify the applicability as an X-ray diagnostic dosemeter.

In Chapter 4, the Dosepix dosimetry demonstrator was employed to investigate the combined influence of the dependence of the normalized response on the mean photon energy and the angle of radiation incidence for the personal dose equivalents $H_\mathrm{p}(10)$, $H_\mathrm{p}(3)$, $H_\mathrm{p}(0,07)$. The dosimetry demonstrator was irradiated by photon reference fields on ISO water slab phantom at facilities of PTB. All national and international requirements according to PTB-A 23.2 and its complement [83, 69] and IEC 61526 [84] with respect to the minimum rated range of use were fulfilled and even surpassed by the measurements. The rated range of use for the combined influence of mean photon

energy and angle of radiation incidence was determined from 12.4 keV to 1250 keV within ±60° for $H_p(10)$ for both pixel types, 20.3 keV to 1250 keV within ±60° for $H_p(3)$ for both pixel types, and 24.6 keV to 1250 keV within ±60° for $H_p(0.07)$ for both pixel types.

Furthermore, the influence of β reference fields defined in ISO 6980-1 [85] on the photon dose indication of $H_p(10)$ was measured in Chapter 4. It was shown with a modified approach of the use of the conversion factors for the Dosepix dosimetry demonstrator that the influence is below 2% and 3% of the reference electron dose at $^{90}Sr/^{90}Y$ for the large and small pixels, respectively. The modified set of conversion factors utilizes all energy bins of Slots 2 and 3, and the four lower energy bins of Slot 1 for photon dosimetry. Additionally, a branching algorithm was developed to classify photon and electron fields. All tested photon and β reference fields were correctly classified when applying a β-window above Slot 1.

Moreover, a prototype of the first active personal dosemeter to monitor the eye lens dose was tested. A system consisting of a single Dosepix detector was utilized for this purpose. The detector has no dedicated filter-cap and is placed within a 3D-printed dosemeter case. The investigations were performed in photon reference fields according to ISO 4037-1, and DIN-6818-1 [67, 110] at facilities of PTB. Influence quantities of interest were the mean photon energy, the angle of radiation incidence, dose rate in the pulse, and the pulse duration of a single pulse. A reduction of the energy range was required since only a single Dosepix detector was utilized. The rated range of use is summarized as 12.4 keV to 248 keV within ±60° for the large and 16.3 keV to 248 keV within ±60° for the small pixels. The normalized response is within limits for the pulse duration between 400 µs, and 10 s for both pixel types. The small pixels have measurements outside the limits at 20 ms due to issues with statistics and the used conversion factors. Furthermore, the dose rate dependence of the normalized response was tested. Two radiation qualities according to IEC 61267 [76], RQR 5 and RQR 8, were used. The normalized response is within limits up to around 4 Sv/h (RQR 8, for data of the variation of pulse duration) and 3.55 Sv/h (RQR 5) for the large, and 34.2 Sv/h (RQR 5) and 34.7 Sv/h (RQR 8) for the small pixels. Overall, the tested prototype shows enormous potential as an active personal dosemeter for individual monitoring of the eye lens dose of occupationally exposed staff.

Chapter 5 covers the capability of the Timepix3 detector with a 300 µm thick silicon sensor as an X-ray polarimeter. It allows position-, time-, and energy-resolved measurement. Investigations in this thesis were performed with respect to polarimetry by means of Compton scattering. The dependence of the azimuth angle, which depends on the linear polarization of the interacting photon, is exploited. Measurements were performed with an unpolarized source, ^{241}Am, and a polarized source that was created by Compton scattering of a collimated unpolarized beam of an X-ray tube with a PMMA target. The unpolarized and polarized nature of both respective sources was demonstrated in the measurements. Polarization of the X-rays was

confirmed by rotating the detector by 90°, which shifted the modulation curve by the same angle within its uncertainties. The scattering targets used were PMMA round bars of different diameters. The investigations of the polarized X-rays showed large modulation factors of about 80%. The modulation factor becomes smaller with increasing target diameter since the accepted scattering angles incident to the detector become larger. Furthermore, multiple Compton scattering in the target increases with its diameter, which further decreases the degree of polarization of the X-rays incident to the Timepix3. The energy range of use of a Timepix3 X-ray polarimeter can be set to at least 30 keV to 80 keV.

A. Conversion Factors

Index i	b_i [keV]	Large Pixels [µSv]	Small Pixels [µSv]
15	12	1.4596E-04	1.1434E-02
14	15	4.6425E-05	4.9917E-03
13	20	1.4386E-04	1.0448E-02
12	25	6.6987E-05	1.5256E-02
11	30	2.0298E-04	7.5552E-03
10	35	2.2466E-04	3.0041E-02
9	40	2.4480E-04	2.3195E-02
8	50	7.3285E-04	1.1014E-01
7	60	8.5205E-04	4.4860E-02
6	70	1.1057E-03	1.9976E-01
5	80	3.1868E-03	1.0786E-01
4	90	2.4054E-03	1.1414E+00
3	100	5.0313E-03	4.4583E-01
2	110	1.2862E-02	6.6919E+00
1	130	1.0974E-02	1.2124E+00
0	150	7.0609E-02	2.0135E+00

Table A.1.: Conversion factors for the large and small pixels of the eye lens dosemeter prototype consisting of one Dosepix detector.

Index i Slot 1	b_i[keV]	$H^*(10)$ [µSv]	Index j Slot 2	b_j[keV]	$H^*(10)$ [µSv]	Index k Slot 3	b_k[keV]	$H^*(10)$ [µSv]
15	12.0	1.4873E-05	31	12.0	4.6970E-04	47	32.0	6.6445E-03
14	18.0	6.8297E-05	30	17.0	6.4403E-05	46	37.0	1.0419E-04
13	21.0	1.3648E-06	29	31.0	8.7045E-05	45	47.0	1.0005E-06
12	24.5	5.5499E-05	28	40.0	1.4592E-04	44	57.5	1.0000E-06
11	33.5	7.8840E-05	27	45.5	1.5972E-04	43	68.5	1.0001E-06
10	43.0	1.4114E-04	26	50.5	1.4174E-04	42	80.0	1.0003E-06
9	53.5	3.7960E-04	25	60.5	2.9200E-04	41	91.5	2.9813E-04
8	66.5	7.0724E-04	24	68.0	6.0129E-05	40	104.0	3.1819E-05
7	81.5	1.4743E-03	23	91.0	8.5874E-04	39	117.0	5.7590E-05
6	97.0	2.3706E-03	22	102.5	1.2910E-03	38	131.0	1.0771E-04
5	113.0	1.7913E-03	21	133.0	2.4440E-03	37	145.0	1.0261E-03
4	131.5	9.5728E-04	20	148.0	1.4274E-03	36	163.5	1.8722E-03
3	151.5	3.3272E-03	19	163.0	4.1654E-03	35	183.5	1.2037E-03
2	173.0	7.1709E-04	18	196.0	2.8437E-03	34	207.5	2.6315E-04
1	200.5	4.4074E-04	17	220.0	8.0929E-03	33	234.5	2.2008E-03
0	236.0	3.0673E-04	16	257.0	3.1759E-03	32	269.5	3.1159E-03

Table A.2.: Conversion factors of the large pixels for the ambient dose equivalent $H^*(10)$ for the Dosepix dosimetry demonstrator.

Index i Slot 1	b_i[keV]	$H'(3, \Omega)$ [µSv]	Index j Slot 2	b_j[keV]	$H'(3, \Omega)$ [µSv]	Index k Slot 3	b_k[keV]	$H'(3, \Omega)$ [µSv]
15	12.0	8.1759E-05	31	12.0	5.0164E-06	47	32.0	2.5958E-03
14	18.0	4.2882E-06	30	17.0	1.8385E-05	46	37.0	1.2119E-03
13	21.0	1.7991E-04	29	31.0	1.7537E-05	45	47.0	1.0005E-06
12	24.5	4.8891E-05	28	40.0	2.0341E-05	44	57.5	1.0001E-06
11	33.5	2.2059E-04	27	45.5	2.3175E-05	43	68.5	1.0000E-06
10	43.0	2.4837E-04	26	50.5	1.3249E-04	42	80.0	1.0003E-06
9	53.5	1.7751E-05	25	60.5	9.2652E-04	41	91.5	1.0969E-04
8	66.5	5.6622E-04	24	68.0	3.4139E-04	40	104.0	3.6833E-05
7	81.5	1.4200E-03	23	91.0	4.3548E-04	39	117.0	4.3387E-05
6	97.0	2.8277E-03	22	102.5	8.9752E-04	38	131.0	8.5312E-05
5	113.0	2.3940E-03	21	133.0	1.6148E-03	37	145.0	8.2157E-05
4	131.5	1.8152E-03	20	148.0	8.0900E-04	36	163.5	2.5124E-03
3	151.5	4.6621E-03	19	163.0	3.9594E-03	35	183.5	6.3239E-04
2	173.0	1.4798E-03	18	196.0	8.1647E-04	34	207.5	5.1933E-04
1	200.5	2.2865E-03	17	220.0	7.0011E-03	33	234.5	2.1042E-03
0	236.0	2.2189E-04	16	257.0	2.6258E-03	32	269.5	2.6426E-03

Table A.3.: Conversion factors of the large pixels for the directional dose equivalent $H'(3, \Omega)$ for the Dosepix dosimetry demonstrator.

Index i Slot 1	b_i[keV]	$H'(0.07, \Omega)$ [µSv]	Index j Slot 2	b_j[keV]	$H'(0.07, \Omega)$ [µSv]	Index k Slot 3	b_k[keV]	$H'(0.07, \Omega)$[µSv]
15	12.0	1.7531E-04	31	12.0	1.0005E-06	47	32.0	4.2448E-03
14	18.0	4.4312E-06	30	17.0	1.8162E-05	46	37.0	1.2683E-04
13	21.0	8.1855E-06	29	31.0	1.6620E-04	45	47.0	1.0002E-06
12	24.5	1.0005E-04	28	40.0	1.9418E-05	44	57.5	1.0006E-06
11	33.5	4.0445E-06	27	45.5	2.1646E-05	43	68.5	1.0003E-06
10	43.0	3.8686E-04	26	50.5	3.1752E-05	42	80.0	1.0004E-06
9	53.5	1.6841E-05	25	60.5	5.3833E-05	41	91.5	1.2054E-04
8	66.5	1.6186E-03	24	68.0	7.6059E-05	40	104.0	5.8899E-05
7	81.5	8.3397E-04	23	91.0	1.1543E-04	39	117.0	6.4072E-05
6	97.0	2.6623E-03	22	102.5	1.8028E-03	38	131.0	1.0682E-04
5	113.0	2.6127E-03	21	133.0	5.0157E-04	37	145.0	1.0854E-03
4	131.5	3.7345E-04	20	148.0	1.6553E-03	36	163.5	1.4246E-03
3	151.5	6.6033E-03	19	163.0	5.0598E-03	35	183.5	6.5843E-04
2	173.0	2.6858E-04	18	196.0	2.3027E-03	34	207.5	1.2304E-04
1	200.5	5.1840E-04	17	220.0	4.5830E-03	33	234.5	3.7677E-03
0	236.0	2.2009E-03	16	257.0	2.7801E-03	32	269.5	2.0019E-04

Table A.4.: Conversion factors of the large pixels for the directional dose equivalent $H'(0.07, \Omega)$ for the Dosepix dosimetry demonstrator.

Index i Slot 1	b_i[keV]	K_{air} [µGy]	Index j Slot 2	b_j[keV]	K_{air} [µGy]	Index k Slot 3	b_k[keV]	K_{air} [µGy]
15	12.0	1.8178E-04	31	12.0	1.0000E-06	47	32.0	9.2839E-04
14	18.0	5.4768E-06	30	17.0	8.3496E-06	46	37.0	1.0000E-06
13	21.0	5.9956E-06	29	31.0	8.2510E-06	45	47.0	1.0001E-06
12	24.5	1.1693E-04	28	40.0	9.7547E-06	44	57.5	1.0001E-06
11	33.5	8.0141E-05	27	45.5	1.1122E-05	43	68.5	5.6925E-05
10	43.0	2.5005E-04	26	50.5	1.6556E-05	42	80.0	1.0000E-06
9	53.5	1.3183E-05	25	60.5	7.8179E-04	41	91.5	1.1599E-04
8	66.5	2.0317E-05	24	68.0	7.4028E-05	40	104.0	6.4821E-05
7	81.5	9.5378E-04	23	91.0	4.9177E-05	39	117.0	8.8262E-05
6	97.0	1.0682E-03	22	102.5	1.0295E-04	38	131.0	1.4681E-04
5	113.0	4.3105E-03	21	133.0	1.6119E-04	37	145.0	1.1600E-04
4	131.5	3.1893E-03	20	148.0	2.6784E-04	36	163.5	5.6218E-03
3	151.5	1.2632E-02	19	163.0	1.7901E-04	35	183.5	1.1124E-03
2	173.0	2.4285E-04	18	196.0	4.2963E-05	34	207.5	9.9206E-05
1	200.5	2.6849E-03	17	220.0	4.9655E-04	33	234.5	8.2033E-05
0	236.0	3.6120E-04	16	257.0	6.0561E-03	32	269.5	4.7810E-05

Table A.5.: Conversion factors of the large pixels for the air kerma K_{air} for the Dosepix dosimetry demonstrator.

Index i Slot 1	b_i[keV]	$H^*(10)$ [µSv]	Index j Slot 2	b_j[keV]	$H^*(10)$ [µSv]	Index k Slot 3	b_k[keV]	$H^*(10)$ [µSv]
15	12.0	1.2673E-03	31	12.0	7.8161E-03	47	32.0	6.1713E-03
14	15.0	9.3996E-04	30	15.0	3.2437E-02	46	38.0	5.8953E-03
13	20.0	2.0339E-05	29	20.0	2.3172E-03	45	45.0	2.0453E-03
12	25.0	1.4541E-07	28	25.0	7.8888E-03	44	50.0	1.4787E-02
11	30.0	6.1414E-03	27	30.0	3.7726E-03	43	55.0	6.8423E-02
10	35.0	3.6366E-03	26	35.0	3.8698E-06	42	60.0	1.9668E-01
9	40.0	9.8044E-05	25	40.0	2.2930E-02	41	65.0	5.4119E-02
8	45.0	1.3495E-03	24	45.0	7.0576E-05	40	70.0	9.0383E-02
7	50.0	3.6961E-02	23	50.0	1.3318E-04	39	75.0	1.6187E-03
6	60.0	4.7821E-02	22	60.0	4.8817E-03	38	80.0	9.0259E-04
5	70.0	8.1977E-02	21	70.0	1.2271E-04	37	85.0	4.1083E-04
4	80.0	6.6062E-04	20	80.0	1.2956E-01	36	95.0	4.9783E-04
3	100.0	1.8729E-01	19	100.0	2.0539E-01	35	105.0	8.2038E-04
2	120.0	2.9565E-03	18	120.0	8.5557E-03	34	120.0	3.2516E-04
1	140.0	1.1893E-03	17	140.0	6.4411E-03	33	140.0	3.7617E-04
0	160.0	3.4855E-02	16	160.0	1.0791E-02	32	160.0	2.3943E-01

Table A.6.: Conversion factors of the small pixels for the ambient dose equivalent $H^*(10)$ for the Dosepix dosimetry demonstrator.

Index i Slot 1	b_i[keV]	$H'(3, \Omega)$ [µSv]	Index j Slot 2	b_j[keV]	$H'(3, \Omega)$ [µSv]	Index k Slot 3	b_k[keV]	$H'(3, \Omega)$ [µSv]
15	12.0	6.4518E-03	31	12.0	1.7401E-04	47	32.0	6.3654E-03
14	15.0	2.5849E-03	30	15.0	2.4817E-02	46	38.0	5.7597E-03
13	20.0	1.9915E-05	29	20.0	5.9914E-03	45	45.0	1.9687E-03
12	25.0	1.4143E-07	28	25.0	1.3163E-02	44	50.0	1.4230E-02
11	30.0	8.4263E-03	27	30.0	5.7822E-05	43	55.0	6.6087E-02
10	35.0	3.0776E-03	26	35.0	3.7723E-06	42	60.0	1.9069E-01
9	40.0	9.5192E-05	25	40.0	2.1727E-02	41	65.0	5.2608E-02
8	45.0	1.1310E-04	24	45.0	6.8025E-05	40	70.0	8.8013E-02
7	50.0	3.3507E-02	23	50.0	1.2820E-04	39	75.0	1.5778E-03
6	60.0	6.2000E-02	22	60.0	1.5513E-03	38	80.0	8.8015E-04
5	70.0	5.7554E-02	21	70.0	1.2323E-04	37	85.0	4.0062E-04
4	80.0	7.0484E-04	20	80.0	1.4435E-01	36	95.0	4.8546E-04
3	100.0	2.1805E-01	19	100.0	2.3913E-01	35	105.0	8.0095E-04
2	120.0	3.9540E-03	18	120.0	1.1442E-02	34	120.0	3.1842E-04
1	140.0	2.1616E-03	17	140.0	1.1706E-02	33	140.0	5.4681E-03
0	160.0	1.3513E-01	16	160.0	4.1839E-02	32	160.0	1.9151E-01

Table A.7.: Conversion factors of the small pixels for the directional dose equivalent $H'(3, \Omega)$ for the Dosepix dosimetry demonstrator.

Index i Slot 1	b_i[keV]	$H'(0.07, \Omega)$ [µSv]	Index j Slot 2	b_j[keV]	$H'(0.07, \Omega)$ [µSv]	Index k Slot 3	b_k[keV]	$H'(0.07, \Omega)$ [µSv]
15	12.0	1.7488E-02	31	12.0	1.7286E-04	47	32.0	6.2553E-03
14	15.0	5.7685E-04	30	15.0	1.2816E-02	46	38.0	5.5906E-03
13	20.0	1.9295E-05	29	20.0	1.1045E-02	45	45.0	1.8849E-03
12	25.0	1.3674E-07	28	25.0	1.3877E-02	44	50.0	1.3502E-02
11	30.0	7.4202E-03	27	30.0	5.5674E-05	43	55.0	6.2421E-02
10	35.0	4.8343E-03	26	35.0	3.6059E-06	42	60.0	1.8020E-01
9	40.0	9.0157E-05	25	40.0	1.8433E-02	41	65.0	4.9925E-02
8	45.0	1.0716E-04	24	45.0	6.4362E-05	40	70.0	8.3964E-02
7	50.0	3.0605E-02	23	50.0	1.2274E-04	39	75.0	1.5122E-03
6	60.0	6.0190E-02	22	60.0	1.3410E-04	38	80.0	8.4599E-04
5	70.0	5.5377E-02	21	70.0	1.2055E-04	37	85.0	3.8566E-04
4	80.0	6.9682E-04	20	80.0	1.4413E-01	36	95.0	4.6766E-04
3	100.0	2.2136E-01	19	100.0	2.4275E-01	35	105.0	7.7337E-04
2	120.0	4.2817E-03	18	120.0	1.2391E-02	34	120.0	3.0852E-04
1	140.0	2.6902E-03	17	140.0	1.4570E-02	33	140.0	3.1201E-02
0	160.0	2.3055E-01	16	160.0	7.1381E-02	32	160.0	1.7088E-01

Table A.8.: Conversion factors of the small pixels for the directional dose equivalent $H'(0.07, \Omega)$ for the Dosepix dosimetry demonstrator.

Index i Slot 1	b_i[keV]	K_{air} [µGy]	Index j Slot 2	b_j[keV]	K_{air} [µGy]	Index k Slot 3	b_k[keV]	K_{air} [µGy]
15	12.0	1.7407E-02	31	12.0	1.3095E-04	47	32.0	4.7391E-03
14	15.0	1.5926E-03	30	15.0	4.4816E-05	46	38.0	3.9012E-03
13	20.0	1.3160E-05	29	20.0	9.4070E-03	45	45.0	1.2509E-03
12	25.0	8.9619E-08	28	25.0	1.6679E-02	44	50.0	8.7147E-03
11	30.0	3.2760E-03	27	30.0	3.5160E-05	43	55.0	3.9534E-02
10	35.0	7.1331E-03	26	35.0	2.2336E-06	42	60.0	1.1269E-01
9	40.0	7.2615E-04	25	40.0	3.5976E-03	41	65.0	3.0983E-02
8	45.0	6.8349E-05	24	45.0	4.1110E-05	40	70.0	5.1955E-02
7	50.0	1.6339E-02	23	50.0	8.1455E-05	39	75.0	9.3710E-04
6	60.0	3.2627E-02	22	60.0	9.2560E-05	38	80.0	5.2716E-04
5	70.0	3.9940E-02	21	70.0	8.8375E-05	37	85.0	2.4359E-04
4	80.0	5.4864E-04	20	80.0	6.0287E-02	36	95.0	3.0172E-04
3	100.0	1.8881E-01	19	100.0	2.0706E-01	35	105.0	5.1144E-04
2	120.0	3.9391E-03	18	120.0	1.1399E-02	34	120.0	2.1042E-04
1	140.0	2.6439E-03	17	140.0	1.4318E-02	33	140.0	7.4642E-02
0	160.0	2.3623E-01	16	160.0	7.3139E-02	32	160.0	1.1018E-01

Table A.9.: Conversion factors of the small pixels for the air kerma K_{air} for the Dosepix dosimetry demonstrator.

Index i Slot 1	b_i[keV]	$H_\mathrm{p}(10)$ [µSv]	Index j Slot 2	b_j[keV]	$H_\mathrm{p}(10)$ [µSv]	Index k Slot 3	b_k[keV]	$H_\mathrm{p}(10)$ [µSv]
15	12.0	1.2393E-05	31	12.0	2.3866E-04	47	32.0	3.2420E-04
14	18.0	3.6370E-05	30	17.0	7.0194E-06	46	37.0	1.5780E-04
13	21.0	4.0000E-05	29	31.0	3.2586E-05	45	47.0	1.9913E-06
12	24.5	8.0175E-05	28	40.0	7.0257E-05	44	57.5	1.5531E-05
11	33.5	1.3868E-04	27	45.5	2.3012E-04	43	68.5	1.4033E-05
10	43.0	1.1361E-04	26	50.5	2.6225E-04	42	80.0	2.8511E-04
9	53.5	1.5853E-04	25	60.5	3.3808E-04	41	91.5	1.4975E-04
8	66.5	1.4955E-04	24	68.0	4.9130E-04	40	104.0	2.4050E-04
7	81.5	4.5061E-04	23	91.0	1.0388E-03	39	117.0	3.6984E-04
6	97.0	5.2572E-04	22	102.5	1.9257E-03	38	131.0	1.7147E-03
5	113.0	1.5671E-04	21	133.0	7.2927E-03	37	145.0	1.8142E-03
4	131.5	1.1338E-03	20	148.0	2.9359E-03	36	163.5	1.2679E-03
3	151.5	1.1496E-02	19	163.0	7.9838E-04	35	183.5	1.1151E-03
2	173.0	1.3199E-02	18	196.0	4.7605E-03	34	207.5	9.1813E-04
1	200.5	9.0194E-04	17	220.0	4.7662E-03	33	234.5	1.3638E-04
0	236.0	2.5439E-03	16	257.0	7.2426E-03	32	269.5	7.2019E-04

Table A.10.: Conversion factors of the large pixels for the personal dose equivalent $H_\mathrm{p}(10)$ for the Dosepix dosimetry demonstrator.

Index i Slot 1	b_i[keV]	$H_\mathrm{p}(10)$ [µSv]	Index j Slot 2	b_j[keV]	$H_\mathrm{p}(10)$ [µSv]	Index k Slot 3	b_k[keV]	$H_\mathrm{p}(10)$ [µSv]
15	12.0	1.2952E-05	31	12.0	1.0687E-04	47	32.0	1.6409E-03
14	18.0	3.9760E-05	30	17.0	4.2418E-06	46	37.0	1.6031E-04
13	21.0	4.4180E-05	29	31.0	1.7552E-04	45	47.0	6.7860E-06
12	24.5	8.3922E-05	28	40.0	1.0554E-04	44	57.5	4.9270E-05
11	33.5	0.0000E+00	27	45.5	2.4144E-04	43	68.5	2.1435E-05
10	43.0	0.0000E+00	26	50.5	7.0851E-04	42	80.0	2.8964E-04
9	53.5	0.0000E+00	25	60.5	3.5470E-04	41	91.5	7.6055E-04
8	66.5	0.0000E+00	24	68.0	4.4760E-04	40	104.0	2.0295E-03
7	81.5	0.0000E+00	23	91.0	2.6457E-03	39	117.0	1.2544E-03
6	97.0	0.0000E+00	22	102.5	2.0204E-03	38	131.0	1.7419E-03
5	113.0	0.0000E+00	21	133.0	2.0885E-03	37	145.0	1.7504E-03
4	131.5	0.0000E+00	20	148.0	3.0803E-03	36	163.5	1.7679E-03
3	151.5	0.0000E+00	19	163.0	4.1875E-03	35	183.5	1.1328E-03
2	173.0	0.0000E+00	18	196.0	3.3431E-03	34	207.5	1.3179E-03
1	200.5	0.0000E+00	17	220.0	5.0006E-03	33	234.5	6.5325E-04
0	236.0	0.0000E+00	16	257.0	2.9578E-02	32	269.5	2.9294E-06

Table A.11.: Conversion factors of the large pixels for the personal dose equivalent $H_\mathrm{p}(10)$ corrected for the electron influence for the Dosepix dosimetry demonstrator.

Index i Slot 1	b_i[keV]	$H_\mathrm{p}(3)$ [µSv]	Index j Slot 2	b_j[keV]	$H_\mathrm{p}(3)$ [µSv]	Index k Slot 3	b_k[keV]	$H_\mathrm{p}(3)$ [µSv]
15	12.0	6.3430E-05	31	12.0	1.5198E-05	47	32.0	8.1290E-06
14	18.0	5.3746E-05	30	17.0	1.2008E-04	46	37.0	1.3766E-02
13	21.0	5.2502E-05	29	31.0	1.4339E-04	45	47.0	1.3556E-03
12	24.5	4.0952E-05	28	40.0	1.5373E-04	44	57.5	2.2996E-03
11	33.5	5.2548E-05	27	45.5	1.1815E-04	43	68.5	5.0627E-04
10	43.0	9.5006E-05	26	50.5	3.5388E-04	42	80.0	1.2579E-03
9	53.5	1.3176E-04	25	60.5	5.2694E-04	41	91.5	2.0019E-03
8	66.5	2.6067E-04	24	68.0	2.3896E-04	40	104.0	9.7670E-04
7	81.5	4.4526E-04	23	91.0	2.1993E-03	39	117.0	1.2760E-03
6	97.0	4.6365E-04	22	102.5	1.1495E-03	38	131.0	1.8166E-03
5	113.0	9.3157E-04	21	133.0	9.0607E-04	37	145.0	1.7738E-03
4	131.5	1.0694E-03	20	148.0	9.5848E-03	36	163.5	5.6184E-04
3	151.5	2.5781E-03	19	163.0	1.8532E-03	35	183.5	1.0914E-03
2	173.0	2.1438E-03	18	196.0	1.0875E-03	34	207.5	5.6965E-04
1	200.5	1.0742E-02	17	220.0	6.5523E-03	33	234.5	3.9636E-04
0	236.0	5.4700E-03	16	257.0	1.9968E-03	32	269.5	1.3621E-03

Table A.12.: Conversion factors of the large pixels for the personal dose equivalent $H_\mathrm{p}(3)$ for the Dosepix dosimetry demonstrator.

Index i Slot 1	b_i[keV]	$H_\mathrm{p}(0.07)$ [µSv]	Index j Slot 2	b_j[keV]	$H_\mathrm{p}(0.07)$ [µSv]	Index k Slot 3	b_k[keV]	$H_\mathrm{p}(0.07)$ [µSv]
15	12.0	1.5446E-04	31	12.0	2.1008E-05	47	32.0	1.6152E-03
14	18.0	2.2800E-05	30	17.0	7.8576E-05	46	37.0	1.5780E-04
13	21.0	7.0654E-05	29	31.0	1.3455E-04	45	47.0	2.2092E-04
12	24.5	6.8800E-05	28	40.0	7.6489E-05	44	57.5	2.9540E-05
11	33.5	4.1280E-05	27	45.5	2.3012E-04	43	68.5	6.9681E-05
10	43.0	1.1361E-04	26	50.5	2.6225E-04	42	80.0	1.0481E-03
9	53.5	1.5853E-04	25	60.5	1.5750E-04	41	91.5	7.4867E-04
8	66.5	5.1119E-04	24	68.0	2.0285E-04	40	104.0	1.7288E-03
7	81.5	4.1376E-04	23	91.0	1.0724E-03	39	117.0	1.0290E-03
6	97.0	5.2572E-04	22	102.5	1.5250E-03	38	131.0	1.7147E-03
5	113.0	3.1543E-04	21	133.0	4.1098E-03	37	145.0	1.7977E-03
4	131.5	2.1788E-03	20	148.0	5.5871E-03	36	163.5	1.7403E-03
3	151.5	1.5563E-03	19	163.0	3.9912E-03	35	183.5	5.5092E-04
2	173.0	1.6668E-03	18	196.0	6.6726E-03	34	207.5	9.1813E-04
1	200.5	9.0194E-04	17	220.0	4.7662E-03	33	234.5	6.4304E-04
0	236.0	2.5439E-03	16	257.0	7.2426E-03	32	269.5	3.8654E-04

Table A.13.: Conversion factors of the large pixels for the personal dose equivalent $H_\mathrm{p}(0.07)$ for the Dosepix dosimetry demonstrator.

Index i Slot 1	b_i[keV]	$H_\mathrm{p}(10)$ [µSv]	Index j Slot 2	b_j[keV]	$H_\mathrm{p}(10)$ [µSv]	Index k Slot 3	b_k[keV]	$H_\mathrm{p}(10)$ [µSv]
15	12.0	1.4657E-03	31	12.0	1.8936E-02	47	32.0	5.0848E-03
14	15.0	8.8544E-04	30	15.0	1.7142E-02	46	38.0	4.7903E-03
13	20.0	2.1249E-03	29	20.0	6.5924E-04	45	45.0	1.6943E-03
12	25.0	2.2256E-03	28	25.0	2.6726E-03	44	50.0	1.2465E-02
11	30.0	7.4463E-04	27	30.0	6.0058E-03	43	55.0	5.8465E-02
10	35.0	5.2419E-03	26	35.0	3.8078E-04	42	60.0	1.6963E-01
9	40.0	5.2348E-03	25	40.0	8.6747E-03	41	65.0	4.6801E-02
8	45.0	1.0618E-02	24	45.0	6.4913E-03	40	70.0	7.8768E-02
7	50.0	2.1639E-02	23	50.0	1.2528E-02	39	75.0	1.4272E-01
6	60.0	8.7448E-03	22	60.0	1.2026E-02	38	80.0	8.1574E-03
5	70.0	9.0425E-03	21	70.0	1.0167E-02	37	85.0	3.6540E-02
4	80.0	8.3650E-02	20	80.0	7.4214E-02	36	95.0	4.4561E-02
3	100.0	1.4923E-01	19	100.0	1.6634E-01	35	105.0	7.3724E-02
2	120.0	6.5038E-01	18	120.0	6.8266E-03	34	120.0	1.8350E-02
1	140.0	8.9100E-04	17	140.0	4.9045E-03	33	140.0	3.4608E-02
0	160.0	5.3093E-03	16	160.0	1.6707E-03	32	160.0	3.2558E-02

Table A.14.: Conversion factors of the small pixels for the personal dose equivalent $H_\mathrm{p}(10)$ for the Dosepix dosimetry demonstrator.

Index i Slot 1	b_i[keV]	$H_\mathrm{p}(10)$ [µSv]	Index j Slot 2	b_j[keV]	$H_\mathrm{p}(10)$ [µSv]	Index k Slot 3	b_k[keV]	$H_\mathrm{p}(10)$ [µSv]
15	12.0	1.4657E-03	31	12.0	1.8936E-02	47	32.0	5.0848E-03
14	15.0	7.7185E-04	30	15.0	1.7142E-02	46	38.0	4.7903E-03
13	20.0	2.1249E-03	29	20.0	6.5924E-04	45	45.0	1.6943E-03
12	25.0	2.2256E-03	28	25.0	3.2716E-03	44	50.0	1.2465E-02
11	30.0	0.0000E+00	27	30.0	6.0058E-03	43	55.0	5.8465E-02
10	35.0	0.0000E+00	26	35.0	3.8078E-04	42	60.0	1.8139E-01
9	40.0	0.0000E+00	25	40.0	3.2783E-02	41	65.0	4.6801E-02
8	45.0	0.0000E+00	24	45.0	6.4913E-03	40	70.0	7.8768E-02
7	50.0	0.0000E+00	23	50.0	1.2528E-02	39	75.0	1.4276E-03
6	60.0	0.0000E+00	22	60.0	1.2026E-02	38	80.0	1.2910E-04
5	70.0	0.0000E+00	21	70.0	1.2555E-01	37	85.0	4.2232E-04
4	80.0	0.0000E+00	20	80.0	7.4214E-02	36	95.0	4.4561E-02
3	100.0	0.0000E+00	19	100.0	1.6634E-01	35	105.0	7.3724E-02
2	120.0	0.0000E+00	18	120.0	6.8266E-03	34	120.0	2.8620E-03
1	140.0	0.0000E+00	17	140.0	2.8187E+00	33	140.0	3.4608E-02
0	160.0	0.0000E+00	16	160.0	1.6707E-03	32	160.0	1.0440E-01

Table A.15.: Conversion factors of the small pixels for the personal dose equivalent $H_\mathrm{p}(10)$ corrected for the electron influence for the Dosepix dosimetry demonstrator.

Index i Slot 1	b_i[keV]	$H_\mathrm{p}(3)$ [µSv]	Index j Slot 2	b_j[keV]	$H_\mathrm{p}(3)$ [µSv]	Index k Slot 3	b_k[keV]	$H_\mathrm{p}(3)$ [µSv]
15	12.0	8.5059E-03	31	12.0	1.3125E-03	47	32.0	2.4077E-03
14	15.0	3.0636E-05	30	15.0	1.9185E-02	46	38.0	6.8979E-01
13	20.0	5.3176E-03	29	20.0	2.3359E-03	45	45.0	2.9384E-03
12	25.0	1.3505E-04	28	25.0	2.0577E-03	44	50.0	8.1707E-03
11	30.0	4.3214E-03	27	30.0	3.9246E-03	43	55.0	2.8922E-02
10	35.0	3.9148E-03	26	35.0	3.5077E-03	42	60.0	5.5006E-02
9	40.0	1.0997E-02	25	40.0	4.7389E-03	41	65.0	3.0920E-02
8	45.0	1.0888E-03	24	45.0	7.6792E-03	40	70.0	5.0014E-02
7	50.0	1.6680E-02	23	50.0	1.0940E-02	39	75.0	7.1654E-02
6	60.0	1.3822E-02	22	60.0	1.5943E-02	38	80.0	3.9969E-03
5	70.0	3.3104E-02	21	70.0	1.7559E-02	37	85.0	2.8347E-02
4	80.0	5.9778E-03	20	80.0	1.0247E-01	36	95.0	3.3716E-02
3	100.0	7.5083E-01	19	100.0	7.1738E-02	35	105.0	3.1768E-02
2	120.0	2.3021E-03	18	120.0	3.9673E-03	34	120.0	2.0728E-02
1	140.0	9.6711E-04	17	140.0	5.1507E-03	33	140.0	1.4176E-02
0	160.0	1.9640E-01	16	160.0	1.8331E-02	32	160.0	8.8217E-02

Table A.16.: Conversion factors of the small pixels for the personal dose equivalent $H_\mathrm{p}(3)$ for the Dosepix dosimetry demonstrator.

Index i Slot 1	b_i[keV]	$H_\mathrm{p}(0.07)$ [µSv]	Index j Slot 2	b_j[keV]	$H_\mathrm{p}(0.07)$ [µSv]	Index k Slot 3	b_k[keV]	$H_\mathrm{p}(0.07)$ [µSv]
15	12.0	1.7734E-02	31	12.0	6.5625E-05	47	32.0	2.4077E-03
14	15.0	1.2863E-03	30	15.0	3.0169E-05	46	38.0	1.5885E-03
13	20.0	4.1105E-03	29	20.0	2.3359E-03	45	45.0	2.9384E-03
12	25.0	2.7009E-03	28	25.0	5.2404E-03	44	50.0	8.1707E-03
11	30.0	2.7517E-04	27	30.0	1.2717E-02	43	55.0	2.8922E-02
10	35.0	2.0983E-04	26	35.0	4.0001E-04	42	60.0	5.5006E-02
9	40.0	2.6925E-03	25	40.0	4.7389E-03	41	65.0	3.0920E-02
8	45.0	2.1123E-02	24	45.0	8.4076E-03	40	70.0	5.0014E-02
7	50.0	1.6680E-02	23	50.0	1.0940E-02	39	75.0	7.1654E-02
6	60.0	1.3621E-02	22	60.0	7.9964E-04	38	80.0	6.2272E-02
5	70.0	1.6590E-02	21	70.0	1.7559E-02	37	85.0	2.8347E-02
4	80.0	9.5563E-02	20	80.0	1.0247E-01	36	95.0	1.9456E-03
3	100.0	5.6588E-01	19	100.0	7.1738E-02	35	105.0	3.1768E-02
2	120.0	2.3021E-03	18	120.0	3.9673E-03	34	120.0	2.0728E-02
1	140.0	8.9985E-01	17	140.0	5.1507E-03	33	140.0	2.5746E-02
0	160.0	1.2166E-02	16	160.0	1.8331E-02	32	160.0	8.8217E-02

Table A.17.: Conversion factors of the small pixels for the personal dose equivalent $H_\mathrm{p}(0.07)$ for the Dosepix dosimetry demonstrator.

Bibliography

[1] Bundesamt für Strahlenschutz (BfS) and Bundesministerium für Umwelt Naturschutz und Reaktorsicherheit (BMU). *Umweltradioaktivität und Strahlenbelastung: Jahresbericht 2018*. URL: https://doris.bfs.de/jspui/bitstream/urn:nbn:de:0221-2021011124821/1/JB2018_2020.pdf.

[2] ICRP. *The 2007 Recommendations of the International Commission on Radiological Protection*. ICRP Publication 103. Ann. ICRP 37 (2-4).

[3] ICRP. *ICRP Statement on Tissue Reactions / Early and Late Effects of Radiation in Normal Tissues and Organs – Threshold Doses for Tissue Reactions in a Radiation Protection Context*. ICRP Publication 118. Ann. ICRP 41(1/2).

[4] A. Omar et al. "Assessment of the occupational eye lens dose for clinical staff in interventional radiology, cardiology and neuroradiology". In: *Journal of Radiological Protection* 37.1 (Jan. 2017), pp. 145–159. DOI: 10.1088/1361-6498/aa559c.

[5] E. Vano et al. "Radiation Cataract Risk in Interventional Cardiology Personnel". In: *Radiation Research* 174.4 (2010), pp. 490–495. DOI: 10.1667/RR2207.1.

[6] O. Hupe, H. Zutz, and J. Klammer. *Radiation Protection Dosimetry in Pulsed Radiation Fields*. Presented at IRPA 13 Glasgow. [Online]. Available: "https://www.irpa.net/members/TS2f.3.pdf".

[7] O. Hupe et al. "Determining the dose rate dependence of different active personal dosemeters in standardized pulsed and continuous radiation fields". In: *Radiation Protection Dosimetry* 187.3 (Sept. 2019). 10.1093/rpd/ncz173, pp. 345–352.

[8] F. Vanhavere et al. "Measurements of eye lens doses in interventional radiology and cardiology: Final results of the ORAMED project". In: *Radiation Measurements* 46.11 (2011). International Workshop on Optimization of Radiation Protection of Medical Staff, ORAMED 2011, pp. 1243–1247. DOI: 10.1016/j.radmeas.2011.08.013.

[9] F. Vanhavere et al. "The use of active personal dosemeters in interventional workplaces in hospitals: comparison between active and passive dosemeters worn simultaneously by medical staff". In: *Radiation Protection Dosimetry* 188.1 (Dec. 2019). 10.1093/rpd/ncz253, pp. 22–29.

[10] O. Ciraj-Bjelac et al. "Risk for radiation-induced cataract for staff in interventional cardiology: Is there reason for concern?" In: *Catheterization and Cardiovascular Interventions* 76.6 (2010), pp. 826–834. DOI: 10.1002/ccd.22670.

[11] O. Ciraj-Bjelac, E. Carinou, and F. Vanhavere. “Use of active personal dosimeters in hospitals: EURADOS survey”. In: *Journal of Radiological Protection* 38.2 (May 2018), pp. 702–715. DOI: 10.1088/1361-6498/aabce1.

[12] European Radiation Dosimetry Group e. V. *EURADOS Report 2012-02. ORAMED: Optimization of Radiation Protection of Medical Staff*. Braunschweig, Apr. 2012.

[13] M. C. Weisskopf. “An Overview of X-Ray Polarimetry of Astronomical Sources”. In: *Galaxies* 6.1 (2018). DOI: 10.3390/galaxies6010033.

[14] S. V. Vadawale et al. “Hard X-ray polarimetry with Astrosat-CZTI”. In: *A&A* 578 (2015), A73. DOI: 10.1051/0004-6361/201525686.

[15] E. Froejdh. “Hybrid Pixel Detectors Characterization and Optimization”. PhD thesis. Mid Sweden University, Sept. 2015.

[16] A. Sopczak. “Timepix3 Luminosity Determination of 13-TeV Proton–Proton Collisions at the ATLAS Experiment”. In: *IEEE Transactions on Nuclear Science* 67.4 (2020), pp. 609–616. DOI: 10.1109/TNS.2020.2966679.

[17] S. Procz et al. “X-ray and gamma imaging with Medipix and Timepix detectors in medical research”. In: *Radiation Measurements* 127 (2019), p. 106104. DOI: 10.1016/j.radmeas.2019.04.007.

[18] N. Stoffle et al. “Timepix-based radiation environment monitor measurements aboard the International Space Station”. In: *Nuclear Instruments and Methods in Physics Research Section A: Accelerators, Spectrometers, Detectors and Associated Equipment* 782 (2015), pp. 143–148. DOI: 10.1016/j.nima.2015.02.016.

[19] S. Schmidt. “Dosimetry and X-ray spectroscopy with the photon counting pixel detector Dosepix”. PhD thesis. Friedrich-Alexander-Universität Erlangen-Nürnberg, Apr. 2021.

[20] D. Haag et al. “Personal Dosimetry in Continuous Photon Radiation Fields With the Dosepix Detector”. In: *IEEE Transactions on Nuclear Science* 68.5 (May 2021), pp. 1129–1134. DOI: 10.1109/TNS.2021.3068832.

[21] T. Michel and J. Durst. “Evaluation of a hybrid photon counting pixel detector for X-ray polarimetry”. In: *Nuclear Instruments and Methods in Physics Research Section A: Accelerators, Spectrometers, Detectors and Associated Equipment* 594.2 (2008), pp. 188–195. DOI: 10.1016/j.nima.2008.06.024.

[22] T. Michel, J. Durst, and J. Jakubek. “X-ray polarimetry by means of Compton scattering in the sensor of a hybrid photon counting pixel detector”. In: *Nuclear Instruments and Methods in Physics Research Section A: Accelerators, Spectrometers, Detectors and Associated Equipment* 603.3 (2009), pp. 384–392. DOI: 10.1016/j.nima.2009.02.032.

[23] F. E. Emery and T. A. Rabson. “Average Energy Expended Per Ionized Electron-Hole Pair in Silicon and Germanium as a Function of Temperature”. In: *Phys. Rev.* 140 (6A Dec. 1965), A2089–A2093. DOI: 10.1103/PhysRev.140.A2089.

[24] H. G. Spieler and E. E. Haller. "Assessment of Present and Future Large-Scale Semiconductor Detector Systems". In: *IEEE Transactions on Nuclear Science* 32.1 (1985), pp. 419–426. DOI: 10.1109/TNS.1985.4336867.

[25] E. Gatti et al. "Dynamics of electrons in drift detectors". In: *Nuclear Instruments and Methods in Physics Research Section A: Accelerators, Spectrometers, Detectors and Associated Equipment* 253.3 (1987), pp. 393–399. DOI: 10.1016/0168-9002(87)90522-5.

[26] A. Korn. "Spektrale und bildgebende Eigenschaften photonenzählender Röntgendetektoren am Beispiel des Medipix-Detektors". PhD thesis. Friedrich-Alexander-Universität Erlangen-Nürnberg, May 2007.

[27] Medipix Collaboration. URL: https://medipix.web.cern.ch/.

[28] W. Wong. "A Hybrid Pixel Detector ASIC with Energy Binning for Real-Time, Spectroscopic Dose Measurements". PhD thesis. Mid Sweden University, May 2012.

[29] A. Krzyzanowska et al. "Characterization of the Photon Counting CHASE Jr., Chip Built in a 40-nm CMOS Process With a Charge Sharing Correction Algorithm Using a Collimated X-Ray Beam". In: *IEEE Transactions on Nuclear Science* 64.9 (2017), pp. 2561–2568. DOI: 10.1109/TNS.2017.2734821.

[30] CERN. URL: https://home.cern/.

[31] Erlangen Centre for Astroparticle Physics. URL: https://ecap.nat.fau.de/.

[32] IBA dosimetry. URL: https://www.iba-dosimetry.com.

[33] T. Gabor. *Simulation und Experimente zur Anwendung eines neuartigen spektroskopischen Pixeldetektors in der Personendosimetrie*. Diplomarbeit, Friedrich-Alexander-Universität Erlangen-Nürnberg (FAU). 2012.

[34] I. Ritter. "Evaluation of a novel energy resolving X-ray detector for radiation monitoring". PhD thesis. Friedrich-Alexander-Universität Erlangen-Nürnberg, 2014.

[35] P. Sievers. *Optimierung und Simulationen zur Messung der Personendosis mit einem neuartigen photonenzählenden Pixeldetektor*. Diplomarbeit, Friedrich-Alexander-Universität Erlangen-Nürnberg (FAU). 2009.

[36] W.S. Wong et al. "A pixel detector asic for dosimetry using time-over-threshold energy measurements". In: *Radiation Measurements* 46.12 (Dec. 2011), pp. 1619–1623. DOI: 10.1016/j.radmeas.2011.06.061.

[37] D. Haag. "Active personal dosimetry with the hybrid pixelated DOSEPIX detector". MA thesis. Friedrich-Alexander-Universität Erlangen-Nürnberg (FAU), 2018.

[38] W. Wong. *Dosepix Readout Chip Description 16.1*. 2016.

[39] T. Poikela et al. "Timepix3: a 65K channel hybrid pixel readout chip with simultaneous ToA/ToT and sparse readout". In: 9.05 (May 2014), pp. C05013–C05013. DOI: 10.1088/1748-0221/9/05/c05013.

[40] H. Krieger. *Grundlagen der Strahlungsphysik und des Strahlenschutzes*. Wiesbaden: Teubner Verlag, 2017.

[41] E.B. Podgorsak. *Radiation Physics for Medical Physicists*. Berlin Heidelberg: Springer Verlag, 2010.

[42] International atomic energy agency (IAEA). *Diagnostic Radiology Physics: A Handbook for Teachers and Students*. Vienna: IAEA, 2014.

[43] M. Stabin. *Fundamentals of Nuclear Medicine Dosimetry*. Berlin Heidelberg: Springer Verlag, 2008.

[44] M.J. Berger et al. *XCOM: Photon Cross Sections Database*. DOI: https://dx.doi.org/10.18434/T48G6X.

[45] R. Bellazzini et al. "X-ray polarimetry with a micro pattern gas detector with pixel readout". In: *IEEE Transactions on Nuclear Science* 49.3 (2002), pp. 1216–1220. DOI: 10.1109/TNS.2002.1039640.

[46] F. Ravotti. "Dosimetry Techniques and Radiation Test Facilities for Total Ionizing Dose Testing". In: *IEEE Transactions on Nuclear Science* 65.8 (Aug. 2018), pp. 1440–1464. DOI: 10.1109/TNS.2018.2829864.

[47] International Commission on Radiological Protection. URL: https://www.icrp.org/.

[48] International Commission on Radiation Units. URL: https://www.icru.org/.

[49] P. Andreo. *Fundamentals of Ionizing Radiation Dosimetry*. Weinheim: WILEY-VCH, 2017.

[50] W.G.Alberts P. Ambrosi et al. *New dose quantities in radiation protection*. 1995.

[51] International Comission on Radiation Units and Measurements. *ICRU Report 51, Quantities and Units in Radiation Protection Dosimetry*. 1980.

[52] ICRP. *Assessment of Radiation Exposure of Astronauts in Space*. ICRP Publication 123. Ann. ICRP 42(4).

[53] International Commission on Radiation Units. "Report 57". In: *Journal of the International Commission on Radiation Units and Measurements* os29.2 (Apr. 2016), NP–NP. ISSN: 1473-6691. DOI: https://doi.org/10.1093/jicru/os29.2.Report57.

[54] U. Ankerhold. "Catalogue of X-ray spectra and their characteristic data : ISO and DIN radiation qualities, therapy and diagnostic radiation qualities, unfiltered X-ray spectra." In: *Catalogue of X-ray spectra and their characteristic data : ISO and DIN radiation qualities, therapy and diagnostic radiation qualities, unfiltered X-ray spectra.* (2000). DOI: https://doi.org/10.7795/110.20190315B.

[55] R. Behrens. "Conversion coefficients for $H'(3;\Omega)$ for photons". In: *Journal of Radiological Protection* 37.2 (Mar. 2017), pp. 354–378. DOI: 10.1088/1361-6498/aa51e8.

[56] K. Bairlein et al. "CONVERSION COEFFICIENTS FROM AIR KERMA TO DIRECTIONAL DOSE EQUIVALENT $H'(0.07)$ FOR PHOTONS". In: *Radiation Protection Dosimetry* 186.4 (Apr. 2019), pp. 513–519. DOI: 10.1093/rpd/ncz060.

[57] R. Behrens. "Air kerma to dose equivalent conversion coefficients not included in ISO 4037-3". In: *Radiation Protection Dosimetry* 147.3 (Dec. 2010), pp. 373–379. DOI: 10.1093/rpd/ncq459.

[58] G. Gualdrini et al. “Air kerma to HP(3) conversion coefficients for photons from 10 keV to 10 MeV, calculated in a cylindrical phantom”. In: *Radiation Protection Dosimetry* 154.4 (Oct. 2012), pp. 517–521. DOI: 10.1093/rpd/ncs269.

[59] International Organization of Standardization (ISO). *Reference radiation fields for radiation protection — Definitions and fundamental concepts*. ISO 29661:2012.

[60] A. Endo on behalf of ICRU Report Committee 26 on Operational Radiation Protection Quantities for External Radiation. “Operational quantities and new approach by ICRU”. In: *Annals of the ICRP* 45.1_suppl (2016), pp. 178–187. DOI: 10.1177/0146645315624341.

[61] M. Voytchev, R. Behrens, and R. Radev. “Latest updates for the IEC standards for active and passive dosemeters”. In: *Radiation Physics and Chemistry* 166 (2020), p. 108509. DOI: 10.1016/j.radphyschem.2019.108509.

[62] European Commission. *RADIATION PROTECTION NO 160. Technical Recommendations for Monitoring Individuals Occupationally Exposed to External Radiation*. European Commission, 2009. URL: https://ec.europa.eu/energy/sites/ener/files/documents/160.pdf.

[63] T. Michel et al. “Low Energy Dosimetry With Photon Counting Pixel Detectors Such as Medipix”. In: *IEEE Transactions on Nuclear Science* 56.2 (Apr. 2009), pp. 417–423. DOI: 10.1109/TNS.2009.2015229.

[64] Physikalisch-Technische Bundesanstalt. *PTB-Anforderungen PTB-A 23.3: Strahlenschutzmessgeräte; Ortsdosimeter zur Messung der Umgebungs- und Richtungs Äquivalentdosis und der Umgebungs- und Richtungs- Äquivalentdosisleistung*. Nov. 2013.

[65] Physikalisch-Technische Bundesanstalt. *Ergänzung der PTB-Anforderungen PTB-A 23.3: Strahlenschutzmessgeräte; Ortsdosimeter zur Messung der Umgebungs und Richtungs- Äquivalentdosis und der Umgebungs- und Richtungs-Äquivalentdosisleistung*. Nov. 2018.

[66] International Electrotechnical Commission (IEC). *Radiation protection instrumentation - Ambient and/or directional dose equivalent (rate) meters and/or monitors for beta, X and gamma radiation - Part 1: Portable workplace and environmental meters and monitors*. IEC 60846-1:2009.

[67] International Organization of Standardization (ISO). *Radiological protection—X and Gamma Reference Radiation for Calibrating Dosemeters and Doserate Meters and for Determining their Response as a Function of Photon Energy—Part 1: Radiation Characteristics and Production Methods*. ISO 4037-1:2019.

[68] International Electrotechnical Commission (IEC). *Medical electrical equipment - Dosimeters with ionization chambers and/or semiconductor detectors as used in X-ray diagnostic imaging*. IEC 61674:2012.

[69] Physikalisch-Technische Bundesanstalt. *Ergänzung der PTB-Anforderungen PTB-A 23.2: Strahlenschutzmessgeräte; Personendosimeter zur Messung der Tiefen- und Oberflächen-Personendosis*. Nov. 2018.

[70] SIEMENS. https://www.oem-xray-components.siemens.com/x-ray-tube.

[71] S. M. Seltzer J. H. Hubbell. *Tables of X-Ray Mass Attenuation Coefficients and Mass Energy-Absorption Coefficients 1 keV to 20 MeV for Elements Z = 1 to 92 and 48 Additional Substances of Dosimetric Interest*. NIST, 1995.

[72] G. Hernandez and F. Fernandez. "A model of tungsten anode x-ray spectra". In: *Medical Physics* 43.8 Part1 (July 2016), pp. 4655–4664. DOI: 10.1118/1.4955120.

[73] G. Hernández and F. Fernández. "xpecgen: A program to calculate x-ray spectra generated in tungsten anodes". In: *Journal of Open Source Software* 1.7 (2016), p. 62. DOI: 10.21105/joss.00062.

[74] International Organization of Standardization (ISO). *Radiological protection—X and Gamma Reference Radiation for Calibrating Dosemeters and Doserate Meters and for Determining their Response as a Function of Photon Energy—Part 3: Calibration of Area and Personal Dosemeters and the Measurement of their Response as a Function of Energy and Angle of Incidence*. ISO 4037-3:2019.

[75] M. Newville et al. *lmfit/lmfit-py 1.0.0, Zenodo*. DOI: https://doi.org/10.5281/zenodo.3588521.

[76] International Electrotechnical Commission (IEC). *Medical diagnostic X-ray equipment - Radiation conditions for use in the determination of characteristics*. IEC 61267:2005.

[77] IAEA. *Radiation Protection and Safety of Radiation Sources: International Basic Safety Standards. IAEA Safety Standards Series No. GSR Part 3. International Atomic Energy Agency*. Vienna 2014.

[78] M. Sommer, A. Jahn, and J. Henniger. "A new personal dosimetry system for HP(10) and HP(0.07) photon dose based on OSL-dosimetry of beryllium oxide". In: *Radiation Measurements* 46.12 (2011). Proceedings of the 16th Solid State Dosimetry Conference , September 19-24 , Sydney , Australia, pp. 1818–1821. DOI: 10.1016/j.radmeas.2011.07.002.

[79] C. Texier et al. "Study of the Photon Radiation Performance of Electronic Personal Dosemeters". In: *Radiation Protection Dosimetry* 96.1-3 (July 2001), pp. 245–249. DOI: 10.1093/oxfordjournals.rpd.a006593.

[80] International Electrotechnical Commission (IEC). *Radiological protection - Characteristics of reference pulsed radiation - Part 1: Photon radiation*. ISO/TS 18090-1:2015.

[81] I. Clairand et al. "Active personal dosemeters in interventional radiology: Tests in laboratory conditions and in hospitals". In: *Radiation Protection Dosimetry* 144.1-4 (Mar. 2011), pp. 453–458. DOI: 10.1093/rpd/ncq556.

[82] D. Haag et al. *Personal Dosimetry in Pulsed Photon Fields with the Dosepix Detector*. 2021. arXiv: 2106.06714 [physics.med-ph].

[83] Physikalisch-Technische Bundesanstalt. *PTB-Anforderungen PTB-A 23.2: Strahlenschutzmessgeräte; Personendosimeter zur Messung der Tiefen- und Oberflächen-Personendosis*. Nov. 2013.

[84] DIN IEC 61526 (VDE 0492-1:2020-08). *Radiation protection instrumentation—Measurement of personal dose equivalents Hp(10) and Hp(0,07) for X, gamma, neutron and beta radiations—direct reading personal dose equivalent meters*. IEC 45B/960/CD:2020.

[85] DIN ISO 6980-1 (VDE 0412-6980-1:2020-09). *Nuclear energy—Reference beta-particle radiation—Part 1: Methods of production*. ISO/CD 6980-1:2019.

[86] R. Behrens. *Monitoring the Eye Lens*. Presented at IRPA 13 Glasgow. [Online]. Available: "https://www.ptb.de/cms/fileadmin/internet/fachabteilungen/abteilung_6/6.3/f_u_e/ts7e_3.pdf".

[87] T. Michel et al. "A fundamental method to determine the signal-to-noise ratio (SNR) and detective quantum efficiency (DQE) for a photon counting pixel detector". In: *Nuclear Instruments and Methods in Physics Research Section A: Accelerators, Spectrometers, Detectors and Associated Equipment* 568.2 (Dec. 2006), pp. 799–802. DOI: 10.1016/j.nima.2006.08.115.

[88] R. Behrens. "Simulation of the radiation fields of the Beta Secondary Standard BSS 2". In: *Journal of Instrumentation* 8.02 (Feb. 2013), P02019. DOI: 10.1088/1748-0221/8/02/p02019.

[89] P. Ambrosi, G. Buchholz, and K. Helmstädter. "The PTB Beta Secondary Standard BSS 2 for radiation protection". In: *Journal of Instrumentation* 2.11 (Nov. 2007), P11002–P11002. DOI: 10.1088/1748-0221/2/11/p11002. URL: https://doi.org/10.1088/1748-0221/2/11/p11002.

[90] DIN ISO 6980-3 (VDE 0412-6980-3:2020-10). *Nuclear energy—Reference beta-particle radiation—Part 3: Calibration of area and personal dosemeters and the determination of their response as a function of beta radiation energy and angle of incidence*. ISO/CD 6980-3:2019.

[91] R. Behrens. "Addendum: Simulation of the radiation fields of the Beta Secondary Standard BSS 2". In: *Journal of Instrumentation* 14.07 (July 2019), A07001–A07001. DOI: 10.1088/1748-0221/14/07/a07001.

[92] Mirion Technologies Dosimetrieservice (AWST). *Technical datasheet of the electronic personal dosimeter EPD Mk2*. URL: https://awst.mirion.com/wp-content/uploads/2020/08/FO75KOM01B-Technisches-Datenblatt-EPD.pdf.

[93] M.J. Berger et al. *Stopping-Power and Range Tables for Electrons, Protons, and Helium Ions*. DOI: https://dx.doi.org/10.18434/T4NC7P.

[94] A. Delgado. *Mixed Field Dosimetry*. IRPA-10, 10th International Congress of the International Radiation Protection Association. [Online]. Available: "https://www.irpa.net/irpa10/pdf/E12.pdf". 2000.

[95] B. V. Worgul et al. "Cataracts among Chernobyl Clean-up Workers: Implications Regarding Permissible Eye Exposures". In: *Radiation Research* 167.2 (2007), pp. 233–243. DOI: 10.1667/RR0298.1.

[96] G. Chodick et al. "Risk of Cataract after Exposure to Low Doses of Ionizing Radiation: A 20-Year Prospective Cohort Study among US Radiologic Technologists". In: *American Journal of Epidemiology* 168.6 (July 2008), pp. 620–631. DOI: 10.1093/aje/kwn171.

[97] E. A. Ainsbury et al. “Radiation Cataractogenesis: A Review of Recent Studies”. In: *Radiation Research* 172.1 (2009), pp. 1–9. DOI: 10.1667/RR1688.1.

[98] M. M. Rehani et al. “Radiation and cataract”. In: *Radiation Protection Dosimetry* 147.1-2 (July 2011), pp. 300–304. DOI: 10.1093/rpd/ncr299.

[99] CORDIS. URL: https://cordis.europa.eu/project/id/211361/reporting.

[100] G. Gualdrini et al. “A new cylindrical phantom for eye lens dosimetry development”. In: *Radiation Measurements* 46.11 (2011). International Workshop on Optimization of Radiation Protection of Medical Staff, ORAMED 2011, pp. 1231–1234. DOI: 10.1016/j.radmeas.2011.08.025.

[101] Physikalisch-Technische Bundesanstalt Braunschweig und Berlin. URL: https://www.ptb.de/cms/fileadmin/internet/fachabteilungen/abteilung_6/6.3/bap/lst23_2n.pdf.

[102] E. A. Ainsbury et al. “Public Health England survey of eye lens doses in the UK medical sector”. In: *Journal of Radiological Protection* 34.1 (Nov. 2013), pp. 15–29. DOI: 10.1088/0952-4746/34/1/15.

[103] J. Domienik et al. “Extremity and eye lens doses in interventional radiology and cardiology procedures: first results of the ORAMED project”. In: *Radiation Protection Dosimetry* 144.1-4 (Dec. 2010), pp. 442–447. DOI: 10.1093/rpd/ncq508.

[104] G. Gualdrini et al. “Eye lens dosimetry: task 2 within the ORAMED project”. In: *Radiation Protection Dosimetry* 144.1-4 (Feb. 2011), pp. 473–477. DOI: 10.1093/rpd/ncr011.

[105] P. Bilski et al. “The new EYE-D™ dosemeter for measurements of HP(3) for medical staff”. In: *Radiation Measurements* 46.11 (2011). International Workshop on Optimization of Radiation Protection of Medical Staff, ORAMED 2011, pp. 1239–1242. DOI: 10.1016/j.radmeas.2011.04.031.

[106] J. Strohmaier and C. Naber. *Untersuchungen zur Strahlenexposition der Augenlinse von beruflich strahlenexponiertem Personal - Vorhaben 3613S40011*. URL: https://doris.bfs.de/jspui/handle/urn:nbn:de:0221-2017112214449.

[107] RaySafeI2. URL: %7Bhttps://www.raysafe.com/sites/default/files/2018-12/5200037-c_i2_spec_leaflet_raysafe_en_web.pdf%7D.

[108] J. Cardoso et al. “CHARACTERIZATION OF AN ACTIVE DOSEMETER ACCORDING TO IEC 61526:2010”. In: *Radiation Protection Dosimetry* 170.1-4 (Sept. 2016), pp. 127–131. DOI: 10.1093/rpd/ncw090.

[109] RaySafeI3. URL: %7Bhttps://www.landauer.com/sites/default/files/product-specification-file/RaySafe$%5C%$20i3.pdf%7D.

[110] DIN-6818-1. *Strahlenschutzdosimeter - Teil 1: Allgemeine Regeln*. Beuth Verlag, Berlin, 2004.

[111] H. Hoedlmoser et al. “New eye lens dosemeters for integration in radiation protection glasses”. In: *Radiation Measurements* 125 (May 2019). DOI: 10.1016/j.radmeas.2019.05.002.

[112] F. Bayer. *Simulationen zur Anwendung photonenzählender pixelierter Halbleiterdetektoren in der Röntgenpolarimetrie*. Diplomarbeit, Friedrich-Alexander-Universität Erlangen-Nürnberg (FAU). 2012.

[113] F. Lei, A.J Dean, and G.L Hills. "Compton Polarimetry in Gamma-Ray Astronomy". In: *Space Science Reviews* 82.3 (1997), pp. 3009–388. DOI: 10.1023/A:1005027107614.

[114] T. Mizuno et al. "Beam test of a prototype detector array for the PoGO astronomical hard X-ray/soft gamma-ray polarimeter". In: *Nuclear Instruments and Methods in Physics Research Section A: Accelerators, Spectrometers, Detectors and Associated Equipment* 540.1 (2005), pp. 158–168. DOI: 10.1016/j.nima.2004.11.009.

[115] S. Lotti et al. "Polarization studies with NuSTAR". In: *Proc SPIE* 8443 (July 2012). DOI: 10.1117/12.925989.

[116] M. C. Weisskopf et al. "Measurement of the X-ray polarization of the Crab nebula." In: *Astrophysical Journal* 208 (Sept. 1976), pp. L125–L128. DOI: 10.1086/182247.

[117] M. C. Weisskopf et al. "A precision measurement of the X-ray polarization of the Crab Nebula without pulsar contamination." In: *Astrophysical Journal* 220 (Mar. 1978), pp. L117–L121. DOI: 10.1086/182648.

[118] W. Coburn and S. E. Boggs. "Polarization of the prompt γ-ray emission from the γ-ray burst of 6 December 2002". In: *Nature* 423.6938 (May 2003), pp. 415–417. DOI: 10.1038/nature01612. arXiv: astro-ph/0305377 [astro-ph].

[119] P. Laurent et al. "Polarized Gamma-Ray Emission from the Galactic Black Hole Cygnus X-1". In: *Science* 332.6028 (Apr. 2011), p. 438. DOI: 10.1126/science.1200848. arXiv: 1104.4282 [astro-ph.HE].

[120] E. Jourdain et al. "SEPARATION OF TWO CONTRIBUTIONS TO THE HIGH ENERGY EMISSION OF CYGNUS X-1: POLARIZATION MEASUREMENTS WITHINTEGRALSPI". In: *The Astrophysical Journal* 761.1 (Nov. 2012), p. 27. DOI: 10.1088/0004-637x/761/1/27.

[121] M. Forot et al. "Polarization of the Crab Pulsar and Nebula as Observed by the INTEGRAL /IBIS Telescope". In: *The Astrophysical Journal* 688.1 (Nov. 2008), pp. L29–L32. DOI: 10.1086/593974.

[122] M. C. Weisskopf et al. "The Imaging X-ray Polarimetry Explorer (IXPE)". In: *Results in Physics* 6 (2016), pp. 1179–1180. DOI: 10.1016/j.rinp.2016.10.021.

[123] J. Jakubek. "Precise energy calibration of pixel detector working in time-over-threshold mode". In: *Nuclear Instruments and Methods in Physics Research Section A: Accelerators, Spectrometers, Detectors and Associated Equipment* 633 (2011). 11th International Workshop on Radiation Imaging Detectors (IWORID), S262–S266. DOI: 10.1016/j.nima.2010.06.183.

[124] S. Reza et al. "Smart dosimetry by pattern recognition using a single photon counting detector system in time over threshold mode". In: *Journal of Instrumentation* 7.1 (Jan. 2012), pp. C01027–C01027. DOI: 10.1088/1748-0221/7/01/c01027.

[125] H. Tsunemi et al. "Detection of X-ray polarization with a charge coupled device". In: *Nuclear Instruments and Methods in Physics Research Section A:*

Accelerators, Spectrometers, Detectors and Associated Equipment 321.3 (1992), pp. 629–631. DOI: 10.1016/0168-9002(92)90075-F.

[126] International Atomic Energy Agency. *Live Chart of Nuclides*. URL: https://www-nds.iaea.org/relnsd/vcharthtml/VChartHTML.html.

[127] S. Agostinelli et al. "Geant4—a simulation toolkit". In: *Nuclear Instruments and Methods in Physics Research Section A: Accelerators, Spectrometers, Detectors and Associated Equipment* 506.3 (2003), pp. 250–303. ISSN: 0168-9002. DOI: https://doi.org/10.1016/S0168-9002(03)01368-8.

[128] J. Allison et al. "Geant4 developments and applications". In: *IEEE Transactions on Nuclear Science* 53.1 (2006), pp. 270–278. DOI: 10.1109/TNS.2006.869826.

[129] J. Allison et al. "Recent developments in Geant4". In: *Nuclear Instruments and Methods in Physics Research Section A: Accelerators, Spectrometers, Detectors and Associated Equipment* 835 (2016), pp. 186–225. ISSN: 0168-9002. DOI: https://doi.org/10.1016/j.nima.2016.06.125.

Acknowledgements

Ich möchte den folgenden Personen und Institutionen für die Unterstützung während meiner Doktorarbeit danken:

Thilo Michel. Danke für die Möglichkeit der Promotion bei dir. Während der Zeit hier habe sehr viel mitgenommen. Auch ein herzliches Danke dafür, dass du dir Zeit genommen hast einige Themen in dieser Arbeit genauer mit mir durchzugehen.

Sebastian Schmidt. Großes Danke für das viele Lesen von Teilen der Arbeit und den konstruktiven und lustigen Dialogen zu allen möglichen Themen!

Florian Beißer. Danke für das Lesen des Kapitels zur Augenlinsendosimetrie und für die Messungen mit dem Augenlinsendosimeter Prototypen.

Arbeitsgruppe Dosimetrie am ECAP. Danke für die sehr angenehme und lebhafte Arbeitsatmosphäre. Es war stets interessant und vor allem amüsant mit euch.

Fachbereich 6.3 der PTB. Danke für anregenden Gespräche in Bezug auf Dosimetrie und für die Möglichkeit des Messens an euren Bestrahlungsanlagen.

Meiner Familie. Herzliches Danke, dass ihr stets für mich da gewesen seid und mich in allen Lebenslagen unterstützt habt!